



**HAL**  
open science

# Transition ductile-fragile du PVC plastifié à différentes vitesses d'impact : compréhension des mécanismes et modélisation

Clément Bertaux

## ► To cite this version:

Clément Bertaux. Transition ductile-fragile du PVC plastifié à différentes vitesses d'impact : compréhension des mécanismes et modélisation. Matériaux. Université Paris sciences et lettres, 2021. Français. NNT : 2021UPSLM058 . tel-03648526

**HAL Id: tel-03648526**

**<https://pastel.hal.science/tel-03648526>**

Submitted on 21 Apr 2022

**HAL** is a multi-disciplinary open access archive for the deposit and dissemination of scientific research documents, whether they are published or not. The documents may come from teaching and research institutions in France or abroad, or from public or private research centers.

L'archive ouverte pluridisciplinaire **HAL**, est destinée au dépôt et à la diffusion de documents scientifiques de niveau recherche, publiés ou non, émanant des établissements d'enseignement et de recherche français ou étrangers, des laboratoires publics ou privés.



**THÈSE DE DOCTORAT**

**DE L'UNIVERSITÉ PSL**

Préparée à MINES ParisTech

**Ductile to brittle transition of plasticized PVC at different impact speeds: understanding of the mechanisms and modelling**

**Transition ductile-fragile du PVC plastifié à différentes vitesses d'impact : compréhension des mécanismes et modélisation**

Soutenue par

**Clément BERTAUX**

Le 17 décembre 2021

Ecole doctorale n° 621

**Ingénierie des systèmes,  
Matériaux, Mécanique,  
Énergétique**

Spécialité

**Sciences et génie des  
matériaux**

**Composition du jury :**

Rafael ESTEVEZ Professeur, Grenoble INP (France)	<i>Président du jury Rapporteur</i>
Gerald PINTER Professeur, Université de Leoben (Autriche)	<i>Rapporteur</i>
KlaraLOOS Docteur, Université de la Bundeswehr, München (Allemagne)	<i>Examineur</i>
Moussa NAÏT ABDELAZIZ Professeur, Polytech Lille (France)	<i>Examineur</i>
CristianOVALLE-RODAS Docteur, Mines ParisTech PSL (France)	<i>Examineur</i>
NicolasAMOUROUX Docteur, Westlake Nakan	<i>Examineur</i>
LucienLAIARINANDRASANA Directeur de recherche, Mines ParisTech PSL	<i>Directeur de thèse</i>





# Acknowledgement

Many thanks to everybody who has made this work possible.

I would like to humbly thank the members of the jury for their involvement in my work, their time, and the discussion during the defense. A special thanks to Rafael Estevez who beat the COVID and a public transportation strike to preside over the jury, on top of being my “rapporteur”. Klara Loos, Gerald Pinter and Moussa Naït Abdelaziz, it would have been a pleasure to do it in front of you, but unfortunately special events made it difficult for you to come to Paris. I thank you, and hope you enjoyed our time together during the defense as much as I did.

Thanks a lot to NAKAN and all the people there who supported me during my research, in chronological order: Nicolas Amouroux, Pascal Marly, Cedric Pasquet, Gabriel Dalloux and Gregory Martin. I hope I gave you as much as I learned from you.

To my supervisors, thank you from the bottom of my heart for your time and support. I have learned so much from you in science. You have always believed in my results and me, and coped with my “strong personality”. Lucien, your strong experience guided my research while leaving me with the final word, when the time came to make decisions. Cristian, you arrived on the project close to the end, but you were there when I had questions and needed help to write.

This work would have never been done without the help of the Centre des Matériaux’s team. Especially without Jean-Christophe. JC, you can’t imagine how important the time with you was to me. You showed me how with a little imagination you can adapt any instrument to analyze “weird” materials. Thank you Stephanie for your fast reaction whenever I needed help. And of course I cannot forget all the other persons for your help whenever I needed it, wherever it was administrative: Catherine, Véronique, Christine and Zak; DIY: René, Vasco, Frédéric and Franck; microscopy: Maria, Gérard, Antoine and Kévin; or the members of the lab who always had a nice word to support me: Anne-Françoise, Marie-Hélène, Samuel, Vladimir and many others.

Thanks to my new friends who made the time fly during this PhD, I was happy to find you there : Chloé, Jonathan, Lenny, Xiang, Aaron, Yannick, Nicolas, Clément, Houssein. Some of you even became some of my closest friends and always had a moment for me when I needed it the most : Jean-Michel, Juan Manuel, Rossen, Alice, Aurélien and Sébastien. See you soon pals!

Thank you to all the people who made this journey possible, from my parents who motivated me for my DUT whereas I was not fond of studies, and supported me when I wanted to

continue in Engineering school. Claire, helping you revise made it easier to find my own path! Thank you Laure for your strong support, you helped me a lot in succeeding my studies since engineering school, and in decision making for my future. You also welcomed me in your family who was always there for support. Thanks a lot Lydie, Patrick and Jeanne.

Laure, you were already cited, but if anybody should be mentioned twice it could only be you. I know I was not always easy to leave during this PhD time but you never let me down, and motivated me back, it didn't matter how hard you needed to kick my \*\*\* in order to put me back on track, you did it tirelessly. I don't know if one day I might have the opportunity to repay you, the love of my life. But one thing I am sure about, I am never ever gonna make you endure it again. Thank you my love.



<b>CHAP 1 :Introduction</b>	<b>7</b>
<b>1. Introduction</b>	<b>8</b>
1.1 Industrial context	8
1.2 Scientific context	10
1.3 Ductile to Brittle Transition Temperature (DBTT)	10
1.3.1 DBTT concepts	10
1.3.1.1 DBTT definition	10
1.3.1.2 DBTT methods of determination	11
1.3.1.3 DBTT determination from results	12
1.3.1.4 DBTT evolution from previous studies	13
1.3.1.5 DBTT transformation into Tdth	14
1.4 Content of the manuscript	15
<b>CHAP 2: Matériaux, échantillons et protocoles expérimentaux</b>	<b>16</b>
<b>2. Materials, specimens, and experimental protocols</b>	<b>17</b>
2.1 Materials	17
2.1.1 Materials for dashboard assembly	17
2.1.1.1 Carrier	17
2.1.1.2 Foam	17
2.1.2 The PVC skin	18
2.1.2.1 Processing and assembly methods	18
2.1.2.2 Physico-chemical characteristics, material controls	21
2.1.2.2.1 Granulometry	21
2.1.2.2.2 Pourability	21
2.1.2.2.3 L*a*b	22
2.1.2.2.4 Glass transition	23
2.1.2.3 Initial microstructure	24
2.1.2.3.1 Optical images	24
2.1.2.3.2 Scanning Electron Microscopy (SEM)	24
2.1.2.3.3 Transmission Electron Microscopy (TEM)	26
2.1.2.3.4 Microtomography	27
2.2 Specimens and structures studied	28
2.2.1 Plates without scoring or unscored	28
2.2.2 Plates with scoring or scored	28
2.2.3 Clamped SENB	29
2.2.4 High Speed Tensile Test's specimens	29
2.3 Experimental protocols	30

2.3.1 Testing machines and associated instrumentation	30
2.3.1.1 Drop tower CEAST9350	30
2.3.1.1.1 Machinery description	30
2.3.1.1.1.1 The clamping system	30
2.3.1.1.1.2 The thermostatic chamber	31
2.3.1.1.1.3 The striker	31
2.3.1.1.2 Data collected and calculated	32
2.3.1.1.3 Test conditions	33
2.3.1.2 Instron High Speed Tensile Test (HSTT)	33
2.3.1.2.1 Testing machine	33
2.3.1.2.1.1 The striker	34
2.3.1.2.1.2 The clamping device	34
2.3.1.2.1.3 The thermostatic chamber	35
2.3.1.2.1.4 The video camera	35
2.3.1.2.2 Data collected	35
2.3.1.2.3 Filtering data using High Passing Band Sensor	36
2.3.1.2.4 Test program	36
2.3.1.3 Instron 5982 for clamped SENB test [43]	37
<b>CHAP3: Mécanismes de rupture sur des échantillons pré-entailés</b>	<b>39</b>
<b>3. Failure mechanisms on precracked specimens</b>	<b>40</b>
3.1 Introduction and organization of the article	40
3.2 Ductile crack initiation and growth on a plasticized Polyvinylchloride during airbag deployment	41
3.2.1 Introduction	41
3.2.2 Background	43
3.2.3 Methods	45
3.2.3.1 Experiments	45
3.2.3.2 Load parameters - Failure criteria	46
3.2.3.2.1 Fractured surface energy density ( $\Gamma$ )	47
3.2.3.2.2 J-integral (J)	47
3.2.3.3 Finite Elements (FE)	48
3.2.4 Results	50
3.2.4.1 SENB experimental data	50
3.2.4.1.1 Crack Opening Displacement (COD)	51
3.2.4.1.2 Crack extension $\Delta a$	55
3.2.4.2 FE simulations	62
3.2.4.2.1 Inverse optimization of the material parameters	62
3.2.4.2.2 Fracture toughness - Elastic calibration factor	63

3.2.4.2.2.1 Fracture toughness $J_c$	63
3.2.4.2.3 Crack propagation	64
3.2.5 Discussion	67
3.2.5.1 From clamped SENB to CEAST test results	67
3.2.5.2 From CEAST results to the full scale test on dashboard	69
3.2.6 Concluding remarks	69
3.3 Conclusion of the article	70
<b>CHAP 4: Essais d'impact</b>	<b>71</b>
<b>4. Impact tests</b>	<b>73</b>
4.1 Impact tests on scored samples	73
4.1.1 Data reduction	73
4.1.1.1 Raw data from testing machines	73
4.1.1.2 Data treatment	74
4.1.2 Selection of experimental data: $R$ , $F_{nl}$ , $Fr$ , $d(F_{nl})$ , $d(Fr)$	77
4.1.3 Comparison of CEAST - HSTT tests at 10 m/s	79
4.1.3.1 Evolution of the impact speed with respect to the deflection	79
4.1.3.2 Instantaneous impact speeds at failure	81
4.1.3.3 Evolution of the stiffness as a function of the test temperature	82
4.1.3.4 $d(F_{nl})$ : deflection at the appearance of the nonlinearity	83
4.1.3.5 $F_{nl}$ : Load at the appearance of the non linearity	84
4.1.3.6 $Enl$ : Energy at the appearance of the nonlinearity	85
4.1.4 Determination of the ductile fracture threshold temperature ( $T_{dth}$ ), comparison between CEAST and HSTT at 10 m/s	88
4.1.5 Extension to impact speeds lower than 10 m/s from CEAST	90
4.1.5.1 Instantaneous impact speeds at failure	90
4.1.5.2 Stiffnesses	91
4.1.5.3 Deflection at failure	92
4.1.5.4 Load at failure	93
4.1.5.5 Energy at failure	94
4.1.5.6 Evolution of $T_{dth}$ with the impact speeds for scored specimens	95
4.1.5.6.1 Plot of the tanh function	95
4.1.5.6.2 $T_{dth}$ determination	96
4.1.6 Extension to impact speeds higher than 10 m/s from HSTT	97
4.1.6.1 Instantaneous impact speeds at failure	97
4.1.6.2 Stiffness	98
4.1.6.3 Deflection at failure	98
4.1.6.4 Load at failure	99
4.1.6.5 Energy at failure	100

4.1.6.6 Evolution of Tdth with the impact speeds for scored specimens	101
4.1.6.6.1 Plot of tanh function	101
4.1.6.6.2 Tdth determination	102
4.1.7 Fracture surfaces for scored samples	102
4.1.7.1 At the macroscopic scale	103
4.1.7.2 At the microscopic scale	104
4.2 Impact tests on unscored samples	106
4.2.1 Comparison of CEAST - HSTT tests at 10 m/s	106
4.2.1.1 Instantaneous impact speeds at failure	106
4.2.1.2 Evolution of the Stiffness with the test temperature	106
4.2.1.3 d(Fr): deflection at failure	107
4.2.1.4 Fr: Load at failure	108
4.2.1.5 Er: Energy at failure	109
4.2.2 Determination of the ductile fracture threshold temperature (Tdth), comparison between CEAST and HSTT at 10 m/s	111
4.2.3 Extension to other impact speeds lower than 10 m/s from CEAST	113
4.2.3.1 Instantaneous impact speeds at failure	113
4.2.3.2 Stiffnesses	114
4.2.3.3 Deflection at failure	114
4.2.3.4 Load at failure	115
4.2.3.5 Energy at failure	116
4.2.3.6 Evolution of Tdth with the impact speeds for unscored specimens	117
4.2.3.6.1 Plot of the tanh function	117
4.2.3.6.2 Tdth determination	118
4.2.4 Extension to impact speeds higher than 10 m/s from HSTT	119
4.2.4.1 Instantaneous impact speeds at failure	119
4.2.4.2 Stiffnesses	120
4.2.4.3 Deflection at failure	120
4.2.4.4 Load at failure	121
4.2.4.5 Energy at failure	122
4.2.4.6 Evolution of Tdth with the impact speeds for scored specimens	123
4.2.4.6.1 Using separate deflection at failure curves	123
4.2.4.6.2 Using separate load at failure curves	123
4.2.5 Fracture surfaces for unscored samples	125
4.3 Tdth comparison between scored and unscored samples	126
4.4 Application to another material	127
4.4.1 Introduction of the material	127
4.4.2 Experimental program	127
4.4.3 Results	128

4.5 Conclusions	130
<b>CHAP 5: Conclusion</b>	<b>131</b>
<b>5. Conclusion and prospects</b>	<b>132</b>
5.1 Conclusion	132
5.1.1 Failure mechanisms	132
5.1.2 Impact tests	133
5.2 Prospects	134
5.2.1 Additional experimental studies	135
5.2.1.1 Three layers 4 points bending	135
5.2.1.2 3D DIC on real conditions dashboard opening	138
5.2.1.3 Thermo-mechanical analysis to study self-heating	139
5.2.2 Finite Elements study	139
5.2.2.1 Meshes	139
5.2.2.2 First results	142
<b>References:</b>	<b>144</b>

## CHAP 1 :Introduction

Nakan est un fournisseur de poudres en PVC plastifié utilisées dans l'industrie automobile afin d'être la couche supérieure d'un ensemble de trois couches composant le tableau de bord des voitures. Au niveau de l'airbag passager, le tableau de bord est fragilisé afin de garantir une ouverture rapide et localisée et avoir un airbag gonflé dans les 10ms pour assurer la bonne sécurité des passagers. Cela doit se vérifier à température ambiante, mais aussi à basses et hautes températures. L'expérience a montré que des fissures pouvaient provoquer une fragmentation et une projection de morceaux de tableau de bord lors de tirs airbags à basses températures. Ces projections sont considérées comme étant des sources de blessures potentielles. Une étude continue sur de nouvelles formulations est réalisée par le partenaire industriel afin de réduire ces risques de projections.

Afin de comparer les matériaux entre eux, plusieurs techniques sont sélectionnées par les chimistes de l'industrie automobile. La plus généralement utilisée est la température de transition vitreuse ( $T_g$ ) obtenue grâce à une Analyse Mécanique Dynamique (AMD) ou une calorimétrie différentielle à balayage (DSC). Bien que cette  $T_g$  fournisse des informations sur le comportement physico-chimique/mécanique du matériau, elle ne prend pas en compte sa rupture. C'est pourquoi la notion de température de transition ductile-fragile (DBTT) a été choisie pour approfondir les connaissances sur la rupture des matériaux de l'étude.

Dans la littérature, la DBTT est une notion déterminée majoritairement grâce aux essais d'impact. Elle est généralement caractérisée par une courbe en forme de "S" lorsque sont tracées l'évolution de la ténacité ou la résilience avec la température. Plusieurs index peuvent ensuite être utilisés pour déterminer la DBTT comme le  $TK_7$  ou le  $TK_{68}$ . Une seconde méthode utilisant l'analyse de faciès de rupture peut aussi être utilisée, où cette fois-ci le ratio de surface de rupture ductile/fragile est utilisé: il s'agit de l'index TFATT50.

Plusieurs études ont déjà montré que la DBTT était une notion qui pouvait évoluer en fonction de différents paramètres, comme la composition chimique ou l'historique des sollicitations mécaniques du matériau. Dans cette étude on s'intéressera plutôt à étudier son évolution en fonction de différentes vitesses d'impact. Pour cela une variante à la DBTT a été choisie, qui serait définie comme la température seuil de rupture ductile  $T_{dth}$ , plus adaptée au contexte industriel, et plus restrictive que la DBTT.

Une description complète de la fabrication des matériaux et des échantillons de l'étude, ainsi que les équipements servant aux différents tests sont présentés dans le chapitre 2. Puis le chapitre 3 propose une étude des mécanismes de rupture sur des échantillons entaillés préalablement aux essais d'impacts du Chapitre 4. Enfin le chapitre 5 présentera les conclusions de l'étude, ainsi que différentes perspectives futures.

# 1. Introduction

## 1.1. Industrial context

Nakan is a provider of PVC powder called PVC slush. This powder is used by Original Equipment Manufacturers (OEMs) and transformed into a PVC skin. This PVC skin will then be part of a three-layer assembly (PVC skin-foam-carrier), used in the automotive industry for car dashboard manufacturing.

For security reasons, the assembly is weakened with a scoring on *the inner wall of the skin* and the carrier thickness is highly reduced alongside the scoring. This weakening *is assumed to enable* fast and localised airbag opening. Security standards compel manufacturers to have airbag opening in less than 10 ms after crash. Based on the company's data, when the airbag opens and inflates it has an estimated opening inflation speed between 25 and 50 m/sec. So far, airbag opening is tested in various temperature and impact speed conditions: from -35°C (cold temperature), 25°C (room temperature), and 85°C (hot temperature).



Figure 1.1: Dashboard before an airbag shot test. Grids of 34 cm x 26 cm sizes were set onto the passenger's airbag window so as to follow the deformation field and the crack progress during the test.

Figure 1.1. illustrates a dashboard mock-up before a full scale test of airbag shot. The region of interest is the window in front of the passenger. Grids of 34 cm x 26 cm sizes were painted onto the PVC outer skin allowing the measurement of the full field deformation and to track the crack path during the test; the scoring direction being horizontal in this picture.

Figure 1.2. shows the typical results of the test when the opening of the skin appears:

- Figure 1.2a shows the deformed and cracked skin at  $-35^{\circ}\text{C}$ . Secondary cracks are noticed, that might induce fragmentation and projection on the passenger [1].
- Figure 1.2b, at  $25^{\circ}\text{C}$ , there is no specific risk due to temperature effect; studies at this temperature enable to have data points reference for neat failure alongside the scoring.
- Figure 1.2c at  $85^{\circ}\text{C}$ , the risk to avoid is a too large strain which could cause a delay in airbag opening - beyond airbag required max opening time. This is called the "ballooning effect".

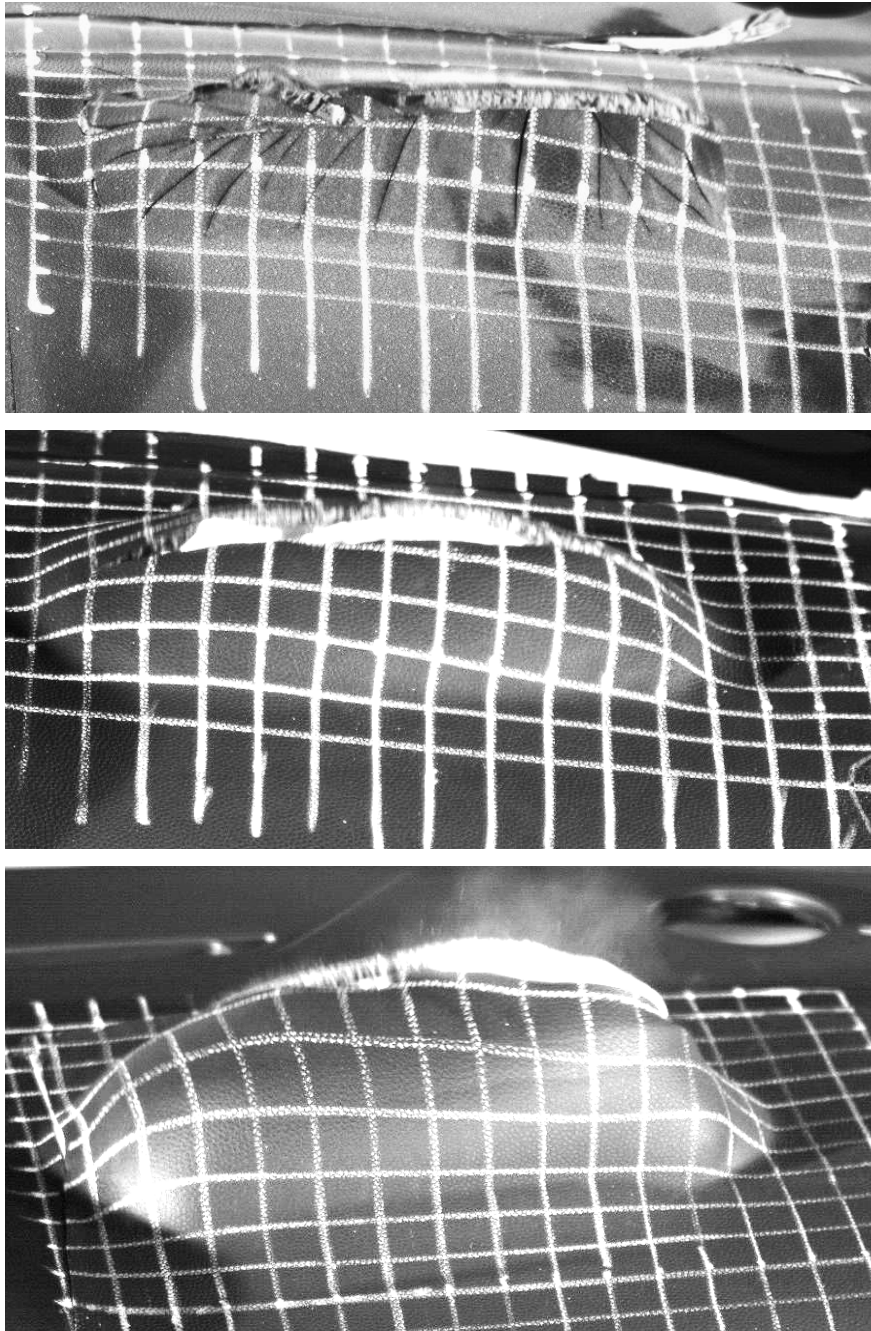


Figure 1.2.: Deformed and cracked grids during the airbag shot tests depending on the temperatures: a)  $= -35^{\circ}\text{C}$  ; b)  $= 25^{\circ}\text{C}$  ; c)  $= 85^{\circ}\text{C}$ .

## 1.2. Scientific context

The objective of the present work is

- To determine the range of test temperatures and impact speeds which allowed an ideal ductile failure of the skin as in Figure 1.2b to be obtained.
- To investigate the effects of a crack-like defect on the material properties, in order to guarantee a failure not brittle and not too ductile.

In the automotive industry, compounders' currently preferred technique to compare materials' properties is Dynamic Mechanical Analysis (DMA) or Digital Scanning Calorimeter (DSC) to obtain the glass transition temperature ( $T_g$ ) as it provides information on physico-chemical/mechanical behavior of the material with the temperature.

In this work, beyond the knowledge of  $T_g$  Ductile to Brittle Transition Temperature (DBTT) will be investigated because it is dealing with the mechanisms of failure.

### 1.2.1. Ductile to Brittle Transition Temperature (DBTT)

The concept of Ductile to Brittle Transition Temperature (DBTT) has been commonly used to characterize materials for such applications. In the literature, the DBTT has been addressed to characterize various industrial structures composed of metals as well as polymers. Three kinds of experiments have been used to define the DBTT:

- Tensile stress–strain curves at various temperatures, strain rates and rubber particles volume fractions of rubber particles [2-7];
- Charpy or Izod impact tests at various temperatures and rubber particles volume fractions [3, 8, 9];
- Fracture mechanics tests for a given specimen geometry (Compact tension or Single Edge Notch Bending) to plot the fracture toughness at various temperatures [10, 11].

The most widely used methods to measure DBTT are impact tests such as Charpy and Izod methods. Those methods consist in studying the evolution of impact strength with respect to temperature, at a constant impact speed.

#### 1.2.1.1. DBTT concepts

##### 1.2.1.1.1. DBTT definition

Ductile to brittle transition temperature (DBTT) is a variable that enables the measurement of the temperature when the material failure changes from ductile to brittle. This variable was first studied on steel but is applicable to multiple materials, including polymers. Charpy was one of the first to work on DBTT with the notion of failure energy at the beginning of

1900's, and developed an instrument to quantify it: the "mouton Charpy", but the definition of DBTT was only determined during World War II. As an example of Charpy's work interest in the industry, following the sinking of the Titanic this method was used to study the Titanic's rivets. After tests analysis, it was realised that the materials did not have the right property: they were brittle and not ductile as they should have been in theory.

Following Charpy's work, DBTT started to be used in monitoring programs for shipbuilding, nuclear industry, and pipes. This enabled engineers to replace the materials before they break. Today, DBTT's applications are still concentrated in those three industrial areas.

#### 1.2.1.1.2. DBTT methods of determination

In the literature, there are two main methods for DBTT determination, used for most materials and experiments: Charpy and Izod [3, 4]. Both of them rely on the same principle: measuring the energy at the failure of the sample. The required instruments are the same: a pendulum with a hammer at its extremity; the weight of the hammer and the hammer-pendulum center length are known.

The hammer is released at a precise and given angle (vs the pendulum vertical). The hammer hits the sample at the vertical of the pendulum (angle = 0°). After the sample's failure, the hammer continues its trajectory up to a new angle with the pendulum vertical. The difference between the release angle and the new angle after impact allows the measurement of the energy absorbed by the material during the impact. The difference between Charpy and Izod methods is due to the material sample's set up during the test.

- Charpy method: the sample is 55mm (length) x 10mm (width) x 10mm (thickness). A notch is machined in the center of the length of the material. The notch can have two different geometries :
  - V-type : the notch root radius  $r$  is equal to 0.25 mm with a depth of 2mm ;
  - U-type : where the notch root radius is set at 1mm and the notch depth is 5mm.

Depending on the geometry, the test will measure the fracture toughness. For this test, the sample was set in order to have both extremities blocked, the hammer will impact the sample on the opposite side to the failure [12].

- Izod method: the sample is 75mm (length) x 10mm (width) x 10mm (thickness). A pre-crack is made in the center of the length of the material. The crack tip has a curvature radius close to zero. The test measures the Izod impact strength, it is a measure of the energy absorbed during the failure divided by the surface of the cross section area of the sample located at the scoring. For this test, one of the sample's extremities is clamped in a vertical position. The other extremity will be impacted by the hammer, on the side of the scoring.

### 1.2.1.1.3. DBTT determination from results

The impact strengths represent the evolution of the material's mechanical properties with a chosen variable (temperature, composition, etc). For example, Figure 1.3 shows energy at failure evolution with temperature. The curve has an S-shaped profile, with a low energy level plateau at the lowest temperatures called "brittle plateau" (100% brittle) and a high energy level plateau at the highest temperatures called "ductile plateau" (100% ductile). In between, there is an area called "transition zone" in which the DBTT is included. In this zone, the sample may present ductile or brittle failure or a combination of both. The brittle and ductile plateaus are also named as lower and upper shelves. The range of temperature of the DBTT can be considered also as a key indicator.

In the literature [13] (in this case for a steel), the DBTT is obtained with three main parameters: TK7, TK68 and TFATT50. The TK7 and TK68 are respectively the temperatures related to an impact strength of 7daJ / cm<sup>2</sup> and an energy at failure of 68 J. The TFATT50 is connected to the crystallinity rate and is considered as the temperature with a crystallinity ratio of 50%.

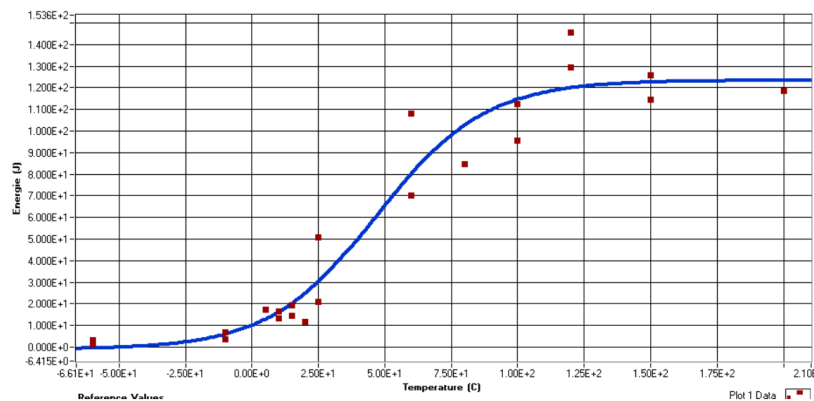


Figure 1.3: Energy at failure evolution with the temperature [13]

The crystallinity rate represents the evolution of the ratio between a brittle part and the total part of a given parameter with a chosen variable (temperature, composition, etc). For example, Figure 1.4 shows the crystallinity evolution with temperature. The curve has also a S-shaped (or a Z-shaped) profile, with a high crystallinity level plateau at the lowest temperatures called "brittle plateau" and a low crystallinity level plateau at the highest temperatures called "ductile plateau". In between, there is an area called "transition zone" in which the DBTT is included. In this zone, the sample is both ductile and brittle.

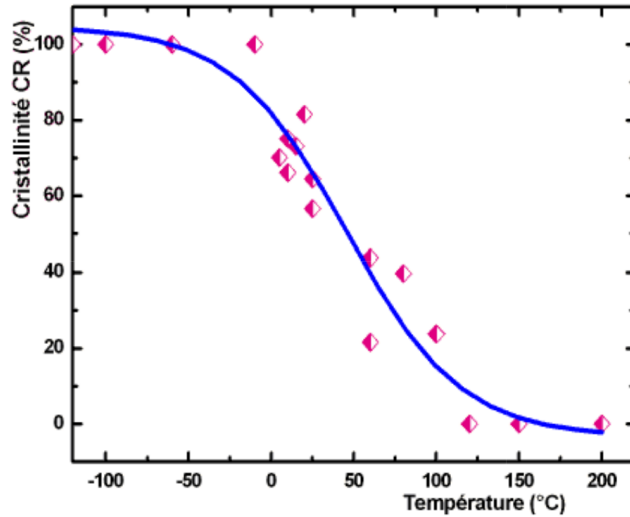


Figure 1.4: Crystallinity evolution with the temperature [13]

With both measurement methods, the DBTT for a same sample should be identical, confirming the fact that material’s mechanical properties are correlated with its fracture surfaces aspects.

#### 1.2.1.2. DBTT evolution from previous studies

The DBTT can be subject to an evolution with different parameters. For instance, CORTE [3] succeeded in showing the evolution of a polymer’s DBTT (PMMA) by increasing the amount of microspheres of elastomer. By doing so the curves started to shift onto the left, as seen on Figure 1.5 representing the impact strength of the different materials with the different amount of elastomer. Another observation possible to identify is the increase of the impact strength level of the brittle plateau with the amount of elastomer [3].

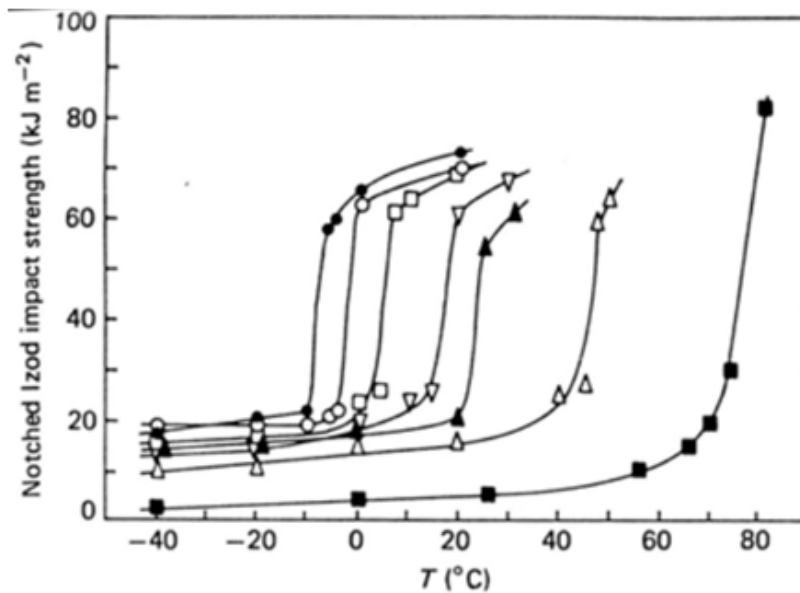


Figure 1.5: Evolution of the DBTT with the polymer's composition [3]

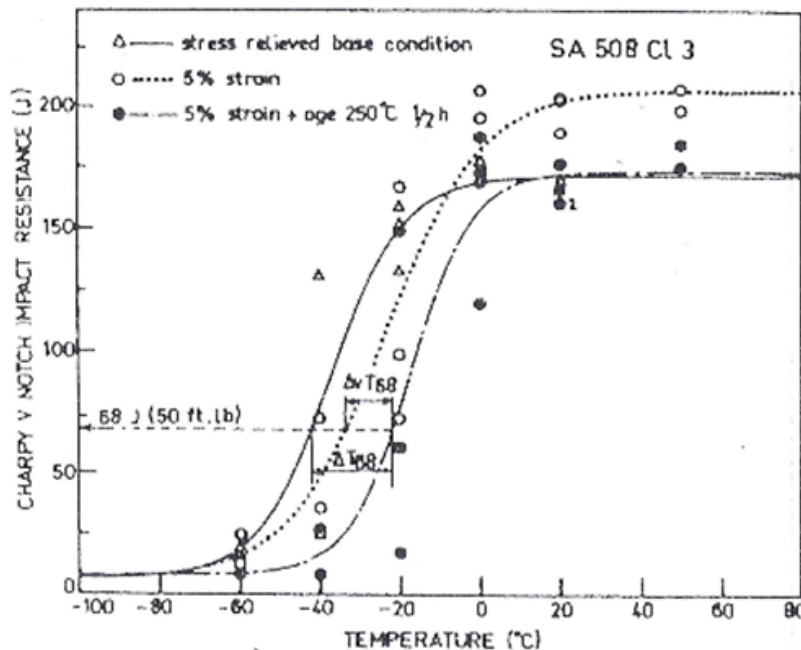


Figure 1.6: Evolution of the notch impact resistance of a sample after strain and temperature ageing [14]

In addition to the material's composition, other conditions can interact with the DBTT. In MARAIS' studies [14], it is shown that the material's history has an impact on the DBTT. As shown on Figure 1.6 representing the notch impact resistance with the temperature, the curves shift onto the right when the sample suffers a pre-strain of 5%. In the meantime the ductile plateau level has increased. Applying a temperature ageing to the pre-strained sample results in a shift of the DBTT, but the ductile plateau is back at its stress relieved level.

The material's composition or the material's history are not the only elements interacting with the DBTT. As we will figure in this study, the impact speed is also a key part in the DBTT's evolution [14].

#### 1.2.1.2.1. DBTT transformation into Tdth

As shown in the industrial context, the dashboard's failure is different whether the materials present a brittle or a ductile failure. In brittle failures the dashboard opening does not follow in any way the weakenings intended. Indeed the crack propagation is not controlled in case of brittle failure and can generate uncontrolled fragmentation or delocalised dashboard openings which is a threat to the passengers' safety.

In order to prevent any of these problems, a new variable is introduced, more suited for this study called the Ductile Failure Threshold Temperature or Tdth. In opposition to the classic DBTT, localized in the middle between the brittle plateau and the ductile plateau, the Tdth would be localized at the beginning of the ductile plateau. This Tdth is then more restrictive than the DBTT because it is located at a higher temperature, where the material would only present ductile properties during the tests [15].

### **1.3. Content of the manuscript**

In this manuscript, the first chapter is entirely dedicated to the description of the environment of the study. Chapter 2 is explaining the composition of the materials which are non conventional PVCs, from its formulation to its transformation into skins. It is followed by the procedure and the details of the specimen for each kind of test carried out. This chapter ends by the presentation of all the instruments used to characterize the material.

Before the study of the Tdth, the ductile failure mechanisms of scored samples were analyzed. Indeed, contrary to what is recommended by the standard [16], unscored samples are not the only kind of specimen treated to analyze the materials. As the material in its real-use condition and most studies surrounding the DBTT/Tdth present a scoring, it was decided to work on both geometries. The results are exposed in chapter 3.

Chapter 4 details all the investigations carried out on impact tests with a wide range of temperatures as well as impact speeds. This has been made possible by two instruments, the CEAST9350 and the High Speed Tensile Test (HSTT) which are going to be compared at the same parameters before extending to other impact speeds (slower with CEAST and faster with HSTT). At the very end, the chapter is going to be revealed if this characterization method gives better results than the glass transition from DMA

## CHAP 2: Matériaux, échantillons et protocoles expérimentaux

Dans les standards actuels de l'industrie, les tableaux de bord des voitures sont équipés d'un système de trois couches de matériaux différents: le *carrier*, la mousse expansée et la peau; chacune de ces couches possède des propriétés propres.

La peau peut être composée de différents types de matériaux. Dans le cas que nous étudions, il s'agit d'une peau en PolyChlorure de Vinyl ou PVC, dit plastifié à cause de ses propriétés plastifiantes non conventionnelles par rapport à un PVC pur. Ces propriétés plastifiantes particulières sont dûes au processus de fabrication du matériau : la poudre en PVC a été produite à partir d'un procédé de polymérisation par suspension. Cette méthode confère au matériau formé une porosité importante, qu'il est alors possible de combler avec des sous-produits. Ces constituants insérés affectent les propriétés physico-chimiques (plastifiants par exemple), mais aussi visuelles (pigments) du PVC. Certains composants comme les stabilisants impactent d'ailleurs les deux types de propriété simultanément. Une fois les sous-produits insérés, la poudre peut alors être transformée en peau, grâce au procédé du rotomoulage. Il s'agit d'une méthode permettant la réalisation de formes complexes dont le principe est de gélifier la poudre de polymères sur les parois d'un moule préalablement chauffé. Ce moule pivote selon les trois axes de rotation possible afin de s'assurer que les moindres recoins soient recouverts de matière.

Tout au long du processus, différents tests sont réalisés afin de s'assurer que les peaux obtenues soient conformes au cahier des charges. Ces tests permettent de contrôler la granulométrie, la coulabilité, la couleur, mais surtout la température de transition vitreuse ( $T_g$ ) via une Analyse Mécanique Dynamique (AMD) qui caractérise le comportement physico-chimique en température du matériau. Cette température  $T_g$  est utilisée lors des phases de développement afin de comparer les différents matériaux entre eux.

Afin d'avoir une idée de la microstructure des peaux précédemment obtenue, celles-ci ont été observées durant l'étude à différentes échelles : à l'œil nu, au Microscope Optique à Balayage (MEB), au Microscope Électronique en Transmission et en Tomographie.

Dans cette étude, les peaux sont étudiées avec plusieurs géométries et avec plusieurs méthodes expérimentales différentes, et sont divisées en trois types d'échantillons. Le premier, majoritaire, est découpé chez le partenaire industriel avec l'aide d'un bras robotique équipé d'une lame dite "froide". Il permet d'obtenir un premier type de peaux non entaillées de dimension 90mm × 90mm × 1mm. Le second type est façonné à partir du premier: une entaille est réalisée avec un ligament restant de 0.6mm d'épaisseur sur toute la largeur du matériau (soit 90mm). Enfin le troisième et dernier type est obtenu à l'aide d'un emporte pièce afin d'avoir une dimension finale de 90mm × 30mm × 1mm (avec l'entaille le long des 30mm).

Ces éprouvettes sont alors testées à l'aide des trois instruments suivants: la CEAST9350 et la machine de Traction à Grande Vitesse (TGV ou HSTT en anglais) pour les essais d'impact, et une [Instron 5982](#) pour les essais de flexion trois points encastres filmés. Pour les essais d'impact, un large spectre de températures et de vitesses d'impact a pu être explorée allant de -24°C pour les températures les plus basses à 30°C pour les températures les plus hautes, et de 2 m/s à 23 m/s pour les vitesses d'impact. Au total, plus de 540 échantillons (sur deux matériaux) ont été testés afin d'obtenir les résultats de ce manuscrit.

## 2. Materials, specimens, and experimental protocols

### 2.1. Materials

#### 2.1.1. Materials for dashboard assembly

##### 2.1.1.1. Carrier

The carrier is the rigid part of the dashboard (figure 2.1.). It is made of short glass fiber reinforced polypropylene (PP) processed by injection molding. The thickness of the material ranges from 2 to roughly 10 mm.

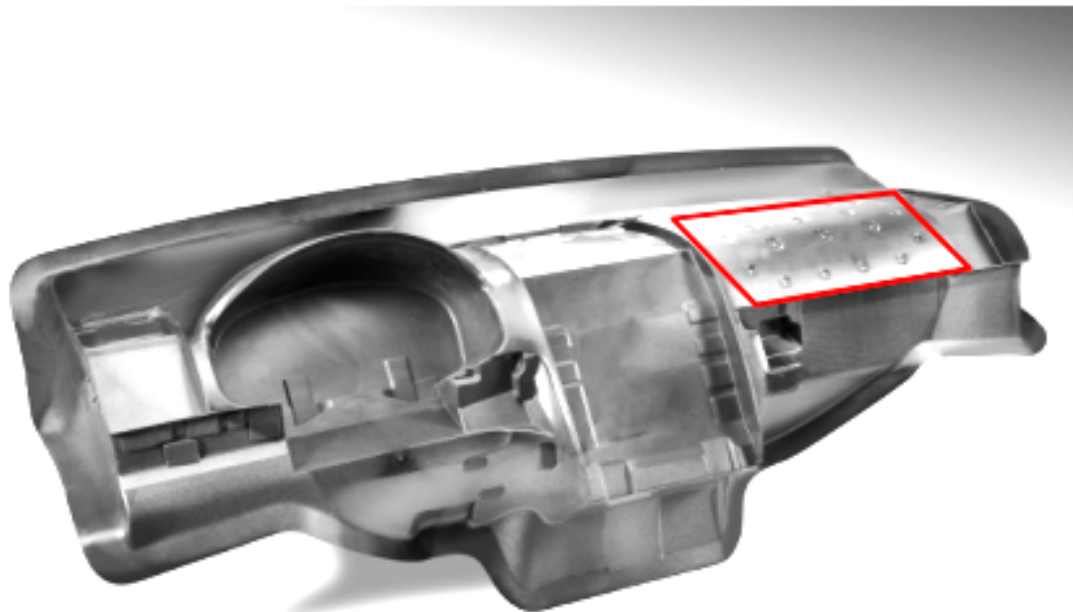


Figure 2.1: Example of a dashboard carrier before the assembly

The location of the air bag box is indicated by the red parallelogram in figure 2.1. From this box, the bag hits first the firing channel where the material dimensions are controlled. In fact, the maximum thickness is now about 5 mm and a reduction was set to locate the failure at the flaps extremities.

##### 2.1.1.2. Foam

A PolyUrethane (PU) foam is then displayed over the PP dashboard so as to carry out a soft and safe surface in case of small shock. This foam results from a reaction between isocyanates and polyols when in contact with a specific catalyst (depending on the reactants). During the polymerization, a gas (CO<sub>2</sub>) is produced and trapped in the rigidifying polyurethane [17, 18], increasing its volume and creating a foam.

The plasticised PVC skin is then put to finish the assembly represented in figure 2.2.



Figure 2.2: Dashboard before an airbag shot

The assembly is composed of three different materials organized in three layers with different purposes. Figure 2.3 illustrates a cross section view of the finished dashboard. It highlights the three different layers and their respective sizes. From top to bottom the layers are constituted of a PolyVinyl Chloride (PVC) skin, a PolyUrethane (PU) foam and then a short glass fiber reinforced polypropylene (PP) shell.

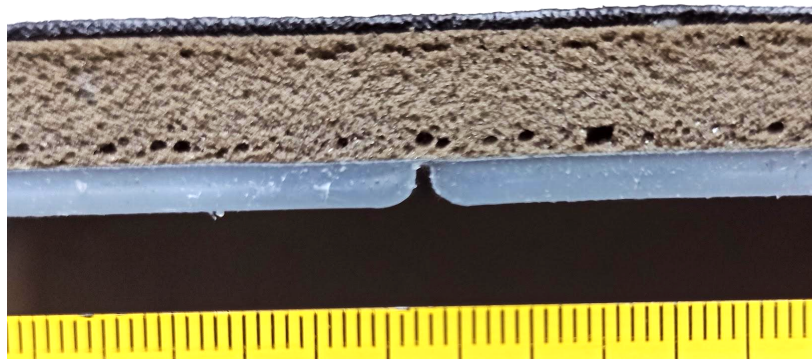


Figure 2.3: The three layers assembly with their characteristic sizes

## 2.1.2. The PVC skin

### 2.1.2.1. Processing and assembly methods

The materials used for the present study were provided by NAKAN. They are composed of a suspension polyvinyl chloride (PVC or SPVC) based powder and transformed into skins using the slush molding method [19, 20]. In order to alter the SPVC's properties to comply with automotive safety, design and comfort, other components were added to the powder such as plasticizers, pigments and stabilizers.

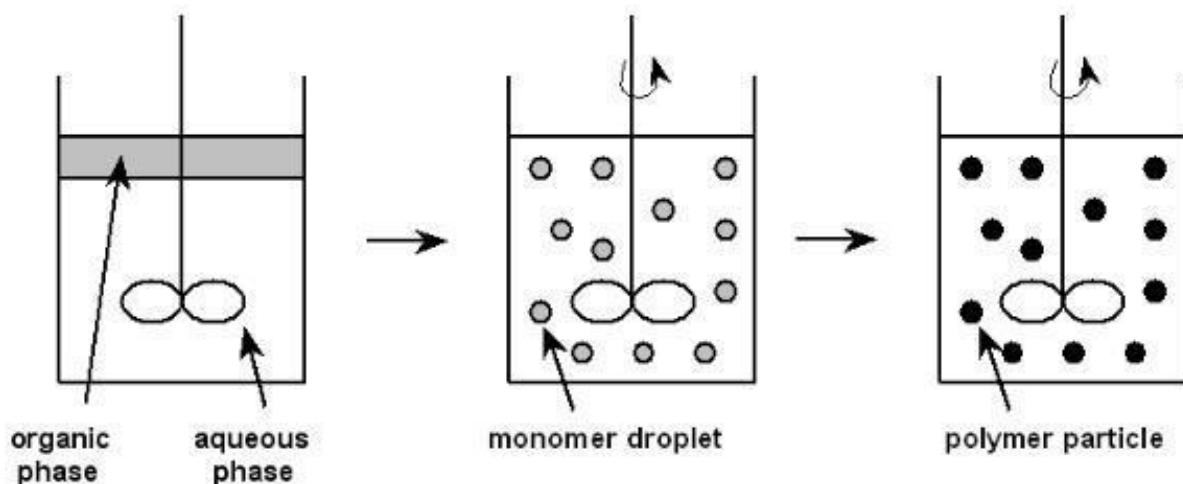


Figure 2.4: Suspension polymerization process of PVC

Suspension polymerization of PVC was achieved by mixing an organic phase (the monomer) and an aqueous phase which are immiscible. The agitation allows the dispersion of multiple monomer droplets inside the aqueous phase. By starting the chemical reaction during the agitation with a catalyst, the monomers are polymerizing inside the droplets to form a polymer particle, in the present case a PVC particle also named SPVC [21-23]. The process of evolution is described in Fig. 2.4.

The SPVC's process presents two advantages for the final application. The first consists of the shape of the PVC at the end of the process: directly a powder. The size of the particles composing the powder can be controlled/modified by changing some parameters, such as the temperature, the ratio between the two phases, the agitation speed or the quantity of catalyst [21, 23]. The second advantage of the process is concerning the pores observed on the SPVC particles. Indeed the pores will be loaded with all the other elements used to modify the SPVC's properties for a better touching experience for the passengers [24, 25].

The most important of the loaded elements inside of the pores are the plasticizers (the plasticizers' names and quantity are kept unspecified for the sake of industrial confidentiality). They are added to improve the flexibility of the material after the transformation into skins. Indeed, the plasticizer's purpose is to be placed between the polymeric chains so as to allow more movements thanks to the added distancing of the chains. As a result, the glass transition temperature ( $T_g$ ) of the resulting material is decreased. Like the glass transition temperature, other material properties are impacted by the plasticizers [26-29]. Thereby, with the quantity of plasticizer added, the tensile and impact strengths will decrease while the elongation at break and the softness will increase (Figure 2.5).

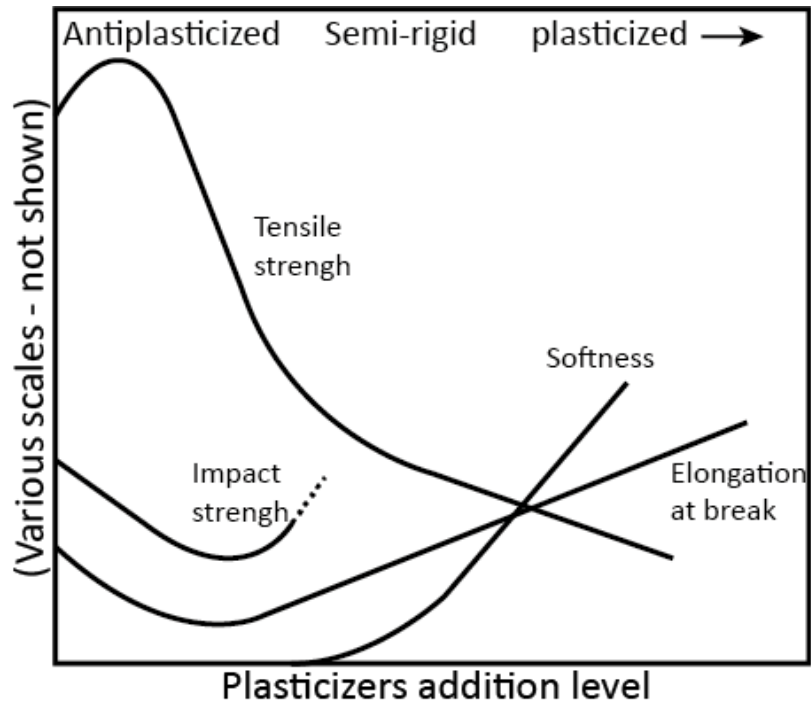


Figure 2.5: Impact of the plasticizer’s quantity on the material properties

With only the PVC powder and the plasticizer, the resulting skins would be white. In order to obtain the color observed on most cars’ dashboard (black, grey or else), other elements have to be added: pigments and stabilizers. Their purpose is mostly aesthetic as to keep the dashboard’s color stable with the time [24, 30].

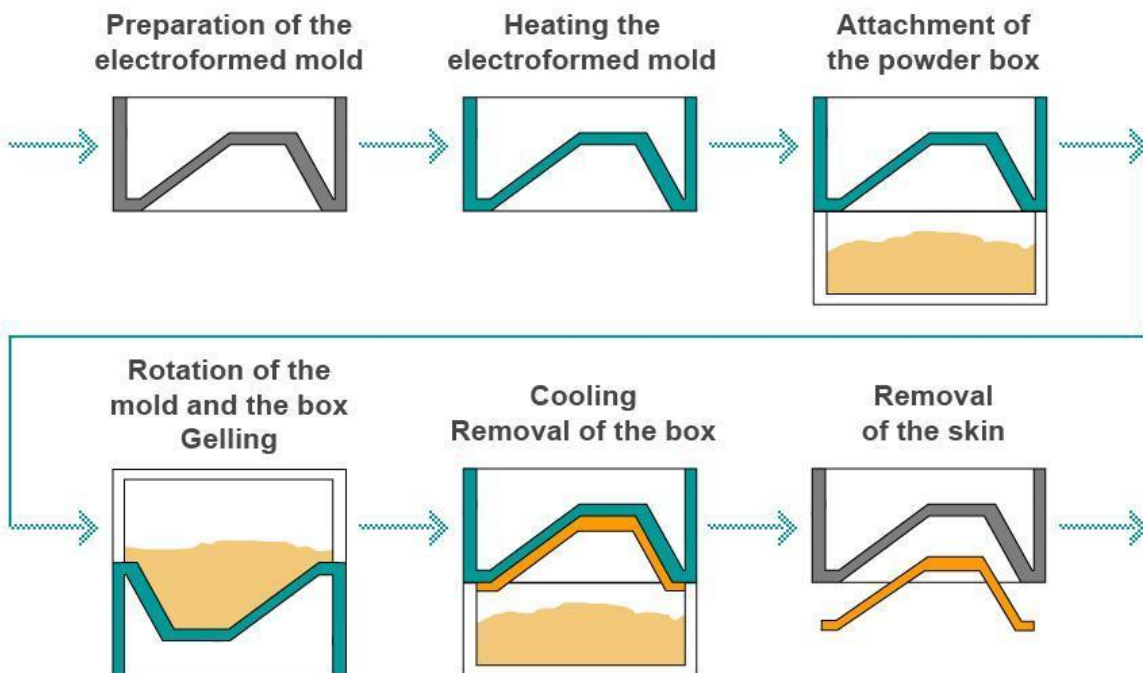


Figure 2.6: Slush molding process’ steps to transform the PVC powder into skins

When all the elements are loaded inside the pores of the SPVC, the powder is ready to be transformed with the slush molding method. This latter consists of preheating a mold with the selected geometry. When the mold reaches the desired temperature, it is attached to a box full of the previous powder. Then, the assembly will rotate in three directions to allow the powder to reach all the surface of the mold [19, 20]. In contact with the mold, the surface of the powder will jellify and each particle will stick together to form the skin. After several rotation cycles, the box is removed and the mold is heated again to obtain a smooth top surface. The mold is then cooled and the skin removed (Figure 2.6). At this stage, the skin is ready to be assembled with the foam and the carrier to obtain the complete dashboard.

For the assembly procedure, the skin of the dashboard is placed in a countermold. The carrier is then placed in front of the skin. The foam reactants are then injected to create an expanded foam that will adhere to both skin and carrier, creating one single assembly.

#### 2.1.2.2. Physico-chemical characteristics, material controls

To achieve a high quality skin with a high level of reproducibility, several tests are carried out at different production steps. When the powder is fully completed, granulometry and pourability tests are used to determine the grain size dispersion of the powder as well as its dryness. These two checks are essential to ensure a better powder transformation into skins. These tests were carried out at Resinoplast/Resichina (the industrial partner) and no information about the instruments used is available.

##### 2.1.2.2.1. Granulometry

The granulometry is the measurement of the average grain size and its size dispersion. Indeed, a control of the grain size and the size dispersion has an influence on the powder's transformation process into skins. Several methods are used for granulometry tests : laser diffraction, dynamic image analysis or sieve analysis. Each method possesses its advantages and drawbacks, such as the size range, the time of the measurement, the shape analysis of a grain, etc [31].

##### 2.1.2.2.2. Pourability

The pourability is the measure of the mobility of the grains composing the powder. This property is influenced by quite every characteristic of the grain, such as its composition, its size distribution, its surface (smooth or rough) or its dryness. This methodology uses the measurement of the time taken by a certain quantity of powder to evacuate from a calibrated aperture following two geometries: Hall's cone [32, 33], see Fig. 2.7, or Carney's cone [34] depending on the pourability of the powder. In general Carney's cone is used when the pourability is not sufficient to use Hall's cone.



Figure 2.7: Hall's cone from the Filab website [35]

After transforming the powder into skins with the slush molding process, few tests are carried out to observe the repeatability of the selected properties between skins/batches. These tests are selected to investigate different conditions, such as the color or the glass transition temperature  $T_g$ , before and after thermal, humidity, and light ageing.

#### 2.1.2.2.3. $L^*a^*b$

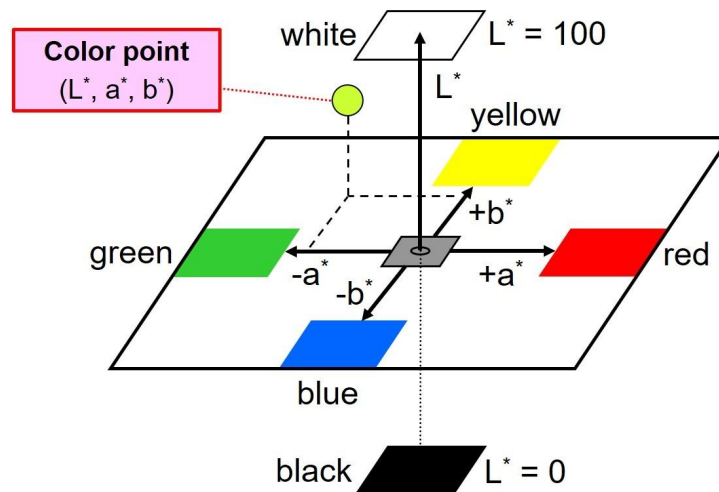


Figure 2.8:  $L^*a^*b$  representation of the colors [36]

It is possible to decompose the color following the CIELAB color space or  $L^*a^*b$  [37, 38]. It expresses color as the superposition of three values  $L$ ,  $a$  and  $b$ . Each value is used to represent a different shade or color. As seen on the Figure 2.8,  $L$  represents the lightness,  $a$  represents either the redness or greenness, depending on its value, and  $b$  either the blueness or yellowness, depending on its value. Because every color is a combination of these three values, several combinations are possible for the same color under light.

Differences might occur when the lights are varying (i.e at dawn, in a tunnel, etc), for that reason OEM (Original Equipment Manufacturer) and car brands are asking to compare the skins' color to a standard under white, ultra-violet and infra-red lights. The combination of pigments used is rethought when one of the light tests (or more) fails.

#### 2.1.2.2.4. Glass transition

After the powder's processing into skins, major actors in the car industry are asking for the determination of the glass transition temperature  $T_g$ , an essential parameter to determine the skins' properties. In order to estimate the future skin's  $T_g$ , it is possible for the compounders to employ the Fox law [39]. It allows to determine an estimation of the final product's  $T_g$  if the compounds'  $T_g$  and ratio are known according to the eq 2.1:

$$\frac{1}{T_{skin}} = \frac{X_1}{T_1} + \sum \frac{X_i}{T_i} \quad (\text{eq 2.1})$$

with:

- $X_i$  as the mass ratio of the compound  $i$
- $T_i$  the glass transition of the compound  $i$

The Dynamic Mechanical Analysis (DMA) enables to identify the glass transition temperature they are looking for. The DMA consists of a series of cycles at small deformation. The instrument returns materials' characteristics such as the storage modulus  $E'$  and loss modulus  $E''$ . The glass transition temperature is reached at  $E''_{max}$ . This is also when  $E'$  decreases.

The  $T_g$  depends on oscillation frequency, i.e. the higher the speed of the cycles, the higher the  $T_g$ . For the PVC skin under study,  $T_g$  is equal to  $-37,8^\circ\text{C}$  (see Figure 2.9). As aforementioned, this corresponds to the maximum value of the Loss modulus  $E''$ . The DMA tests were carried out by the industrial partner.

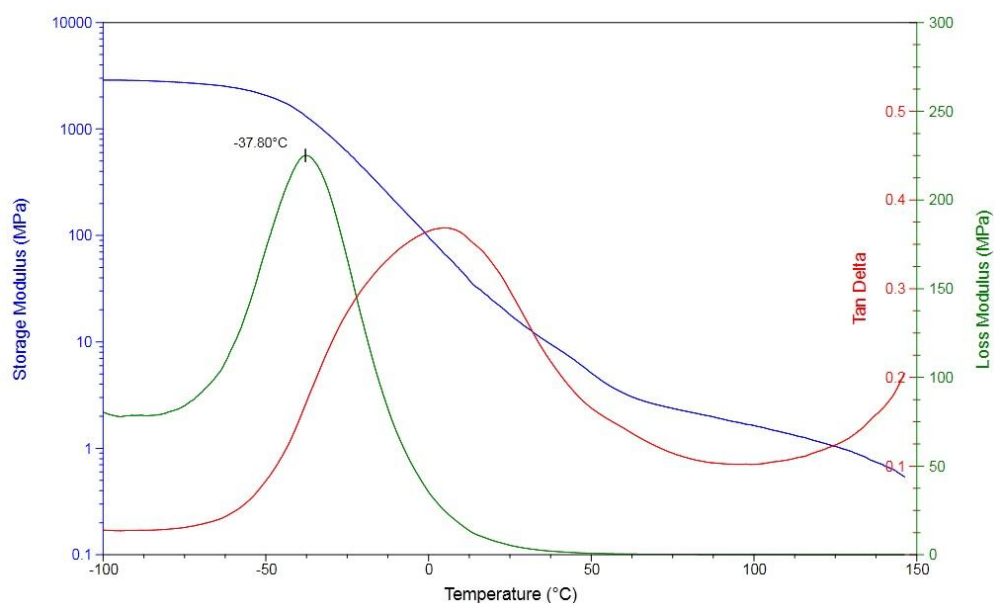


Figure 2.9: DMA results on material 1

### 2.1.2.3. Initial microstructure

#### 2.1.2.3.1. Optical images

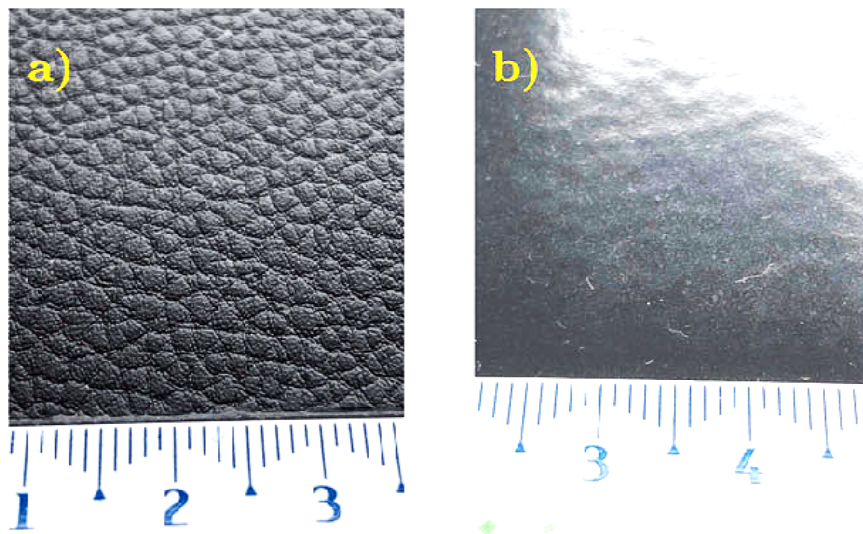


Figure 2.10: Views of the two sides of the PVC skins: a) the external side (patterned) ; b) internal side (smooth)

In Fig. 2.10, the two sides of the skin are presented :

- **The external side** (side a) is in contact with the mold - hence exposed to the highest temperature. The skin pattern order of magnitude is millimeter;
- **The internal side** (side b) is opposite to the mold - hence, at first, not directly exposed to the source of high temperature. This side is then reheated to remove the remaining powder grains and make sure the material is compact. Since then the side becomes a “smooth” surface.

#### 2.1.2.3.2. Scanning Electron Microscopy (SEM)

The Figures 2.11 represent SEM pictures taken with a SEM ZEISS Sigma 300 at the Centre des Matériaux.

- **Samples' preparation:**

A (1 cm x 1 cm) sample material was cut from the skin sheet to examine the microstructures at the two surfaces of the skin. Moreover, a (1 mm x 1 cm) sample was used to study the skin 's microstructure in its thickness.

Each of the samples was taped on a carrier with double face tape to observe the selected surface (top, i.e. the patterned side, bottom, i.e. the smooth side, and through-thickness)

The samples were covered with a 2 nm coating of conducting metal (Gold – Palladium (Au-Pd)) to ensure the electrical conductivity of the surface, which is a requirement for SEM use on polymers. Then, they were painted with silver lacquer for electron dissipation, in order to avoid electron accumulation causing material melting. Once these steps completed, the samples are ready to be studied with the SEM. All of the SEM observations were carried out with EHT = 5kV.

- Figure 2.11a (top view): the pattern remains partially visible, light grey areas appear, requiring to resort to additional magnification for proper identification
- Figure 2.11b (top view): pattern is not visible anymore due to the magnification (x200). The light grey areas appear to be “sharp” particles inside the polymer matrix. They could be the additives.
- Figure 2.11c (bottom view): the material looks quite smooth overall. However, some defects appear such as small holes. They may come from porosity or/and from a material retraction during cooling. Those imperfections might improve the adhesion of foam during the foaming for the three-layers assembly.
- Figure 2.11d (thickness view): the top of the sample is not even, it is the surface in contact with the mold, there is a pattern. The opposite surface is completely straight. The through-thickness surface on the picture shows the presence of some random spherical-shaped porosity. The biggest porosity visible on the picture has a diameter around 250  $\mu\text{m}$ . The presence of such a porosity would induce scatter in the mechanical properties that will be studied.

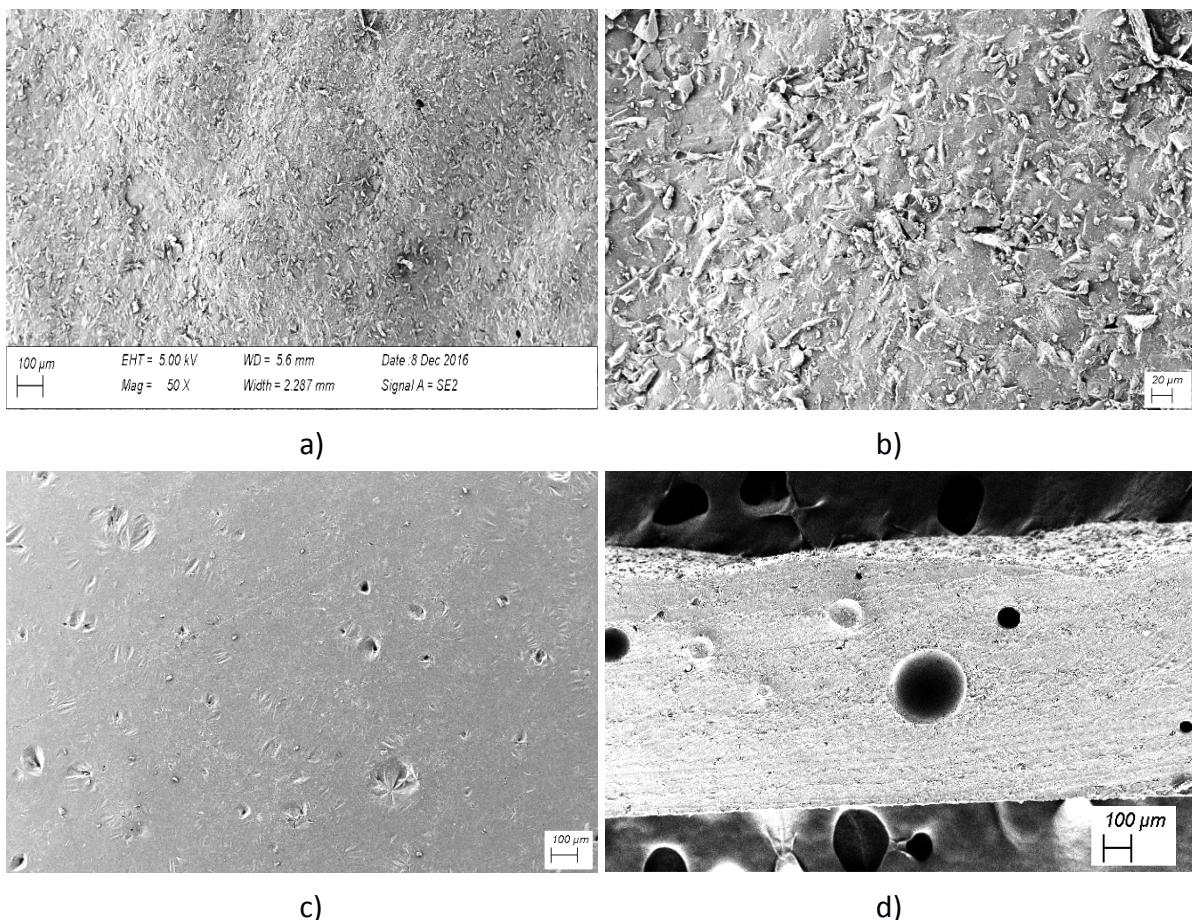


Figure 2.11: SEM examinations of the skin surfaces at various scales: a) and b) the external side of the skin (patterned) ; c) the internal side of the skin (smooth) ; and d) through-thickness view of the skin

#### 2.1.2.3.3. Transmission Electron Microscopy (TEM)

To go further, a Transmission Electron Microscope (TEM) was used to observe the different layers accumulated during the slush molding. The TEM enables different observation techniques, through the materials, which provides additional information about the microstructure.

Samples' preparation:

All the samples were covered by an epoxy resin on all the surfaces to make them more rigid. The epoxy resin was then trimmed to obtain a "pointy" extremity where the skin is surfacing - the rest of the sample remains covered by the epoxy (see pictures in Figure 2.12).

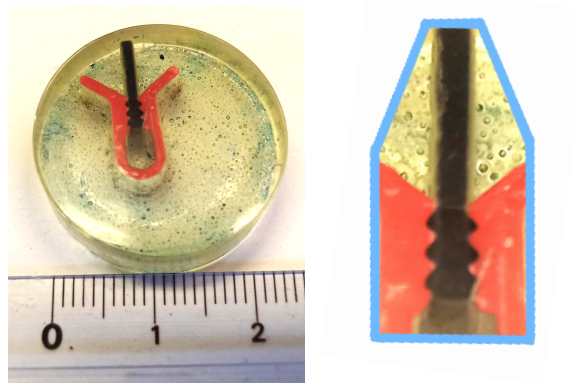


Figure 2.12: Skin samples covered with an epoxy resin and trimmed for the microtome preparation

A cryogenic microtome with a diamond blade is then used to cut several layers of materials, each with a 50/20 nm thickness: after frosting the sample with liquid nitrogen, the microtome program activates the blade's cutting movement (slow and cyclic). The sample slice is then sliding along the blade to the surface of a water bath. The slices are then collected and placed on a TEM-specific grid for TEM observation. The grids were then put inside the TEM.

After several trials, the blades were activated for manual cutting at high speed; given the material's viscosity, it prevented the microtome cutting neat slices, this new technique was used. The aforementioned technique proved to be much more efficient and allowed neat slices to be obtained.

Although the images shown in Figure 2.13 are of good quality, they don't enable to identify the different layers and patterns of the investigated samples.

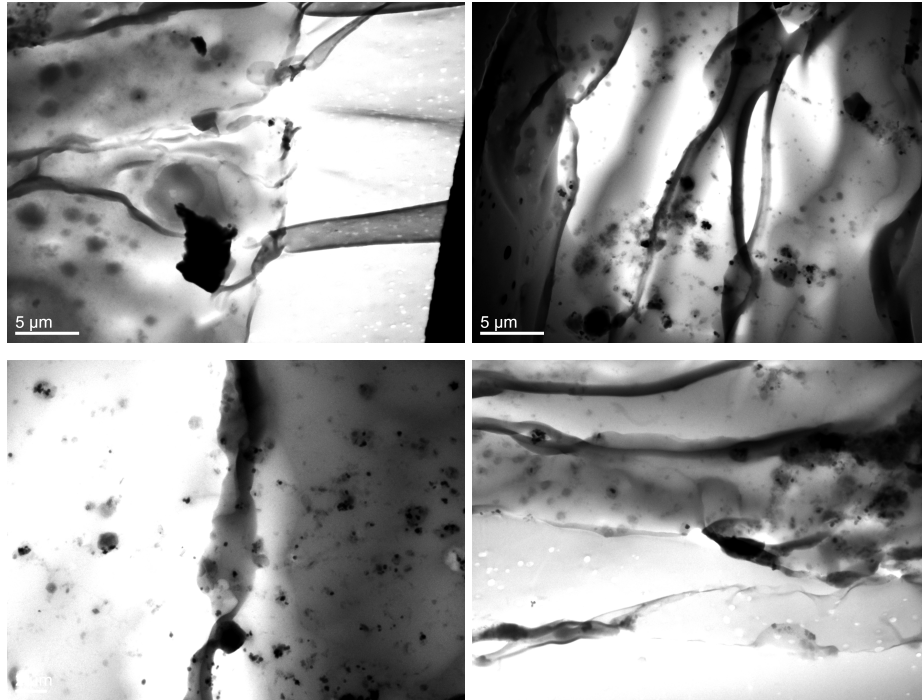


Figure 2.13: TEM examinations of a skin slice cut by using an ultra-microtome

#### 2.1.2.3.4. Microtomography

The tomography is used to provide a 3D through-thickness view. In this case, the view was used to identify the porosity.

- *Samples' preparation*

No peculiar preparation of the sample is required.

Figure 2.14 shows spherical pores in the whole volume of the examined sample. They are of various sizes and randomly distributed in the material. The industrial partner considers that the porosity is well controlled by the manufacturing process.

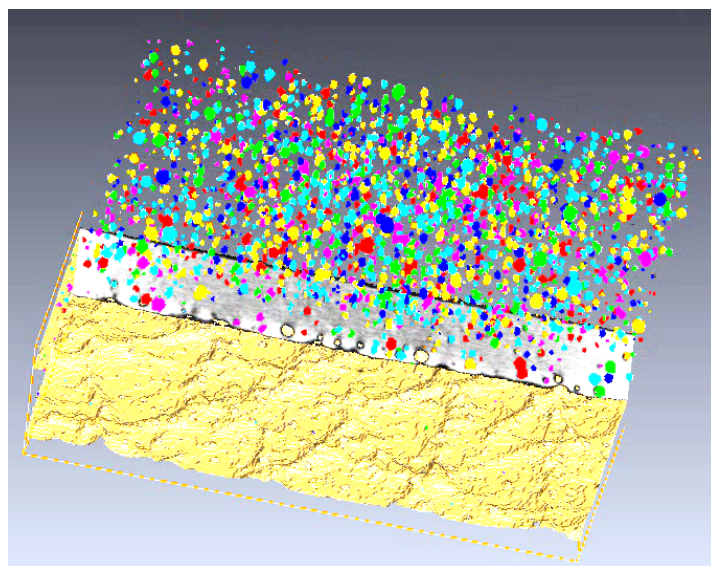


Figure 2.14: Skin tomogram, after image segmentation treatment, showing the pores in various colors (labelling)

## 2.2. Specimens and structures studied

### 2.2.1. Plates without scoring or unscored

The skins were transformed in RESICHINA with a reduced size replica of an industrial slush molding line especially optimized for Research and Development (R&D) specimens. From the skins, obtained with a flat leather patterned mold, samples for unscored impact test were prepared with a thickness of 1.1 mm (thickness used for real application). The last part was done in NAKAN with the cutting of 90 mm × 90 mm square samples to ease its disposition inside the instruments (jaws sizes), with a cutting robot arm (figure 2.15).

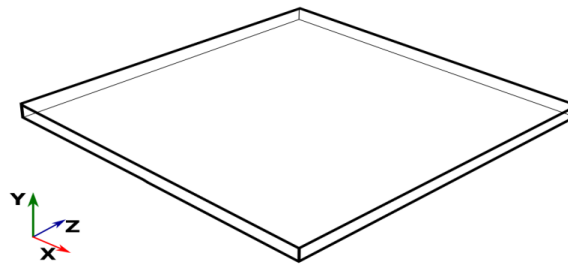


Figure 2.15: Representation of an unscored sample

### 2.2.2. Plates with scoring or scored

Instead of the samples used for unscored impact tests (subsection 2.2.1), the dashboard's skin presents a pre-crack in order to ease and localize its failure during the airbag opening. So, as to better analyse the real geometry of the skin in the engineering structure, this scoring was added as a pre-crack from the plates machined for unscored impact tests. For the operation, the skins are placed on a vacuum table to prevent any displacement, , then, using a laser distance controller, the robot arm cut in the middle of the sample's length deep enough to keep a remaining ligament of thickness 0.6 mm (Fig. 2.16). For better reproducibility between the specimens, the same robot arm was used f. This condition is motivated by the desire to obtain a ratio score depth – total thickness around 0.5. Actually, the ratio stays with a small uncertainty due to the real thickness of the skin and the pattern. These samples are referred to as scored or pre-cracked specimens.

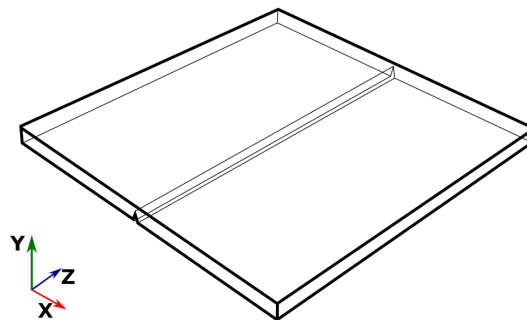


Figure 2.16: Representation of scored sample

### 2.2.3. Clamped SENB

Like the scored specimens for impact tests (subsection 2.2.2), the samples for SENB tests present a pre-crack. For a better control and reproducibility of the sample (scoring included), a punch was machined to cut directly in the scored plate (subsection 2.2.2). It is composed of two parallel blades spaced by a metallic filler. The remaining size of the samples is then: 90 mm × 29.8 mm × 1.1 mm (Fig. 2.17).

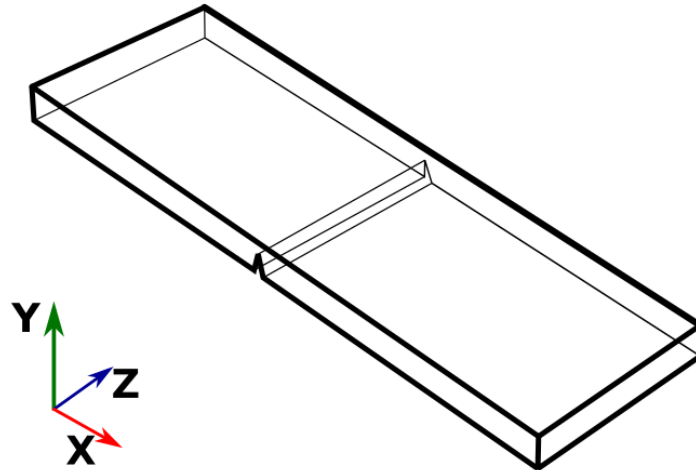


Figure 2.17: Representation of a clamped SENB specimen

### 2.2.4. High Speed Tensile Test's specimens

The purpose of the HSTT tests being the extension of the impact test database to higher impact speeds, the specimen conditions/dimensions are the same as the unscored/scored samples, namely: 90 mm × 90 mm × 1.1 mm, with a 0.5 ratio scoring depth – total thickness for the scored samples.

## 2.3. Experimental protocols

### 2.3.1. Testing machines and associated instrumentation

#### 2.3.1.1. Drop tower CEAST9350

##### 2.3.1.1.1. Machinery description

Inspired by the ISO standard 6603-2 [16, 40], most of the impact tests were carried out in RESICHINA using an Instron CEAST9350 drop tower impact system. The samples used, described in subsections 2.2.1 and 2.2.2, were gripped along circular jaws located in a thermostatic chamber, opening only when the striker starts moving for the test. The CEAST9350 is composed of three/four different parts with specific functions (Figure 2.18).



Figure 2.18: Presentation of CEAST9350 and its parts

##### 2.3.1.1.1.1. The clamping system

The clamping system is composed of circular jaws with a diameter of 40 mm. It is used to hold the edge of the samples, allowing the impact of the area of interest. The circular jaws

are disposed in order to let the striker (see Figure 2.19) impact the specimens placed on its center. For scored materials, a tracking system was developed to position the samples ensuring the pre-crack to go through the center of the impact zone.

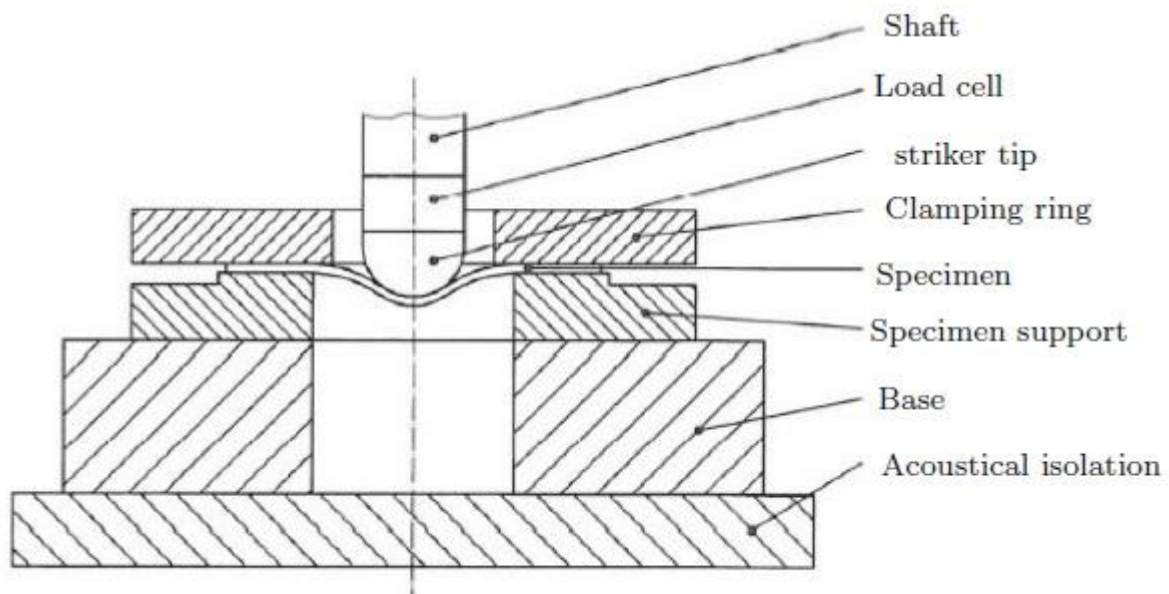


Figure 2.19: Description of the clamping system [16]

#### 2.3.1.1.1.2. *The thermostatic chamber*

The clamping system is located in a thermostatic chamber. The documentation furnished with the CEAST9350 indicates that the temperature inside the chamber can vary from -70°C to +150°C with a temperature gradient guaranteed by the constructor of  $\pm 2^\circ\text{C}$ . The chamber temperature is controlled by electro-valves releasing liquid nitrogen to reach low temperatures, and a resistance to reach the high ones. When the desired temperature is stabilized inside the chamber, a waiting time of thirty minutes is necessary for the material to ensure it reaches the room temperature. A small variation of the test temperature can be introduced when the test begins, due to a small hatch opening a few seconds before the impact.

#### 2.3.1.1.1.3. *The striker*

The striker is a cylindrical metal stem with a 20 mm radius round end. It represents the impact part of the CEAST9350. Indications from the constructor recommend its use for impact speeds going from 1 m/s to 25 m/s. Actually, depending on the studied materials, an impact speed higher than 10 m/s generates vibrations that can alter the quality of the results. Then, the selected impact speeds for our database were: (2; 4.4; 6; 10 m/s), with 4.4 m/s as the advised impact speed from the standards [16]. For low impact speeds  $v_0$  (e.g. 2 m/s), the drop from a calculated height is enough (potential and kinetic energies), whereas for higher impact speeds (e.g. 10 m/s), an energy carrier is required to provide enough energy to reach the impact speed targeted.

### 2.3.1.1.2. Data collected and calculated

The same experimental program (except from the temperature range) was performed for unscored and scored thin plates. For each testing condition, tests were repeated at least three times for reproducibility purposes.

The rough data obtained after the tests were composed of the real experimental time ( $t$ ), the load at every time step  $F(t)$ , and the initial speed of the striker ( $v_0$ ). Therefore, the deflection/displacement ( $u$ ) is computed as follows [41]:

$$u(t) = v_0 \cdot t - \frac{1}{m} \cdot \int_0^t \left( \int_0^t F(t) \cdot dt \right) \cdot dt \quad (\text{eq 2.1})$$

where:

- $t$  is the running time (sec);
- $v_0$  (m/s) is the initial speed of the impactor before hitting the sample ;
- $m$  is the mass of the striker (5.3 kg);
- $F$  (N) is the measured load at time  $t$  .
- $u(t)$  in mm is the displacement at time  $t$

Knowing the computed displacement ( $u$ ), the CEAST9350 gives also the energy absorbed by the sample during the test, in Joule, with the following relation:

$$E(u) = \int_0^u F(u) \cdot du \quad (\text{eq 2.2})$$

where:

- $F(u)$  in N is the load at the displacement  $u(t)$
- $E(u)$  in J is the energy absorbed by the sample at the displacement  $u(t)$

The instantaneous impact speed is also calculated and given by the CEAST testing machine such that:

$$v(t) = v_0 - \frac{1}{m} \cdot \int_0^t F(t) \cdot dt \quad (\text{eq 2.3})$$

2.3)

where:

- $t$  (s) is the running time ;
- $v_0$  (m/s) is the measured initial speed of the impactor before hitting the sample ;
- $v(t)$  in m/s is the displacement at the moment  $t$

### 2.3.1.1.3. Test conditions

The temperatures explored for the tests on unscored samples were: (-24, -21, -18, -15, -12, -9, -6, -3, 0, 5, 10, 15, 20, 25°C). The data range is adapted with the material, its condition (unscored or scored) and the impact speed investigated. Table 3.1. summarizes all the impact conditions tested. The total number of tests carried out was 126, as mentioned in table 3.1.

Total = 126		Temperatures (°C)												
		-24	-21	-18	-15	-12	-9	-6	-3	0	5	10	15	20
Speed (m/s)	2	3	3	3	3	3		3		3	3	3	3	3
	4.4			3	3	3	3	3	3	3	3	3	3	3
	6			3	3	3	3	3	3	3	3	3	3	3
	10				3		3	3	3	3	3	3	3	3

Table 3.1 : Test program for unscored samples

The temperatures explored for the tests on scored samples are: (-6, -3, 0, 5, 10, 15, 20, 25°C). The data range is adapted with the material, its condition and the impact speed investigated. Table 3.2 shows all the impact conditions tested for scored samples. The total number of performed tests for scored specimens was 93.

Total: 93		Temperatures (°C)							
		-6	-3	0	5	10	15	20	25
Speed (m/s)	2	3		3	3	3	3	3	3
	4,4	3	3	3	3	3	3	3	3
	6	3	3	3	3	3	3	3	3
	10	3	3	3	3	3	3	3	3

Table 3.2 : Test program for scored samples

In the latter tables (3.1-2) the yellow parts show the different impact speeds investigated, the blue parts indicate the temperature inside the thermostatic chamber, and the green parts give us the repetition number for each condition of speed and temperature.

### 2.3.1.2. Instron High Speed Tensile Test (HSTT)

#### 2.3.1.2.1. Testing machine

As mentioned in the Introduction, airbag opening speed is estimated between 25 m/s and 50 m/s. The CEAST speed limit is 10 m/s, which does not correspond to required speed. Experimental setup enabling to reach these high speeds was required. The HSTT testing machine at the Centre des Matériaux allowing an impact speed up to 23 m/s was selected.

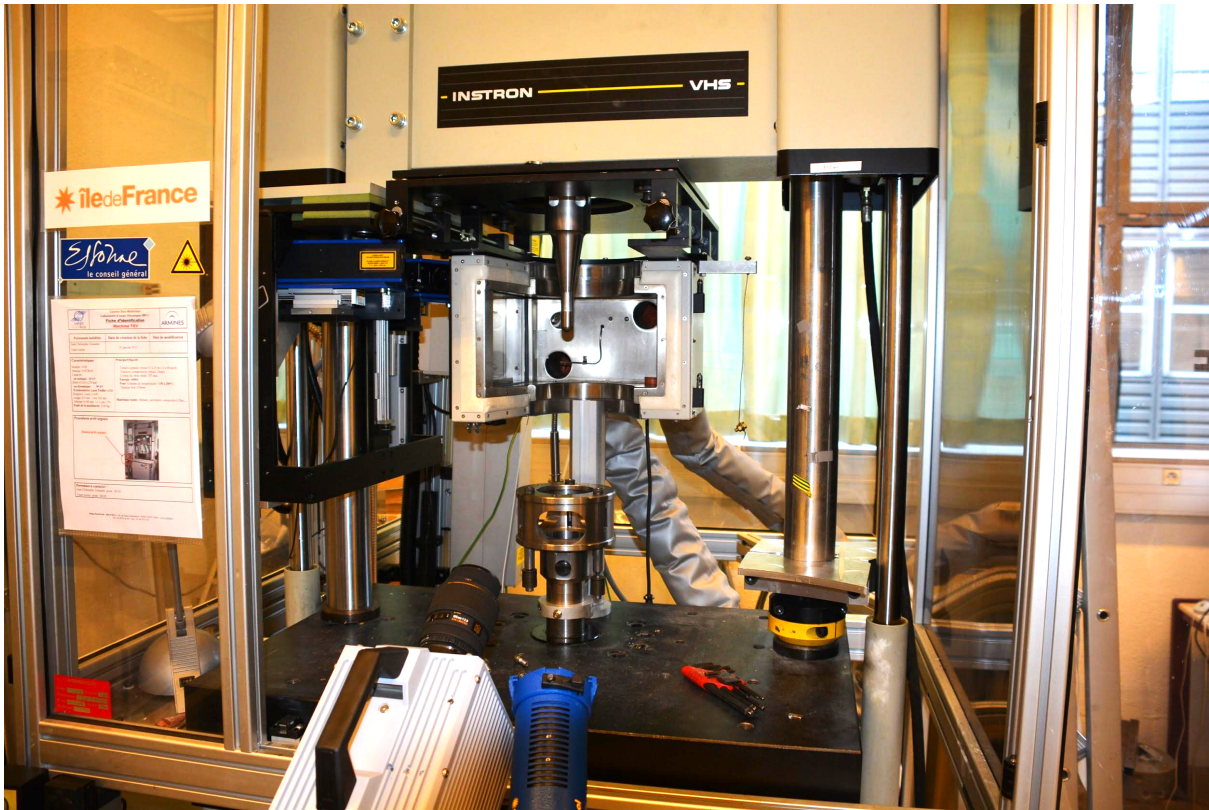


Figure 2.20: Instron HSTT testing machine with its instrumentation

Figure 2.20 shows the Instron HSTT machine, which is composed of 3 main parts:

#### 2.3.1.2.1.1. *The striker*

The striker consists of a cylindrical metal stem with a 20 mm radius round end representing the impact part of the HSTT. Impact speeds going from 1 m/s to 23 m/s can be monitored. Whereas, for the CEAST machine, the striker was the mobile part, for HSTT it is the fixed part, being located in the thermostatic chamber. Therefore, instead of being an integrated component of the striker, the load cell is placed far from the tip of the striker (instrument assembly necessity). The striker and the load cell are linked by a metallic bar made of the same metal as the striker.

#### 2.3.1.2.1.2. *The clamping device*

The clamping system, which immobilizes the sample during the test, was adapted so that jaws were identical to that of the CEAST. This required two rings machined at the Centre des Matériaux' workshop. The clamping system is composed of circular jaws with an intern diameter of 40 mm. The circular jaws are disposed in such a way that the striker (see below) impacts precisely the center of the specimen. For scored materials, a tracking system was developed to position the samples ensuring the pre-crack to go through the center of the impact zone. Contrary to the CEAST, the clamping system is not immobile in the thermostatic chamber. It is moving with the piston, vertically from the bottom.

#### 2.3.1.2.1.3. *The thermostatic chamber*

The thermostatic chamber, allowing a given temperature to be maintained during the tests, is controlled by electro-valves releasing liquid nitrogen to reach low temperatures, and a resistance to reach the high ones. A circular aperture is machined at the size of the clamping device to allow its vertical displacement with the piston.

For tests at a given temperature, the clamping system moves up, inside the thermostatic chamber, through the aperture until the sample reaches the desired temperature (at least thirty minutes, like for the CEAST). In order to improve testing, a second distinct thermostatic chamber was disposed close to the HSTT. All the samples were inserted in it until they reached the given test temperature, verified by an embedded thermocouple. Once, at temperature, they were moved from thermostatic chamber number two to thermostatic chamber number one (installed on HSTT). The resting time is then reduced to five minutes because the samples are already at the desired temperature.

At the beginning of the test, the piston moves down to have a short run-up before impaling the materials in the striker. Uncertainty is introduced when the test begins, due to the time spent outside of the thermostatic chamber, hence not at the right temperature.

#### 2.3.1.2.1.4. *The video camera*

High frequency video camera, to analyse the mechanisms of deformation during the test, was used. When used during the tests, the camera was set to record up to 6000 images per second. At 23m/s, with this frame rate, the camera managed to capture about only 20 pictures from the moment the striker impacted the skin to the failure.

#### 2.3.1.2.2. Data collected

The biggest difference between the CEAST and HSTT lies in the fact that a piston-activated impact is used instead of a fallen impact system. Additionally, more parameters are measured during the test: the actual deflection and load. It should be pointed out that the deflection is measured instead of being calculated, like in the CEAST system in eq. (1). The images produced by the camera are also synchronized with the deflection and load.

From these measured data, the impact speed  $v(t)$  and the energy  $E(t)$  are numerically calculated as follows:

$$v(t) = \frac{d_{t+\Delta t} - d_t}{\Delta t} \quad (\text{eq 2.4})$$

$$E(d) = \sum \frac{F_{t+\Delta t} + F_t}{2} \cdot (d_{t+\Delta t} - d_t) \quad (\text{eq 2.5})$$

#### 2.3.1.2.3. Filtering data using High Passing Band Sensor

The first results obtained with the HSTT were not concluding. Indeed, during a high speed impact test a high level of oscillations starting from the striker to the load cell (along the metallic bar), created during the impact of the sample, are perturbing the signal obtained [42].

To overcome this phenomenon, an experimental protocol designed by Pr Gerard Gary was used [<https://sites.google.com/view/transalgo/high-passing-band-sensor>]. This protocol measures the oscillations alongside the metallic bar in three different positions thanks to a strain gauge, in order to mathematically remove them. An example is displayed on Figure 2.21, showing the raw results before and after using the oscillation filter.

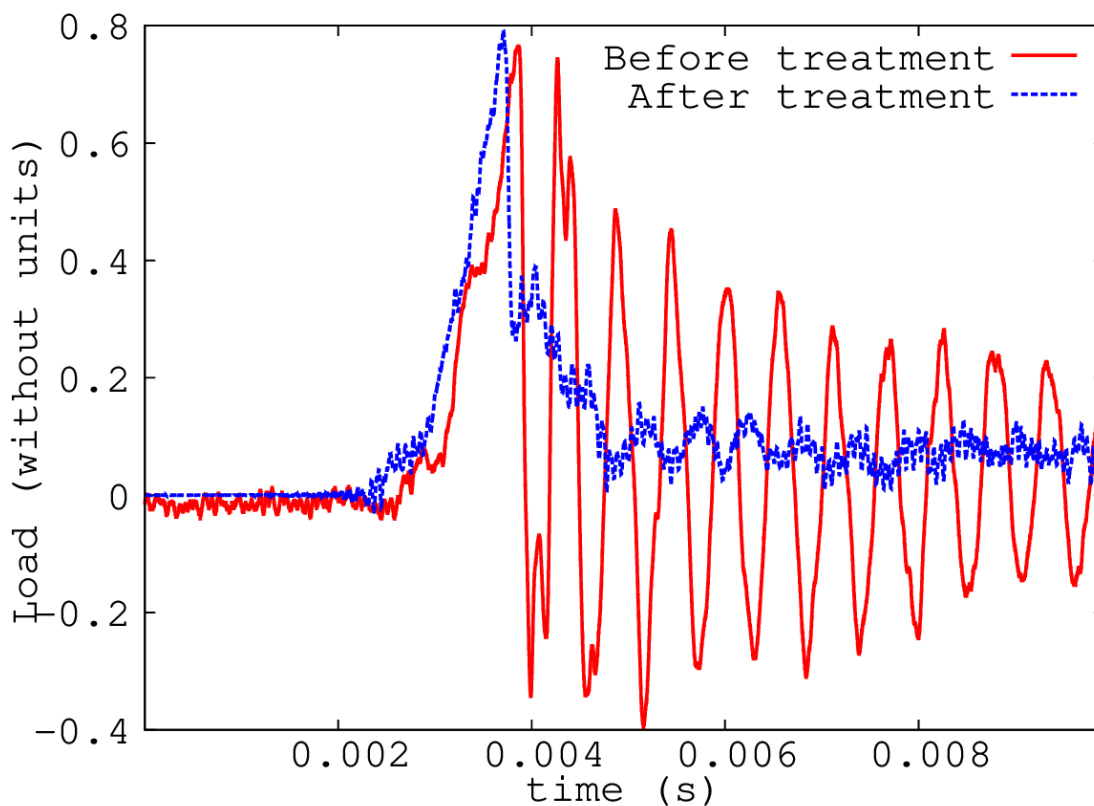


Figure 2.21: Raw load versus running time obtained from the HSTT instrument at 10 m/s and 25°C, before and after using the oscillation filter

#### 2.3.1.2.4. Test program

The temperatures explored for the tests on unscored samples are: (-10, 0, 10, 15, 20, 30)°C and for scored samples: (-10, 0, 10, 20, 25, 30)°C. The data range was adapted with the material, its condition (unscored or scored) and the impact speed investigated, in order to have enough data where the Temperature of Ductile failure Threshold (Tdth) range is assumed. The Tables 3.3-4 list all the impact test conditions performed on the HSTT machine. The yellow part shows the different impact speeds investigated, the blue part

indicates the temperature inside the thermostatic chamber, and the green part gives the repetition number for each condition of speed and temperature. For unscored and scored specimens, the total number of tests was 54 each.

Total=54		temperatures (°C)					
		-10	0	10	15	20	30
speed (m/s)	10	3	3	3	3	3	3
	15	3	3	3	3	3	3
	23	3	3	3	3	3	3

Table 3.3: Test program with HSTT machine for unscored samples

Total=54		Temperatures (°C)					
		-10	0	10	20	25	30
speed (m/s)	10	3	3	3	3	3	3
	15	3	3	3	3	3	3
	23	3	3	3	3	3	3

Table 3.4: Test program with HSTT machine for scored samples

### 2.3.1.3. Instron 5982 for clamped SENB test [43]

To better understand the mechanisms of ductile crack initiation and propagation near the impacted zone of the scored thin sample, SENB clamped specimens were tested using an Instron 5982 (load capacity 100 kN), with an additional and adapted load cell of 1 kN.

Figure 2.22 shows the top view of the experimental setup where the span of the rollers was fixed at 30 mm. Moreover the impactor pin and the rollers had the same root radius of 2 mm. The plasticized PVC being extremely soft/flexible, unlike the classical SENB setup, specific jaws were designed to prevent any sample displacement during the test. It should be mentioned that the same boundary conditions were applied for the impact tests of pre-cracked thin plates. The data collected during the test consisted of the load and the corresponding deflection.

Figure 2.23 details the region near the crack tip in the undeformed state: the impactor was slightly lowered in order to obtain a picture with the mouth of the crack opened. A video

camera was placed in front of one of the side surfaces so as to synchronize the load and the deflection recorded with the crack opening displacement and the advance of the crack. Due to the large strain experienced by the material, the camera had to be motorized to follow the position of the sample. The deflection speed used for the tests was selected to match that of the camera's motor, which was 6 mm/s.



Figure 2.22: Top view of the experimental setup for SENB tests

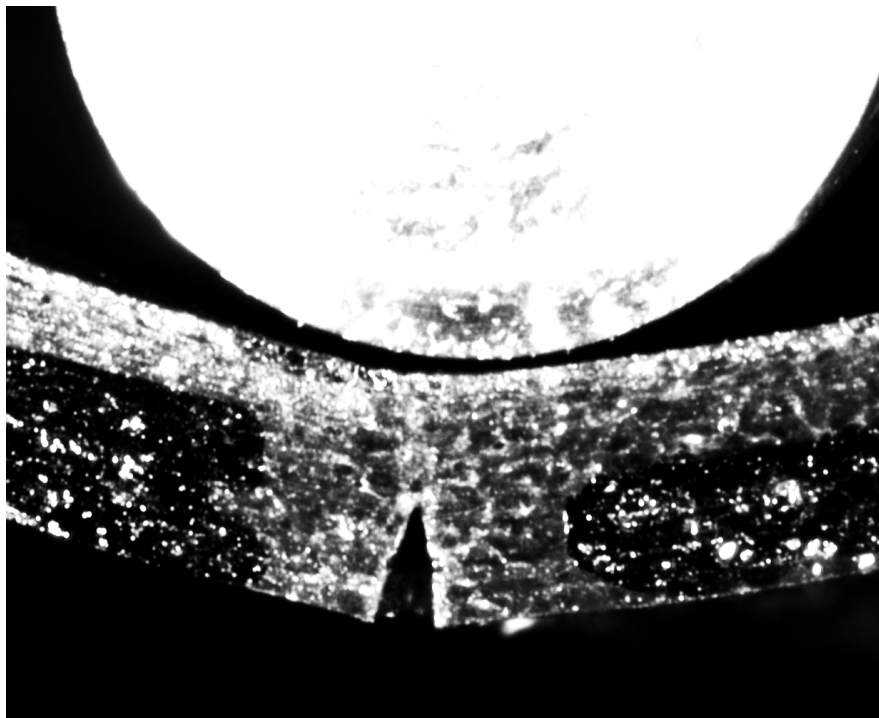


Figure 2.23: Side view captured by the motorized camera during a test

## CHAP3: Mécanismes de rupture sur des échantillons pré-entailés

Ce chapitre est une reproduction de l'article publié dans *Journal of Theoretical, Computational and Applied Mechanics* et intitulé : "Ductile crack initiation and growth on a plasticized Polyvinyl Chloride during airbag deployment" soit initiation et propagation d'une fissure ductile sur un polychlorure de vinyl (PVC) durant un déploiement d'airbag.

Une bonne connaissance de la propagation de l'entaille dans le matériau est requise pour analyser le comportement sous impact d'échantillons pré-entailés. Grâce aux essais de flexion trois points encastés, il est possible d'étudier les notions de paramètre de chargement et de critère de rupture.

Le paramètre de chargement est la variable pertinente combinant la charge appliquée et les longueurs caractéristiques de la fissure et du corps fissuré. Le critère de rupture consiste en la valeur critique de la variable susmentionnée. Cette réflexion se concentre donc sur les deux paramètres de chargement suivants: la densité d'énergie de la surface fracturée, notée  $\Gamma$  correspondant à l'aire sous la courbe de la charge en fonction de la déflexion, liée à l'aire du ligament restant ; et l'intégrale  $J$  recommandée par la mécanique non linéaire de la rupture . Les deux critères de rupture correspondants sont respectivement la résilience ( $\Gamma_c$ ) et la ténacité ( $J_c$ ).

L'optimiseur de Z-set a d'abord été utilisé pour obtenir un jeu de coefficients de matériau en utilisant les courbes de charge en fonction du déplacement d'ouverture de la fissure. Ensuite, les valeurs de l'intégrale  $J$  avec une fissure propageante ont été calculées en utilisant la technique de de Lorenzi. La comparaison de ces valeurs avec celles de l'intégrale  $J$  obtenue par sa formule analytique a permis d'obtenir une estimation du facteur de calibration  $\eta_p$ .

L'étude du paramètre de chargement et du critère de rupture ont permis de déduire que la ténacité du PVC plastifié étudié était de 10,8 kJ/m<sup>2</sup> environ, valeur proche de celle rapportée dans la littérature pour le PVC modifié. L'exploitation de la base de données expérimentales, associée à la simulation par éléments finis de la propagation de la fissure, a ensuite permis d'établir le facteur de calibration  $\eta$  de cette éprouvette SENB encastée , en fonction du rapport de profondeur de la fissure.

Cette étude a notamment permis d'observer que l'amorçage de la fissure apparaît lorsque la courbe de charge en fonction de la déflexion dévie de la linéarité. La fissure se propage ensuite à travers le ligament restant. Ce résultat important sera utilisé dans l'interprétation des peaux pré-fissurées de telle sorte que l'énergie de rupture sera considérée à l'apparition de la non linéarité. Cette conclusion sera utilisée dans le chapitre suivant.

## 3. Failure mechanisms on precracked specimens

### 3.1. Introduction and organization of the article

In this chapter the failure mechanisms were analysed, notably the study of the ductile crack initiation and growth observed on a clamped Single Edge Notch Bending (SENB) specimen tested at room temperature, i.e. 23°C, and with a quasi-static loading. The basic results were recently published in an article entitled “Ductile crack initiation and growth on a plasticized Polyvinylchloride during airbag deployment” in the *Journal of Theoretical, Computational and Applied Mechanics* [43]. The article is reproduced here.

It is organized as follows :

- The introduction section deals with the same context of the study, as already shown in the present manuscript;
- Part two is related to the background in a previously published paper entitled “Impact speed dependency of the ductile failure threshold temperature for a plasticized polyvinylchloride” in *Continuum Mechanics and Thermodynamics* [15]. For the sake of simplicity, it is advised to skip these two first parts of the paper. Indeed, in part one, most of the information was already explained in the document Introduction, and in part two, the study will be detailed further with the impact experimental results (here the tests chronology was inverted for a better understanding);
- Part three explains the methods used along the study, such as the experimental equipments and protocols, relevant mechanical parameters for the analysis, the basis of the Finite Element (FE) method;
- Part four displays the results obtained following the methods observed on chapter two on the clamped SENB tests, in order to measure/calculate the fracture toughness in the framework of the Fracture Mechanics. The difference between classical and clamped SENB specimens was investigated by calculating the specific calibration factor  $\eta$  function. Moreover, video acquisition during the tests allowed to determine the time where the crack (re)-initiated;
- Part five offers a discussion about the transferability of the results from the clamped SENB specimens to the impact test carried out with CEAST and HSTT instruments. These latter are the main objectives of the subsequent sections in this chapter;
- Part six ends the chapter with the concluding remarks of the study.

## 3.2. Ductile crack initiation and growth on a plasticized Polyvinylchloride during airbag deployment

With the goal of ensuring the security of passengers for the automotive industry, the present work addresses the ductile fracture process of plasticized PVC. Dedicated clamped single edge notch bending (SENB) specimens were used to characterize the mechanisms of crack initiation and propagation for the studied material. The exploitation of the experimental database associated with finite element simulation of the crack propagation allowed, on the one hand, the calibration factor  $\eta_p$  of this specific SENB specimen to be established, as a function of the crack depth ratio. On the other hand, the fracture toughness of the studied plasticized PVC was estimated to be  $10.8 \text{ kJ/m}^2$ , a value which was close to that reported in the literature for modified PVC. By using this fracture toughness value, a methodology aiming at the prediction of ductile crack initiation of the PVC skin integrated into a real dashboard (full scale test) was proposed.

### 3.2.1. Introduction

The correct deployment of airbag spreading is a major concern for the security of passengers in the automotive industry. The design and elaboration of the dashboard is one of the key features for obtaining the required specifications. Plasticized PVC skins are commonly used for the top surface of the three layers of the dashboard.

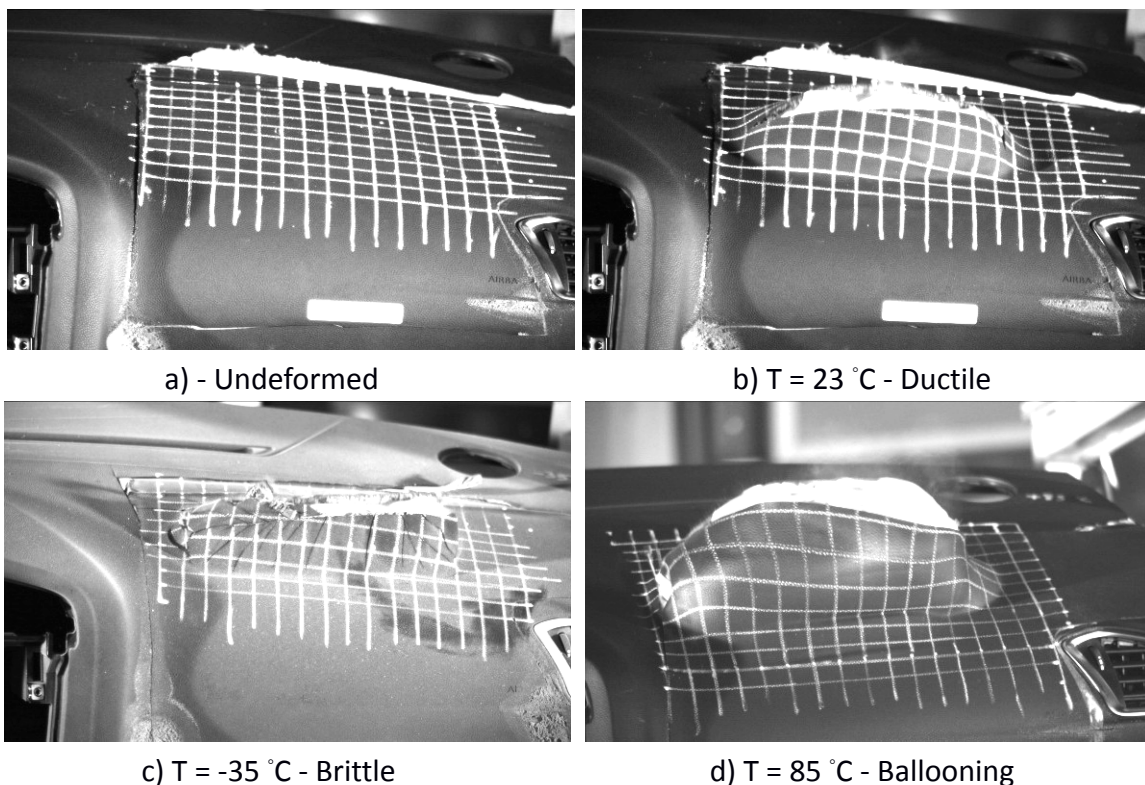


Figure 3.1: Tests at full scale of an air-bag deployment: a) Undeformed state of the airbag window; b) correct ductile tearing at 23 °C; c) brittle failure at -35 °C where secondary transverse cracks can be observed; d) ballooning effect at 85 °C inducing delay or non opening.

To assess the role of the system in the spreading of the airbag, full scale tests have been carried out at various temperatures. Figure 3.1 illustrates some salient results of these tests which allow a better analysis of the deformation and failure of the opening of windows on the airbag box during deployment. The grid cell size was about 10 mm in the initial undeformed state (Figure 3.1a). From these tests, it was observed that:

- At 23 °C (Figure 3.1b), a net ductile tearing of the skin, following the scoring direction and accompanied by the deformation of the top surface of the airbag box, was observed. This is the desired fracture process. Using Digital Image Correlation (DIC) software, the impact speed applied to the PVC skin was estimated to be around 25 m/s;
- At -35 °C (Figure 3.1c), but at the same impact speed, a brittle failure of the skin occurred with small deformations. The main crack was on the surface plane and followed the direction of the inner score already made on the plasticized PVC outer skin. The presence of secondary transverse cracks could be noticed. These may provoke fragmentation [1] of the dashboard, accompanied by the projection of the pieces of the material and so would be dangerous for the passengers;
- At 85 °C (Figure 3.1d), at the same impact speed, a significant deformation of the box together with an extreme extension of the skin delayed the opening time, if it occurred, as ballooning could prevent the opening of the box. This situation is the most dangerous condition which needs to be avoided even though the ultimate failure could also be qualified as ductile.

Full scale experiments, as reported above, are very costly. Therefore, a research programme was elaborated to directly test the plasticized PVC skin [15]. One grade of plasticized PVC was selected, the most common one used in the automotive industry. PVC skin plates were provided by the Westlake Global Compound company. Scoring was added as a pre-crack on the samples using a robot for better reproducibility. The desired ratio between the score depth and the total thickness was about 0.5.

Standardized Charpy tests [44, 45] are commonly recommended to characterize the failure of plastics by impact. They enable the determination of the impact strength of the material by utilizing notched specimens with precise notch root radius. In the present work, the robot cut induced a more acute crack with a notch root radius tending to zero. Moreover, the knowledge of the impact strengths allows the classification of plastics regarding their brittle fracture behaviour. As the desired failure mode is the ductile one for the plasticized PVC under study, this constitutes a limitation for the use of Charpy tests. Indeed, for very ductile plastics, the specimen may not fail after the impact. In this extreme case of no failure, the impact strength cannot be determined. Additionally, as mentioned above (test at 85 °C), this is the most dangerous situation. The aim of this work is then to characterize the ductile failure of the plasticized PVC, by using the fracture mechanics tools.

To achieve this goal, the present paper starts by recalling previous results [15] where the domain of interest, in terms of temperatures and impact speeds that emphasizes the ductile failure of the material, has been determined. Then, the methods used are described in the following section. The design of an experimental setup adapted to the material so as to

obtain ductile failure characteristics is developed. The load parameters and the failure criteria for ductile fracture of polymers proposed by fracture mechanics theory [46, 47] are introduced. The Finite Element analysis allowing the computation of the load parameters for complex cracked geometries is described at this stage. The section listing the results follows, starting from the specific mechanisms of crack initiation and growth, proper for the studied plasticized PVC. The fracture toughness of the material was determined by taking these mechanisms into account. The relationship between the obtained fracture toughness and the impact strength is then established. The last part of the chapter consists of a set of discussions that propose a methodology to predict the ductile crack initiation on the PVC skin integrated into the dashboards thanks to the knowledge of the fracture toughness of the material.

### 3.2.2. Background

Impact tests were carried out using an Instron CEAST 9350 drop tower impact system [16]. The samples, consisting of thin and soft plates, had to be gripped along a circular section. Details of the CEAST 9350 machine have been described elsewhere [15]. About one hundred test results have been analysed, corresponding to 3 tests for each selected test temperature: (-6, -3, 0, 5, 10, 15, 20, 25°C) and each selected impact speed: (2, 4.4, 6, 10 m/s).

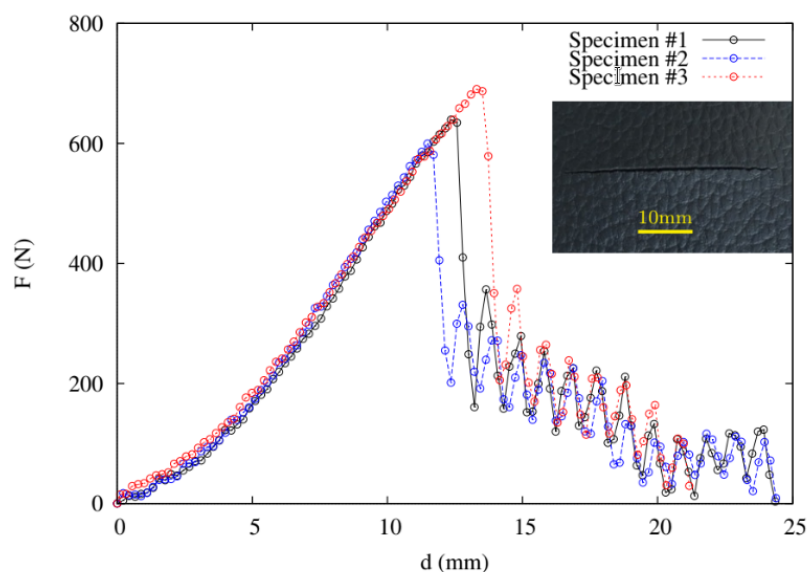


Figure 3.2: Load (F) versus deflection (d) curves for scored thin plates tested at 4.4 m/s and 20 °C. Ductile fracture surface at the macroscopic scale is shown.

The load versus deflection curves for the three tests at 20 °C and at an impact speed of 4.4 m/s are shown in Figure 3.2. A first loading stage was observed up to a load of about 650 N. Then, a first load drop appeared followed by a gradual decrease with apparent oscillations. The slope of the first drop appeared to be the same for the three tests. Additionally, the fracture surfaces of the tested samples exhibited characteristics of ductile failure.

From the load versus deflection curves, four main characteristic mechanical parameters were deduced:

- The stiffness of the system that corresponded to the slope of the linear part of the curve  $\frac{\Delta F}{\Delta d}$ , where F is the load and d is the deflection;
- The deflection and the load at failure, respectively  $d_f$  and  $F_f$ , related to the last point before the abrupt drop of the load, *i.e.* at the onset of failure;
- The fracture energy  $A_f$  determined by integration of the area under the load *versus* deflection curve up to  $(d_f, F_f)$ :

$$A_f = \sum_{i=1}^F \frac{(F_i + F_{i-1})}{2} \cdot (d_i - d_{i-1}) \quad (\text{eq 3.1})$$

The so-called impact strength here consisted in relating the fracture energy in eq. (3.1) to the fracture surface area  $\Phi(t - a)$  where  $\Phi$  is the diameter of the hemispherical impactor, 't' is the thickness of the skin, and 'a' is the crack depth. In fact, this operation consisted of integrating the area under the net stress *versus* the deflection curve; the net stress being the ratio of the load per unit of the fractured surface.

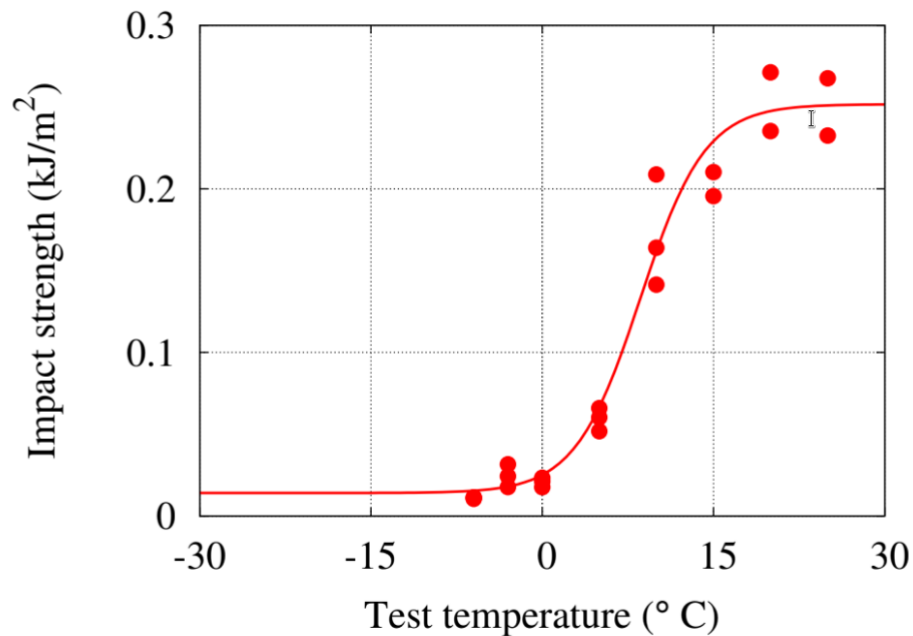


Figure 3.3: Evolution of the impact strength with respect to the test temperature.

The evolution of the impact strength of the studied plasticized PVC for the impact speed of 4.4 m/s as a function of the test temperature is shown in figure 3.3. Attention should be paid here to the upper shelf corresponding to the ductile mechanisms of failure. Typically, it could be concluded that, under these test conditions, the impact strength of the plasticized PVC was about 0.25 kJ/m<sup>2</sup>.

The extension of this result to the other impact speeds was assessed by determining how the Ductile Failure Threshold Temperature ( $T_{dth}$ ) evolved with respect to the impact speed as illustrated in Figure 3.4. Although the impact speed of 25 m/s was not reached in this study, this plot indicated that  $T_{dth}$  tended to stabilise and would be lower than 20°C. This has been confirmed by the ductile failure obtained for the full scale test at 23°C shown in Figure 1b. Theoretically, the impact strength value of 0.25 kJ/m<sup>2</sup> determined on the upper shelf is not dependent on the impact speed. On the other hand, for pre-cracked specimens, the

relationship between the impact strength and the fracture toughness has been investigated in several research papers on metals [48]. The present work aims at the determination of the fracture toughness of the plasticized PVC under study by using the fracture mechanics approach.

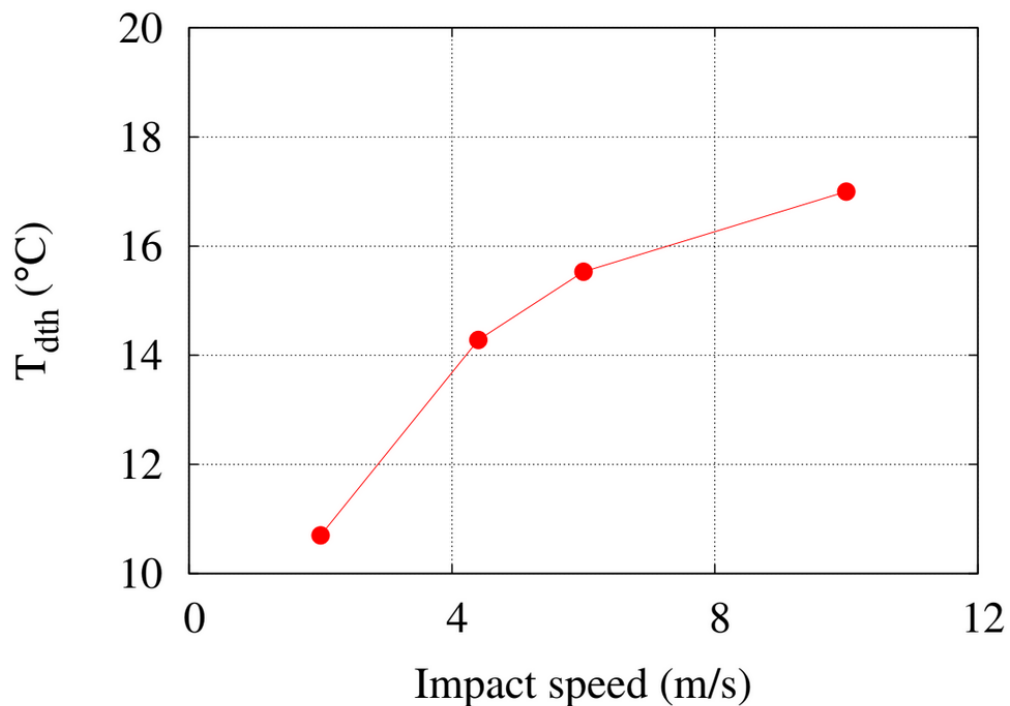


Figure 3.4: The temperature to ductile fracture threshold ( $T_{dth}$ ) as a function of the impact speed.

### 3.2.3. Methods

#### 3.2.3.1. Experiments

PVC skin plates of 90 mm × 90 mm size and with 1.2 mm ± 0.1 mm thickness were provided by the Westlake Global Compound company. Scoring was added as a pre-crack on the plates using a robot for better reproducibility. The desired ratio between the score depth and the total thickness was about 0.5. The robot cut the material so as to keep a retentive ligament thickness of 0.6 mm. This implied an uncertainty on the crack depth ratio due to the real thickness of the skin and the roughness of the pattern on its top surface.

Rectangular specimens were then machined from the scored thin plates, using a punch especially assembled for better dimension reproducibility. The main dimensions of these rectangular scored samples were 90 mm in length and 29.8 mm in width. They mimic the fracture mechanics Single Edge Notch Bending (SENB) specimens for rigid plastics. The initial contact between the impactor and the sample constituted the major difference from the above mentioned CEAST test and the present experiments: a point and a line, respectively for the hemispherical impactor of CEAST and for the present SENB-like specimen.

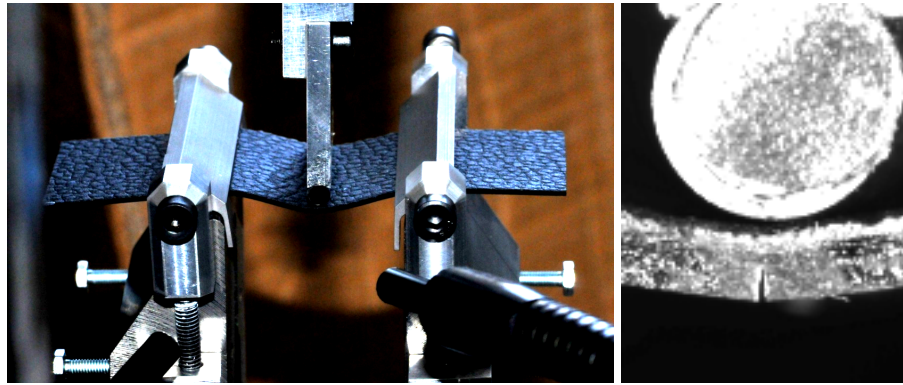


Figure 3.5: Experimental setup for clamped Single Edge Notch Bending (SENB) test: a) Top view where the patterns on the top skin of plasticized PVC plate can be observed; b) Details of the non deformed crack tip

To better understand the mechanisms of ductile crack initiation and propagation near the impacted zone of the scored thin sample, SENB specimens were tested using an Instron 5982 (up to 100 kN force capacity), with an additional and adapted load cell of 1 kN. Figure 3.5a illustrates the top view of the experimental setup where the span “S” of the rollers was fixed at 30 mm. Moreover, the impactor pin and the rollers had the same root radius of 2 mm. The plasticized PVC being extremely soft/flexible, unlike the classical SENB setup, specific jaws were designed to prevent any sample displacement during the test. It should be mentioned that the same boundary conditions were applied for the impact tests of pre-cracked thin plates. The data collected during the test consisted of the load and the corresponding deflection.

Figure 3.5b details the region near the crack tip in the undeformed state. A video camera was placed in front of one of the side surfaces so as to synchronize the load and the deflection recorded with the crack opening displacement and the advance of the crack. Due to the large strain experienced by the material, the camera had to be motorized to follow the position of the sample. The test’s deflection speed, of about 6 mm/s, was selected to match that of the motor.

### 3.2.3.2. Load parameters - Failure criteria

Fracture mechanics approach uses the concept of load parameter and failure criterion. The load parameter is the relevant variable combining the applied load and the characteristic lengths of the crack and the cracked body. The failure criterion consists of the critical value of the aforementioned variable [46, 47, 49-51].

This work focuses on two load parameters: a kind of fractured surface energy density, noted as  $\Gamma$  corresponding to the area under the load *versus* deflection curve (eq. (1)), related to the

area of the remaining ligament; and the J-integral recommended by the nonlinear fracture mechanics. The two corresponding failure criteria are the impact strength ( $\Gamma_c$ ) [48, 52] and the fracture toughness ( $J_c$ ), respectively.

### 3.2.3.2.1. Fractured surface energy density ( $\Gamma$ )

This parameter coming from the load and the deflection that was measured during the test can be written as:

$$\Gamma = \frac{A(F,d)}{B \cdot (W-a)} \quad (\text{eq 3.2})$$

with:

- A(F, d) the area under the load *versus* deflection curve;
- B the thickness of the specimen;
- W the Width of the specimen;
- a the crack depth.

In the present study, in line with the commonly used terminology of the fracture mechanics, the thickness B and the width W of the specimen, in eqs. 3.2 and 3.3, correspond respectively to the width and the thickness of the machined rectangular specimens.

For dedicated Charpy notched specimens, the critical surface energy density at failure (maximum load) corresponds to the impact strength of the material. Here, although a sharp crack is considered,  $\Gamma_c$  will be considered as the impact strength. The evolution of the  $\Gamma$  parameter with respect to the deflection should be analyzed so as to better understand the limits of this key parameter for an engineering approach.

### 3.2.3.2.2. J-integral (J)

In fact, for pre-cracked specimens, the curve to be analysed should be the load *versus* the crack opening displacement (COD). This latter variable is more local than the deflection. However, its measurement was not as easy: it came from video acquisition. The area under this curve is known to be related to the J-integral, the load parameter recommended in non-linear fracture mechanics analysis [46, 47].

$$J_t = \eta_e \cdot \frac{A_e(F,COD)}{B \cdot (W-a)} + \eta_p \cdot \frac{A_p(F,COD)}{B \cdot (W-a)} \quad (\text{eq 3.3})$$

with:

- B the thickness of the specimen;
- W the Width of the specimen;
- a the crack depth;
- $\eta_e$  and  $\eta_p$ , respectively elastic and plastic calibration factors dependent on the crack

depth ratio, the geometry of the specimen and the type of test. According to Williams [46], this factor is assumed to be constant and equal to 2 for classical SENB geometry. For the present clamped SENB specimen, these factors are unknown;

- $A_e(F, COD)$  and  $A_p(F, COD)$ , respectively the elastic and plastic areas under the load-crack opening displacement curve. The partition between these areas can be obtained once the linear correction of the load *versus* COD curve [47] had been operated.

For the sake of simplicity, many studies for polymer materials utilized only the plastic part of the J-integral [46].

$$J_p = \eta_p \cdot \frac{A_t(F, COD)}{B \cdot (W - a)} \quad (\text{eq 3.4})$$

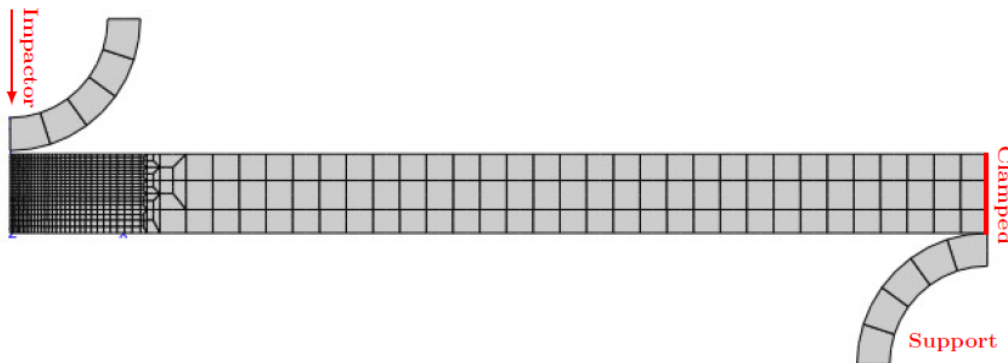
where  $A_t(F, COD)$  is now the total energy corresponding to the total area under the load-crack opening displacement curve.

The critical value (at the maximum load) is defined as the fracture toughness of the material [10, 53]. For impact speed, the fracture toughness is described by MacGillivray [54].

It is worth noting that equations (3.2) and (3.4) differ in the  $\eta_p$  factor and the relationship between the deflection and the notch opening displacement.

### 3.2.3.3. Finite Elements (FE)

Clamped SENB specimens tests were simulated using an in-house FE code: Z-set suite computing solution (<http://zset-software.com/>).



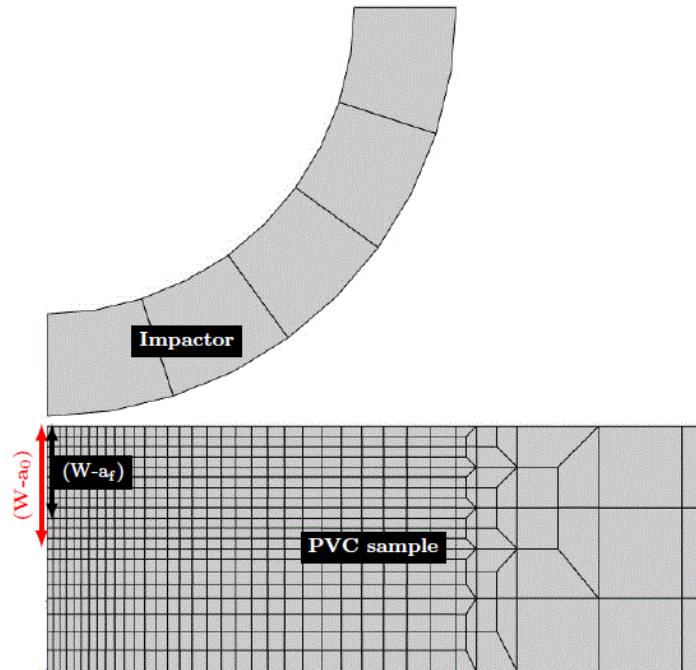


Figure 3.6: Mesh of the clamped SENB specimen: a) Side view of the half specimen; b) Details of the crack tip region (refined meshes). *Note: Size of refined mesh = 50  $\mu\text{m}$  so that  $a_0 - a_f = 150 \mu\text{m}$  corresponds to the maximum crack extension before brittle failure.*

The FE computation used 2D iso-parametric plane strain elements with reduced integration<sup>1</sup>. Only one half of the specimen was meshed. Figure 3.6a illustrates the meshes for the PVC sample, the impactor and the roller. Near the crack tip, the meshes were refined (Figure 3.6b) so as to obtain an element side of 50  $\mu\text{m}$  at the crack tip. The initial ( $W-a_0$ ) and final ( $W-a_f$ ) remaining ligaments are shown respectively by red and black arrows.

The loading was controlled by the displacement of the impactor during the test (deflection). The numerical approach used here did not intend to predict the failure of the specimen but dealt with a FE simulation of the crack propagation by imposing the history of the crack extension included in the experimental data from video camera acquisition. An attempt was then made to simulate the crack initiation and growth using the “release nodal degree of freedom” (rndof) technique [55, 56]. This was done numerically by gradually releasing the nodes (in 6 steps for 3 quadratic elements) from the initial to the final remaining ligament, following the crack growth rate obtained experimentally.

The Z-set optimizer routine was first utilized to obtain a set of material coefficients using data from the load *versus* crack opening displacement curves. Then, the J-integral values with a propagating crack were computed using the *de Lorenzi* technique [57]. The comparison of these values with those of eq. (3.4) allowed the estimates of the  $\eta_p$  calibration factor to be achieved.

<sup>1</sup> In Zset, reduced integration is only used for quadratic elements.

### 3.2.4. Results

The upper shelf impact strength was of key interest for engineering structures such as the skin of the dashboard. It was estimated to be  $0.25 \text{ kJ/m}^2$  from macroscopic data: the load and the deflection. In this section, attention will be paid to the quasi-static tests (ductile fracture) carried out on clamped SENB specimens at room temperature  $T = 23^\circ\text{C}$  and with an impact speed of  $6 \text{ mm/s}$ .

Figure 3.7 illustrates the side view of a deformed sample obtained from the video camera. The transverse cylindrical impactor moved down allowing the opening of the scored line. From this test, the load, the crack opening displacement (COD) and the crack extension ( $\Delta a$ ) at the lateral surface were synchronized thanks to the embarked video-camera system. From this view graph, a large extension of the remaining ligament, leading to a crack tip opening displacement with an order of magnitude larger than the crack extension, was observed. At this deformed state,  $\Delta a$  and COD measurements were relative. They might be subjected to uncertainties.

#### 3.2.4.1. SENB experimental data

The thinness and softness of the plasticized PVC material made it difficult to perform the tests. For reproducibility purposes, seven tests were carried out at the same loading conditions. Only three of them were selected here to be presented since their reliability was considered as correct.

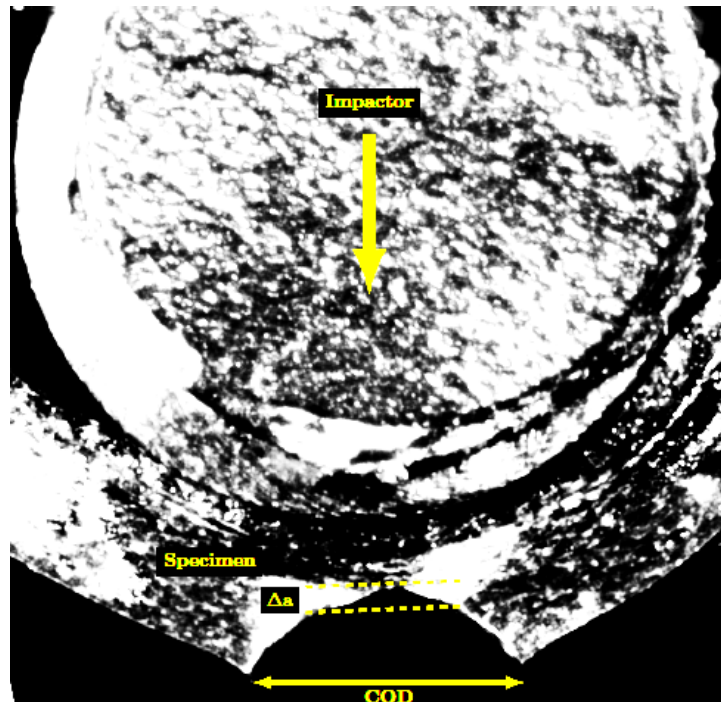
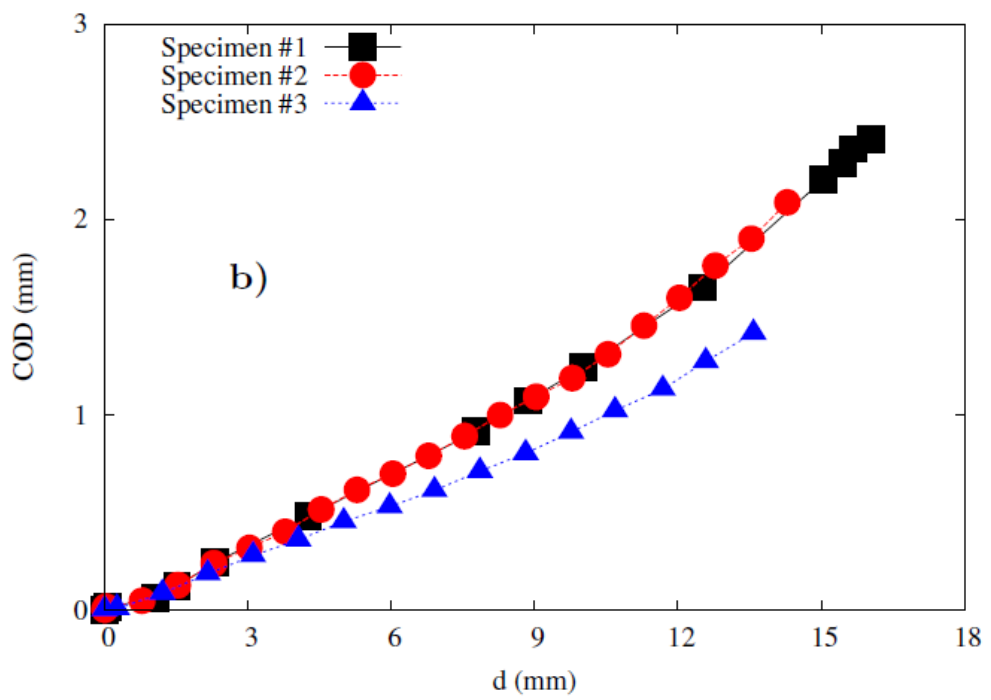
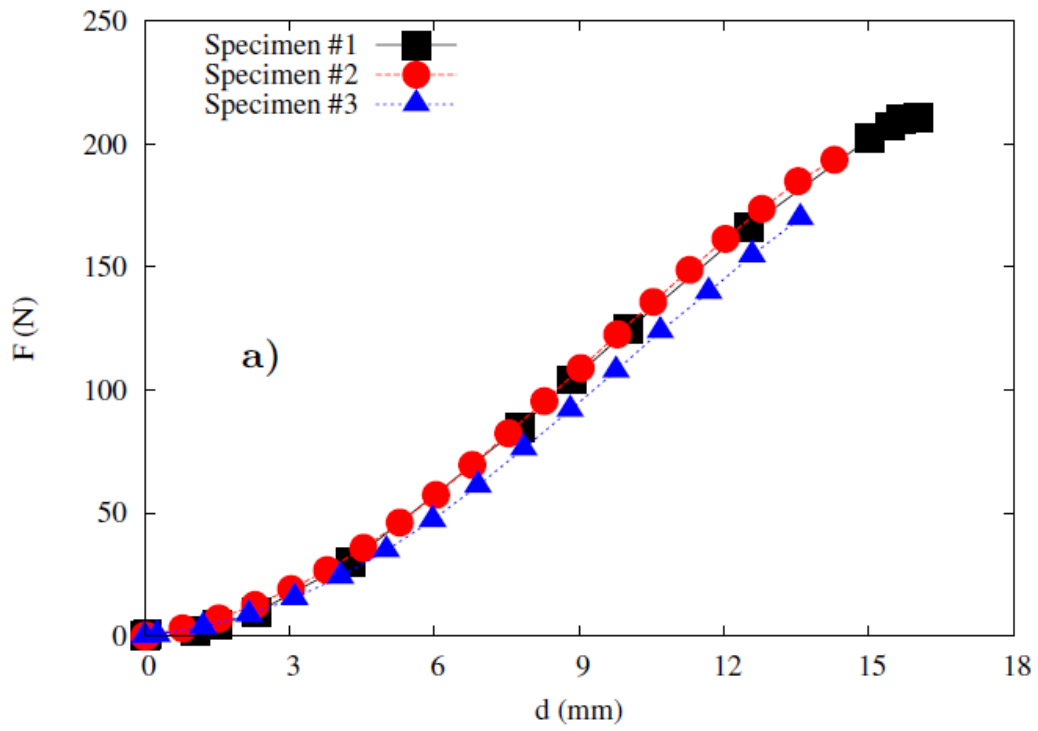


Figure 3.7: Details of the blunted crack tip during the deformation; measurements of the Crack Opening Displacement (COD) and the crack extension ( $\Delta a$ ).

### 3.2.4.1.1. Crack Opening Displacement (COD)



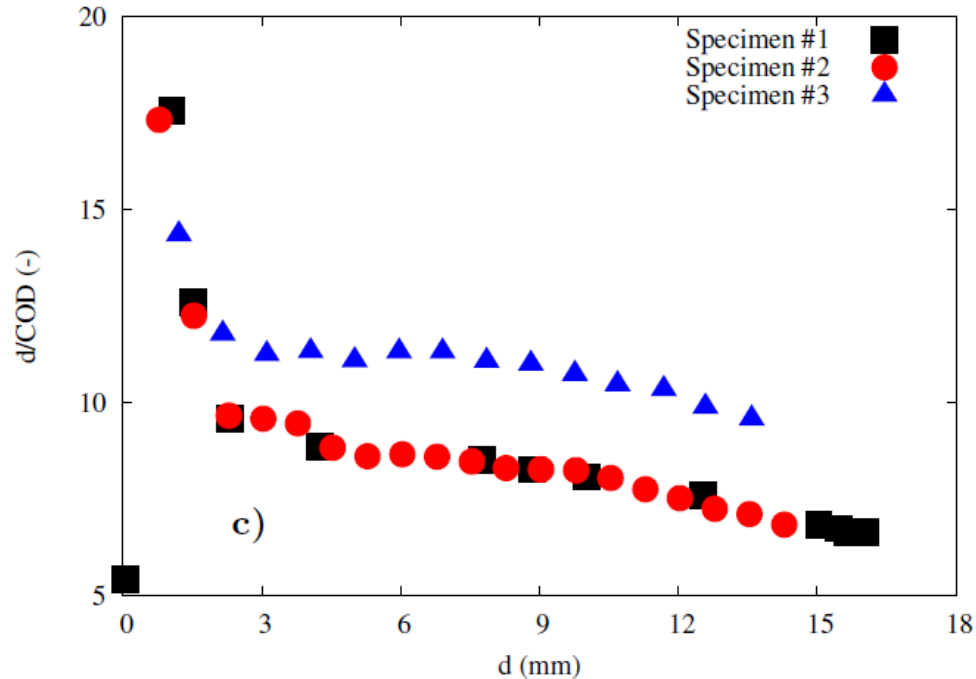


Figure 3.8: Experimental data obtained from quasi-static tests on clamped SENB specimens at room temperature: a) Load vs. deflection; b) crack opening displacement COD vs. deflection; c) the evolution of the ratio between the deflection and the COD.

The aim of Figure 3.8 was the analysis of the implication of the Crack Opening Displacement (COD) measurements to the classical load vs. deflection curve (Figure 3.8a). The experimental data were obtained from the three clamped SENB specimens with respect to the deflection. In Figure 3.8a, the initial inflexion was due to the gradual compression applied to the scored thin plate. A small linear part was observed after this inflexion, followed by a slight nonlinearity when approaching the maximum load. This latter point corresponded to the critical load at failure.

Figure 3.8b plots the COD as a function of the deflection. By contrast to what was reported with the usual SENB geometry [11], non-linearities could be noticed in the relationship between the deflection and the COD. To go further, the evolution of the ratio of the deflection by the COD was plotted in Figure 3.8c. A transient stage could be observed up to a deflection of 3 mm. This could be attributed to the gradual compression of the specimen in the beginning of the test. Then, between 3 mm and 8 mm approximately, this ratio exhibited either a stabilization at 11.5 for Specimen #3, or a very small decreasing rate for Specimen #1 and Specimen #2. The last ones showed good reproducibility and the average value of the ratio was estimated to be 8.

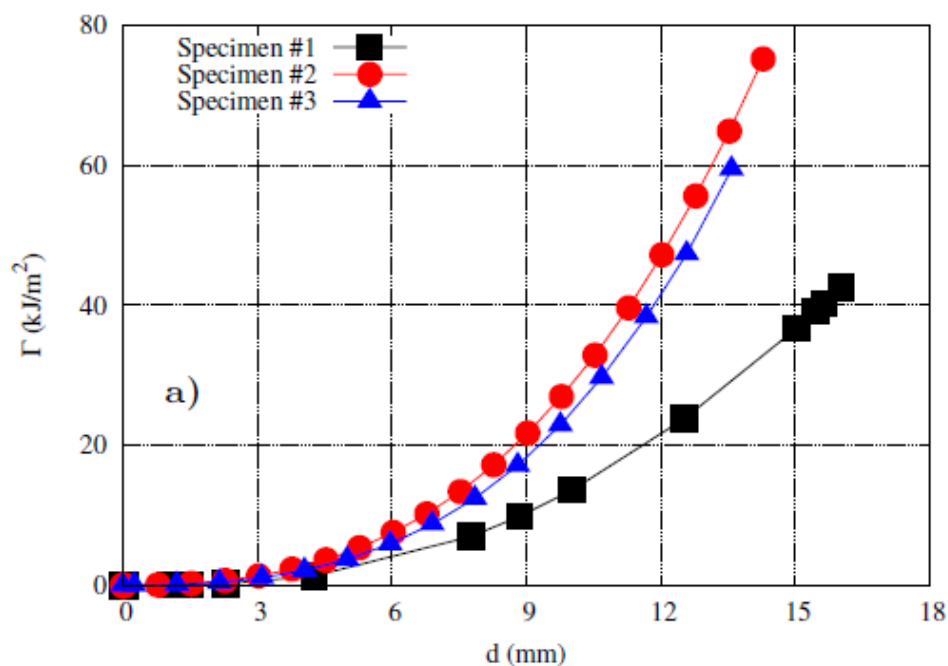
In the last part of the loading (from a deflection of 8 mm up to the failure), a continuous decrease of this ratio was observed, clearly highlighting non linearity between the deflection and the COD.

The use of these macroscopic measurements together with the COD allowed the calculation of respectively  $\Gamma$  (see eq.(3.2)) and  $J_p/\eta_p$  (see eq.(3.4)). Recall that  $A(F, d)$  in eq.(3.2) and  $A_t(F, COD)$  in eq.(3.4) were numerically integrated over the loading:  $\Gamma$  and  $J_p/\eta_p$  depend on the loading step. Their critical values  $\Gamma_c$  and  $J_p/\eta_p$  have to be determined at the moment of the failure. It should be noted that for classical (*i.e.* non clamped) SENB specimens the COD is proportional to the deflection and the calibration factor is known. Therefore, the two load parameters, as well as their critical values, differ by a fixed multiplier factor. The above mentioned non linearities motivated further analysis concerning the material and specimen geometry under study.

Figure 3.9a shows a continuous increase of  $\Gamma$  as a function of the deflection for the three specimens. While good agreement was obtained for Specimen #2 and Specimen #3, a large deviation was observed for Specimen #1.

An attempt was then made to plot  $J_p$  (see eq. (3.4)) with respect to the deflection. Since the calibration factor  $\eta_p$  was unknown, the study focused on the reduced load parameter  $J_p/\eta_p$  in Figure 3.9b. The same conclusion as for  $\Gamma$  could be mentioned although the values were one order of magnitude lower.

Table 3.1 summarizes the values at failure of the characteristic parameters. A large scatter could be observed in  $\Gamma_c$  and  $J_p/\eta_p$  in the two last columns. Furthermore, the scattered  $\Gamma_c$  values significantly differed from the impact strength in the ductile plateau given in Figure 3.3: (0.25 kJ/m<sup>2</sup>*i.e* factor 100). This is problematic from a mechanical engineering viewpoint. Indeed,  $\Gamma_c$  value is required for the design and the safety of the airbag window during the deployment.



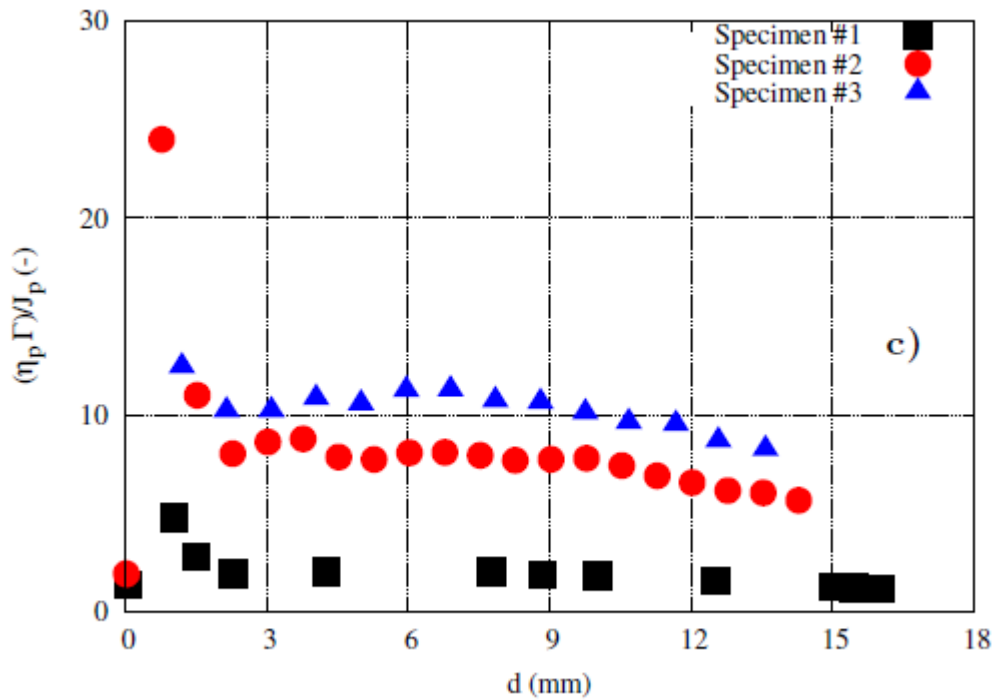
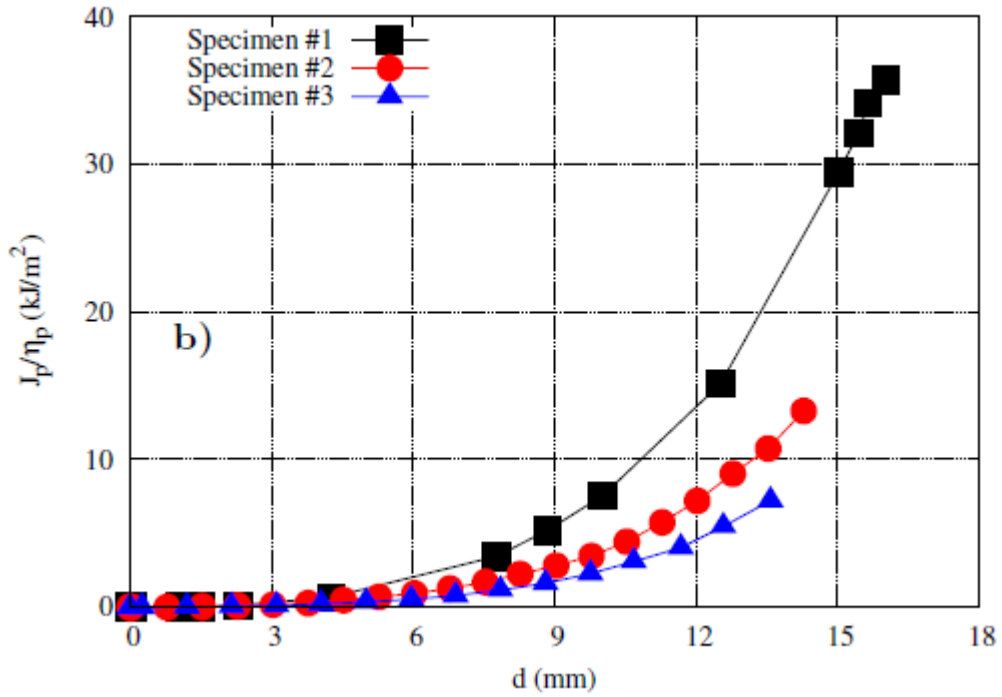


Figure 3.9: Evolution as a function of the deflection of: a) The fracture energy related to the net cross section area; b) The J-integral related to  $\eta$ ; c) The ratio between the two above mentioned parameters

Table 3.1: Values at failure of the collected experimental data (deflection, load and COD), followed by the fractured surface energy density  $\Gamma_c$  and fracture toughness  $J_c/\eta_p$  calculated as the values at failure of respectively  $\Gamma$  and  $J_p/\eta_p$ .

Specimens	d (mm)	F(N)	COD (mm)	$\Gamma_c$ (kJ/m <sup>2</sup> )	$\frac{J_c}{\eta_p}$ (kJ/m <sup>2</sup> )
#1	16.04	210.8	2.41	42.5	37.5
#2	14.29	193.6	2.09	75.2	13.3
#3	13.59	169.9	1.42	59.4	9.21

Further analysis was carried out by focusing on the ratio of  $\Gamma$  to  $J_p/\eta_p$ . In fact, from eqs. (3.2) and (3.4), this ratio could be expressed as follows:

$$\frac{\eta_p \cdot \Gamma}{J_p} = \frac{\eta_p \cdot d}{COD} \quad (\text{eq. 3.5})$$

It can be seen that this ratio is a function of the unknown calibration factor  $\eta_p$  and the ratio of the deflection to the COD already plotted in Figure 3.8c. Figure 3.9c shows the evolution of the ratio  $\frac{\eta_p \cdot \Gamma}{J_p}$  as a function of the deflection. As expected, the curve followed the same trends as that of  $\frac{d}{COD}$  in Figure 3.8c. It should however be mentioned that the calibration factor  $\eta_p$  is dependent on the crack depth ratio  $a/W$ . Therefore, for a stationary crack, its constant value can be deduced, allowing the determination of both  $J_p$  and the multiplication factor between the impact strength and the fracture toughness.

By applying this methodology for the data in Table 3.1, *i.e.* for the values at failure,  $\eta_p$  was estimated to be 0.17, 0.83 and 0.67 respectively for Specimens #1, #2 and #3. This large scatter cannot be used as such in a mechanical engineering calculation for design and safety. Further investigation was carried out and developed in the following.

#### 3.2.4.1.2. Crack extension $\Delta a$

For the three specimens, the evolution of the crack extension during the test was plotted with respect to the deflection in Figure 3.10a. A key point arose from the curves altogether: the crack systematically initiated very early, at a deflection of about 8 mm, corresponding to a load of about 80 N; that is, less than half of the load at failure mentioned above. After this initiation, the crack progressed quasi-linearly as the deflection increased. The maximum crack extension measured at the lateral surface, just before the failure of the specimen, was about 0.15 mm. Figure 3.10a clearly evidenced that the crack was not stationary: the depth ratio  $a/W$  evolved from 0.5 to 0.625 when the deflection ran from 8 mm to about 15 mm.

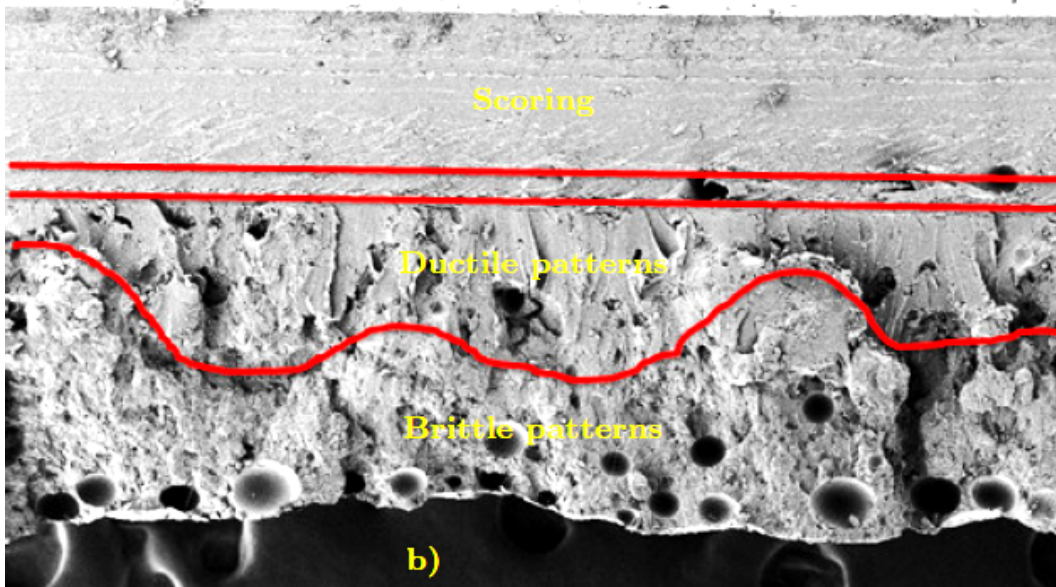
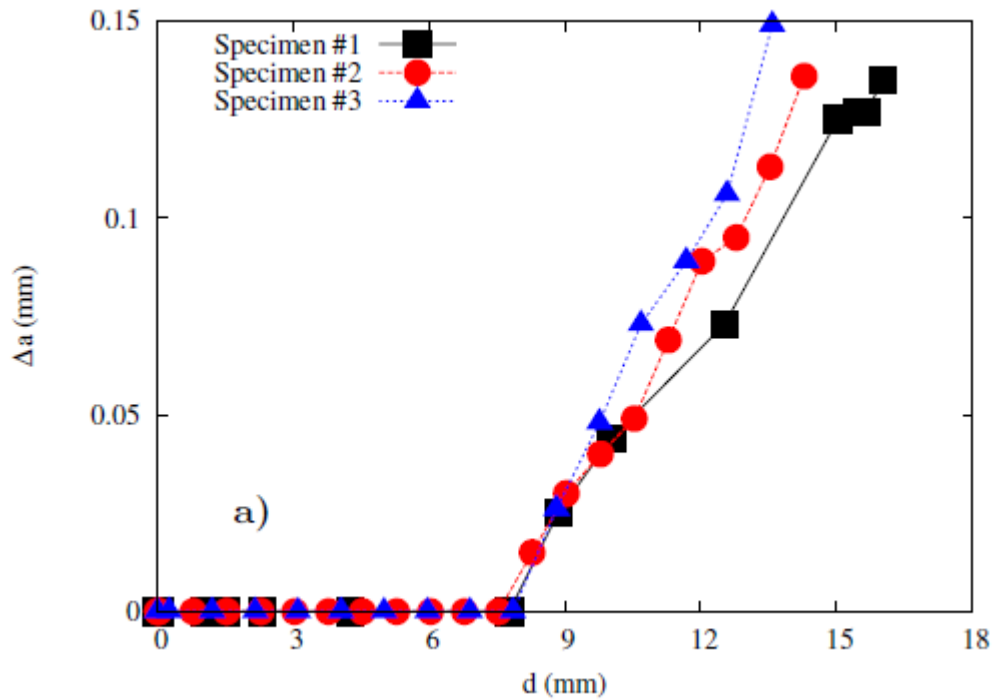


Figure 3.10: Information about the cracking: a) Evolution of the crack extension  $\Delta a$  with respect to the deflection; b) Representative SEM examination of the fracture surface.

Fracture surface examinations were carried out by Scanning Electron Microscopy so as to analyse the through thickness crack extension. Figure 3.10b illustrates the main features observed on a representative fracture surface after the tests (with permanent set). The initial crack implanted by the robot (scoring) exhibited a specific fracture surface with some apparent striations due to the marks of the blade of the robot. Ahead of this pre-existing crack, an area surrounded by the two red straight lines showed some deformed fibrils that could be attributed to the blunting of the initial crack. This pattern was then followed by a

rather flat surface with non-regular crack extension. This was considered as a ductile crack surface where the ductile crack propagation occurred. One can refer to Figure 3.7 to observe the side views of the blunting and the ductile crack extension. Beyond this latter, a more rugged surface, assumed to be a brittle pattern, appeared up to the end of the thickness. The deduced scenario could be summarized as follows, consecutively with increasing deflection:

- Blunting of the crack tip;
- Ductile crack initiation;
- Stable crack growth (ductile tearing);
- Rapid crack growth: this ultimate “brittle” failure did not have the same characteristics as that obtained at very low temperature. Indeed, this happened after the ductile tearing, thus, at a larger crack depth ratio and no fragmentation of the sample was observed.

Table 3.2: Key experimental data at the crack initiation and at the failure of the specimens.

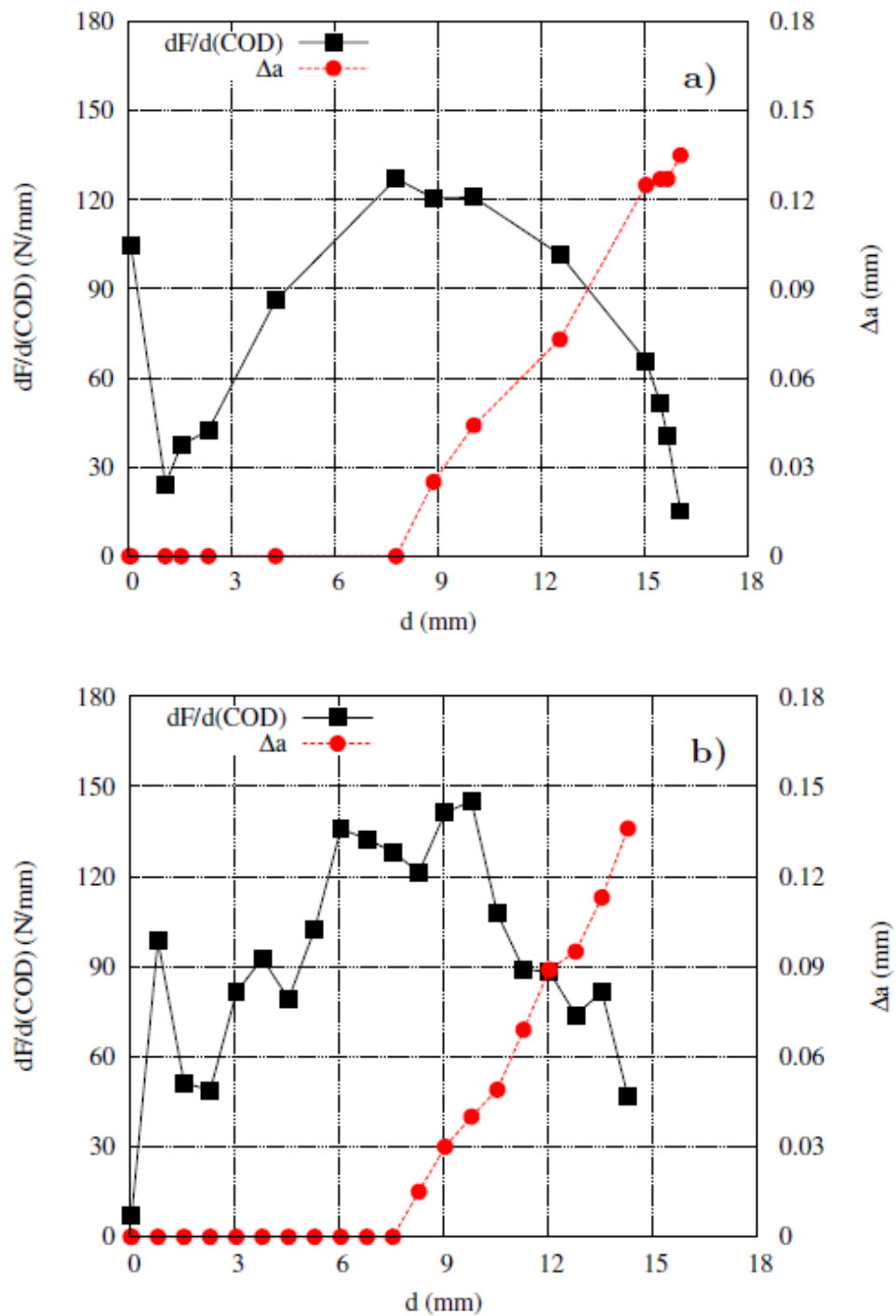
Specimens	$\Delta a$ (mm)		d (mm)		F (N)		COD (mm)	
	init.	fail.	init.	fail.	init.	fail.	init.	fail.
#1	0	0.14	7.77	16.04	84.9	210.8	0.91	2.41
#2	0	0.14	7.53	14.29	82.4	193.6	0.89	2.09
#3	0	0.15	7.86	13.59	76.3	169.9	0.71	1.42

The observed surface was not exactly at mid-thickness so that the average depth might be larger elsewhere. Several bubbles (voids/cavities), with an average diameter of about 0.05 mm, were observed on the fracture surfaces. Although their effects were not in the scope of this study, it can be expected that their presence affected the reproducibility of the experimental data.

It can be deduced from these observations that the maximum load and the crack initiation did not coincide. The key experimental data at both crack initiation and the failure of the specimen were gathered in Table 3.2.

When using the fracture mechanics concepts, the curve to be analysed should be the load vs. the crack opening displacement (COD). Following Hale and Ramsteiner [47], a linear correction had to be operated so as to prevent the effects of the nonlinearity due to penetration of the loading pins into the sample. To this end, the stiffness – defined as the inverse of the compliance of the specimen – was calculated as the derivative, point by point, of the load with respect to the COD:  $dF/d(\text{COD})$ . The evolutions of this stiffness as a function of the applied deflection were plotted in figs. 3.11a-c, superimposed with the evolution of

the crack extension, corresponding to the second Y-axis. Two significant conclusions could be deduced from these curves:



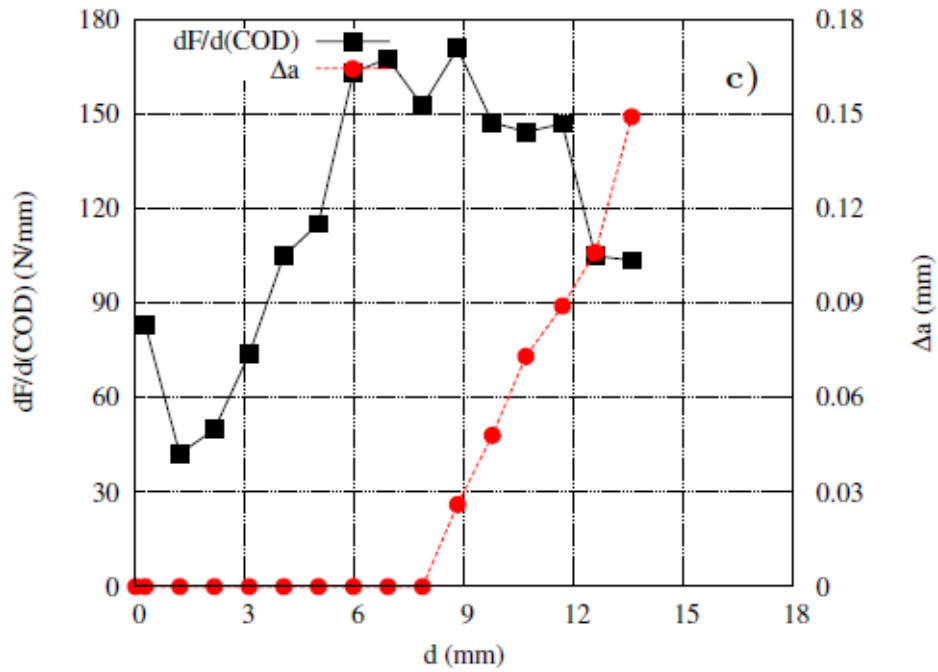
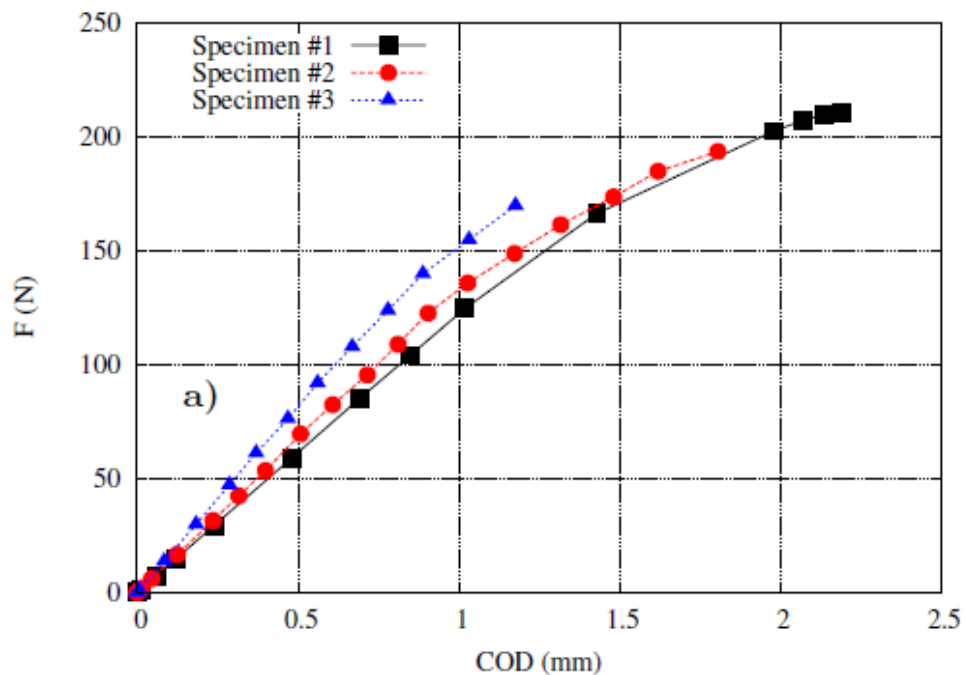


Figure 3.11: Decrease of the stiffness correlated to the increase of crack extension for: a) Specimen #1; b) Specimen #2; c) Specimen #3.

- In contrast to the classical SENB data, the linear correction affected a larger part of the load vs. COD curve. There was no plateau of the stiffness corresponding to the elastic compliance of the curve;
- The stiffness decreased as soon as the crack extension started to progress; meaning that the non linearity in the load vs. COD curve was essentially due to the crack initiation and growth, but not to the plasticity.



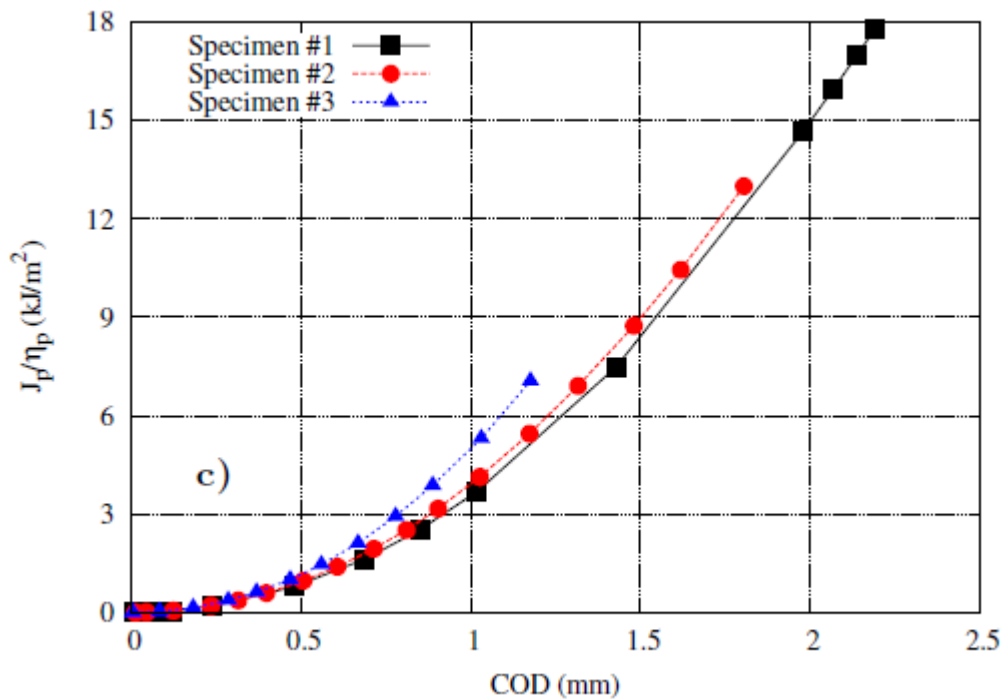
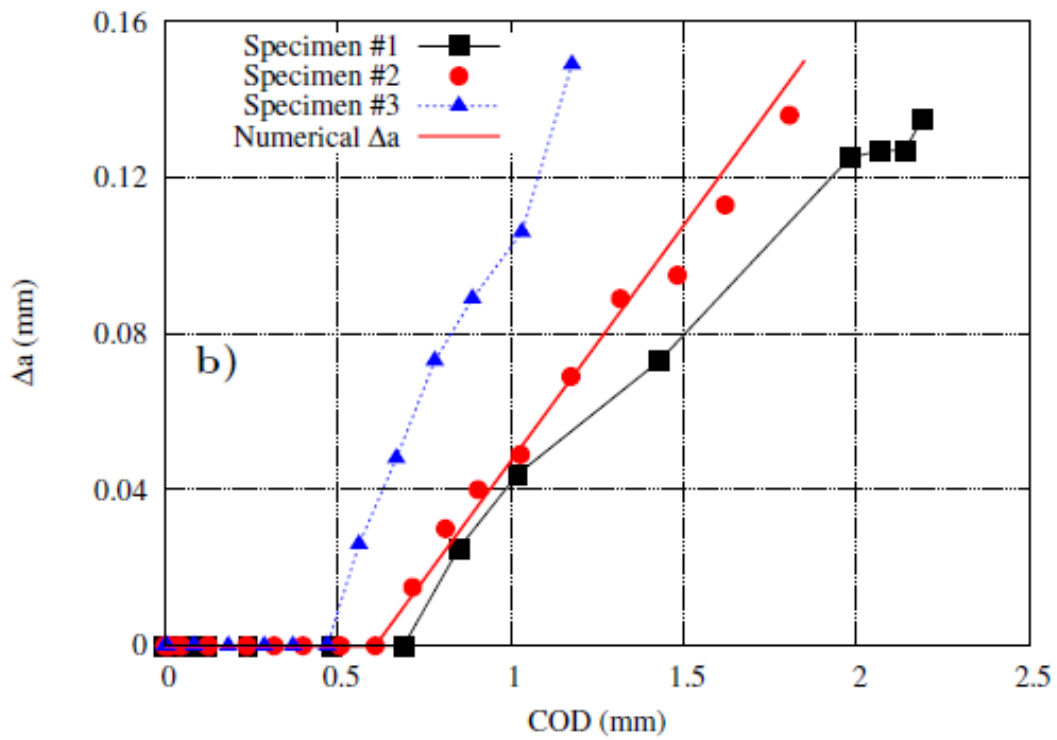


Figure 3.12: Evolution as a function of the COD of: a) The load “F”; b) The crack extension  $\Delta a$ ; c) The J-integral related to  $\eta_p$ .

In order to prepare for fracture mechanics concepts to be applied, namely using finite elements (FE) analysis, the same key curves as in figs. 3.8-9 were plotted, once the linear correction has been applied, as a function of the COD in Figure 3.12.

Figure 3.12a displays the load vs. COD curves showing the corrected linear part. The stiffness was estimated to be  $140 \pm 20$  N/mm. The last experimental points corresponding to the failure of the specimens, a large scatter could be observed concerning the COD at failure. Especially, the curve of Specimen #3 had a small COD at failure in comparison with the two others.

As mentioned above, the trend of the crack extension as a function of the COD in Figure 3.12b showed stable growth of about 0.15mm before the abrupt failure: the crack depth ratio  $a/W$  evolved from 0.5 to 0.625. Again, Specimen #3 showed a steeper slope meaning a more brittle failure. The solid red line in Figure 12b illustrates a fit of the crack extension of Specimen #2. This was used as a boundary condition for the FE release nodal degree of freedom technique (see Section 3.2.3.3.).

The knowledge of the crack extension allowed the calculations of  $J_p/\eta_p$  (eq. (4)) by updating the actual crack depth. In Figure 3.12c, after correction of the linear part,  $J_p/\eta_p$  was plotted as a function of the COD. These curves showed less scatter and smaller values of  $J_p/\eta_p$  than in Figure 3.9b.

Table 3.3: Load parameter  $J_p/\eta_p$  calculated from experimental data after linear correction of the COD.

Specimens	$\Delta a$ (mm)		COD (mm)		F (N)		$\frac{J_p}{\eta_p}$ (kJ/m <sup>2</sup> )	
	init.	fail.	init.	fail.	init.	fail.	init.	fail.
#1	0	0.14	0.69	2.19	84.9	210.8	1.64	17.8
#2	0	0.14	0.61	1.81	82.4	193.6	1.40	13.0
#3	0	0.15	0.47	1.18	76.3	169.9	1.01	7.06

Table 3.3 displays the characteristic values of the main mechanical parameters obtained experimentally followed by the corresponding  $J_p/\eta_p$ . Apart from Specimen #3,  $J_p/\eta_p$  at crack initiation was 10 times less than at failure.

Specimen #2 data set was selected for the FE simulation of propagating crack. Indeed, Specimen #3 was mentioned to exhibit some deviation compared with the two others; whereas Specimen #1 showed a peculiar crack growth behaviour at the onset of the failure (see black full square in Figure 3.12b).

### 3.2.4.2. FE simulations

The purpose of the FE simulations was essentially to numerically compute the J-integral load parameter so as to compare it with that of eq. (3.4). J-integral being dependent on the crack depth, three specific conditions were simulated:

- A stationary crack with the initial crack depth  $a_0$ ;
- A stationary crack with the ultimate crack depth  $a_f$ ;
- A propagating crack from  $a_0$  to  $a_f$ .

Furthermore, the release nodal degree of freedom (rndof) technique was assigned to follow the fit of the crack extension (red solid line) in Figure 3.12b.

#### 3.2.4.2.1. Inverse optimization of the material parameters

Before computing the J-integral load parameter, the material parameters were determined by using an inverse method of optimization in the Zset suite. This optimization was performed using the load vs. COD with the propagating crack. Therefore, the simulated curve –to be compared with the experimental one– accounted for the crack growth using the rndof technique. A simple elasto-plastic model was used during the optimization.

Figure 3.13a illustrates the comparison of the experimental (full circles) with the simulated (solid line) load vs. COD curves, obtained from the optimized material parameters. The oscillations observed in the simulation response were due to the discrete crack growth applied on the three isoparametric elements ahead of the crack tip.

Figures 3.13b-c show the opening stress contour map on the deformed specimen (left) and the deformed crack tip (right), respectively at the onset of crack initiation (crack depth =  $a_0$ ) and at the onset of the brittle failure, that is, at the end of the ductile crack propagation leading to a crack depth of  $a_f$ .

Note that the remaining ligament ( $W-a_0$ ) is longer in Figure 3.13b than in Figure 3.13c, with ( $W-a_f$ ). This indicated that the numerical crack growth was actually operated. Furthermore, the impactor was observed to detach from the top of the PVC specimen at these loading steps. This phenomenon was also experimentally observed –even though not very clear– in Figure 3.7.

Once the material parameters were obtained, two simulations with stationary cracks ( $a_0$  and  $a_f$ ) were carried out so as to compare the compliance of the system (see Figure 3.13a):

- Red full square symbols correspond to the crack depth  $a_0$ . Obviously, the load vs. COD was in line with that of the propagating crack. Moreover, this curve was linear, meaning that linear fracture mechanics concept should be valid before the crack initiation;

- Blue full triangles represented the crack depth  $a_f$ . The compliance was clearly larger (lower stiffness) due to larger crack depth. The end of the load vs. COD showed a slight hardening, that probably was due to the contact configuration in figs.13b-c. However, the last point coincided with the propagating crack simulation.

#### 3.2.4.2.2. Fracture toughness - Elastic calibration factor

Zset finite element code is provided with a routine allowing numerical J integral to be computed using the *de Lorenzi method* [57]. For common fracture mechanics specimens such as SENB or CT, the numerical J-integral is correlated with  $J_p$  if the experimental and numerical load vs. COD curves are in good agreement, as this is the case in Figure 3.13a. Therefore FE J-integral, noted as  $J_{FE}$ , was assumed to be reliable for the clamped SENB specimen.

Seven  $J_{FE}$  were requested to Zset FE code according to the crack progress: at the initial crack depth ( $a_0$ ), then at each crack extension of 25  $\mu\text{m}$  until the final crack depth prior to failure ( $a_f$ ). The stabilization of  $J_{FE}$  was checked thanks to 8 rows of elements surrounding each of the seven crack tips. Typically, it was obtained from the second or the third row of elements. Of course, if the crack tip did not correspond to that of the rndof procedure, the computed  $J_{FE}$  at this location was ignored.

In Figure 3.14, the seven values of  $J_{FE}$  were plotted with respect to the COD as black full square symbols. The blue full circle symbols were attributed to the “experimental”  $J_p/\eta_p$ .

##### 3.2.4.2.2.1. *Fracture toughness $J_c$*

The determination of the fracture toughness requires the load vs. COD curve so as to calculate J-value and the corresponding crack extension  $\Delta a$ . As pointed out by Baldi *et al.* [49], a clear transition from the crack blunting phase to the fracture propagation is not easy to observe, especially for 3D crack shape in opaque polymers. It is often proposed to take, either the J-value at the maximum load or the J-value at a given amount of crack extension (0.2 mm for instance). In the present work, the fracture toughness  $J_c$  was assumed to be the value of  $J_{FE}$  at the crack initiation. From Figure 3.14, it was estimated to be 10.8  $\text{kJ/m}^2$ . This value is very close to that obtained by Hale and Ramsteiner [47] for a modified PVC:  $J_{0.2}=10.2 \text{ kJ/m}^2$ .

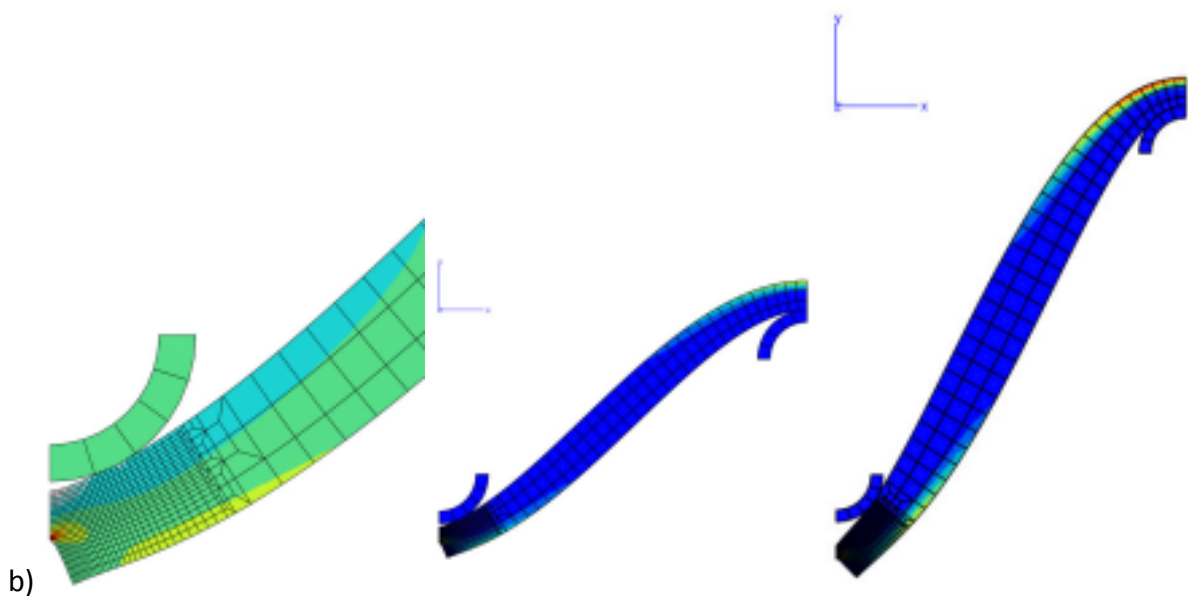
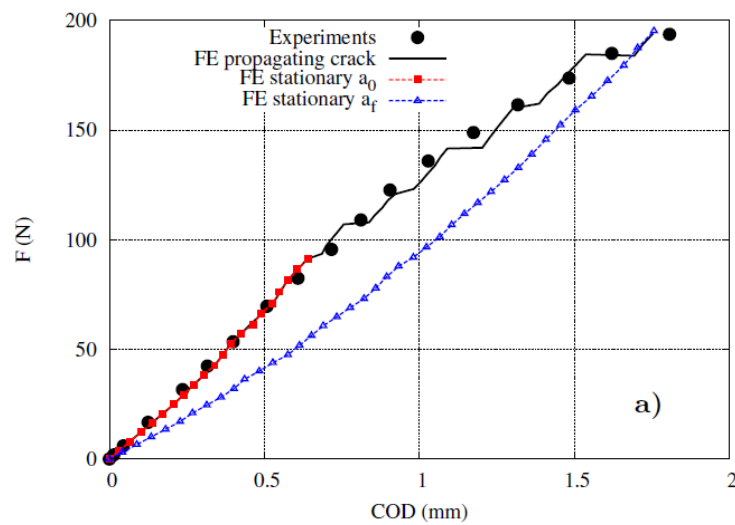
Once the fracture toughness obtained, the evaluation of the calibration factor was attempted by using the value of  $J_p/\eta_p=1.4 \text{ kJ/m}^2$  at crack initiation for Specimen #2 in Table 3. The calculation allowed an estimate of  $\eta_p \approx 8$  for the clamped SENB with  $a/W = 0.5$ , at least for the plasticized PVC under study. It should be mentioned that:

- This value is 4 times higher than that of classical (non clamped) SENB specimen;
- By considering eq. (3) and Figure 3.13a, where the load vs. COD was mentioned to be linear up to the crack initiation, it could be assumed that the obtained calibration

factor was actually the elastic one  $\eta_e$ . Indeed, at this stage,  $A_p(F, COD) = 0$  and  $A_e(F, COD)$  corresponds to the area of the triangle  $(0, F, COD)$  at the crack initiation;

- The fracture toughness  $J_c = 10.8 \text{ kJ/m}^2$  should be used for the prediction of the crack initiation on engineering structures. In Particular, CEAST scored specimen tests [15], on the one hand, and on the window of the airbag box located in the dashboard, on the other hand. As soon as the J-integral can be computed or calculated, the prediction consists of a comparison between the value of J-integral with  $J_c$ .

### 3.2.4.2.3. Crack propagation



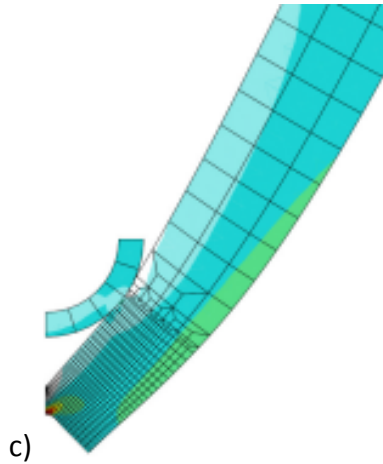


Figure 3.13: a) The load vs. COD curves for various configurations; Opening stress contour map on the deformed crack tip: b) at the end of the linear part; c) at the end of the ductile crack growth.

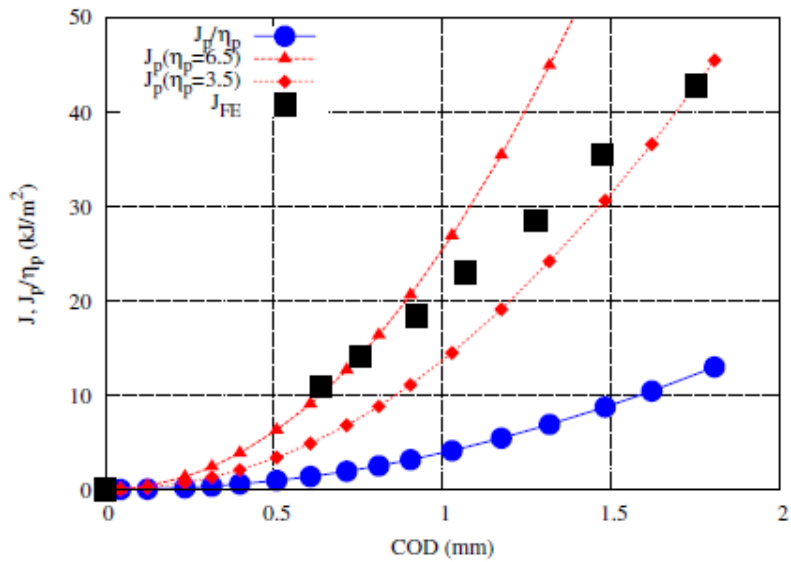


Figure 3.14: The J-integral related to  $\eta_p$  as a function of the COD

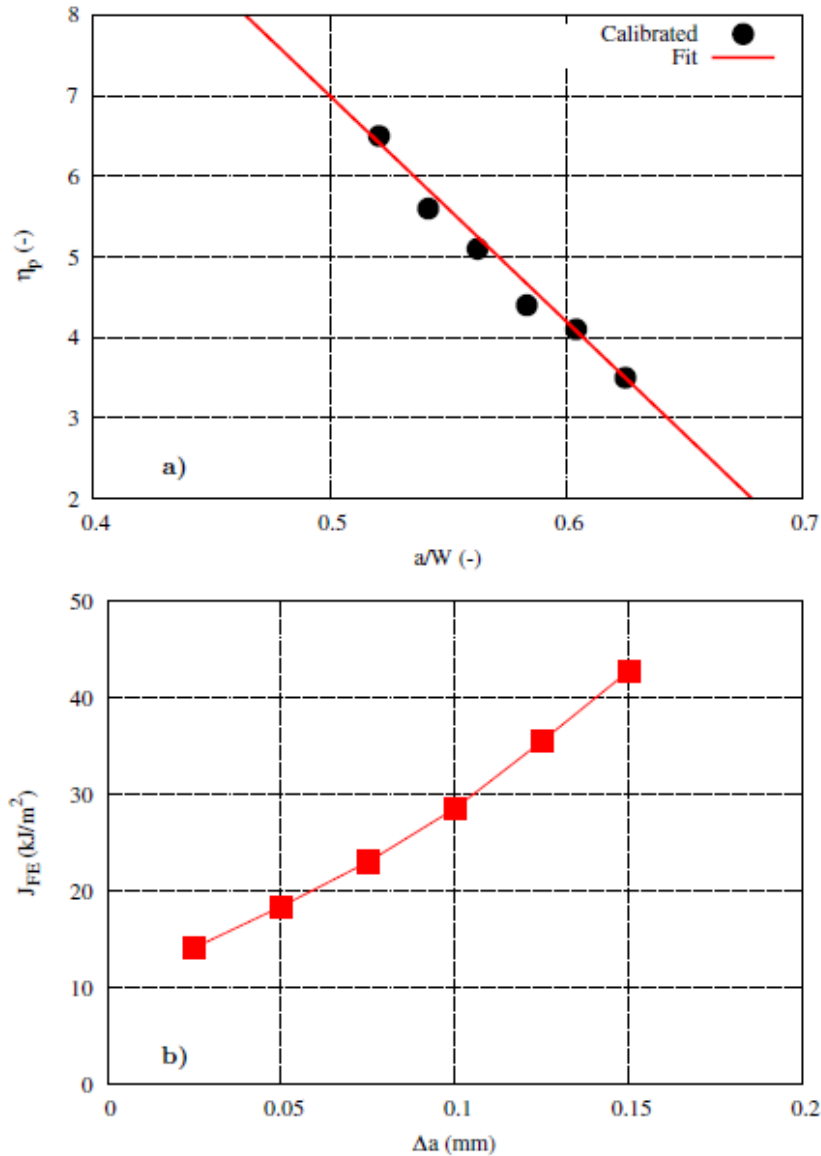


Figure 3.15: The calibration factor  $\eta_p$  as a function of the crack depth ratio  $a/W$ .

Once the crack had initiated, the next experimental points dealt with crack growth ( $\Delta a \neq 0$ ). The load vs. COD curve exhibited non linearity. In strict logic, this implies to separate the two calibration factors  $\eta_e$  and  $\eta_p$  in eq. (3.3), themselves depending on the crack depth ratio. To overcome this difficulty, the use of eq. (3.4) was proposed here. The evolution of  $\eta_p$  as a function of  $a/W$  was determined by using the total area under the load vs. COD curve. To this end, a multiplicative factor was attributed to each of the six remaining  $J_{FE}$  in Figure 3.13a, so as for the “experimental”  $J_p/\eta_p$  curve to intersect this point. The red curves with triangle and diamond symbols in Figure 3.14 exemplified this approach for, respectively, the second and the last  $J_{FE}$  values. These multiplicative factors were plotted as a function of the crack depth ratio in Figure 3.15a. A linear evolution of the  $\eta_p$  calibration factor could then be established, allowing an access to J-integral by using eq. (3.4) whatever the crack depth ratio.

Taking advantage of  $J_{FE}$  associated with  $\Delta a$ , an attempt was made to establish the crack growth resistance (R) curve of the studied plasticized PVC. The testing protocol for conducting J-crack growth resistance curve tests on plastics consists of using multiple specimens with various crack depths [47]. Recent works carried out under the direction of the Technical Committee 4, "Polymers, Polymer Composites and Adhesives", of the European Structural Integrity Society (ESIS TC4) suggested the use of two specimens so as to obtain the R-curve [50, 51]. The following results represent a contribution to this active work on fracture of plastics.

Figure 3.15b displays J- $\Delta a$  from Specimen #2 data assisted by FE analysis. The six points allow the prediction of the ductile crack growth in this material on a small amount of crack extension. However, when attempting to plot the blunting line, it was far below this J- $\Delta a$  curve. This blunting assumed to be semi-circular [46] theoretically can be estimated to be half of the crack tip opening displacement. As mentioned above, Figure 3.7 showed a large blunting of the crack tip. This result could have been expected. Further assessment should be carried out before safely using the present J- $\Delta a$  curve.

### 3.2.5. Discussion

This section focuses on the methodology allowing the transferability [58] of the clamped specimen results, in terms of crack initiation and propagation, into the CEAST tests first and by extension to the dashboard. A major assumption should be outlined here: the temperature and the impact speed selected locate the test in the upper shelf of the fracture toughness curve. The ductile mechanisms operate and  $J_c=10.8 \text{ kJ/m}^2$  and the R-curve are considered to be valid.

#### 3.2.5.1. From clamped SENB to CEAST test results

Recall that the geometries of the impactors were circular (round bar) and hemispherical for the clamped SENB and the CEAST tests, respectively. The mechanisms of crack initiation and growth differed in the portion of the process zone in the remaining ligament. Whereas for clamped SENB the whole width (29.8 mm) was involved, in the CEAST specimen the sequence was as follows:

- when the impactor tip entered in contact with the top surface of the sample at the end of the remaining ligament, only a small portion of the diameter ( $\Phi$ ) of the impactor was concerned with the crack initiation;
- this initiated crack propagated through the thickness;
- the displacement of the hemispherical impactor induced lateral crack propagation, *i.e.* perpendicular to the direction of the impactor displacement.

The approach should be based on the crack initiation, *i.e.* as soon as  $J_c=10.8 \text{ kJ/m}^2$  is

reached. For CEAST tests, only the load vs. deflection was available. For mechanical engineering purposes, namely the safety engineering design of structures, the salient question is how to determine the ductile crack initiation from these data.

By using a FE code, the approach consists of computing the J-integral value on the meshed CEAST specimen using an elastic-visco-plastic model. The experimental load vs. deflection curve should be in agreement with the simulated one at each test temperature and impact speed. When the J-integral reaches the fracture toughness value  $10.8 \text{ kJ/m}^2$ , the crack initiation is supposed to be established and the computation should be stopped.

The analytical approach is more complex. Recall that at the crack initiation for clamped SENB specimens, the load vs. COD curve was linear so that, on the one hand, the calibration factor is equal to the elastic one ( $\eta_e \approx 8$ ); on the other hand, Figure 8c indicated that the deflection of about 8 mm is proportional to the COD.

Since the crack initiation was detected at the COD where the stiffness (inverse of the compliance) decreased, it should be also valid for the stiffness in terms of load vs. deflection curve. This operation was carried out directly on the data of the CEAST tests in Figure 2. For the three tests, the stiffness increased first up to a deflection of 8 mm, then stabilized between 8 mm and 10 mm to decrease at last. The crack initiation was assumed to occur at 10 mm for CEAST tests at  $23^\circ\text{C}$  and 4.4 m/s. To go further, the energy  $A(d = 10\text{mm})$  according to eq. (3.1) is equal to  $2 \pm 0.1 \text{ J}$ . This energy should be related to the fractured surface used to determine the impact strength ( $\Phi(W - a_0)$ ), giving  $0.11 \text{ kJ/m}^2$ . This value is twice lower than the upper shelf impact strength in Figure 3.3 ( $0.25 \text{ kJ/m}^2$ ). But, it corresponds to the actual crack initiation, in agreement with the fracture toughness of the material. This “impact strength at crack initiation” should be assessed by using all the CEAST experimental data:

- by determining the deflection from which the stiffness decreases;
- by integrating the area under the load vs. deflection curve up to the selected deflection, so as to estimate the energy at crack initiation;
- by relating this energy to the area of the remaining ligament assumed to be  $\Phi(W - a_0)$ .

Using this consolidated value should be recommended regarding the significant result of the present work.

### 3.2.5.2. From CEAST results to the full scale test on dashboard

For a real engineering structure like the dashboard, only FE analysis would be efficient for the prediction of the crack initiation to allow the correct deployment of the air bag. To this end, the window of the air bag box (Figure 3.1) should be meshed in detail. The three layers of materials as well as the scoring in the PVC skin should be discretized with sufficiently refined meshes. The challenge is to reduce the numerical cost of such a study.

The same material parameters of elasto-visco-plastic model that have been identified for the CEAST tests at the temperatures and impact speeds located in the upper part of the diagram of Figure 3.4 should be used.

The boundary conditions should be associated with the kinetic energy due to the airbag deployment. The safe opening of the window, in ductile mechanisms, corresponds to the precise conditions (time, temperature, loading. . . ) allowing the J-integral to attain the fracture toughness of the material.

Once this goal achieved, many parameters of interest can be optimised to ensure a safe deployment of the air bag:

- the formulation and the processing of the material to obtain an efficient time and temperature dependent constitutive model;
- the drawing of the scoring as straight line, Y or U or L shaped that already exist;
- the score depth ratio: it was shown that for 0.625 a net brittle failure, without branching or fragmentation of the skin, occurred;
- the kinetic energy due to the air bag display.

### 3.2.6. Concluding remarks

The desired fracture process allowing the safety of the passengers during the deployment of the airbag in the automotive industry is the ductile failure. Full scale experiments on dashboard showed that the impact speed was estimated to be 25 m/s at 23 °C, a ductile failure of the skin –made of plasticized PVC– was evidenced. This result was in agreement with the domain of temperatures and impact speeds established with drop tower tests at lower speeds/temperatures [15].

Dedicated clamped SENB specimens were used to characterize the mechanisms of ductile crack initiation and propagation for the studied material. In contrast to the route recommended by nonlinear fracture mechanics, the crack initiation occurred before the maximum load prior to the final failure of the specimen. In fact, it was observed when the loss of linearity in the load vs. COD appeared. Thanks to the “release nodal degree of freedom” procedure the in-house FE code allowed the simulation of the crack extension to

be performed. The calibration factor of the clamped SENB specimen with respect to the crack depth ratio was established. Moreover, the fracture toughness  $J_c$ , defined as the numerical J-integral at the crack initiation, was evaluated to be  $10.8 \text{ kJ/m}^2$ , in agreement with values reported in the literature.

Focusing on the crack initiation, the corresponding impact strength for the previous drop tower tests in the upper shelf was corrected. Instead of the previous  $0.25 \text{ kJ/m}^2$  this critical value was reduced to  $0.11 \text{ kJ/m}^2$ . The modified fracture toughness and the impact strength values were proposed in the methodology allowing the ductile crack initiation to be predicted:

- for the drop tower test results, where the COD and the crack extension were not available. Two methods were proposed:
  - by running FE analysis of the test and selecting the time when the J-integral reached the value of  $10.8 \text{ kJ/m}^2$ ;
  - by detecting the loss of linearity in the load vs. deflection curve for which the fractured surface energy density was equal to  $0.11 \text{ kJ/m}^2$
- for the dashboard, where the plasticized PVC skin was integrated. Once the whole structure was meshed, FE simulation of the airbag display should be performed up to the time when the numerical J-integral reached the value of  $10.8 \text{ kJ/m}^2$

It was mentioned that using FE code would allow the optimization of many parameters to lead to a safe deployment of the air bag.

### 3.3. Conclusion of the article

The main conclusions that will be used as the remainder of the manuscript are:

- The crack initiation appeared when the load versus deflection deviated from the linearity. The crack then propagates through the remaining ligament. **This important result will be used in the interpretation of scored skins such that the energy of failure will be considered at the appearance of the non linearity;**
- The fracture toughness of the studied plasticized PVC was estimated to be  $10.8 \text{ kJ/m}^2$ . This value which was close to that reported in the literature for modified PVC should be the reference value at the **upper shelf of a ductile-brittle transition temperature** diagram;
- The exploitation of the experimental database associated with FE simulation of the crack propagation allowed, on the one hand, the calibration factor  $\eta$  of this specific SENB specimen to be established, as a function of the crack depth ratio;
- The resistance curve (R-curve) of the material could be plotted thanks to the numerical J-integral and the experimental consecutive crack depths.

## CHAP 4: Essais d'impact

Pour analyser correctement tous les essais d'impact effectués dans le but d'étudier la  $T_{dth}$  et de la comparer à la  $T_g$ , une étape d'identification et de traitement des données est nécessaire. En effet, pour des essais à basses températures notamment, l'amplitude du signal est du même ordre de grandeur que le bruit. Une fois cette étape réalisée, l'identification des paramètres clés a été effectuée : à savoir la rigidité, les forces à l'apparition de la non-linéarité et à la rupture, les déflexions à l'apparition de la non-linéarité et à la rupture, et enfin les énergies correspondantes. Comme mentionné dans le chapitre précédent, pour les échantillons pré-entaillés les grandeurs à l'apparition de la non-linéarité ont été considérées.

Les résultats des essais réalisés sur les machines CEAST et TGV (=HSTT) ont été comparés pour une vitesse de 10 m/s, seule vitesse d'impact testée avec les deux machines. L'objectif était d'analyser si l'évolution des paramètres mesurés était comparable, afin de pouvoir explorer une gamme de vitesses d'impact bien plus large qu'avec un seul instrument. Il s'est avéré que les vitesses d'impact au moment de la rupture étaient légèrement surestimées par la TGV par rapport à la CEAST. Cependant, l'écart étant de l'ordre de 1% à 2%, son effet peut être considéré comme négligeable. Bien que des différences dans les résultats entre les deux machines ont été observées lors des essais à basses températures, les  $T_{dth}$  mesurées par la méthode de l'optimisation via la fonction  $\tanh$  étaient pratiquement identiques. En conclusion, l'utilisation des deux instruments de mesures afin d'étendre les essais à plus hautes et plus faibles vitesses d'impact a été validée.

L'étude des vitesses d'impact inférieures à 10 m/s a été réalisée sur la machine CEAST tandis que les essais à plus hautes vitesses ont été effectués sur la TGV. Sur tous les paramètres étudiés (rigidités, forces, déflexions et énergies), il a été possible d'observer un décalage des courbes selon la vitesse d'impact, avec une augmentation de la fragilité avec la vitesse d'impact. Ce résultat a de nouveau été observé lorsque la  $T_{dth}$  (identifiée à l'aide de la fonction  $\tanh$ ) a été tracée par rapport à la vitesse d'impact : les résultats obtenus ont montré que la  $T_{dth}$  augmentait de manière continue et linéaire avec la vitesse d'impact pour les matériaux entaillés.

La même étude a été effectuée avec les échantillons non entaillés. Alors que des similitudes ont été observées dans les évolutions des rigidités, forces et déflexions avec la température entre les deux machines, il n'a pas été possible de comparer les courbes des énergies à 10 m/s. En effet, seuls les résultats de la CEAST possédaient un profil en "S". Ainsi sur les matériaux non entaillés la fonction  $\tanh$  n'est pas utilisable. Une seconde méthode, validée sur les éprouvettes entaillées, a consisté en l'identification de la  $T_{dth}$  grâce aux changements de pente des courbes forces et déflexions. Bien que moins précise, cette méthode a permis de déterminer approximativement les températures seuils de rupture ductile pour la TGV. Comme pour les échantillons entaillés, la  $T_{dth}$  augmentait de manière continue et linéaire avec la vitesse d'impact pour les matériaux non entaillés. Lors des observations des résultats, une variation particulière des résultats à hautes vitesses et températures a aussi été relevée ; un phénomène d'auto échauffement pourrait en être la cause.

En comparant l'évolution des  $T_{dth}$  pour les deux géométries d'éprouvette, l'étude a permis de conclure que les évolutions étaient identiques et que l'écart entre les  $T_{dth}$  restait le même quelle que soit la vitesse d'impact. L'augmentation de la  $T_{dth}$  ne dépend donc pas de la géométrie de l'éprouvette mais de la nature du matériau. Il s'agit ici de la première

différence observée entre la Tdth et la Tg, car la Tg ne fournit aucune information sur les différences de performances entre les matériaux entaillés et non entaillés.

Une étude plus réduite, uniquement sur la CEAST, d'un second matériau de PVC plastifié de formulation différente a été réalisée. En ne se basant que sur la Tg, le second matériau est jugé moins performant que le premier. Les premiers résultats sur matériaux non entaillés ont permis de valider cette information. En effet, le matériau 2 possédait une Tdth plus élevée que le matériau 1. Par contre, l'écart entre les deux géométries pour ce second matériau était bien plus faible que pour le premier, le rendant ainsi plus performant sur les essais entaillés, ce que ne décrit pas la Tg. Or, dans la réalité, les deux matériaux sont bien entaillés dans les tableaux de bord. Les observations ont permis d'identifier que les quatre courbes possédaient la même pente et de déduire que l'évolution de la Tdth était une propriété intrinsèque à la famille des PVCs. Ainsi, l'écart de Tdth entre deux formulations reste le même quelle que soit la vitesse d'impact.

## 4. Impact tests

### 4.1. Impact tests on scored samples

The following subsections were based on the paper “Impact speed dependency of the ductile failure threshold temperature for a plasticized polyvinylchloride” published in *Continuum Mechanics and Thermodynamics* [15]. This paper highlighted only the CEAST tests’ results. Additionally, the data treatment dealt with the industrial practice for which the energy at maximum load is selected without any data treatment.

On the following sections, in addition to CEAST tests, HSTT tests were carried out in order to cover a larger range of temperatures and deflection speeds. Besides, a data reduction process is applied so as to isolate the relevant parameters on the load-deflection curves and prevent more perturbation in the results. Then, different comparisons between HSTT’s and CEAST’s results at 10 m/s, energy calculated by CEAST or using a numerical integration, and energy at failure vs at non linearity appearance were added to the initial paper.

Following results, in section 3.1, the test data on scored samples are first exploited here. In fact, 93 tests were carried out with the CEAST, and 54 more with the HSTT for a total of 147 tests on scored specimens. The temperature ranges from  $-10^{\circ}\text{C}$  to  $30^{\circ}\text{C}$  with impact speeds from 2 m/s to 10 m/s for CEAST and 10 m/s to 23 m/s with the HSTT. They are followed by test results on unscored samples, with 126 tests carried out with the CEAST and 54 with the HSTT (total of 180 tests). The temperature ranges from  $-24^{\circ}\text{C}$  to  $30^{\circ}\text{C}$  with impact speeds from 2 m/s to 10 m/s for CEAST and 10 m/s to 23 m/s with the HSTT.

As the Impact speed of 10 m/s is covered by both CEAST and HSTT, this preset velocity was selected to better understand the difference of results induced by the two machines. It should be remembered that while the HSTT is measuring and recording the time, deflection, and load; the CEAST measures only time, load and initial velocity and calculates current deflection speed, deflection and energy from eqs 3.1, 3.2, and 3.3.

#### 4.1.1. Data reduction

##### 4.1.1.1. Raw data from testing machines

During the experiments, the duration of impact tests ranges from  $4 \cdot 10^{-3}$  sec for HSTT tests at 23 m/s and  $-10^{\circ}\text{C}$  to  $40 \cdot 10^{-3}$  sec for CEAST tests at 2 m/s and  $25^{\circ}\text{C}$ . In most cases, unless the maximum acquisition frequency was reached, the data were over sampled so as to obtain the more detailed evolution of the signal. Accordingly, massive data were obtained and the dynamic character of the tests induced oscillations in the raw data.

Figure 4.1 illustrates load-deflection curves issued from CEAST tests at 10 m/s for test temperatures ranging from  $-3^{\circ}\text{C}$  to  $20^{\circ}\text{C}$ . Each data set contains about 20,000 lines. The profile of the load-deflection curve changes according to the test temperature for a given deflection speed. Vertical arrows indicate the first load drop highlighting the failure of the sample [40, 59]. It can however be observed that the maximum load does not systematically coincide with this load drop, especially at low temperatures (see Figures 4.1d-f). In order to ease the exploitation of the experimental data, a data treatment process dealing with a reduction of the sampling was systematically carried out.

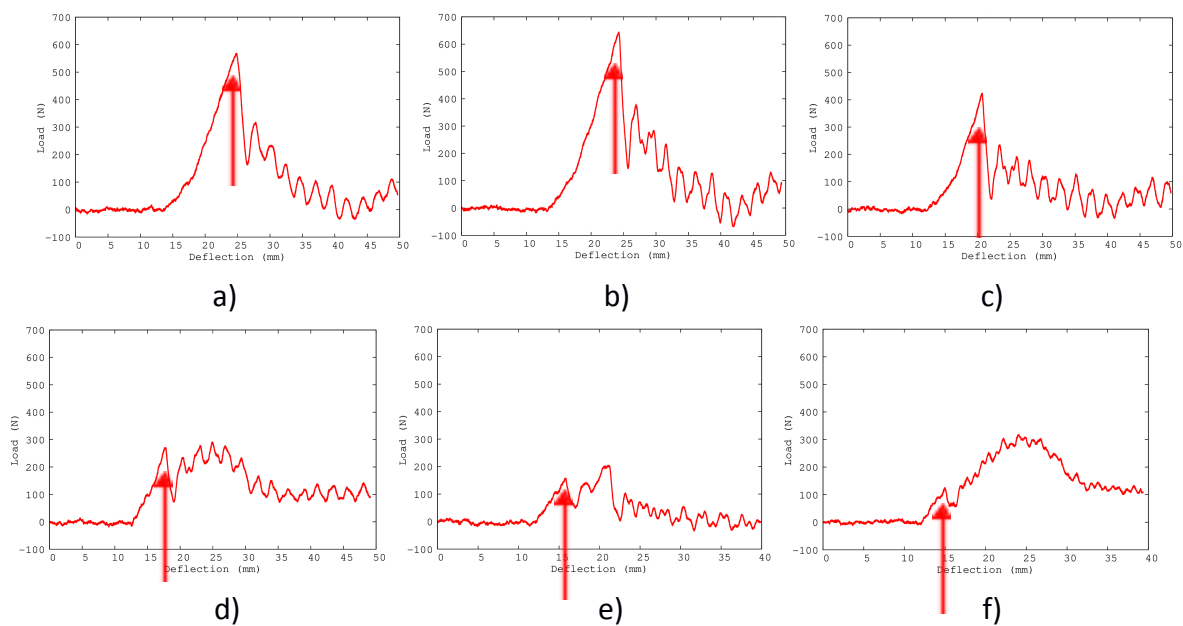


Figure 4.1: Load versus deflection curves on raw data from the CEAST tests for an impact speed of 10 m/s at : a)  $20^{\circ}\text{C}$  ; b)  $15^{\circ}\text{C}$  ; c)  $10^{\circ}\text{C}$  ; d)  $5^{\circ}\text{C}$  ; e)  $0^{\circ}\text{C}$  ; and f)  $-3^{\circ}\text{C}$ .

#### 4.1.1.2. Data treatment

As mentioned previously, when the raw data is obtained from the CEAST or HSTT machines, the results show oscillations and a lot of unnecessary experimental points. For instance, the curve in Fig 4.2 shows the raw data of the evolution of the load versus time for an impact speed of 10 m/s and a test temperature of  $20^{\circ}\text{C}$  on the HSTT machine. This curve is composed of more than 20,000 points. For some curves the number of points can reach 60,000 points (e.g. CEAST 2 m/s at high temperatures).

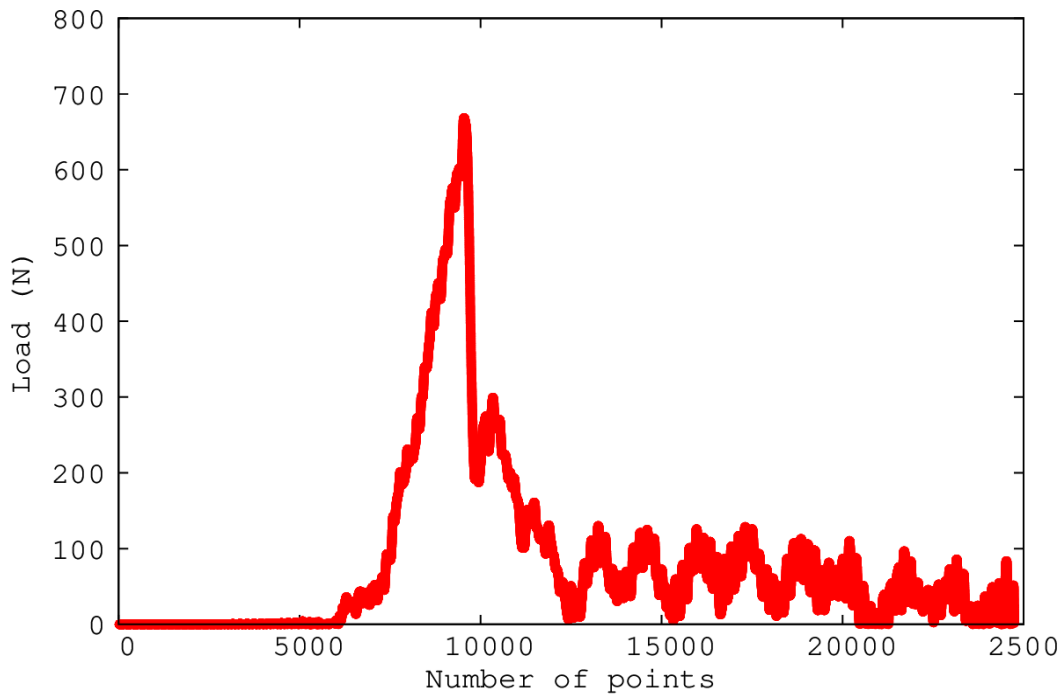


Figure 4.2: Representation of the raw data obtained during an impact test on the HSTT machine for an impact speed of 10 m/s at 20°C.

The first step to clean the raw data is then to select only the “real test data” points corresponding to the increasing load until failure. In general, from the 20,000 to 60,000 raw points, only between 5,000 to 8,000 are selected, as shown in Fig 4.3.

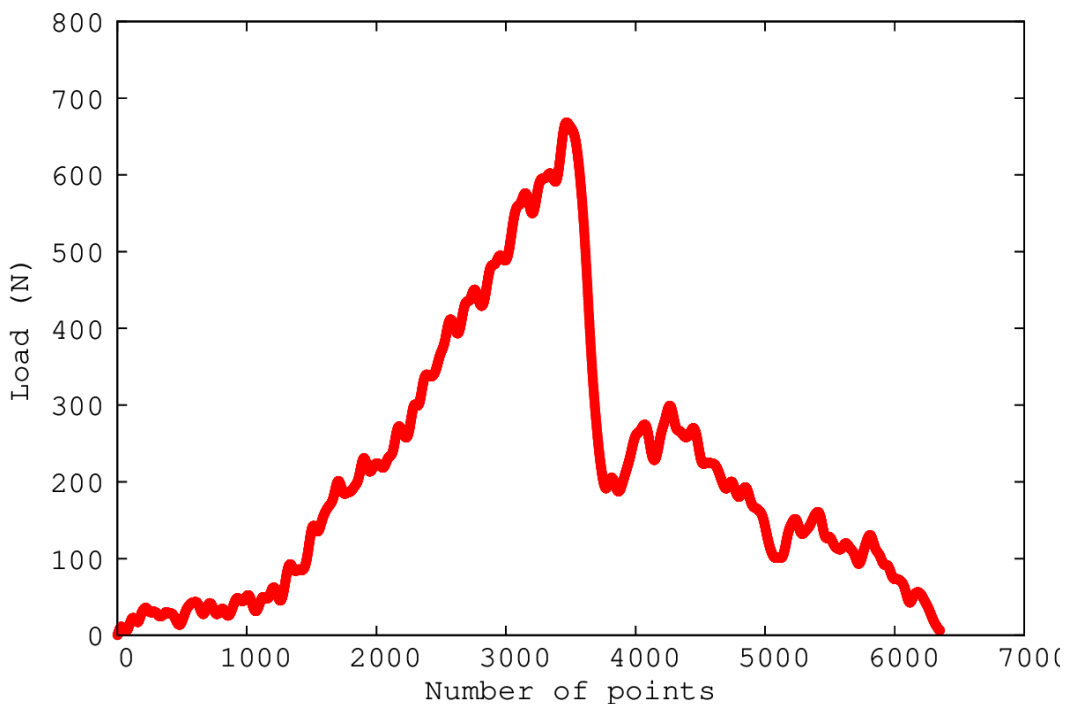


Figure 4.3: Data reduced to 5,000 experimental points over the 20,000 original ones in Figure 4.2

Then, from the 5,000 points' "test" curve, only a few representative points are kept. The objective is to select the minimum number of points but allowing the evolution of the load slopes (non linearity, maximum load, load drop...) to be kept. A worked example of the "test" curve, in fig.4.3, is shown in Fig. 4.4, where only 53 points were definitely saved.

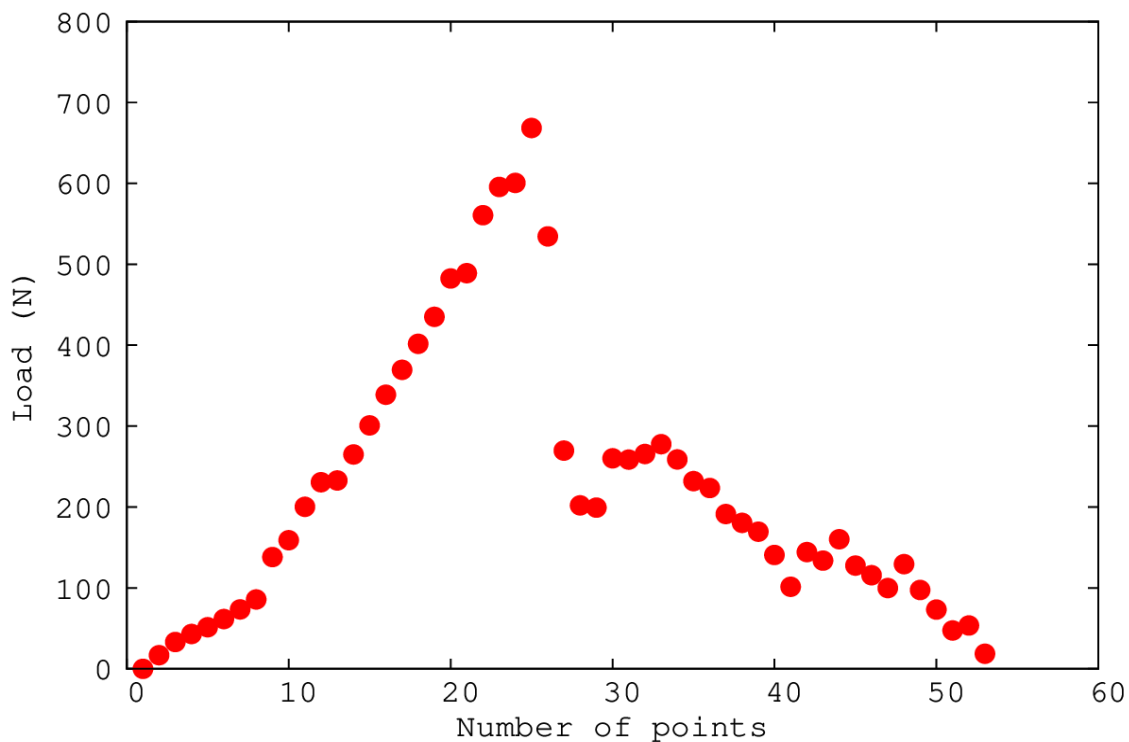


Figure 4.4: Representation of the remaining 53 points from the experimental 20,000 points

In fig.4.4, it can be noticed that the linearity of the "reduced" experimental data begins at about the 10th point. Actually, the concave shape of the curve in the beginning corresponds to the progressive surface contact between the hemispheric striker and the flat sample. This should be removed for a correct analysis of the data. The treatment is similar to the linear correction for SENB specimens [47]. It should be noted that in the article [15] this operation was not applied to the CEAST data.

To determine the stiffness of the system, the slope of the linear part of the curve, i.e. the slope of the secant line, is calculated. Once the stiffness is estimated, a straight line is superimposed on the experimental data to verify and, if necessary, to correct the magnitude of the stiffness (see Figure 4.5). Moreover, the post-treated zero-deflection point is defined.

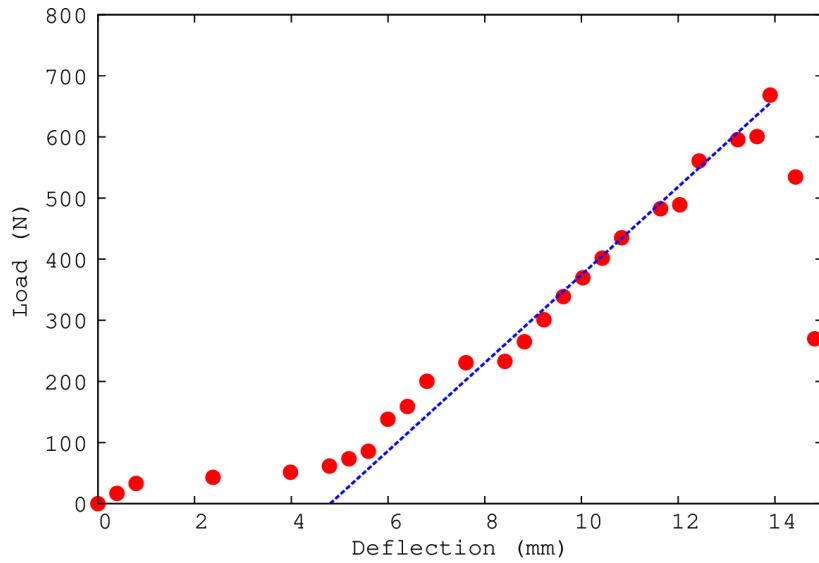


Figure 4.5: Replacement of the first part of the curve by a linear function to check the stiffness and to proceed to a reset (zero load-deflection) of the curve (here a correction of 4.8 mm deflection was needed)

The next step consists of collecting the parameters of interest from the clean data set.

#### 4.1.2. Selection of experimental data: $R$ , $F_{nl}$ , $F_r$ , $d(F_{nl})$ , $d(F_r)$

In order to highlight the parameters-collecting method, Figure 4.6 displays the corrected load-deflection curve of a HSTT test at 10 m/s and 20°C. The linear correction, characterized by the dashed blue line, allows the identification of the parameters of interest used in the following.

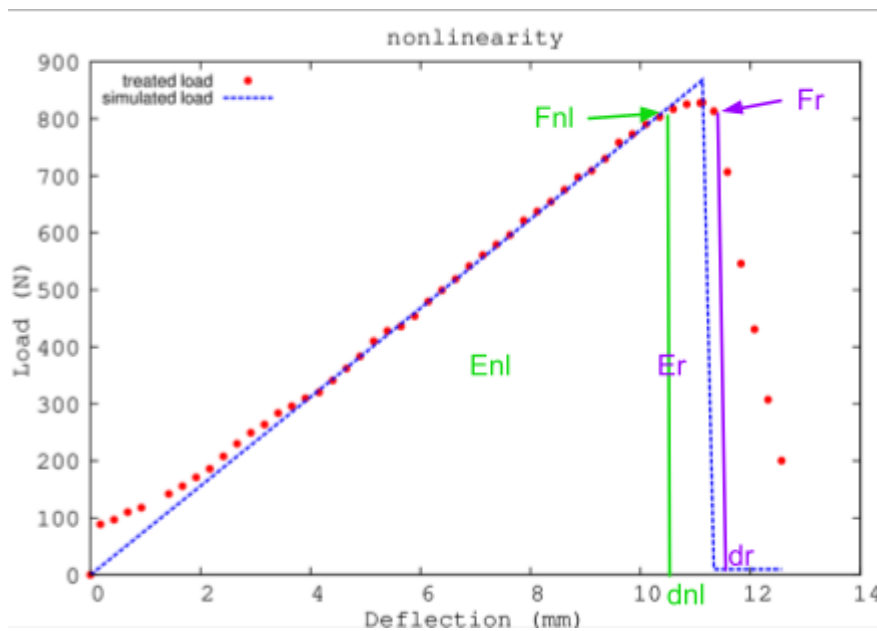


Figure 4.6: Identification of  $R$ ,  $F_{nl}$ ,  $F_r$ ,  $d(F_{nl})$ ,  $d(F_r)$ ,  $E_{nl}$  and  $E_r$

- The stiffness (R standing for “Rigidity”): as already mentioned, the stiffness is represented by the slope of the initial linear part of the curve. It is to be mentioned that the stiffness of the whole system combined several mechanical parameters such as the Young’s modulus and the Poisson ratio of the PVC material, the friction coefficient between the PVC and the metallic impactor, which could change depending on the test temperature: either in nitrogen vapour at low temperatures or in air at high temperatures.
- At the appearance of the non linearity
  - The load at non-linearity  $F_{nl}$  is detected at the deviation from the stiffness line. As mentioned in subsection 4.1,  $F_{nl}$  is assumed to coincide with the crack initiation which corresponds to the appearance of through thickness crack in the remaining ligament. The width of this initial crack is less than the diameter of the hemispherical impactor. The consecutive non linear part is related to the widening of this initial through-thickness small crack, by a lateral crack growth. The length of this non linear part is dependent on the impact speed and the temperature.
  - The deflection corresponding to  $F_{nl}$  named  $d(F_{nl})$ : this is the corrected deflection (with reset) at  $F_{nl}$ ;
  - The instantaneous deflection speed at  $F_{nl}$  ( $V_{nl}$ )
  - The energy at the appearance of the non linearity ( $E_{nl}$ ): this energy corresponds to the area under the load versus deflection curve until  $F_{nl}$ . The numerical integration was performed for both HSTT and CEAST data sets. In the beginning of the test (deflection less than 2 mm in fig.4.6) the integration is carried out on the dashed line so as to avoid erroneous data during the establishment of the full contact between the sample and the striker. Note that for CEAST tests the energy computed on the raw data using eq. (2.2) was collected at this stage.
- Prior to the load sudden drop
  - The load at complete rupture of the sample ( $F_r$ ) : this load is the one before the sudden drop. The hemispherical striker has crossed the entire remaining thickness of the scored sample. The crack might continue its lateral propagation at this stage.
  - The deflection corresponding to  $F_r$  called  $d(F_r)$ : the corrected value of the deflection prior to the load drop.
  - The instantaneous deflection speed at  $F_r$  ( $V_r$ )
  - The energy prior to the load drop ( $E_r$ ): the same procedure as for  $E_{nl}$  was applied by numerically integrating the area under the load versus deflection curve up to  $F_r$ . This was done for both HSTT and CEAST data sets. The linear part is considered in the beginning of the test (deflection less than 2 mm in Figure 4.6). In the nonlinear part beyond  $F_{nl}$  (deflection greater than 10.5 mm in

Figure. 4.6) the integration is operated on the real experimental points. For CEAST tests, again the energy computed on the raw data using eq. (2.2) was collected in order to compare it with the integrated value.

### 4.1.3. Comparison of CEAST - HSTT tests at 10 m/s

With the aim of comparing the test results from the two testing machines (HSTT and CEAST), the impact speed of 10 m/s was selected, at various temperatures.

#### 4.1.3.1. Evolution of the impact speed with respect to the deflection

The first step, in order to compare the results from the two instruments with the same impact test conditions, is to verify the evolution of the desired impact speed. Recall that the impact speed is calculated for CEAST (eq. 2.3) while it is measured for HSTT.

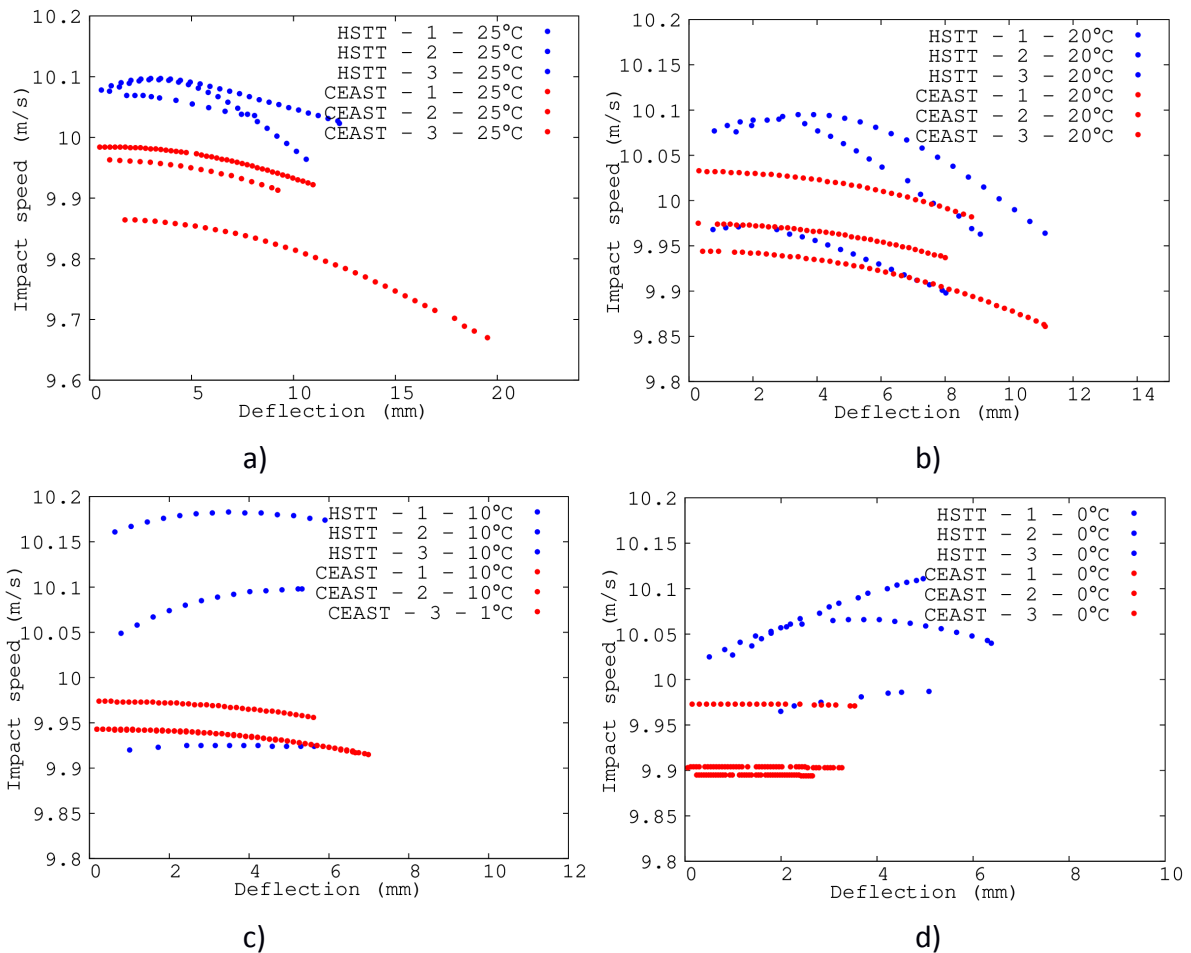


Figure 4.7 : Evolution of the deflection speed during impact tests for four temperatures: a) 25°C ; b) 20°C; c) 0°C ; d) 10°C.

As an example, four graphs displaying the evolution of the striker's speed during impact tests are shown in Figure 4.7. The red full circles represent the tests carried out with the CEAST whereas the blue full circles exhibit the HSTT's tests. None of these curves present a constant profile at 10 m/s:

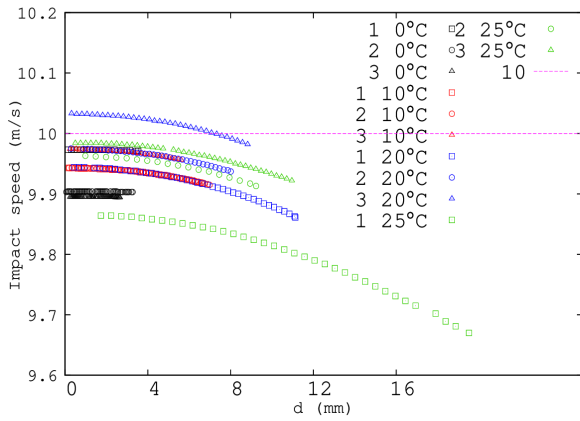
- The HSTT curves are slightly over-estimated as they are mostly evolving between 10 m/s and 10.2 m/s. Also, their shape is changing with an increase/decrease trend ( $\sim 0.1$  m/s) during the test.
- The CEAST curves, on the contrary, are under-evaluating the preset speed. Most curves start below 10 m/s, and the striker's speed is decreasing all along the test, sometimes down to 9.7 m/s.

These differences, as small as they are ( $\sim 1\%$  or  $2\%$ ), can affect the results and create small variations.

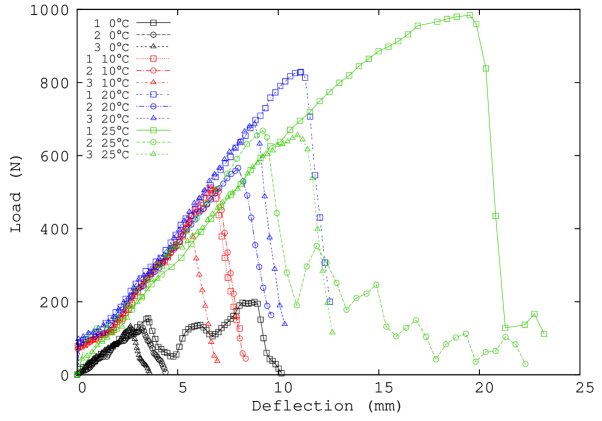
Figure 4.9a displays, for CEAST, the evolution of the impact speed at various testing temperatures and the prescribed speed of 10 m/s, drawn as a pink dashed line. It can be observed that apart from specimen #3, tested at  $20^{\circ}\text{C}$ , the initial speeds for CEAST tests were all less than the prescribed 10 m/s. Moreover, considering eq. 2.3 implying a continuous decrease of the speed and due to the nature of the test (falling object), it can be assumed that CEAST tests will never reach the prescribed impact speed.

The load versus deflection curves at various temperatures are plotted in fig.4.9b. At positive temperatures, less oscillation and two nonlinearities can be noticed: at the beginning and at the end of the curve. In opposition, for the three tests carried out at  $0^{\circ}\text{C}$  (black open symbols), the load versus deflection curves are linear up to the load drop: no linearity could be noticed. It should be noted also that for CEAST tests, the maximum loads are drastically reduced at  $0^{\circ}\text{C}$  (about 100 N).

The counterparts for the HSTT testing machine are illustrated in Figure 4.10. Most of the curves in Figure 4.10a are above the prescribed deflection speed of 10 m/s. The evolution of this speed during the tests differs from that calculated by CEAST. Indeed, for HSTT the impact speed is first increasing, then it may either decrease or continue increasing. Concerning the load versus deflection in Figure. 4.10b, all of the curves are rather linear from the beginning to the maximum load. The decrease of maximum load is progressive. The maximum load values at  $0^{\circ}\text{C}$  are greater than 400 N, by contrast to 100N for CEAST.

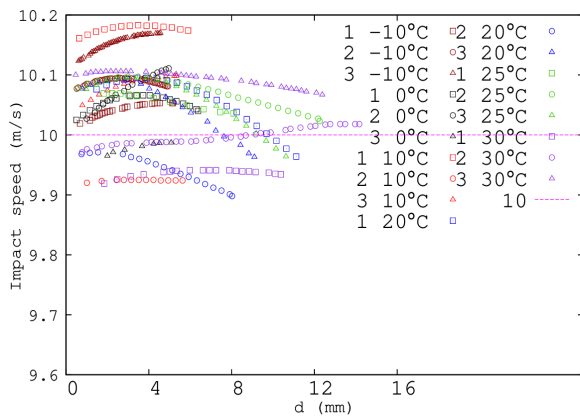


a)

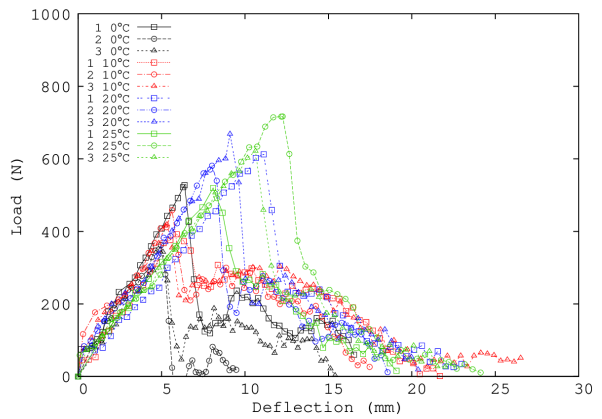


b)

Figure 4.9: Evolution of some characteristic curves for CEAST testing machine at various temperatures: a) the calculated striker's speed; b) the load versus deflection curves



a)



b)

Figure 4.10: Evolution of some characteristic curves for HSTT testing machine at various temperatures: a) the measured striker's speed; b) the load versus deflection curves.

#### 4.1.3.2. Instantaneous impact speeds at failure

Due to the observed variation of the deflection speed during the tests, we will refer to the instantaneous values corresponding to  $F_{nl}$  and  $F_r$  in the following.

Figure 4.11 shows the instantaneous deflection speed at  $F_{nl}$  (appearance of the nonlinearity) considered as the crack initiation. Clearly, CEAST tests in red are mostly underestimated in terms of deflection speed.

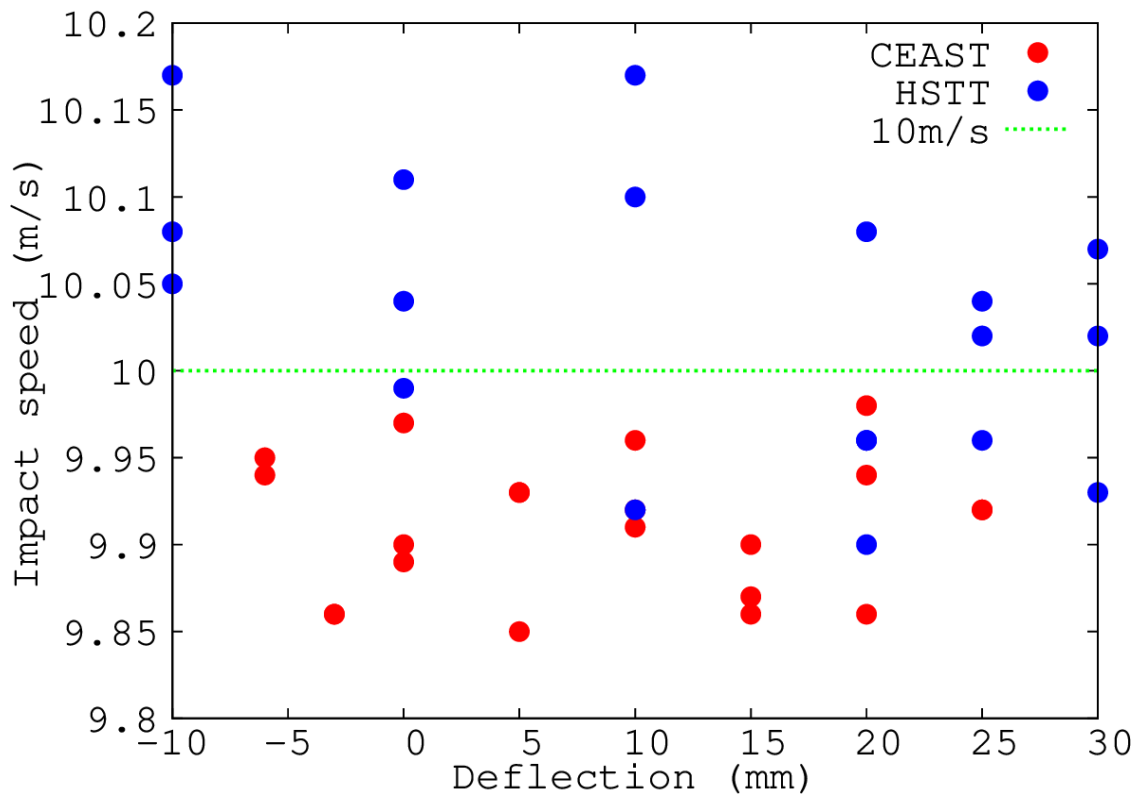


Figure 4.11: Instantaneous impact speed at the appearance of the nonlinearity  $F_{nl}$  for both CEAST and HSTT. The dashed line represents the preset impact speed of 10 m/s.

#### 4.1.3.3. Evolution of the stiffness as a function of the test temperature

The comparison between the results from the two instruments starts with the stiffness, represented on Figure 4.12. While the stiffness registered with the HSTT is decreasing continuously from 90 N/mm at  $-10^{\circ}\text{C}$  to 50 N/mm at  $30^{\circ}\text{C}$ , the profile for the CEAST shows peculiar inflexions. Indeed, starting at about 60 N/mm at  $-6^{\circ}\text{C}$ , from  $-3^{\circ}\text{C}$  to  $5^{\circ}\text{C}$  the value of the stiffness increases from 40 N/mm to 80 N/mm at  $20^{\circ}\text{C}$  before decreasing to 65 N/mm at  $25^{\circ}\text{C}$ . It can be noticed that such variations of the stiffness at negative temperatures are correlated with that of the instantaneous impact speeds. Interestingly, from  $10^{\circ}\text{C}$  to the highest temperatures, the stiffness for the CEAST and HSTT are in the same order of magnitude. It can be concluded that the effects of the impact speed are more significant at negative temperatures.

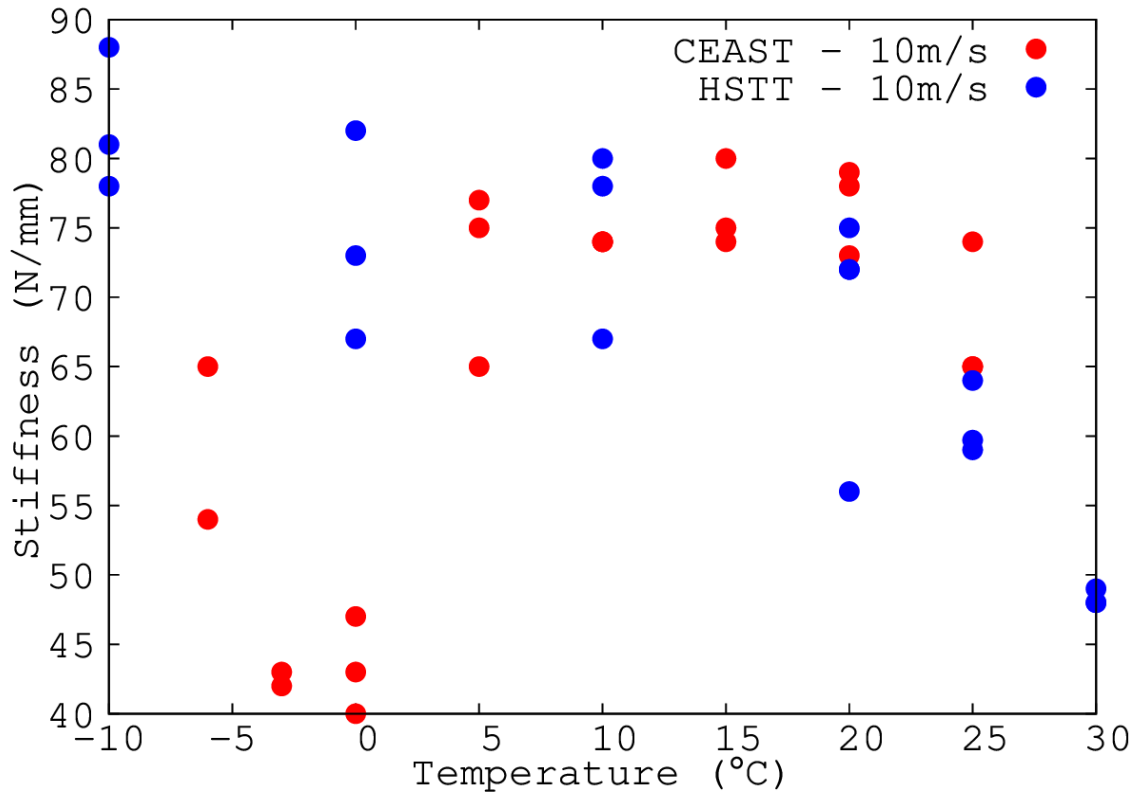


Figure 4.12: Comparison of the stiffnesses with respect to the test temperature.

#### 4.1.3.4. $d(F_{nl})$ : deflection at the appearance of the nonlinearity

The deflection is one of the parameters used in the energy calculation. Its evolution, as a function of the test temperature, is illustrated in figure 4.13. Figure 4.13 displays the deflection at the appearance of the nonlinearity as a function of the test temperature, as they were obtained from the data set.

In a similar way than the stiffness, from 10°C to the highest temperature, the  $d(F_{nl})$  for the CEAST and HSTT are in the same order of magnitude (even if HSTT results are more scattered). A difference in the trend appears again at the lowest temperature:

- Variation of HSTT's deflection's slope at around 10°C with a less sharp slope at low temperatures (from 6 mm at 10°C to 5 mm at -10°C)
- CEAST's slope diminution appears at around 5°C and the variation is smaller than HSTT's (from 4 mm at 5°C to 3 mm at -5°C)
- In consequence, a gap is observable below 10°C and -10°C between CEAST's and HSTT's deflections, respectively.

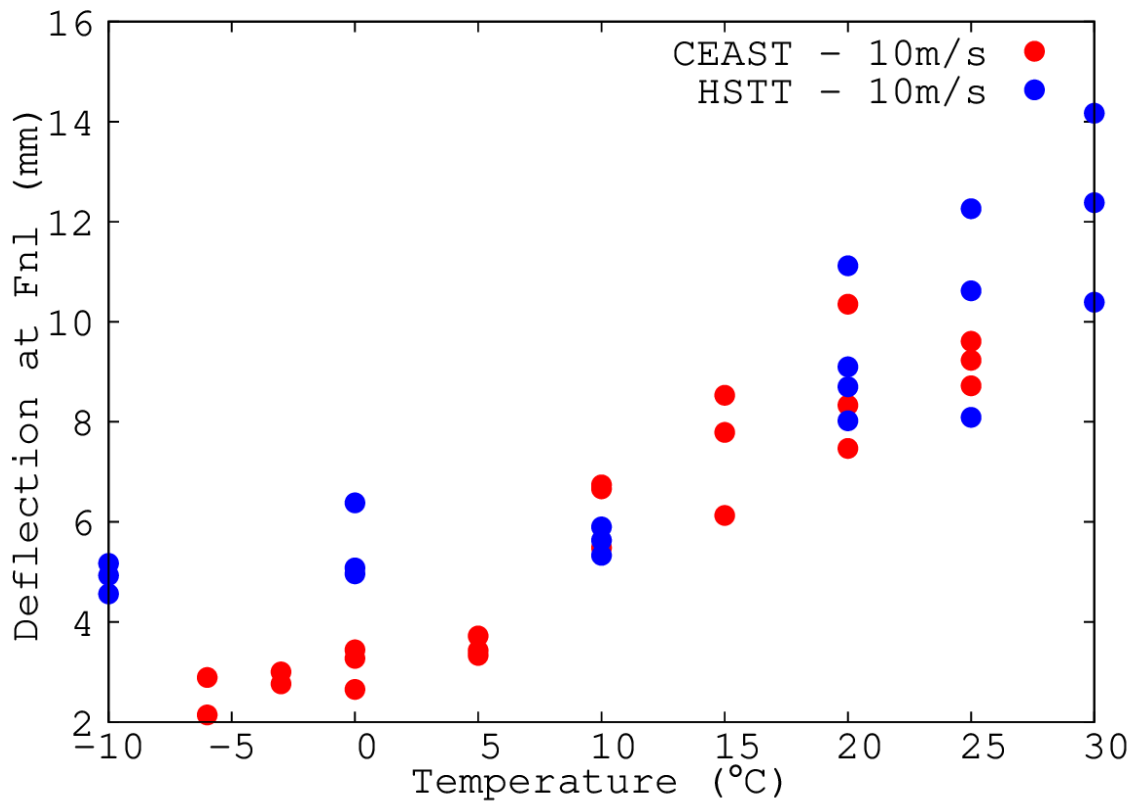


Figure 4.13: Deflection at the appearance of the nonlinearity with respect to the test temperatures at 10 m/s.

#### 4.1.3.5. $F_{n1}$ : Load at the appearance of the non linearity

The loads at the appearance of the nonlinearity ( $F_{n1}$ ) are compared in Figure 4.14. For both instruments the curve's profile possesses the same S-shape. At low temperatures (-10°C to 10°C) the brittle plateaus are located. Although they are both present and noticeable, the levels of the plateau are not the same. The plateau of the HSTT is around 400 N while the CEAST's is around 150 N. Starting from 10°C to the highest temperatures, both curves are completely overlaid.

Interestingly, from 10°C to the lowest temperatures, the gap observed in Figure 4.13 is present in Figure 4.14 in the same trend (HSTT's values are higher than CEAST's ones).

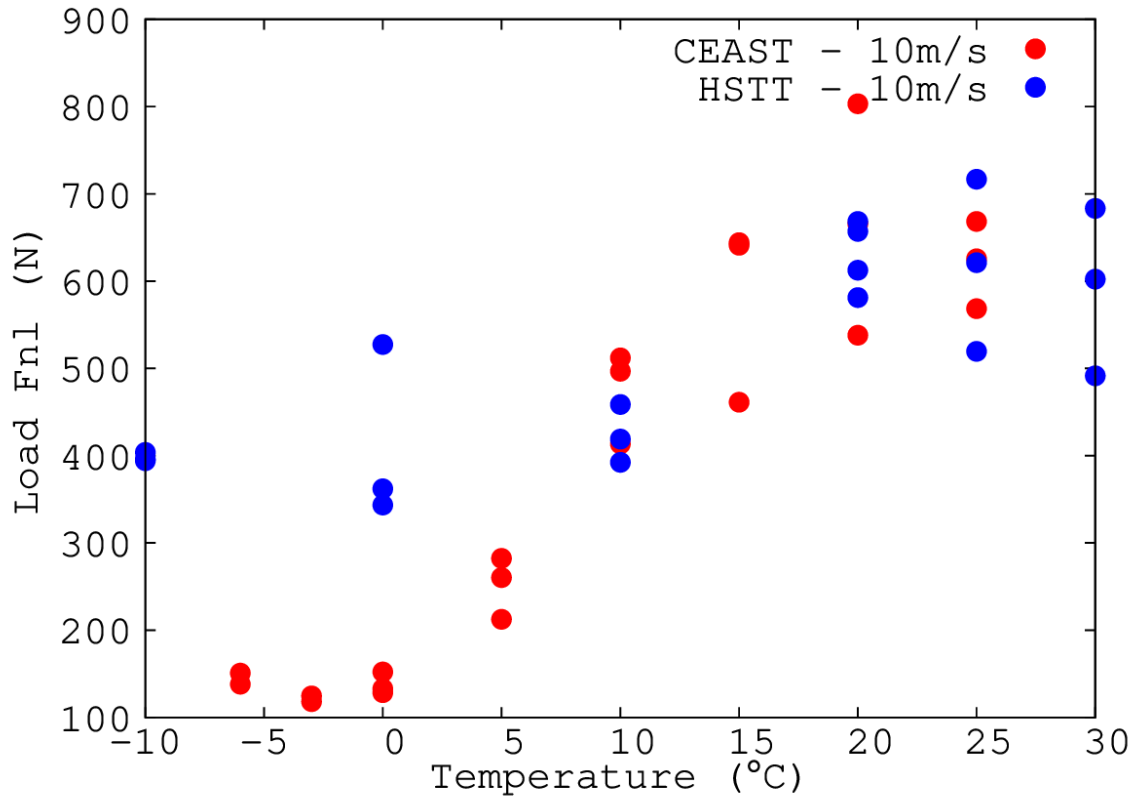


Figure 4.14: Loads at the appearance of the nonlinearity  $F_{nl}$  with respect to the test temperature

#### 4.1.3.6. $E_{nl}$ : Energy at the appearance of the nonlinearity

$E_{nl}$  is the combination of  $F_{nl}$  and  $d(F_{nl})$ . Actually, this quantity being calculated in the linear part of the curve, it is considered as the area of the triangle  $(0, F_{nl}, d(F_{nl}))$ , i.e.  $F_{nl} \cdot d(F_{nl}) / 2$ .

Fig. 4.15a presents the evolution, as a function of the test temperature, of  $E_{nl}$  calculated with the as-recorded  $F_{nl}$  and  $d(F_{nl})$ . The first observations bring out the following comments:

- different  $E_{nl}$  level at low temperature coinciding with the results observed with  $F_{nl}$  and  $d(F_{nl})$  ( $E_{nl}$  being the combination of both)
- scatter results obtained at high temperature ( $T > 15^\circ\text{C}$ )

Semi-logarithmic representation of  $E_{nl}$  versus test temperature is shown in fig.4.16 to better highlight the S-shaped curve. Even if the HSTT's curve is much more squeezed than CEAST's, the S-shape is still recognizable.

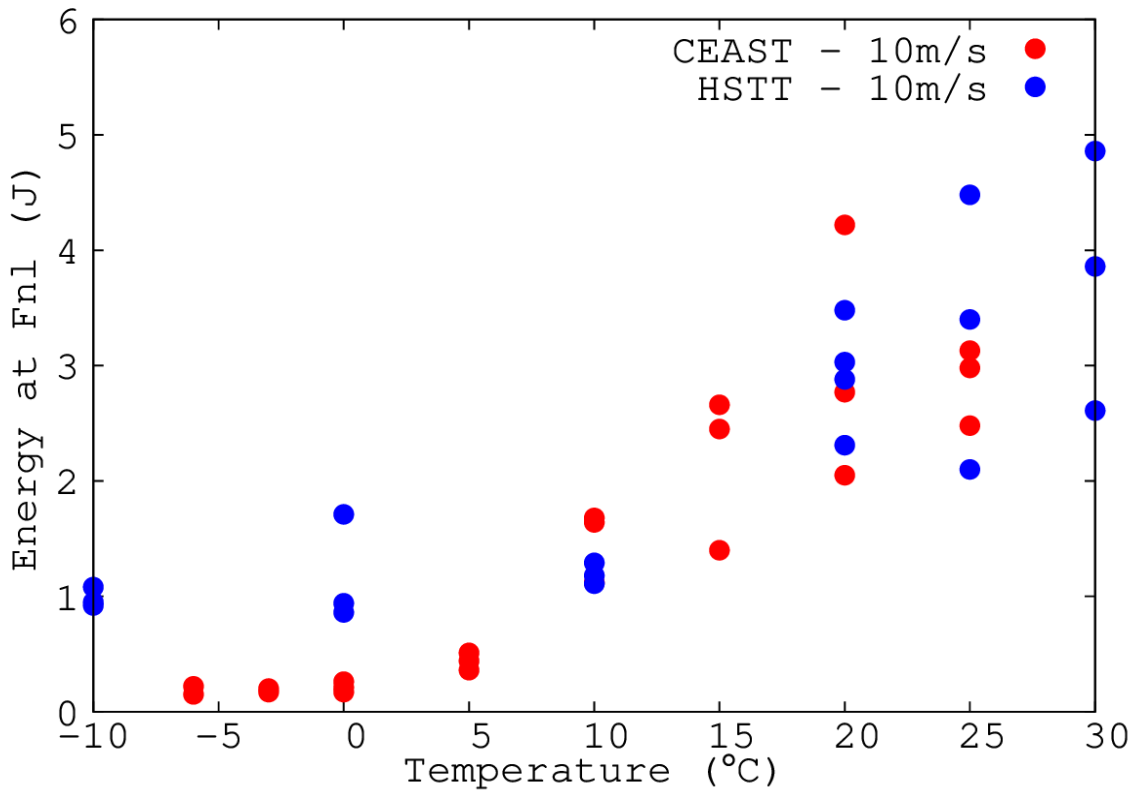


Figure 4.15: Energy at the appearance of the nonlinearity  $F_{nl}$  with respect to the test temperature

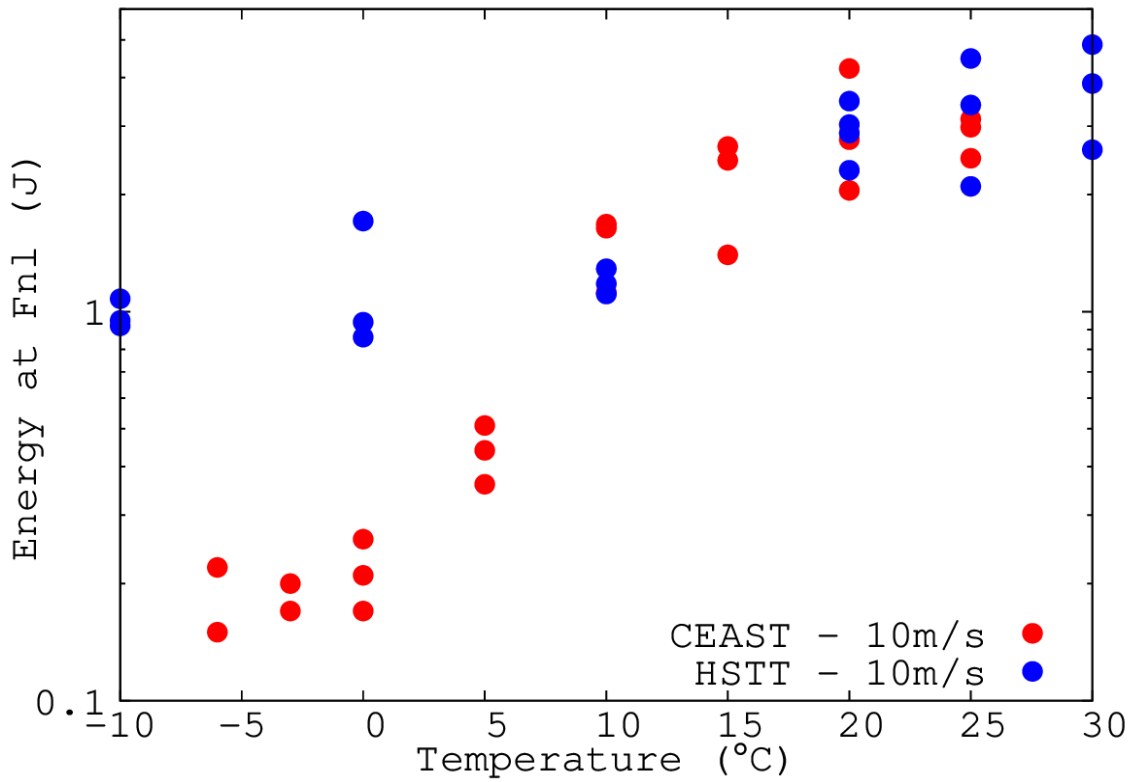


Figure 4.16:  $F_{nl}$  versus test temperature in a semi-logarithmic scale

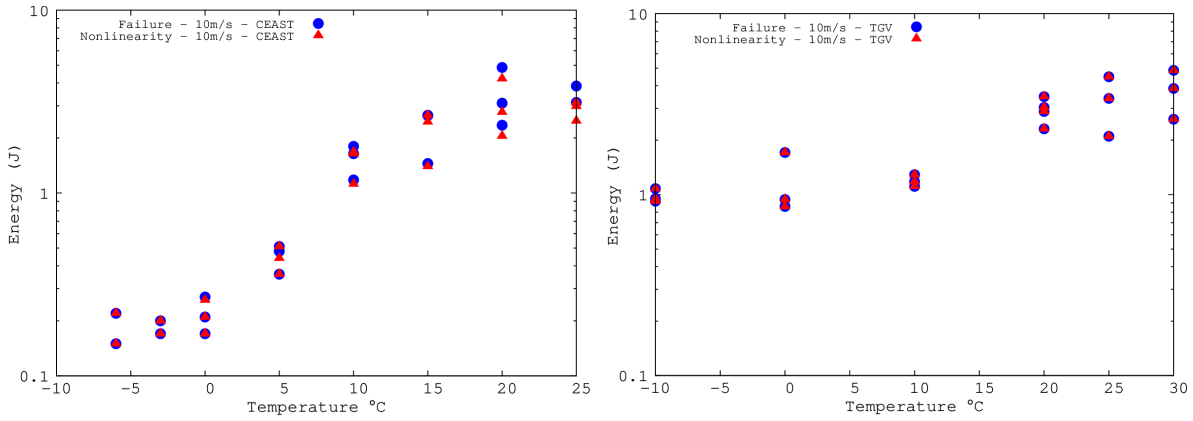


Figure 4.17: Comparison between  $E_{nl}$  and  $E_r$  : a) CEAST ; b) HSTT.

The difference between  $E_{nl}$  (Nonlinearity) and  $E_r$  (Failure) for CEAST and HSTT are shown on Figure 4.17. In Figure 4.17a, displaying the CEAST results, it is noticed that both  $E_{nl}$  and  $E_r$  are identical at low temperature ( $T \leq 0^\circ\text{C}$ ), but  $E_r$  starts to be slightly higher than  $E_{nl}$  when the temperature is superior to  $0^\circ\text{C}$ .

On the contrary, for HSTT (Figure 4.17b) the two energies were systematically similar. This means that no nonlinearity appeared in the load versus deflection curve whatever the test temperature. Following Laiarinandrasana et al. [43],  $E_{nl}$  was considered as the energy at failure for the scored sample.

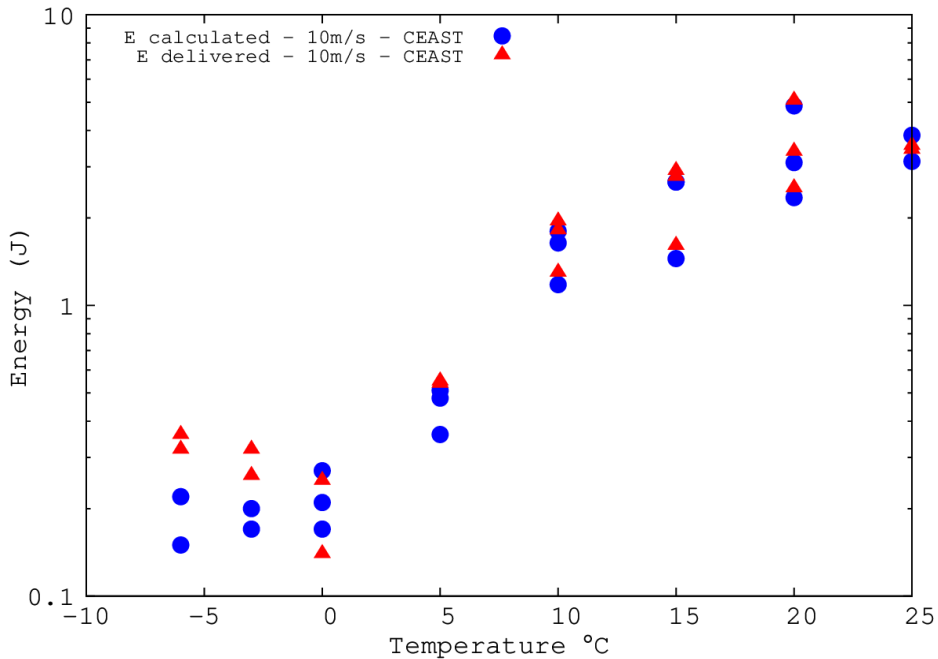


Figure 4.18: Comparison of the energy at failure delivered by the CEAST software and the one calculated by integrating the area under the load versus deflection curve

In the case of the CEAST, the energy calculation used by the firm software is based on the raw load and deflection data (eq 2.1 and 2.2). But, as seen on 4.1.1.2, the raw data had to be cleansed to be exploitable (removing the noise, the compression on the sample around the striker, the repositioning of the beginning of the test, etc...). Recalculating the energy at failure obtained after the cleansing should then modify the result. Figure 4.18 shows the effect of the cleansing on the Energy at failure on a semi-logarithmic diagram. It is observable that the cleansing reduces the energy value at every temperature, but also that it impacts more the lowest temperature, surely because the results obtained have the same level as the noise. At high temperature the two energies at failure are quite similar. Therefore, for the upper shelf (ductile part) one can use the energy delivered by the CEAST machine, without any further operations.

#### 4.1.4. Determination of the ductile fracture threshold temperature ( $T_{dth}$ ), comparison between CEAST and HSTT at 10 m/s

As already mentioned, the evolution of  $E_{nl}$  will be used instead of  $E_r$ . In the literature, the impact strength or the fracture toughness are the most common methods to determine the DBTT [3], or in our case the  $T_{dth}$  [15]. All of these global approaches are based on the energy-cracked surfaces ratio. The only information about crack initiation is based on the appearance of nonlinearity in the load versus deflection curve. Therefore, the transition temperature was determined using only the evolution of  $E_{nl}$  with the temperature (Figure 4.16). Following [60, 61],  $\tanh$  function was proposed to fit the experimental data. The equation is described in eq. 4.6.

$$E_{max}(T) = \left( E_D - \frac{\Delta E}{2} \right) + \frac{\Delta E}{2} \times \tanh\left( \frac{T - T_{dth} + \frac{\Delta T}{2}}{\frac{\Delta T}{2}} \right) \quad (\text{eq 4.1})$$

With:

$E_D$  = energy value of the ductile plateau

$\Delta E$  = energy value of the difference between the ductile and brittle plateaus

$T_{dth}$  = Ductile Failure Threshold Temperature [15]

$\Delta T$  = temperature difference between the ductile and brittle plateaus

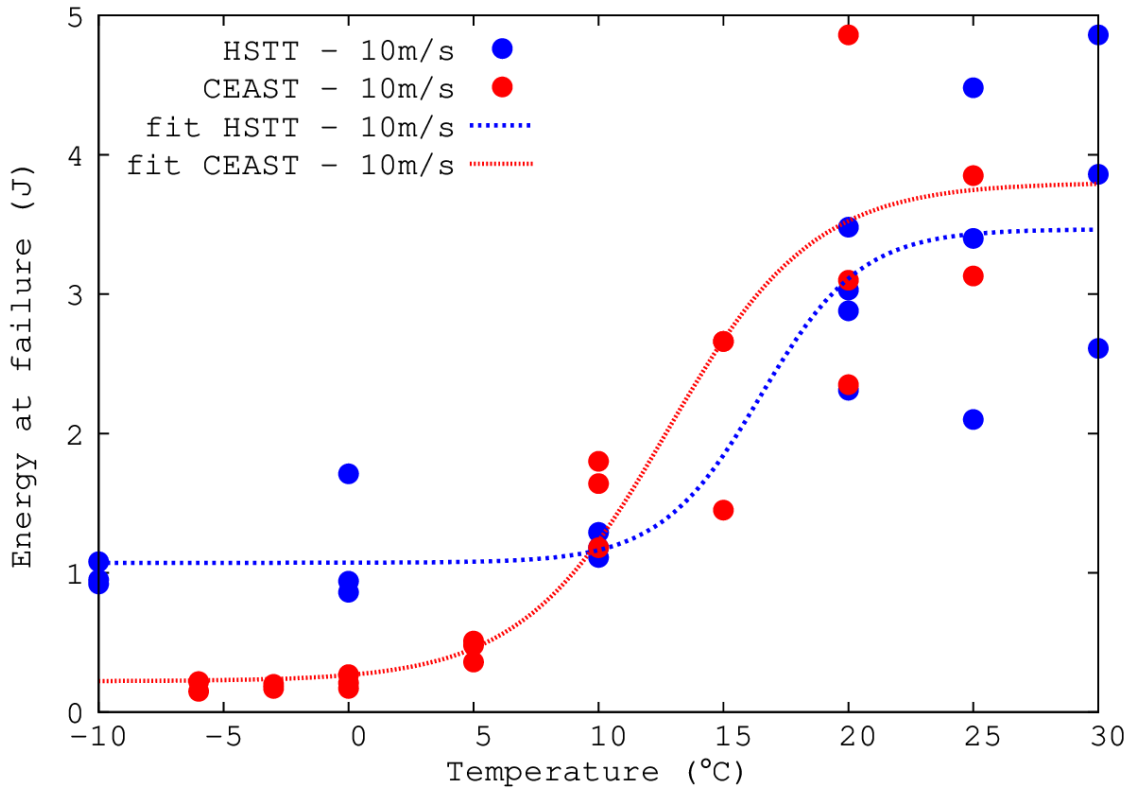


Figure 4.19: Merged experimental points from HSTT and CEAST (fig.4.16) compared with fitting  $\tanh$  function.

The transition temperature  $T_{dth}$  was directly determined by optimization, using the  $\tanh$  function in eq. 4.1. The result is a  $T_{dth}$  around 20°C for both instruments (see data in table 4.1), which is in line with what was mentioned in figs. 4.14-15.

It can be concluded that for scored samples, tested at 10 m/s on both HSTT and CEAST testing machines, the  $T_{dth}$  observed was similar and it was legit the use of both instruments to increase the range of the Impact speed for the study.

Instrument	$E_D$	$\Delta E$	$\Delta T$	$T_{dth}$
CEAST	3	2.8	15.2	19.3
HSTT	3.4	2.4	8.4	19.5

Table 4.1: Coefficients used to parameter the  $\tanh$  function for 10 m/s's scored-curves

#### 4.1.5. Extension to impact speeds lower than 10 m/s from CEAST

Impact speed of 10 m/s was investigated on both HSTT and CEAST machines in order to compare the data sets and to better analyze the differences on these data. As seen in chapter 3, description of both instruments, a wider range of impact speeds was investigated. In this subsection, for impact speeds lower than 10 m/s only the CEAST was used. The investigated impact speeds were respectively : 2 m/s, 4.4 m/s, and 6 m/s. It is to be noted that:

- 4.4 m/s is the impact speed recommended by the standards [16];
- The actual impact speed by CEAST is calculated using the impulse formula (eq. 2.3);
- From the integrated velocity, the deflection and the energy at any time are calculated as well;
- The failure is assumed to be the appearance of the nonlinearity in the load versus deflection curve.

The structure of this subsection will follow the same as that of subsection 4.1.3, related to CEAST-HSTT data comparison, apart from the data reduction which is common to all data.

##### 4.1.5.1. Instantaneous impact speeds at failure

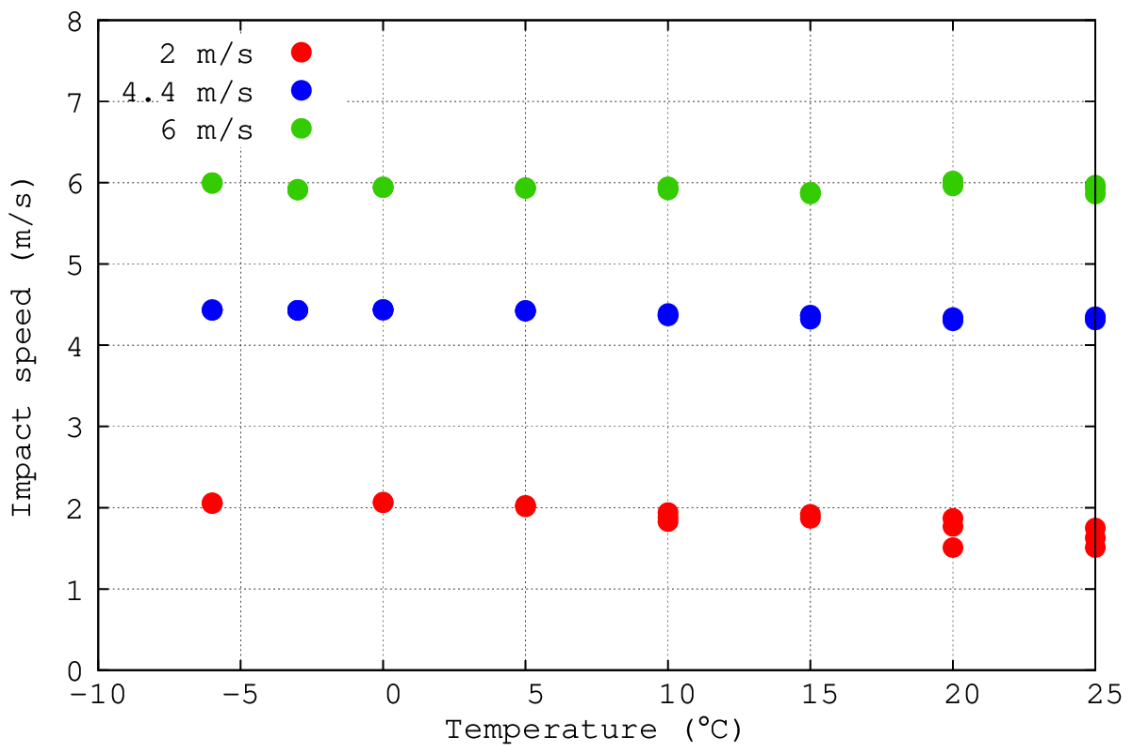


Figure 4.20: Instantaneous impact speed at failure on CEAST tests at prescribed velocities of 2 m/s, 4.4 m/s and 6 m/s

Figure 4.20 illustrates the velocity at failure for the three prescribed impact speeds. The calculated velocities are less than or equal to the prescribed ones ; moreover, they are slightly lower when the test temperature increases. Probably due to that ductile failure requires longer time and the velocity is continuously decreasing, according to eq. 2.3, and by the nature of the test (falling object).

#### 4.1.5.2. Stiffnesses

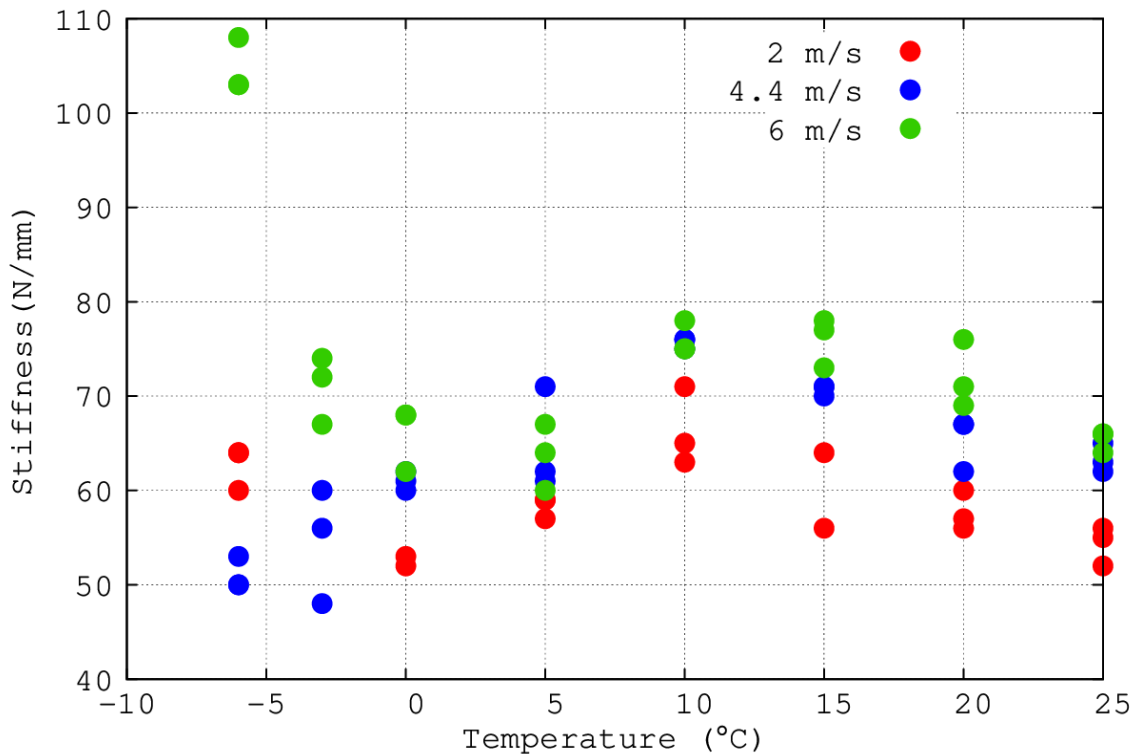


Figure 4.21: Stiffness on CEAST tests at prescribed velocities of 2 m/s, 4.4 m/s and 6 m/s

In Figure 4.21 the stiffness with respect to the test temperature for the three prescribed impact speeds is shown . Apart from -6°C, the lower the impact speed, the lower the stiffness. Aside of a regular evolution of the stiffness with the impact speed, the curves present unexpected evolutions:

- A maximum at 10°C, before a significant decrease at high temperature, probably due to the softening;
- A minimum (inflexion) at 0°C for 2 m/s and 6 m/s;
- In comparison with the overall data, values abnormally high for 6 m/s at -6°C.

### 4.1.5.3. Deflection at failure

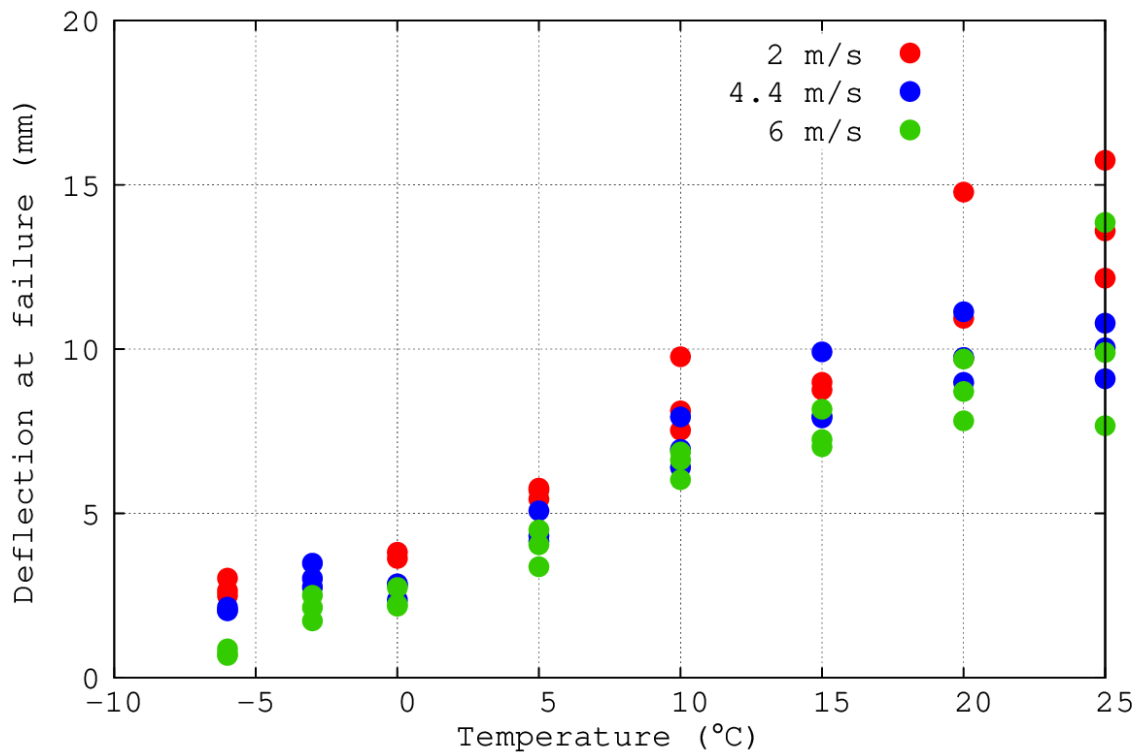


Figure 4.22: Deflection at failure on CEAST tests at prescribed velocities of 2 m/s, 4.4 m/s and 6 m/s

Figure 4.22 depicts the deflections at failure with respect to the test temperature for the three prescribed impact speeds. The graph shows a continuous increase of the deflection at failure with the temperature which is different for the impact speeds:

- The curve seems linear at 2m/s,
- an inflection begins between 15°C and 20°C for 4.4m/s and 6m/s.
- A small inflexion might be perceived below 0°C

At the same temperature, the lower the impact speed, the higher the deflection at failure; furthermore, the experimental points are more scattered at high temperature ( $10^{\circ}\text{C} \leq T \leq 25^{\circ}\text{C}$ ).

#### 4.1.5.4. Load at failure

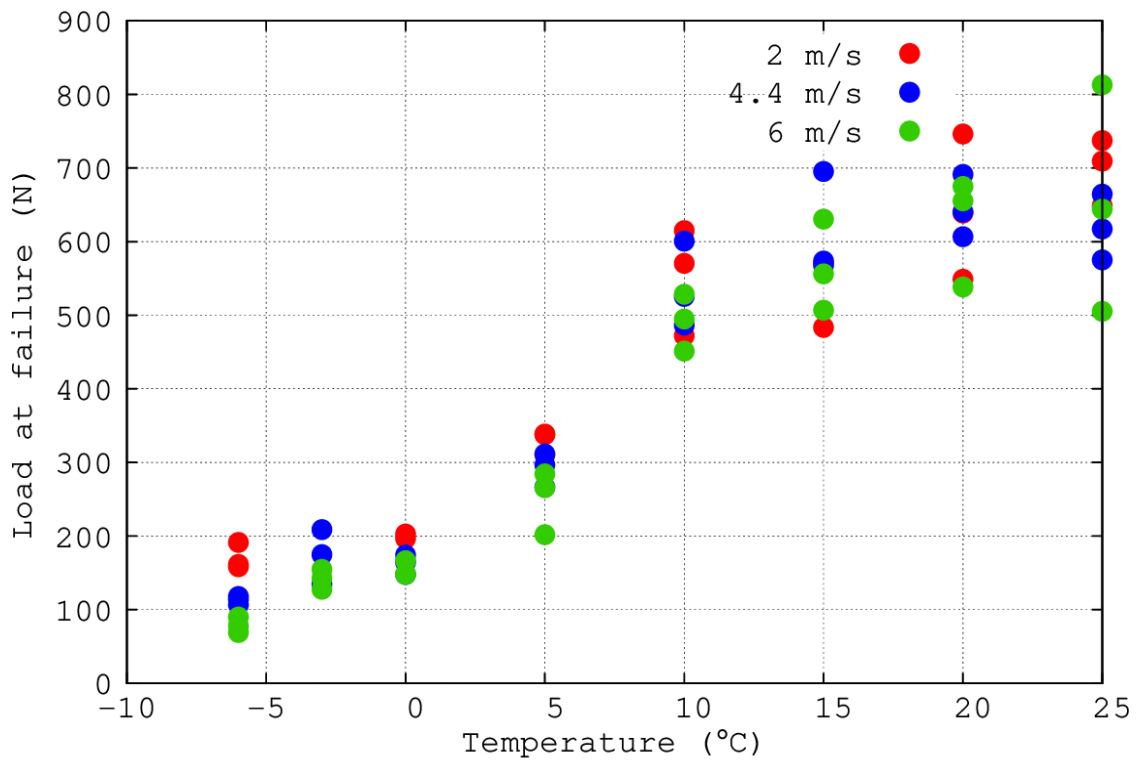


Figure 4.23: Load at failure on CEAST tests at prescribed velocities of 2 m/s, 4.4 m/s and 6 m/s

Figure 4.23 plots the loads at failure as a function of the test temperature for the three prescribed impact speeds. The curves in the graph display a continuous increase of the load at failure with the temperature. In addition, independently of the impact speed, a clear S-shape trend is observed. However, the curves also have some unexpected evolutions:

- Up to 5°C, for a given temperature, the lower the impact speed, the higher the load at failure;
- more scattered experimental points at high temperature, from 10°C.

By looking at both deflection and load's curves, it is possible to guess a temperature range for the  $T_{dth}$  transition by looking at the curve profiles' variations. Thus, for the three impact speeds shown on Figures 4.22-23, the guessed  $T_{dth}$  are gathered in the table 4.2.

Impact speed (m/s)	2	4.4	6
$T_{dth}$ (°C +/- 2°C)	10	15	15

Table 4.2: Guessed  $T_{dth}$  from the deflection and load curves with a +/-2°C approximation

#### 4.1.5.5. Energy at failure

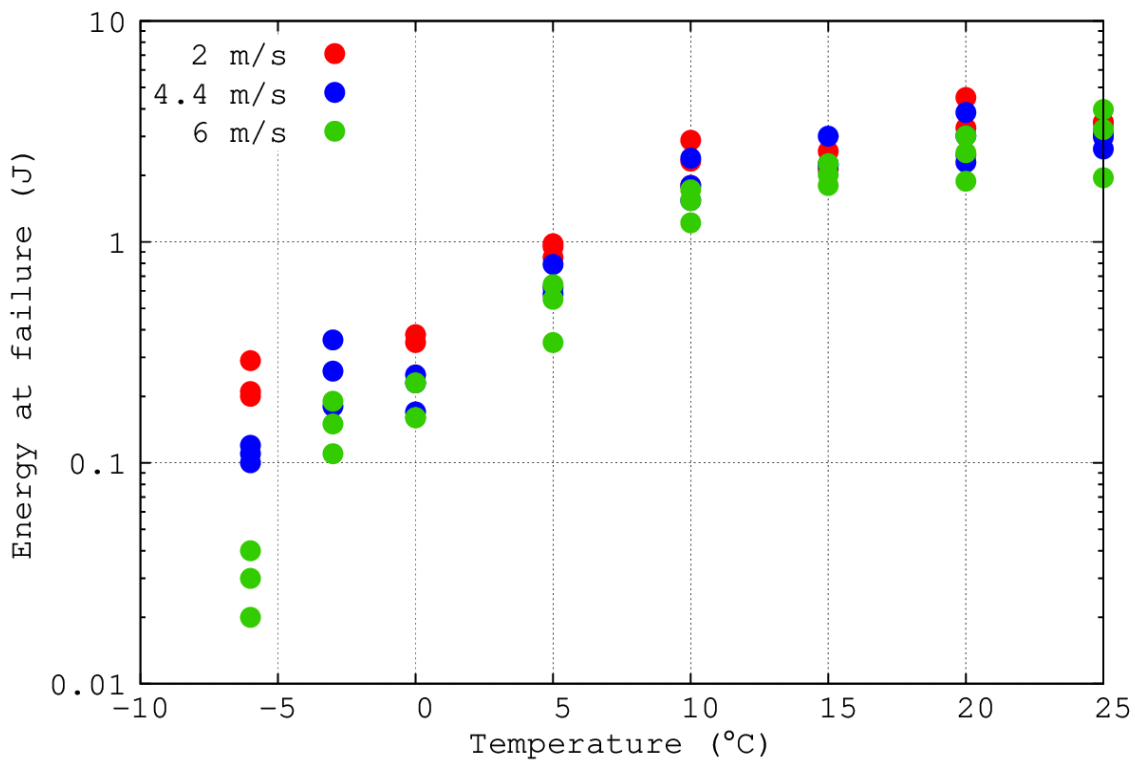


Figure 4.24: Energy at failure on CEAST tests at prescribed velocities of 2 m/s, 4.4 m/s and 6 m/s

In Figure 4.24 the energy at failure is plotted with respect to the test temperature for the three prescribed impact speeds, in a semi-logarithmic graph. The results shown in the graph are key curves used to determine the  $T_{dth}$ . Its evolution presents a continuous increase of the energy at failure with the temperature, as expected: the energy is the combination of the deflection and the load, both increasing with the temperature. The upper shelf energy is close for the three impact speeds, around 3 J. The lower shelf seems not to be reached, in terms of energy at failure, but it won't be constraining since the  $T_{dth}$  needs only the upper shelf. Besides, the lower the impact speed, the higher the energy at failure.

For CEAST tests a comparison between the energy at failure given by the software (without correction) and that integrated by the area under the corrected load versus deflection curve is required. Figure 4.25 illustrates this comparison at the three prescribed impact speeds.

In the domain of interest (upper shelf / ductile plateau) the difference is negligible. As a consequence, the values delivered by the CEAST testing machine can be used.

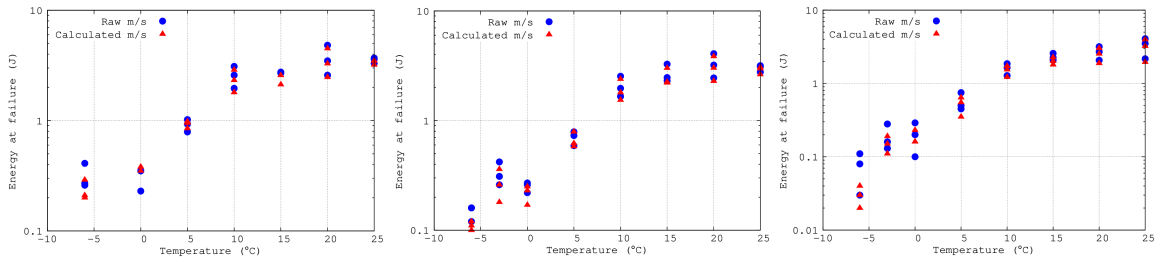


Figure 4.25: Comparison of the energies at failure on CEA tests at prescribed velocities of 2 m/s, 4.4 m/s and 6 m/s

From Figure 4.25 and only by judging from the curves' profiles, it can be assumed that the  $T_{dth}$  for the tests at 2 m/s, 4.4 m/s and 6 m/s are respectively around 10°C, 15°C and 15°C.

#### 4.1.5.6. Evolution of $T_{dth}$ with the impact speeds for scored specimens

##### 4.1.5.6.1. Plot of the *tanh* function

Following the same procedure as in subsection 4.1.2.7, Figure 4.26 plots the fitted *tanh* function representing the evolution of the energy at failure with the temperature for all impact speeds applied to the CEA testing machine. The optimization procedure allowed the following results to be established. For each impact speed the brittle plateau is recognizable at the lowest temperatures and possesses the same value : 0.15 J. After the transition zone for higher temperatures appears the ductile plateau. For impact speeds of 4.4 m/s, 6 m/s, and 10 m/s this plateau has a value between 2.5 J and 3 J, but for 2 m/s it reaches 3.3 J. If the 10 m/s curve is put aside, it is interesting to notice that the plateaus' values seem to decrease with the impact speed. It might be a consequence of the embrittlement of the material. The parameters used for the *tanh* function are displayed in table 4.3.

Impact speed (m/s)	$E_D$	$\Delta E$	$\Delta T$	$T_{dth}$	Gussed Tdth (+/- 2°C)
2	3.2	3.1	8.8	11.9	10
4.4	2.9	2.8	10.3	13.8	15
6	2.8	2.7	10.6	14.9	15
10	3	2.8	15.2	19.3	20

Table 4.3: Coefficients used to parameter the *tanh* function for CEA's curves

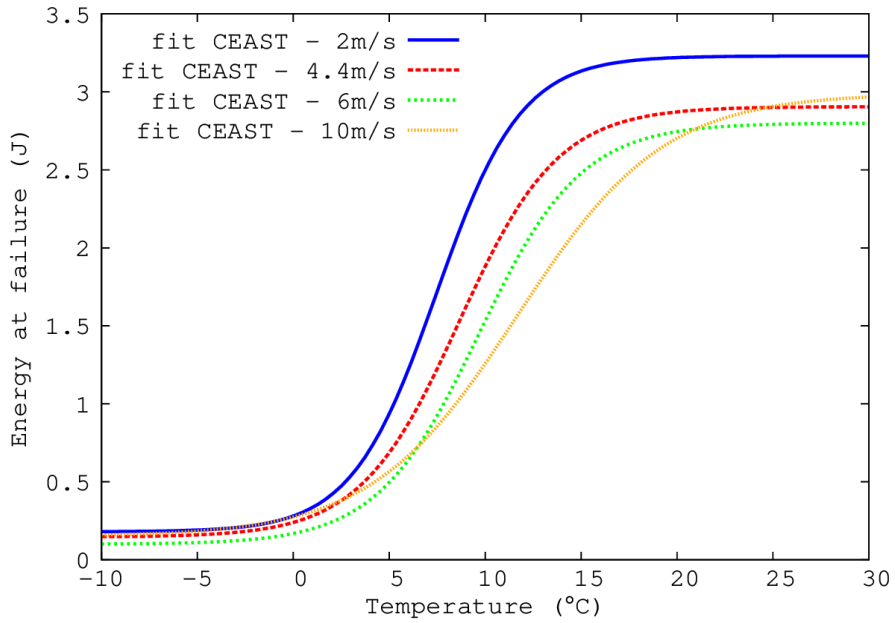


Figure 4.26 : Fitted energy at failure as a function of the temperature for every impact speed

#### 4.1.5.6.2. $T_{dth}$ determination

Now that the threshold temperature ( $T_{dth}$ ) ensuring the ductile fracture is determined for all impact speed conditions with scored samples using CEAST testing machine (4.1.2.5), it is now possible to observe its evolution in Figure 4.27. The scale of the impact speed includes deliberately the highest impact speed tested at the HSTT.  $T_{dth}$  value starts from 11.9°C at 2 m/s to reach 19.3°C at 10 m/s. The increase seems to be quite linear.

It is also interesting to notice that the guessing method, from the observation of the deflection and load curves, shows  $T_{dth}$  with a slight error in comparison with the *tanh* function.

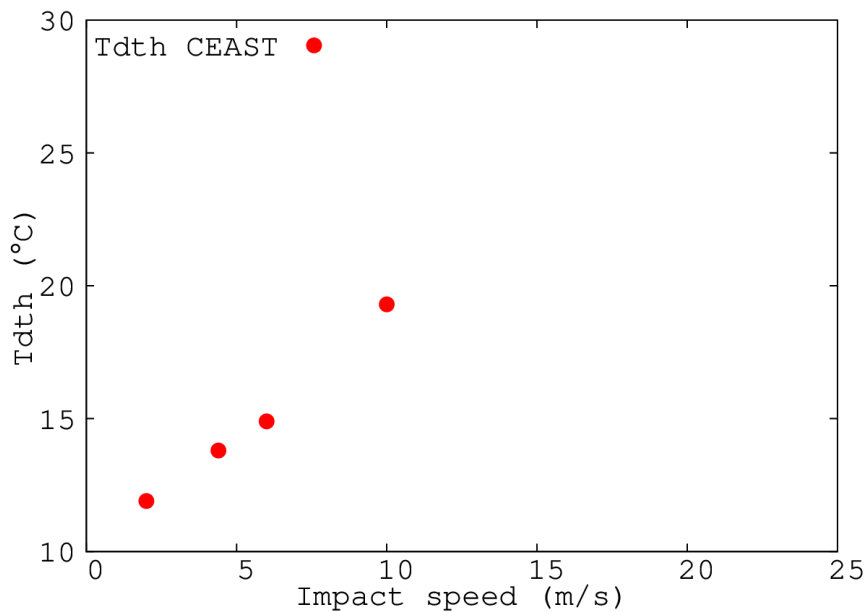


Figure 4.27 : Evolution of the  $T_{dth}$  with respect to the prescribed impact speed for scored skins

#### 4.1.6. Extension to impact speeds higher than 10 m/s from HSTT

The same approach, as in subsection 4.2.5, is followed but concerns the tests carried out on the HSTT testing machine, with impact speeds of respectively 15 m/s and 23 m/s. It is to be noted that:

- The impact speed of the airbag shot is evaluated at about 25 m/s;
- The objective is then to investigate the extension of fig. 4.41 at higher speeds;
- The impact speed on the HSTT machine is derived from the measured deflection;
- The failure is, again, assumed to occur at the appearance of the nonlinearity in the load versus deflection curve.

The structure of this subsection will follow the same as that of subsection 4.2.5, apart from the comparison of the energy at failure, since HSTT does not deliver this energy.

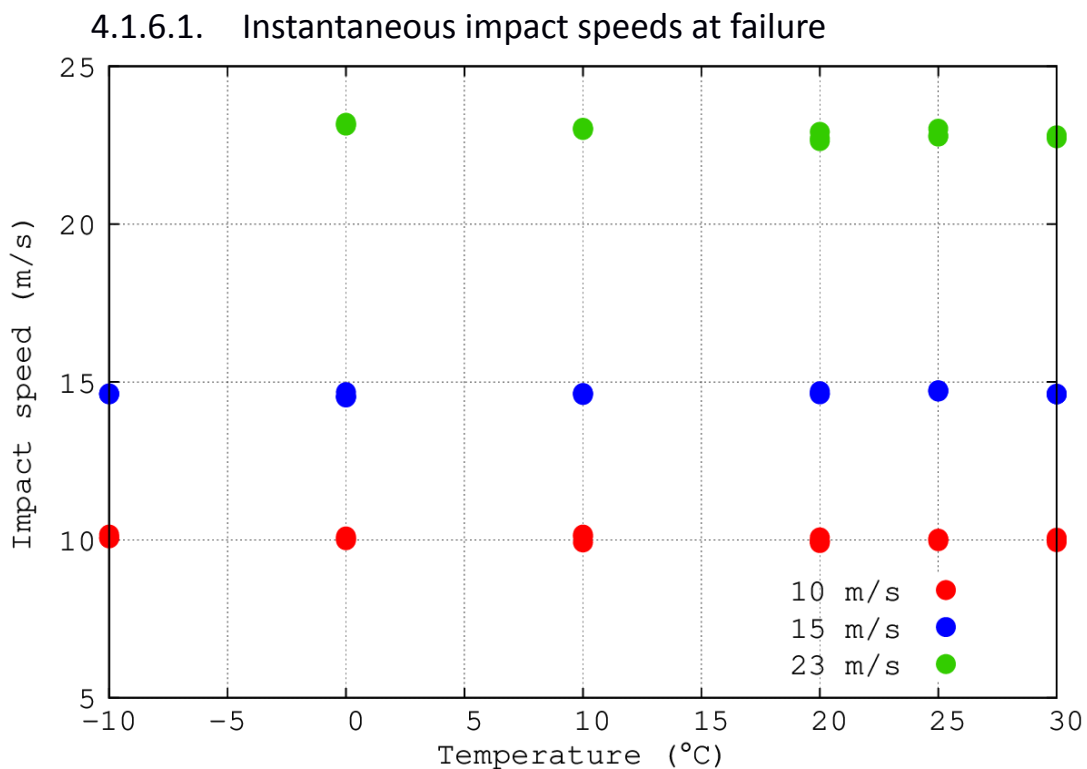


Figure 4.28: Instantaneous impact speeds at failure on HSTT tests at prescribed velocities of 10 m/s, 15 m/s and 23 m/s

Figure 4.28 illustrates the velocity at failure for the already presented 10 m/s and the two other prescribed impact speeds of 15 m/s and 23 m/s. The recorded velocities at failure correspond to the prescribed ones. In contrast to the CEAST tests, there is no decrease in the velocity at failure with an increasing temperature, apart from 23 m/s. It is due to the nature of the test: piston activated versus falling object.

#### 4.1.6.2. Stiffness

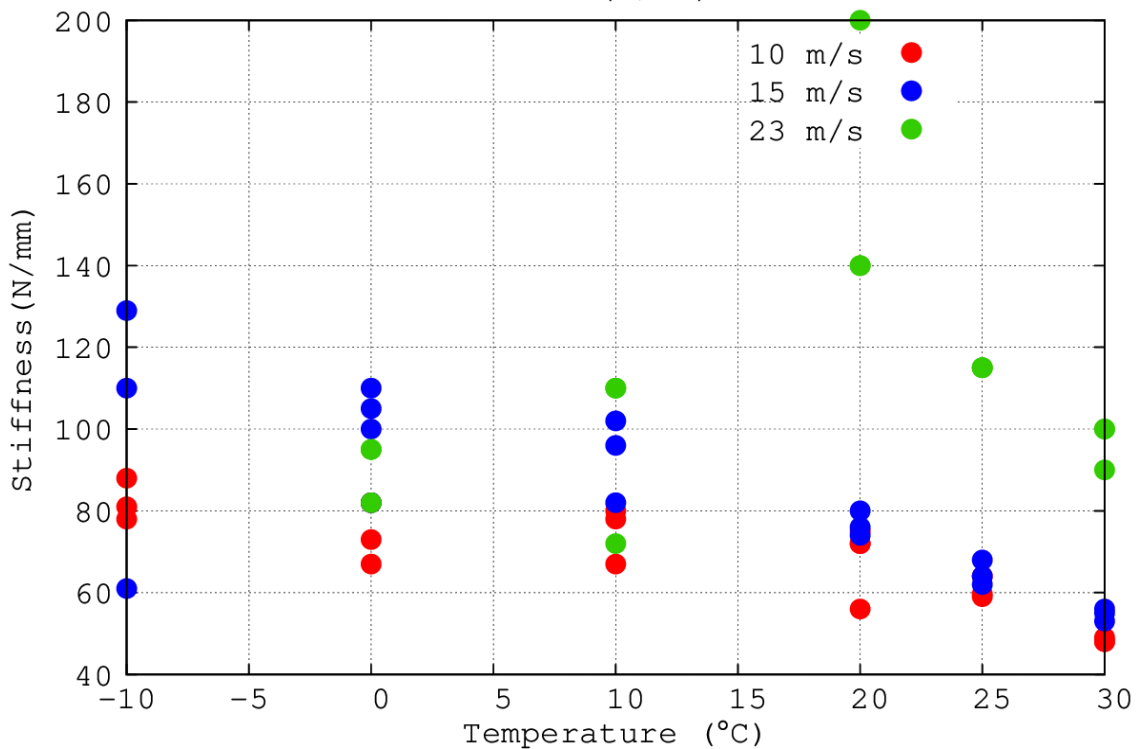


Figure 4.29: Stiffness on HSTT tests at prescribed velocities of 10 m/s, 15 m/s and 23 m/s

In Figure 4.29 the stiffness with respect to the test temperature for the three prescribed impact speeds are shown. A change in the slope, i.e. inflexion point, is observed at 10°C: small slope from -10°C to 10°C and steeper slope from 10°C to higher test temperatures. Also, peculiar trends appear for the stiffness of the tests at 23 m/s between 20°C and 30°C, and at lower temperature than 10°C: a large scatter and stiffness values lower than at high temperature.

#### 4.1.6.3. Deflection at failure

Figure 4.30 depicts the deflections at failure with respect to the test temperature for the three prescribed impact speeds. As expected and seen at lower impact speeds, a continuous increase of the deflection at failure with the temperature is noticed. This time, two changes of slope are observed between 10°C and 20°C, showing small inflexions of S-shaped curves. At the same temperature, the lower the impact speed, the higher the deflection at failure. Moreover, the experimental points are more scattered at high temperature; but, the scatter at 23 m/s is significantly lower than 10 m/s and 15 m/s, which are in the same order of magnitude.

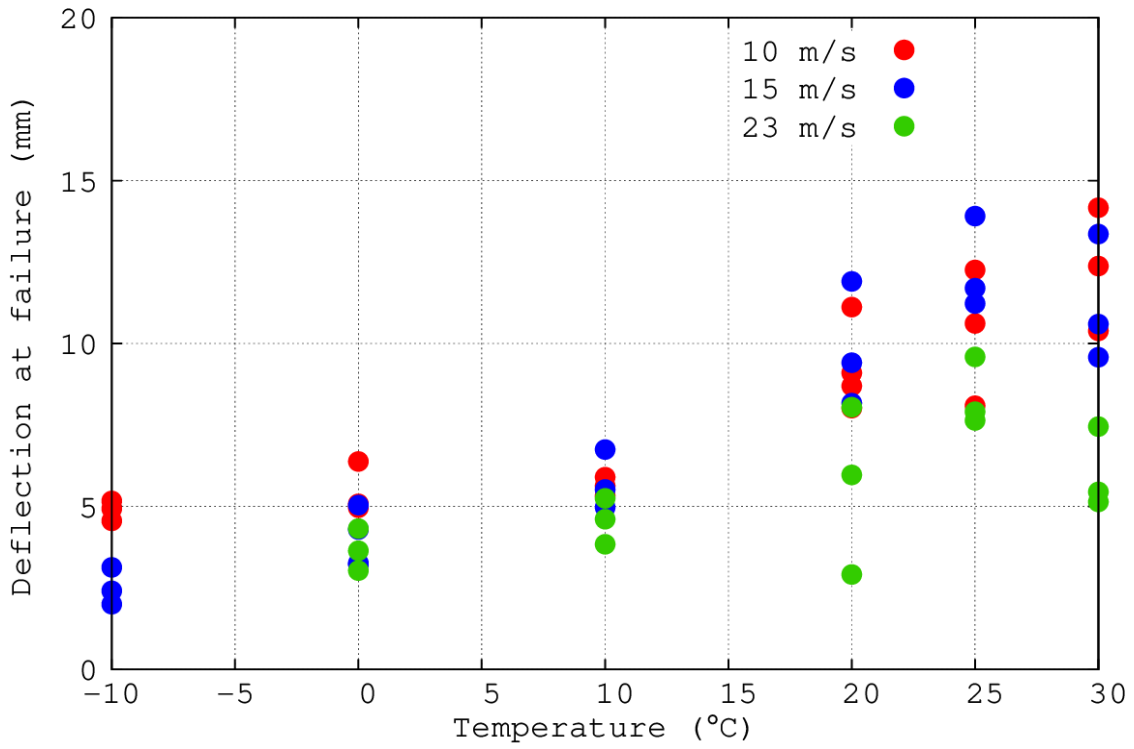


Figure 4.30: Deflection at failure on HSTT tests at prescribed velocities of 10 m/s, 15 m/s and 23 m/s

#### 4.1.6.4. Load at failure

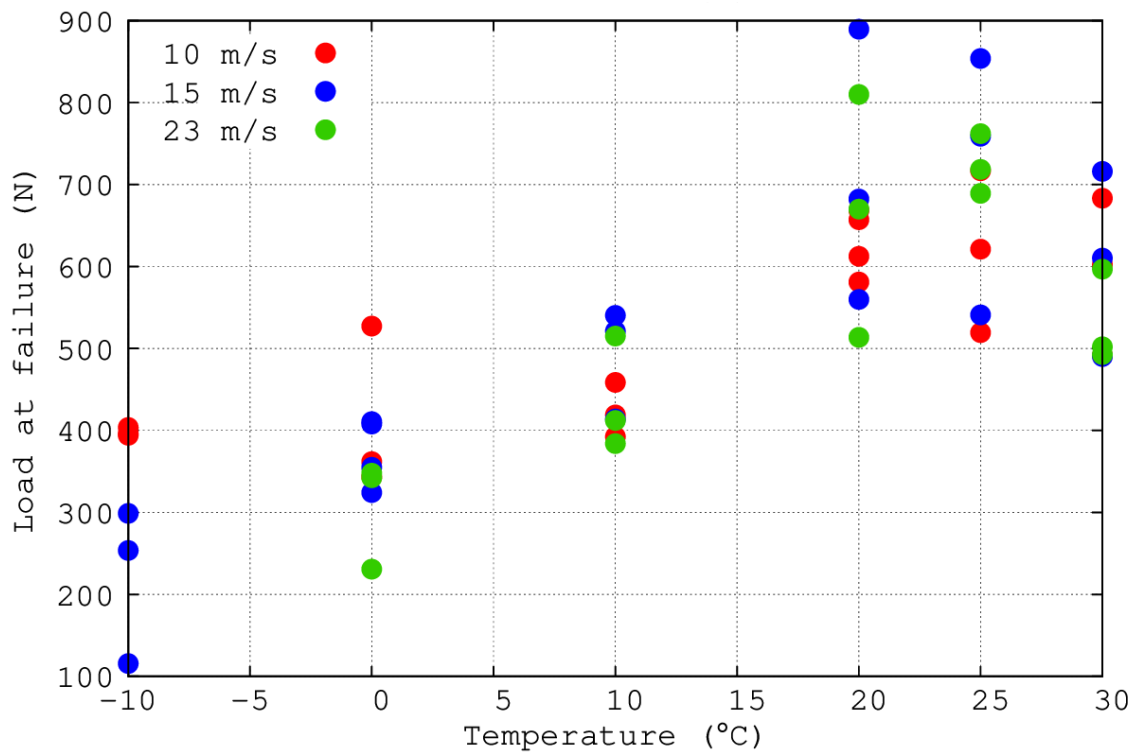


Figure 4.31: Load at failure on HSTT tests at prescribed velocities of 10 m/s, 15 m/s and 23 m/s

Figure 4.31 plots the loads at failure as a function of the test temperature for the three prescribed impact speeds. Again, the graph shows a continuous increase of the load at failure with the temperature, with more perceptible S-shaped curves than on the deflections. Up to 0°C, for a given temperature, the lower the impact speed, the higher the load at failure, but then it becomes more scattered at high temperature (from 10°C). All data are included in the same scatter band. All curves seem to stabilize from 20°C.

#### 4.1.6.5. Energy at failure

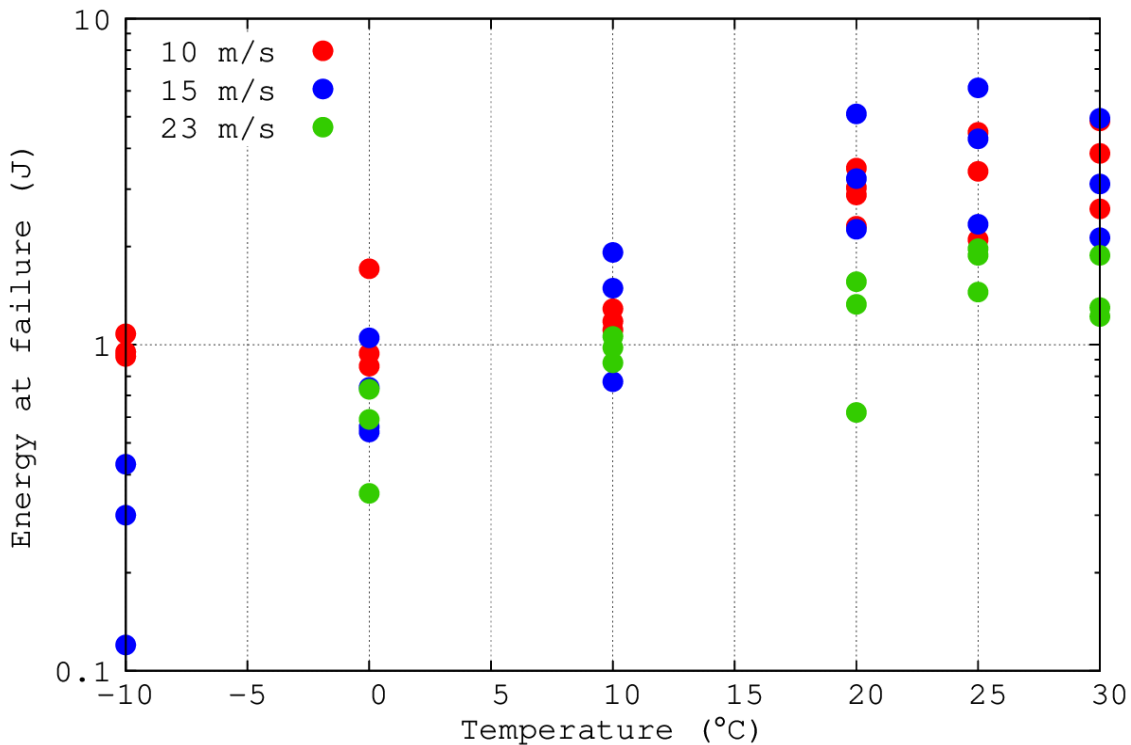


Figure 4.32: Energy at failure on HSTT tests at prescribed velocities of 10 m/s, 15 m/s and 23 m/s

In Figure 4.32 the energy at failure is plotted with respect to the test temperature for the three prescribed impact speeds, in a semi-logarithmic graph. As for the CEAST, it is a key graph used to determine the  $T_{dth}$ . It displays an increase of the energy at failure with the temperature until reaching a plateau between 20°C and 25°C. The trend is the combination of the deflection and load at failure trends. The upper shelf energy is about 4 J for two impact speeds (10 and 15 m/s) but lower than 2J for 23 m/s. Unlike 10 m/s, the lower shelf seems not to be reached, in terms of energy at failure. But at negative temperatures, the lower the impact speed, the higher the energy at failure.

#### 4.1.6.6. Evolution of $T_{dth}$ with the impact speeds for scored specimens

##### 4.1.6.6.1. Plot of $\tanh$ function

Following the same procedure as in subsection 4.2.2.7, Figure 4.33 plots the fitted  $\tanh$  function representing the evolution of the energy at failure with the temperature for all impact speeds data from the HSTT testing machine. The optimization procedure allowed the following results to be established. After the transition zone, for higher temperatures, appears the ductile plateau. For impact speeds of 10 m/s and 15 m/s this plateau has a value around 4 J, but for 23 m/s it reaches only 1.5 J. At this stage, the energy at the upper shelf can be assumed to be 4 J after the previous analysis from both CEAST and HSTT data at 10 m/s. The parameters used to draw the  $\tanh$  function are available in table 4.4.

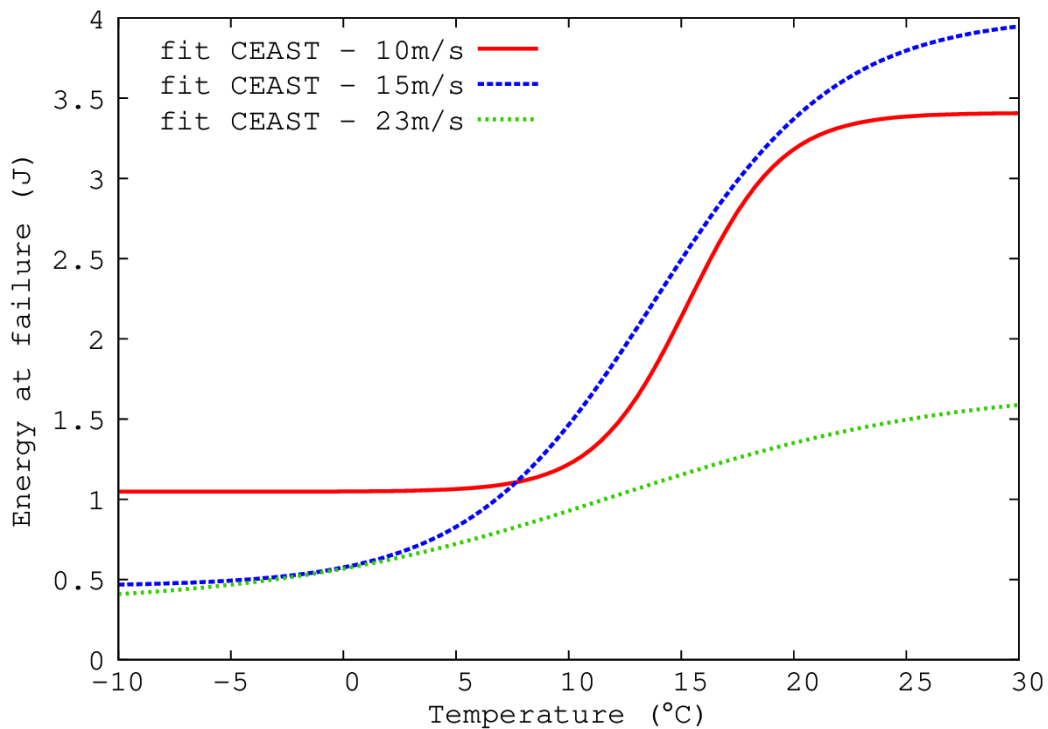


Figure 4.33 : Fitted energy at failure as a function of the temperature for every impact speeds (without semi-logarithmic scale)

Impact speed (m/s)	$E_D$	$\Delta E$	$\Delta T$	$T_{dth}$
10	3.4	2.4	8.4	19.5
15	4	3.6	16.4	22.3
23	1.7	1.4	30	27.1

Table 4.4: Coefficients used to parameter the  $\tanh$  function for the HSTT's curves

#### 4.1.6.6.2. $T_{dth}$ determination

Now that the threshold temperature ( $T_{dth}$ ), ensuring the ductile fracture, is determined for all impact speed conditions with scored samples using the HSTT testing machine, it is now possible to observe its evolution in Figure 4.34.  $T_{dth}$  value starts from 19.5°C at 10 m/s to reach 27.1°C at 23 m/s (determined on table 4.4). The increase seems to be linear (Figure 4.34a).

The Figure 4.34b gathered the  $T_{dth}$  collected from CEAST and HSTT testing machines. It highlights that the  $T_{dth}$  increases linearly no matter what instrument is used, from 12°C at 2 m/s to 27°C at 23 m/s.

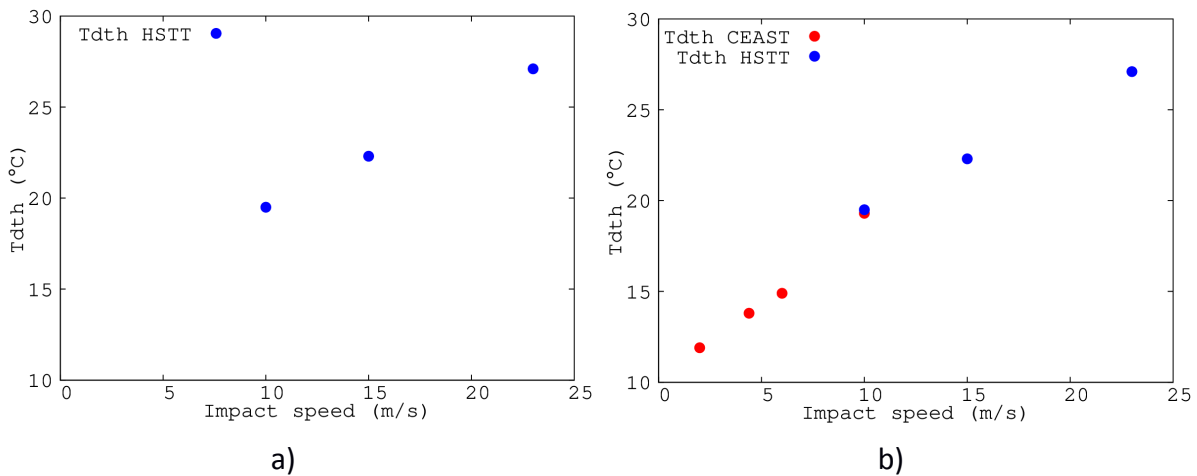


Figure 4.34 : Evolution of the  $T_{dth}$  with respect to the prescribed impact speed for scored skins a) HSTT only b) CEAST and HSTT

#### 4.1.7. Fracture surfaces for scored samples

The fractography dealing with the study of the fracture surfaces can also be used to identify brittle and ductile failure. The ISO 6603 standard [16] recommends the association of the macroscopic surface aspects to the load versus deflection curve's profiles to validate the test for unscored samples.

In this work, an attempt was made to apply the same approach for scored samples at both macroscopic and microscopic scales.

#### 4.1.7.1. At the macroscopic scale

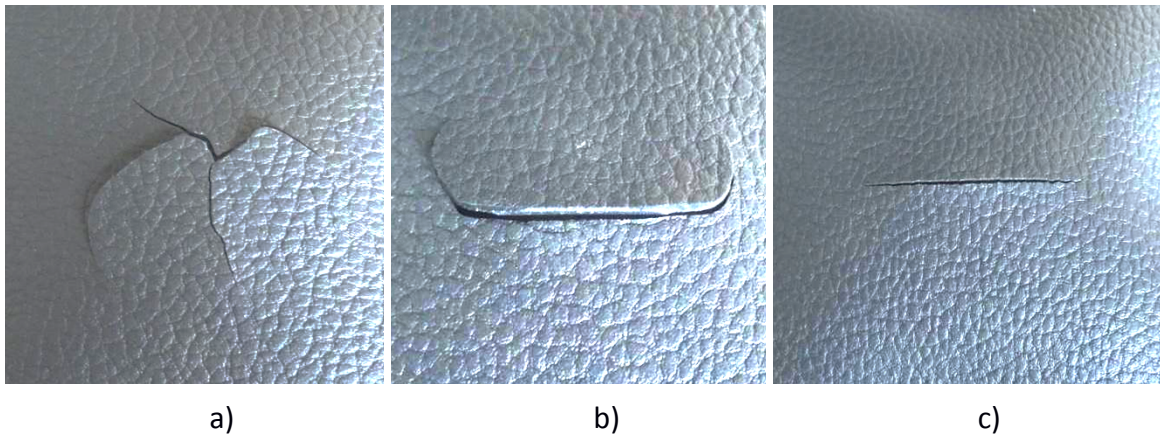


Figure 4.35: Aspect of the fracture surfaces after the impact tests on scored samples (initial score on the opposite surface): a) Brittle at 4.4 m/s and  $-6^{\circ}\text{C}$  ; b) Transition at 4.4 m/s and  $5^{\circ}\text{C}$ ; c) Ductile at 4.4 m/s and  $20^{\circ}\text{C}$

Some *post-mortem* characteristic surfaces were selected so as to relate the mode of failure to the aspects of the fracture at the macroscopic scale. For a low temperature test (Figure 4.35a), at 4.4m/s and  $-6^{\circ}\text{C}$ , a star shaped fracture surface was observed. In this case, the load versus deflection curve is linear up to the load drop ( $F_{nl} = F_r$ ). The failure is assumed to start when the tip of the striker impacts the material and propagates radially. A close observation of the samples showed no plastic strain reinforcing this failure scenario.

For intermediate temperatures, in the transition zone, Figure 4.35b is related to a test at 4.4 m/s m/s and  $5^{\circ}\text{C}$ . The fracture surfaces show a failure on the pre-crack at the tip of the impact striker, but deviate from the scoring direction on both ends of the crack at some point during the test.

For a high temperature test (4.4 m/s and  $20^{\circ}\text{C}$ ) (Figure 4.35c), the fracture surface was observed to be a straight line along the pre-existing scoring. The failure shows a slight strain around the tip of the striker impact, and the failure's length is greater than the striker's radius. These points indicate that the crack propagation is divided in two steps. During the first step, the crack is nucleated and grows through the thickness of the skin before propagating in the width along the scoring line, during the second step. Some tests were equipped with a video camera to follow this sequence. Figure 4.36 shows some synchronized images from the HSTT test at 23 m/s and  $28^{\circ}\text{C}$ . It should be mentioned that the acquisition frequency and the image resolution were not good enough to obtain the precise moment of crack nucleation and through thickness growth.

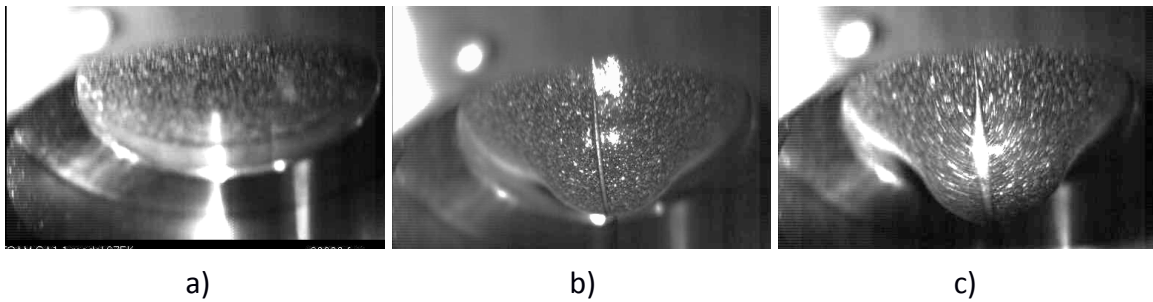


Figure 4.36 : Pictures at the extrados of the impact tests at three characteristic steps: a) before the crack nucleation ; b) through thickness crack appearance; c) impactor completely crossing the skin after lateral crack propagation

#### 4.1.7.2. At the microscopic scale

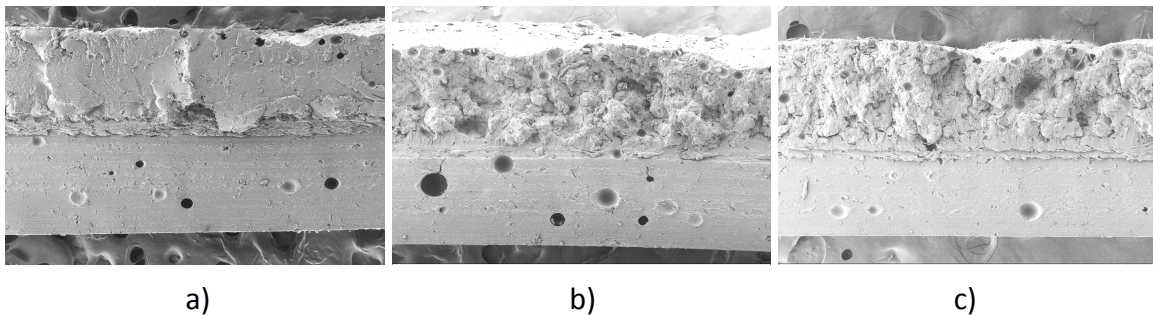


Figure 4.37: Fracture surfaces with progressive change in ductile area : a) Brittle at 10 m/s and -6°C ; b) Transition at 10 m/s and 5°C; c) Ductile at 10 m/s and 25°C

Following Laiarinandrasana et al. [62], the fracture surfaces on broken specimens were SEM examined. Figure 4.37 illustrates these fracture surfaces allowing the identification of brittle and ductile areas. It is shown that the higher the temperature (or the lower the speed) the larger the ductile area. From figure 4.37, a parameter called brittle area ratio (or brittleness rate) is introduced as the measured brittle area divided by the overall deformed fracture area.

Figure 4.38 shows a continuous decrease of the brittle area ratio with the temperature associated with a very large scatter band at higher temperatures. Without an S-shaped (or here Z-shaped) curve, it was concluded that the determination of  $T_{dth}$  is more difficult with this approach.

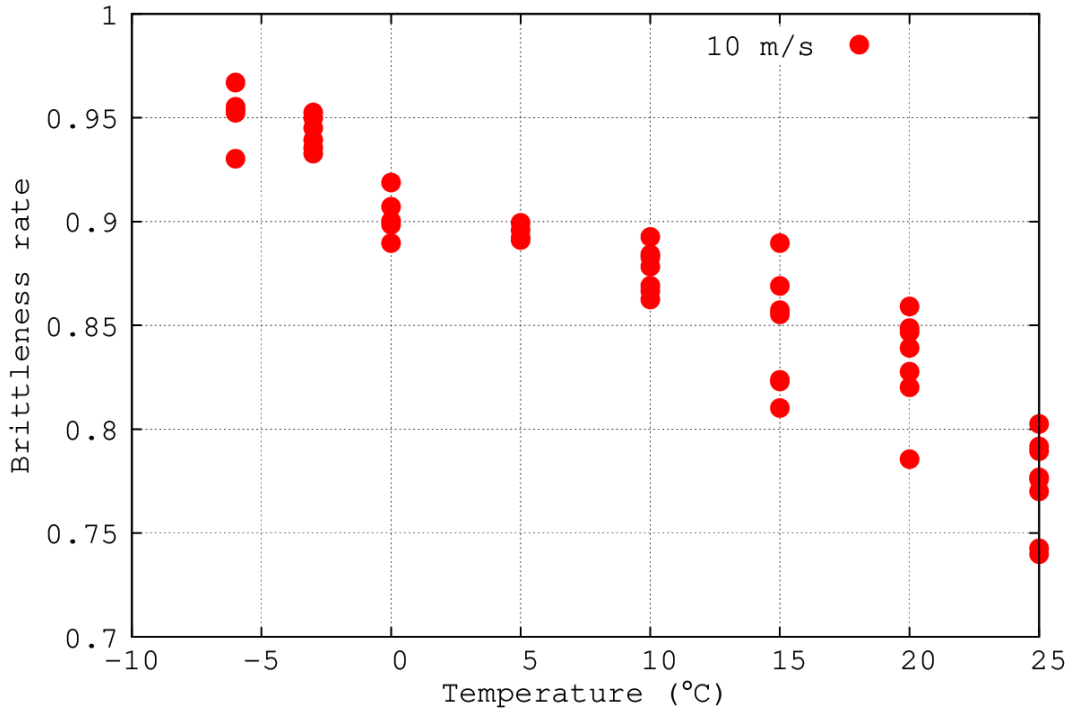


Figure 4.38: Brittleness surface area with respect to the test temperature at an impact speed of 10 m/s

As expected for the four impact speeds studied (2 m/s, 4.4 m/s, 6 m/s, and 10 m/s) in Figure 4.39, the impact speed increases the embrittlement of the specimen response (higher brittleness rate).

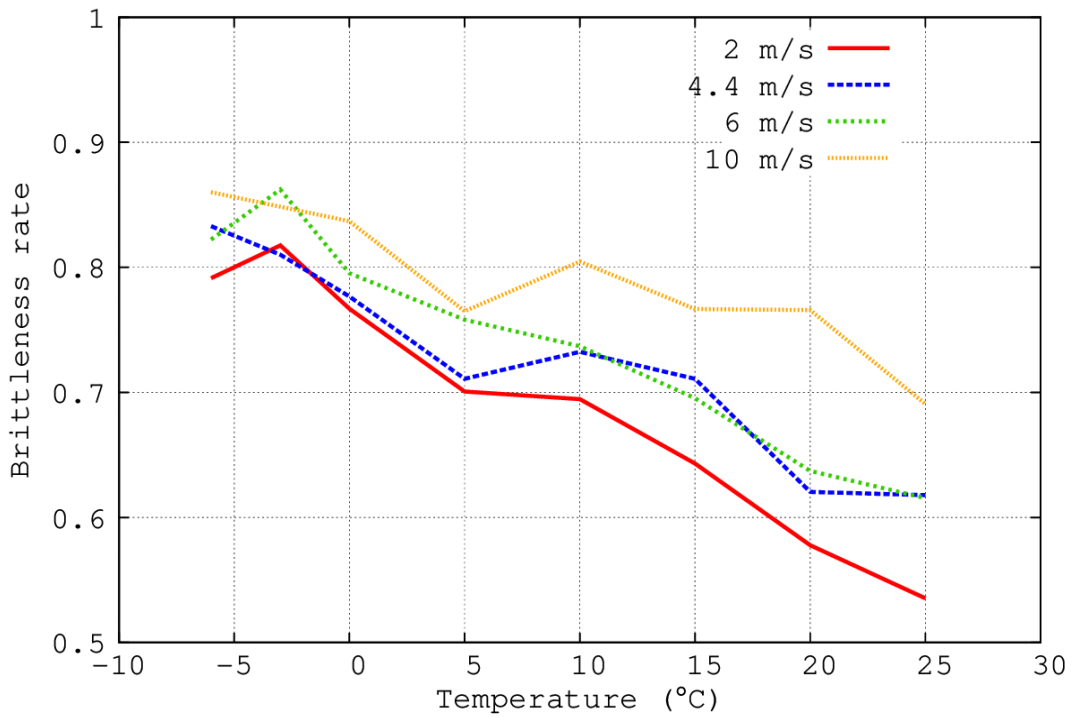


Figure 4.39: Brittleness surface area evolution for four impact speeds: 2 m/s, 4.4 m/s, 6 m/s, and 10 m/s

## 4.2. Impact tests on unscored samples

The same data treatment as for scored samples was applied to unscored ones. The same parameters were collected:  $R$ ,  $V_{nl}$ ,  $V_r$ ,  $F_{nl}$ ,  $F_r$ ,  $d(F_{nl})$ ,  $d(F_r)$ . The structure of subsection 4.2 follows the same as subsection 4.1 without the data reduction description.

This time, the nonlinearity in the load versus deflection curve was observed to be related to the impactor crushing through the skin, moving a spherical cap ahead of the tip. Therefore, the failure corresponds really to the maximum load prior to the drop (progressive or not).

### 4.2.1. Comparison of CEAST - HSTT tests at 10 m/s

#### 4.2.1.1. Instantaneous impact speeds at failure

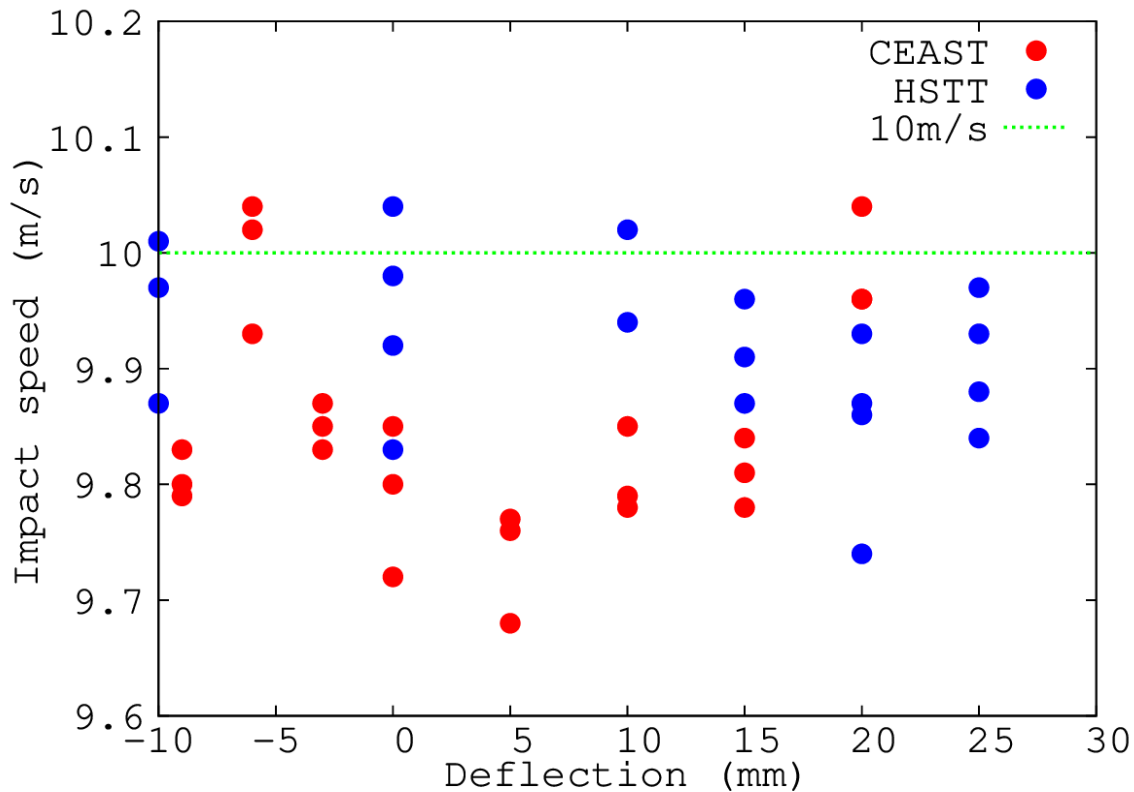


Figure 4.40: Instantaneous impact speed at the maximum load prior to the complete failure for both CEAST and HSTT. The dashed line represents the preset impact speed of 10 m/s.

Figure 4.40 shows the instantaneous deflection speed at  $F_r$  - considered as the crack initiation. CEAST tests in red are mostly underestimated in terms of deflection speed apart from tests at  $-6^{\circ}\text{C}$  and  $20^{\circ}\text{C}$ .

#### 4.2.1.2. Evolution of the Stiffness with the test temperature

The comparison between the two instruments on unscored samples starts with the stiffness, represented on Figure 4.41. In contrast with the scored specimens, both CEAST and HSTT

show the stiffness decreasing continuously, from 100 N/mm at -10°C to 65 N/mm at 25°C. They both present a high level of dispersion and interestingly in the same range. Also, both seem to have an inflection around 5°C with a slightly faster decrease at higher temperatures.

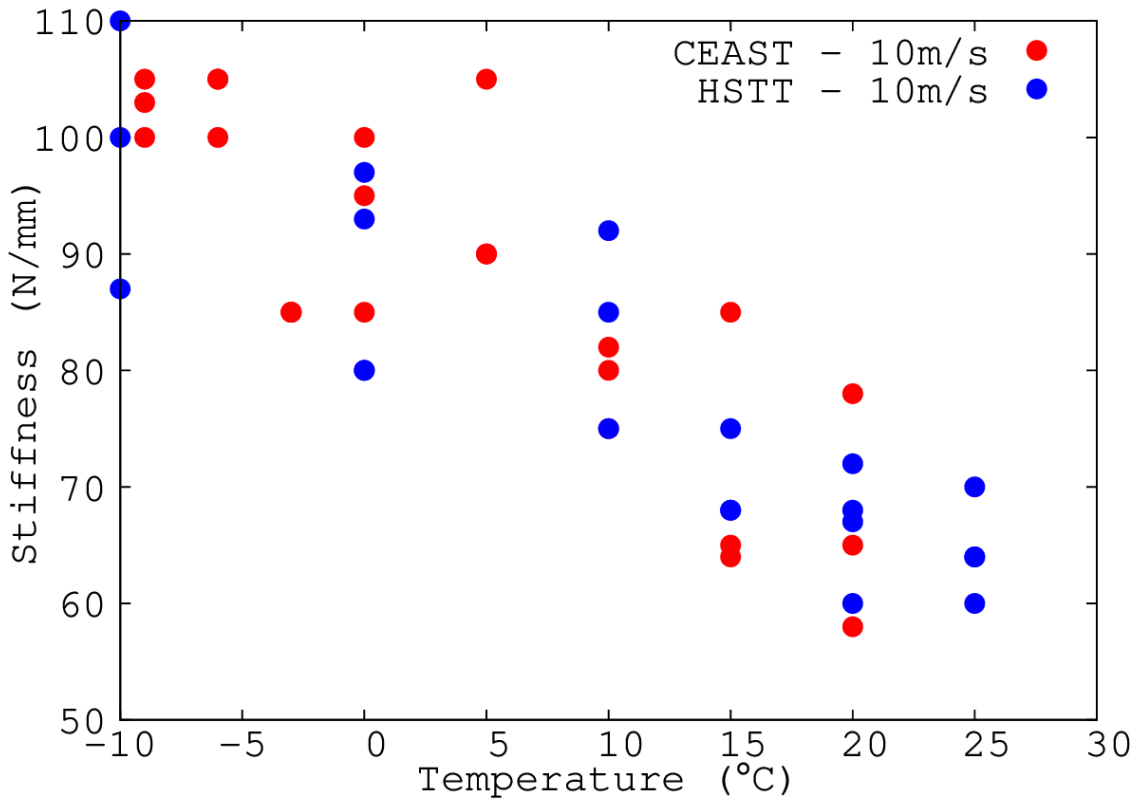


Figure 4.41: Stiffnesses evolution with respect to the test temperature for both CEAST and HSTT at 10 m/s

#### 4.2.1.3. $d(F_r)$ : deflection at failure

Fig. 4.42 displays the deflection at failure as a function of the test temperature, as they were obtained from the data set. Whereas the CEAST experimental points display an S-shaped curve with a plateau starting around -5°C until 15°C, no s-shaped trend from the HSTT is shown. The HSTT's curve is already stable at low temperature until reaching 10°C. The plateaus' level difference is about 4 mm. Interestingly, both instruments are presenting unexpected results at temperatures higher than 10°C: a new increase that was not noticeable with scored specimens. This peculiar increase is suspected to be due to heat build-up effects at higher temperatures ( $T > 10^\circ\text{C}$ ) which increase the deflection at failure.

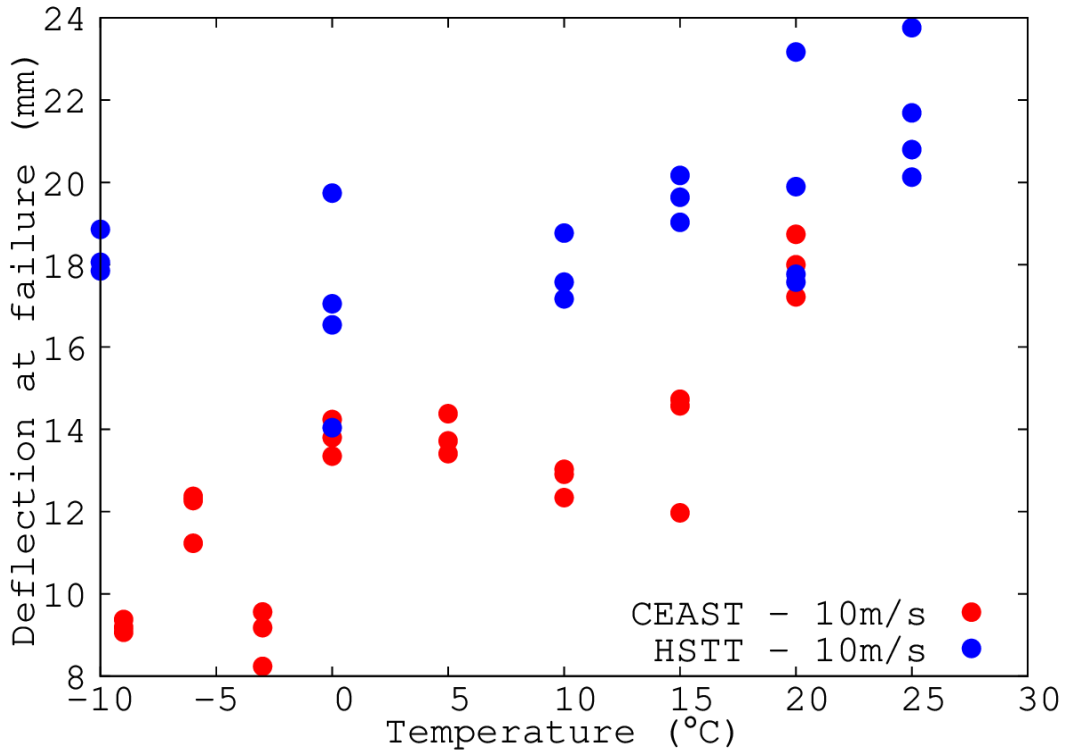


Figure 4.42: Comparison between the deflection at failure with respect to the test temperatures at 10 m/s

#### 4.2.1.4. $F_r$ : Load at failure

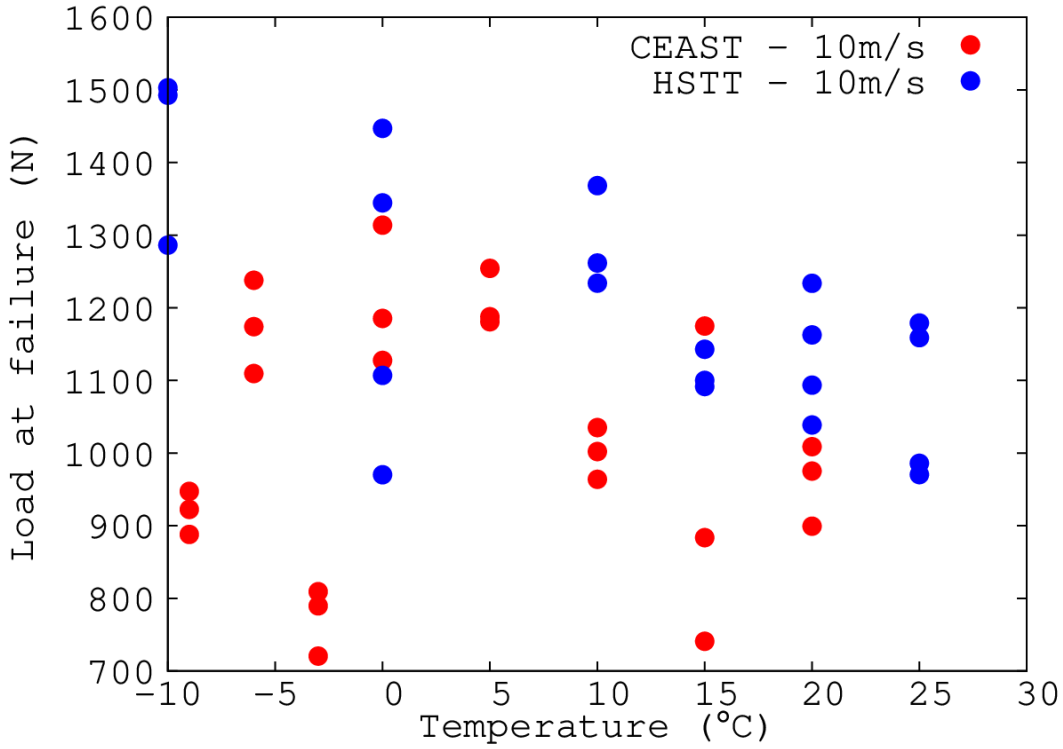


Figure 4.43: Load at failure  $F_r$  with respect to the test temperature for HSTT and CEAST at 10 m/s

The loads at failure ( $F_r$ ) are compared in Figure 4.43. Below 0°C the curve profiles differ. While the HSTT results are stable around 1400 N, CEAST’s experimental points increase (apart from -3°C tests). Then, for both instruments, the curve’s profile possesses the same trend until the highest temperatures: a continuous decrease (even if there is a level difference of 200 N). It is to be noticed that both instruments present a high level of dispersion. As for the deflection, a heat build-up effect is suspected to be linked to the decrease in  $F_r$  at high temperature.

#### 4.2.1.5. $E_r$ : Energy at failure

$E_r$  is the combination of  $F_r$  and  $d(F_r)$ .

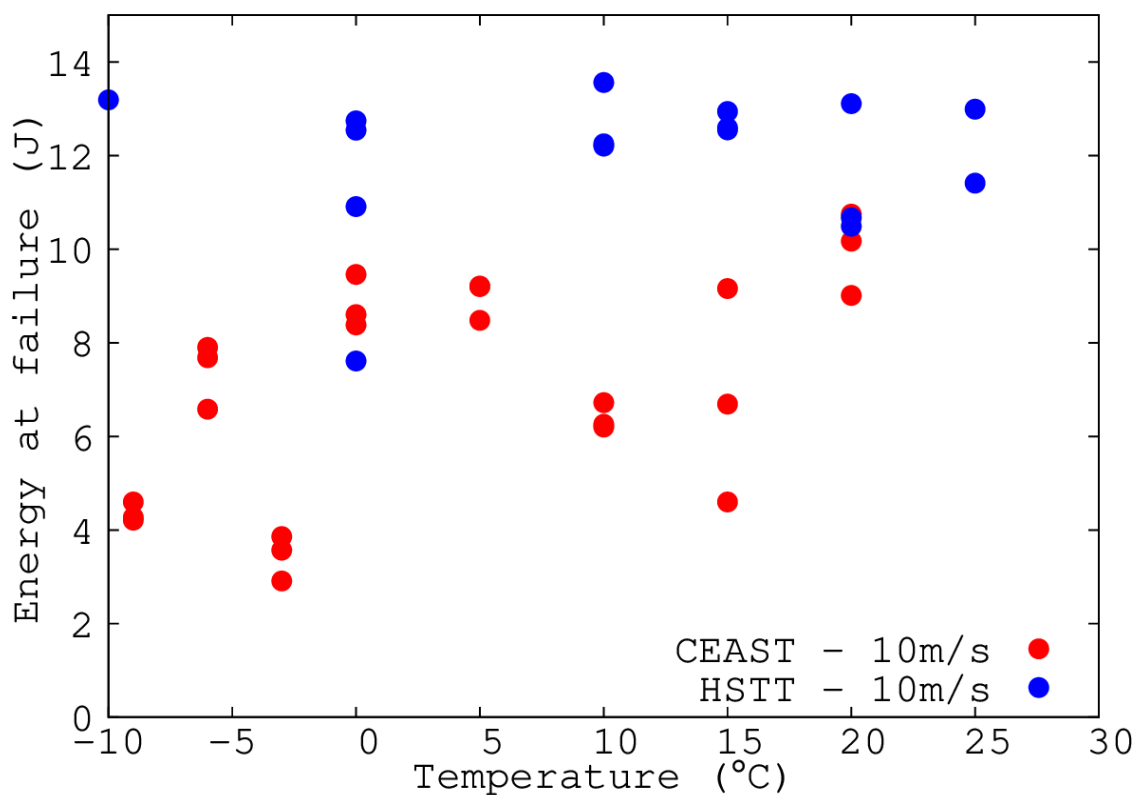


Figure 4.44: Energy at failure  $E_r$  with respect to the test temperature for HSTT and CEAST at 10 m/s

Figure 4.44 presents the evolution, as a function of the test temperature, of the energy at failure calculated with the as-recorded load and deflection at failure. A difference in the “plateau” energy is noticed with 13 J for HSTT and 9 J for the CEAST. While HSTT results seem to remain stable (probably the deflection’s increase is compensated by the load’s decrease), the CEAST’s experimental points present the S-shaped curve used to determine the  $T_{dth}$ . It is even more noticeable with Figure 4.45 where a semi-logarithmic graph is employed. Using the inflexion-point method, in a qualitative way, to determine the  $T_{dth}$ , it can be approximated to 0°C for CEAST’s results.

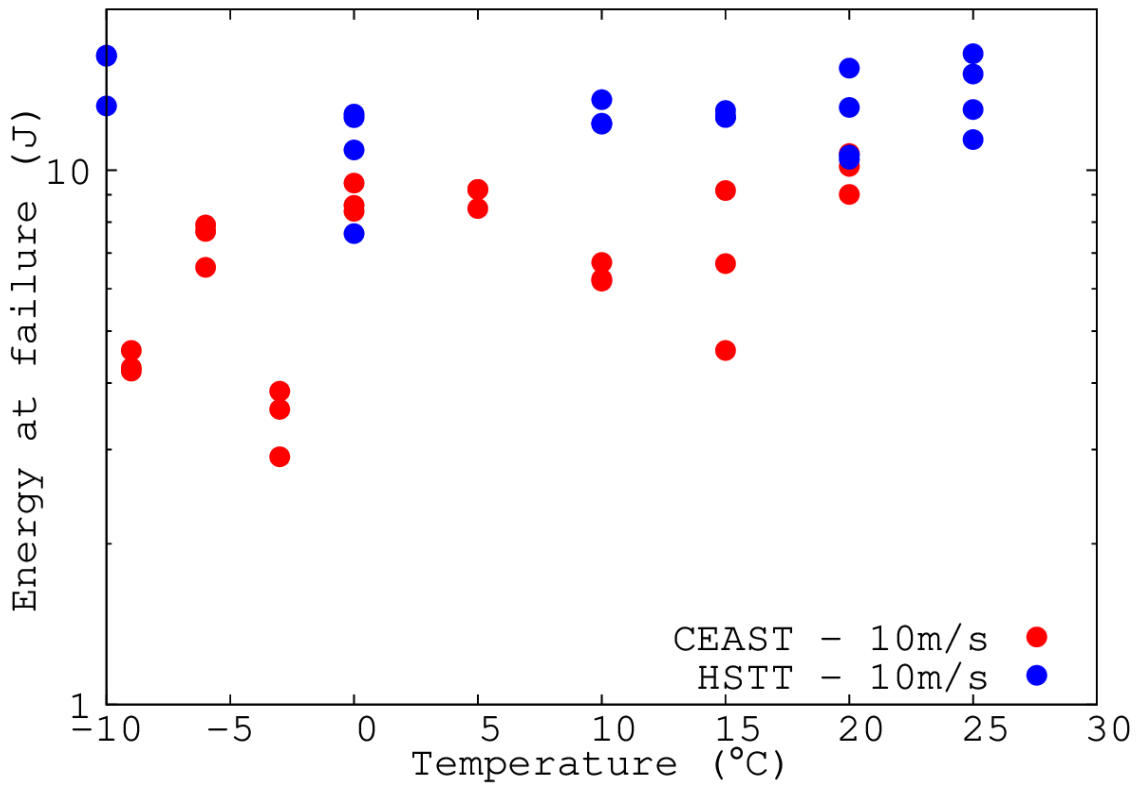


Figure 4.45:  $E_r$  versus test temperature in a semi-logarithmic scale

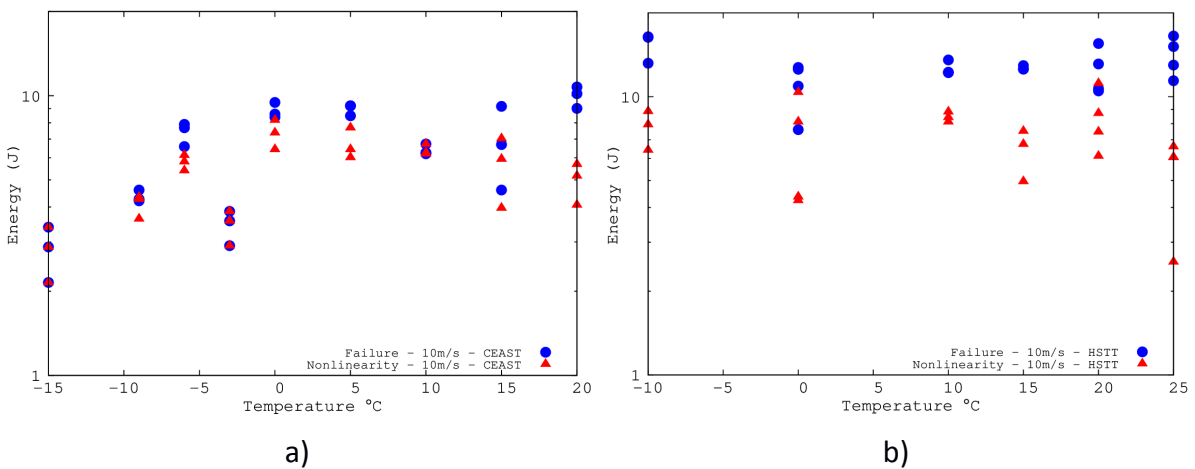


Figure 4.46: Comparison between  $E_{ni}$  (Nonlinearity) and  $E_r$  (Failure): a) CEAST ; b) HSTT.

The difference between  $E_{ni}$  and  $E_r$  for CEAST and HSTT is shown on Figure 4.46. This difference indicates how significant the nonlinear part is, before the failure.

In Figure 4.46a, displaying the CEAST results, it is noticed that both  $E_{ni}$  and  $E_r$  are identical at very low temperature ( $T \leq -10^\circ\text{C}$ ), but  $E_r$  becomes higher than  $E_{ni}$  with an increasing temperature. By ignoring results at  $-3^\circ\text{C}$  and  $10^\circ\text{C}$ , the difference in the two energies increases with the temperature.

For HSTT (Figure 4.46b), the two energies were systematically different. This means that significant nonlinearity appeared in the load versus deflection curve whatever the test temperature. This partly justified the positive shift of the temperature for HSTT tests' results. Indeed, results at  $-10^{\circ}\text{C}$  shows that the material is ductile. For unscored samples,  $E_r$  was considered as the energy at failure.

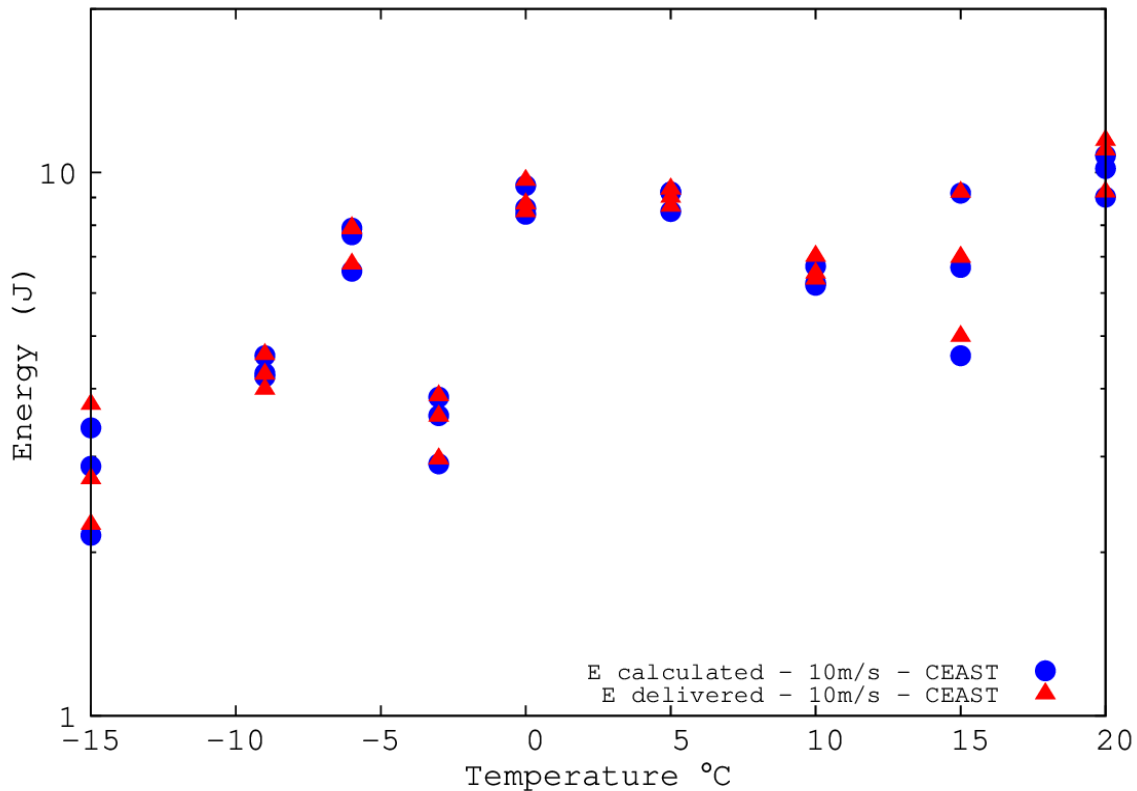


Figure 4.47: Comparison of the energy at failure delivered by the CEAST software with that calculated by integrating the area under the load versus deflection curve

Slight difference was observed between the two energies, delivered by the CEAST software with that calculated by integrating the area under the load versus deflection curve, in Figure 4.47, the most significant being at  $-15^{\circ}\text{C}$ . Therefore the energy at failure given by the CEAST software can be used for comparative material performance purposes.

#### 4.2.2. Determination of the ductile fracture threshold temperature ( $T_{\text{dth}}$ ), comparison between CEAST and HSTT at 10 m/s

The same procedure using *tanh* function was applied on the  $E_r$  curves from Figure 4.45.

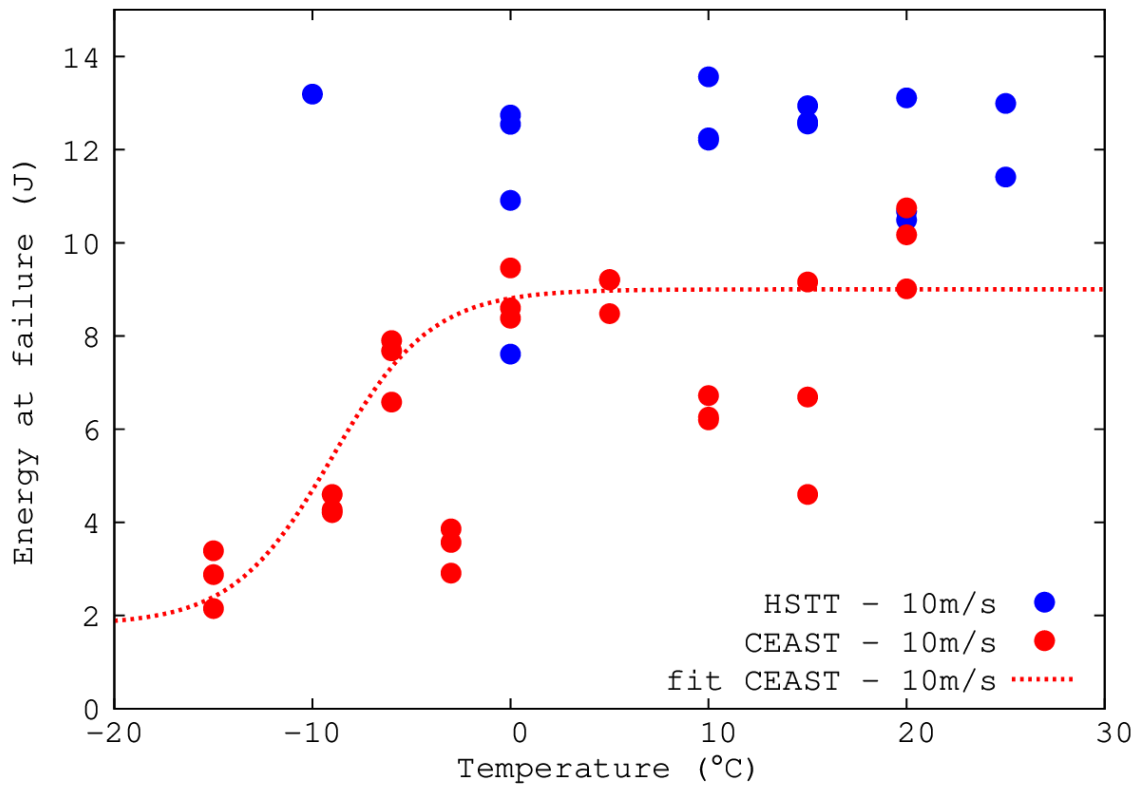


Figure 4.48 : Experimental points from HSTT and CEAST (fig.4.46) compared with fitting  $\tanh$  function.

The transition temperature  $T_{dth}$  was directly determined by optimization, using the  $\tanh$  function (eq. (4.6)). For unscored samples tested at 10 m/s on the CEAST testing machine gives a  $T_{dth} = -3^\circ\text{C}$ .

There are not enough points on HSTT for good information, but around  $0^\circ\text{C}$  the points seem to start decreasing. If the point at  $-10^\circ\text{C}$  is ignored, it is possible to imagine a  $T_{dth}$  around  $-3^\circ\text{C}$  as well (also by knowing that for scored materials CEAST and HSTT showed the same  $T_{dth}$ ), as shown on Figure 4.49 and table 4.5.

Instrument	$E_D$	$\Delta E$	$\Delta T$	$T_{dth}$
CEAST	9.2	6.9	9.5	-2.9
HSTT	12.2	6.9	10.5	-2.9

Table 4.6: Coefficients used to parameter the  $\tanh$  function for 10 m/s's unscored curves

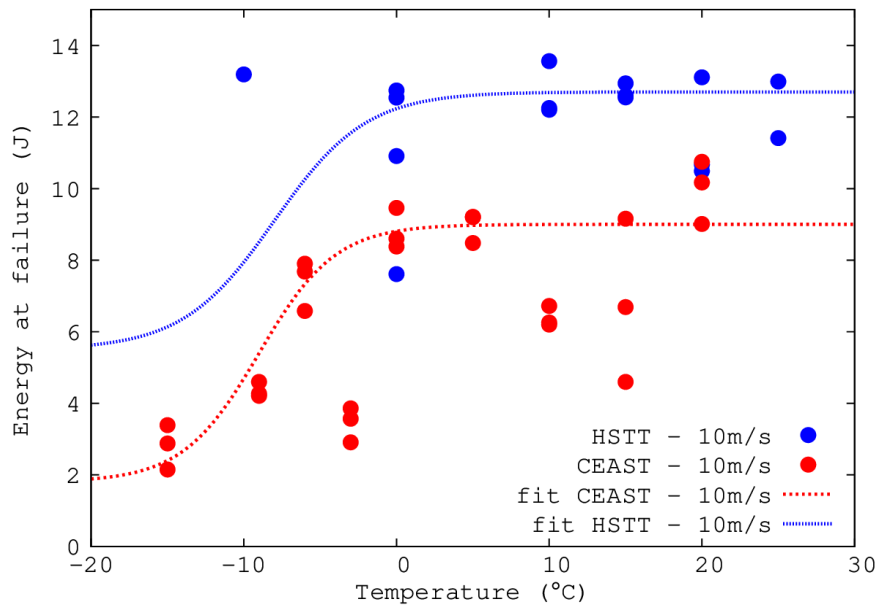


Figure 4.49 : Experimental points from HSTT and CEAST (fig.4.45) compared with fitting *tanh* function, extrapolation for the HSTT curve.

### 4.2.3. Extension to other impact speeds lower than 10 m/s from CEAST

The structure of this subsection will follow the same as that of subsection 4.1.4 related to data for unscored samples.

#### 4.2.3.1. Instantaneous impact speeds at failure

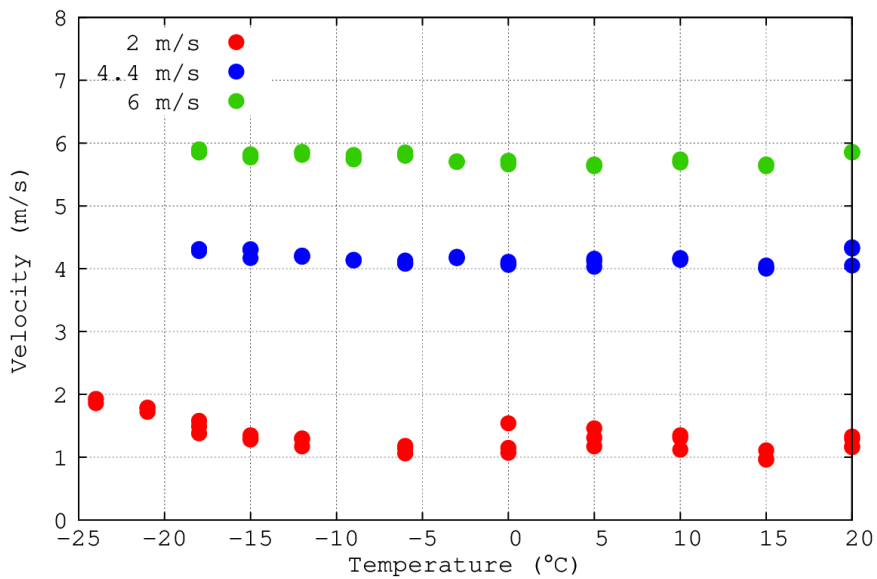


Figure 4.49: Instantaneous impact speed at failure on CEAST tests at prescribed velocities of 2 m/s, 4.4 m/s and 6 m/s

Figure 4.49 illustrates the velocity at failure for the three prescribed impact speeds. The velocities given by CEAST software are systematically underestimated in comparison with the prescribed ones. It is due mostly to the nature of the test (falling object). In comparison with the scored tests, the impact speeds are decreasing even more. Without the scoring, the stress is not concentrated at the tip of the crack anymore, and the thickness is greater. It allows the material to absorb more energy before the failure, thus it has a greater impact on the impact speed decreasing as seen in the 2 m/s tests.

#### 4.2.3.2. Stiffnesses

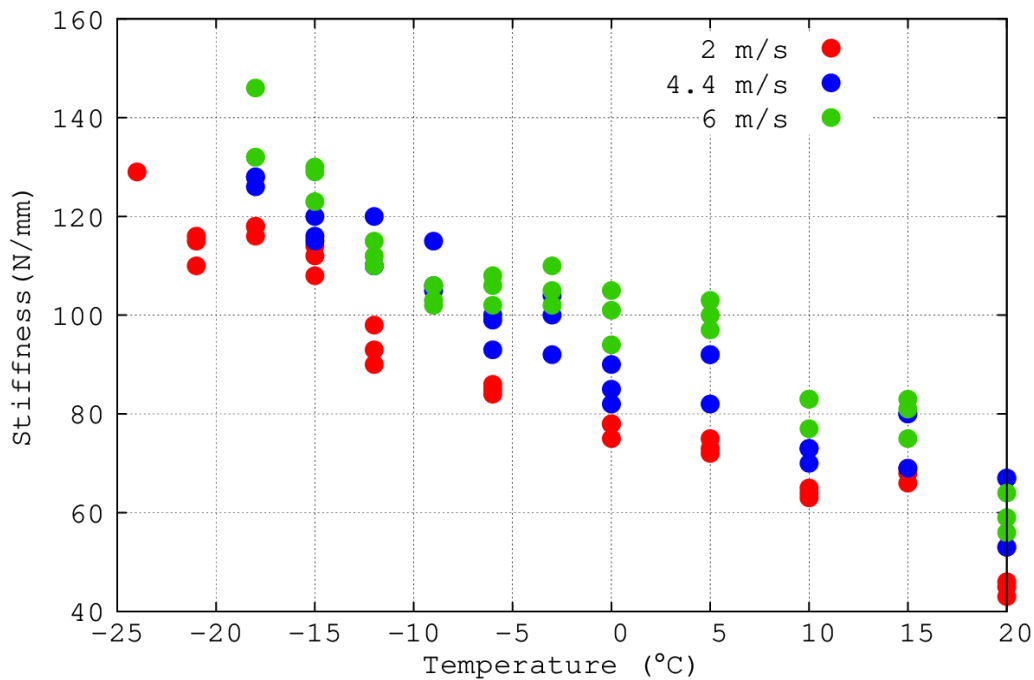


Figure 4.50: Stiffness on CEAST tests at prescribed velocities of 2 m/s, 4.4 m/s and 6 m/s

In Figure 4.50 the stiffness with respect to the test temperature for the three prescribed impact speeds (2 m/s, 4.4 m/s and 6 m/s) are shown. As expected, it shows a continuous decrease of the stiffness with the temperature; moreover, the lower the impact speed, the lower the stiffness. In comparison with scored samples' data, the values presented in Figure 4.50 are higher.

#### 4.2.3.3. Deflection at failure

Figure 4.51 depicts the deflections at failure with respect to the test temperature for the three prescribed impact speeds. As seen with the 10 m/s curves (Figure 4.42), the deflection at failure increases continuously with the temperature. Perceptible S-shape curves followed by an increase at high temperature (heat build-up suspected) are shown. At the same temperature, the lower the impact speed, the higher the deflection at failure.

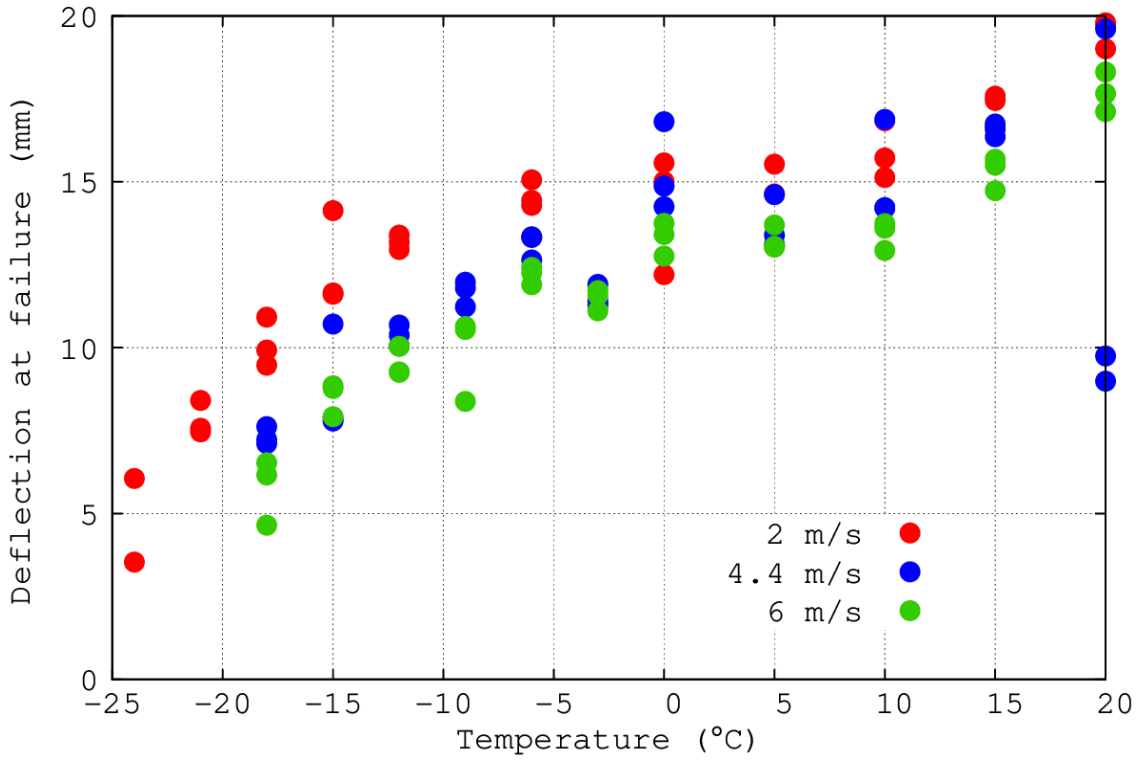


Figure 4.51 : Deflection at failure on CEAST tests at prescribed velocities of 2 m/s, 4.4 m/s and 6 m/s

#### 4.2.3.4. Load at failure

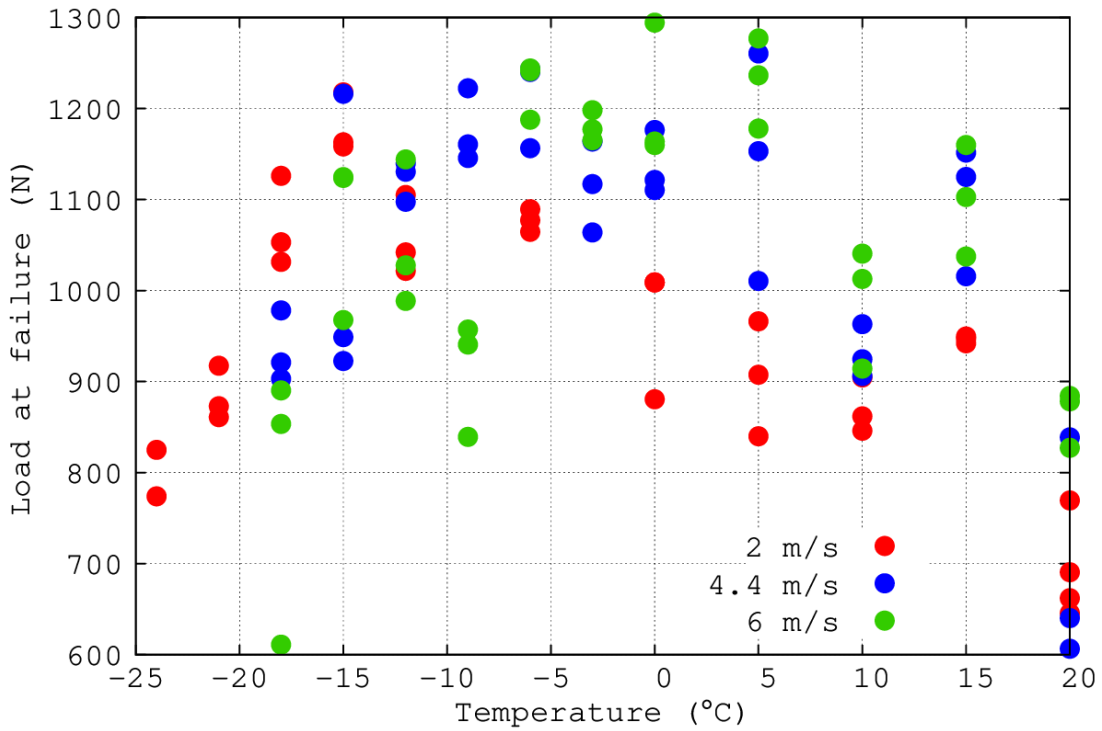


Figure 4.52: Load at failure on CEAST tests at prescribed velocities of 2 m/s, 4.4 m/s and 6 m/s

Figure 4.52 plots the loads at failure as a function of the test temperature for the three prescribed impact speeds. The curves are shaped like an inverted parabola with a large scatter. At low temperature it is noticeable that the lower the impact speed, the higher the load at failure. Meanwhile, at high temperature: the lower the impact speed, the lower the load at failure. In other words, the curves are shifting to the right.

For low temperature, it was noticed that for each impact speed the results present a high stiffness with low deflection at failure and low load at failure, the characteristics of stiffening and embrittlement. Meanwhile, at high temperature, the experimental points show a low stiffness with high deflection at failure and low load at failure associated with an increase in softening and ductility (toughening).

#### 4.2.3.5. Energy at failure

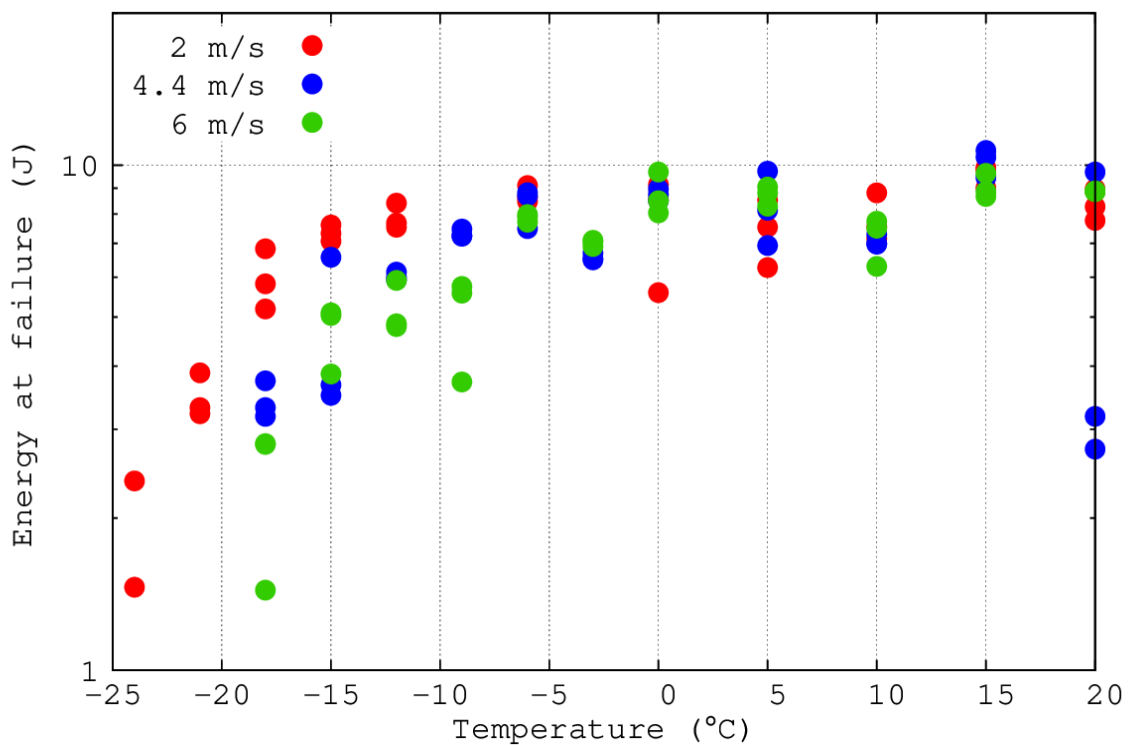


Figure 4.53: Energy at failure on CEAST tests at prescribed velocities of 2 m/s, 4.4 m/s and 6 m/s

In Figure 4.53 the energy at failure is plotted with respect to the test temperature for the three prescribed impact speeds, in a semi-logarithmic graph. It presents key curves used to determine the  $T_{dth}$ . The curves display a continuous increase of the energy at failure with the temperature and the trend is the combination of that of the deflection and load at failure. The upper shelf energy is close for the three impact speeds, between 8 J and 9 J. In terms of the energy at failure, the lower shelf seems not to be reached. But, at negative temperatures, the lower the impact speed, the higher the energy at failure.

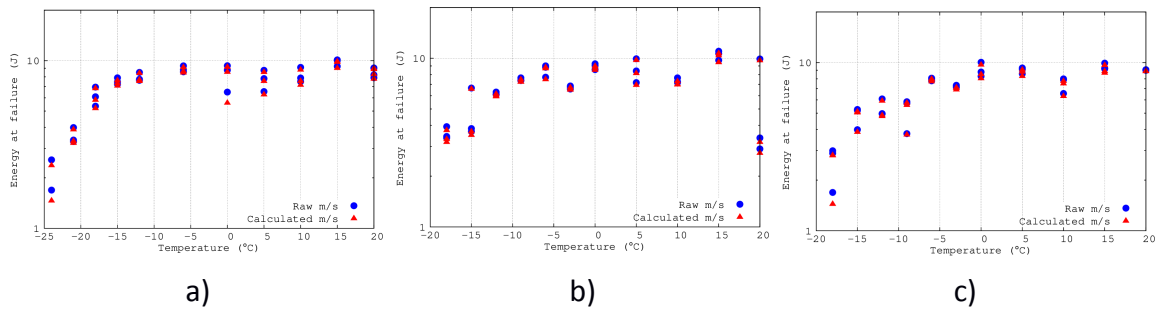


Figure 4.54: Comparison of the energies at failure on CEAST tests at prescribed velocities of 2 m/s, 4.4 m/s and 6 m/s

For CEAST tests a comparison between the energy at failure given by the software (without correction) and that integrating the area under the corrected load versus deflection curve is required. Figure 4.54 illustrates this comparison at the three prescribed impact speeds. In the domain of interest (upper shelf / ductile plateau) the difference is slight. As a consequence, the values delivered by the CEAST testing machine can be used.

The temperature of the starting of the plateau (called earlier the inflexion point method) shows  $T_{dth}$  equals to  $-15^{\circ}\text{C}$  at 2 m/s;  $-5^{\circ}\text{C}$  at 4.4 m/s and  $-3^{\circ}\text{C}$  at 6 m/s. Recall for 10 m/s the  $T_{dth}$  is evaluated at  $-3^{\circ}\text{C}$  by the *tanh* function.

#### 4.2.3.6. Evolution of $T_{dth}$ with the impact speeds for unscored specimens

##### 4.2.3.6.1. Plot of the *tanh* function

Following the same procedure as in subsection 4.2.2.7, Figure 4.55 plots the fitted *tanh* function representing the evolution of the energy at failure with the temperature for all impact speeds applied to the CEAST testing machine. The optimization procedure allowed the following results to be established. After the transition zone, for higher temperatures, the ductile plateau is observed. For impact speeds of 2 m/s and 6 m/s this plateau has a value 8.3 J, but for 4.4 m/s and 10 m/s it reaches 9.3 J. The parameters used for the *tanh* function are displayed in table 4.7.

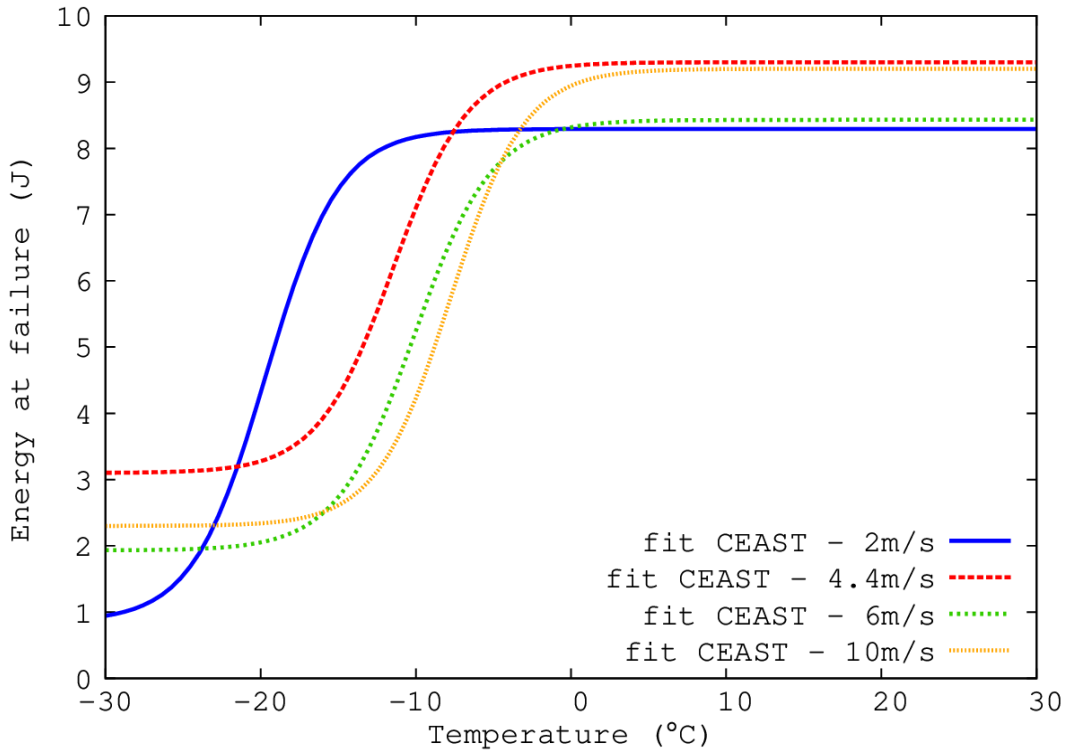


Figure 4.55 : Fitted energy at failure as a function of the temperature for every impact speeds

Impact speed (m/s)	$E_D$	$\Delta E$	$\Delta T$	$T_{dth}$	Guessed $T_{dth}$ (+/- 2°C)
2	8.3	7.4	9.4	-15	-15
4.4	9.3	6.2	9.7	-6.6	-5
6	8.4	6.5	11.1	-5.1	-3
10	9.2	6.9	9.5	-2.9	-3

Table 4.7: Coefficients used to parameter the *tanh* function for HSTT's curves

#### 4.2.3.6.2. $T_{dth}$ determination

Now that the threshold temperature ( $T_{dth}$ ) ensuring the ductile fracture is determined for all impact speed conditions with unscored samples using CEAST testing machine (4.1.2.5), its evolution can be studied, see Figure 4.56.  $T_{dth}$  value starts from -15°C for an impact speed of 2 m/s to reach -3°C at 10 m/s. The  $T_{dth}$  is also increasing with unscored samples, but contrary to the scored specimens, it does not seem to be linear.

It is also interesting to notice that the inflexion point method with the observation of the deflection and load curves shows  $T_{dth}$  with a slight error in comparison with the *tanh* function.

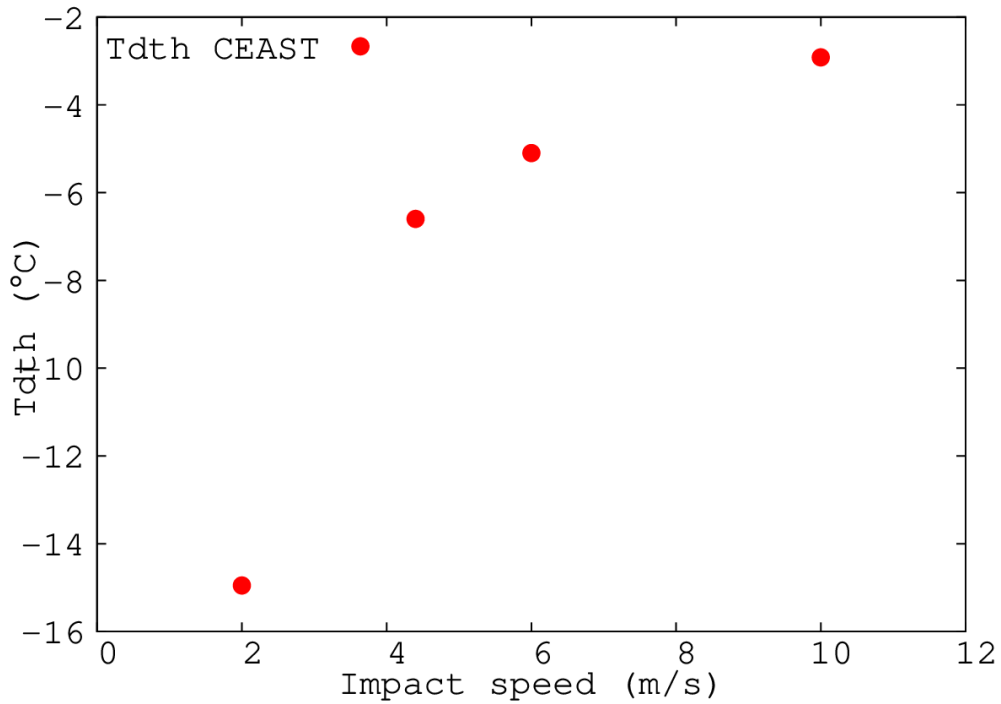


Figure 4.56 : Evolution of the  $T_{dth}$  with respect to the prescribed impact speed for scored skins

#### 4.2.4. Extension to impact speeds higher than 10 m/s from HSTT

##### 4.2.4.1. Instantaneous impact speeds at failure

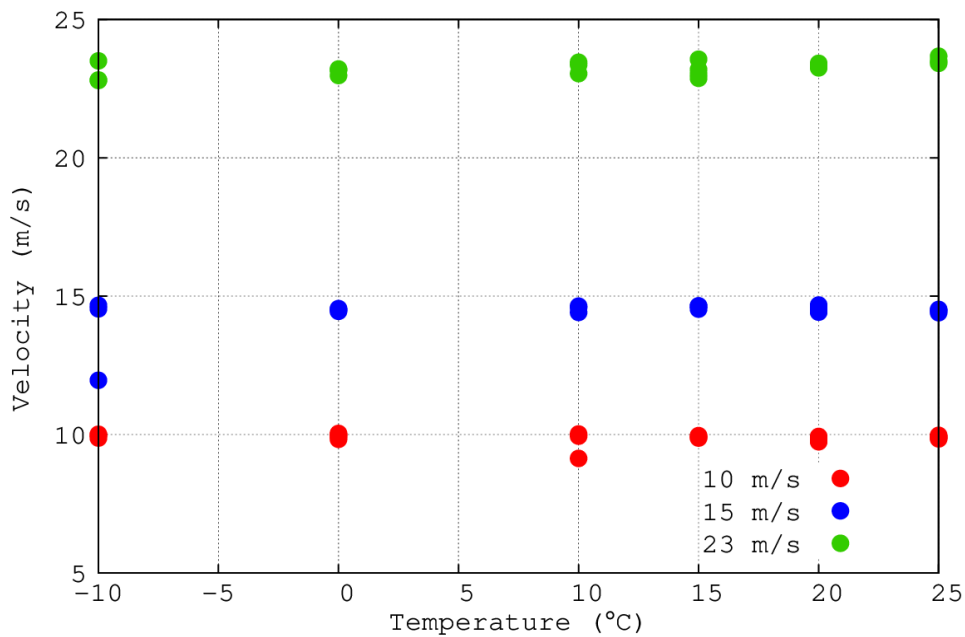


Figure 4.57: Instantaneous impact speed at failure on HSTT tests at prescribed velocities of 10 m/s, 15 m/s and 23 m/s

Figure 4.57 illustrates the velocity at failure for the already presented 10 m/s and the two other prescribed impact speeds of 15 m/s and 23 m/s. The recorded velocities at failure correspond to the prescribed ones. Only one abnormal point is observed at 15 m/s and -10°C, which are lower than the others. The experimental points will be ignored.

#### 4.2.4.2. Stiffnesses

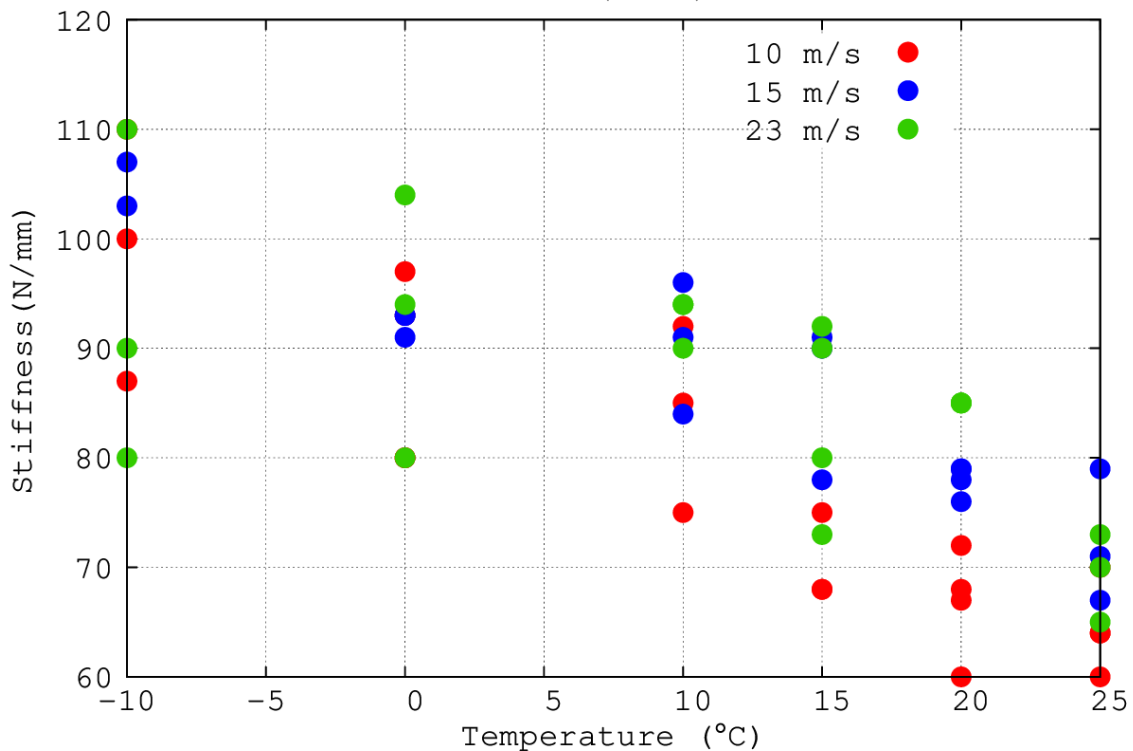


Figure 4.58 : Stiffness on HSTT tests at prescribed velocities of 10 m/s, 15 m/s and 23 m/s

In Figure 4.58 the stiffness with respect to the test temperature for the three prescribed impact speeds are shown. A change in the slope, i.e. inflexion point, is observed between 0°C and 10°C with a small slope from -10°C to 0°C and a steeper slope from 10°C to higher test temperatures. For temperatures higher than 10°C: the lower the impact speed, the lower the stiffness. As aforementioned, the abnormal point at 15 m/s and -10°C was ignored.

#### 4.2.4.3. Deflection at failure

Figure 4.59 depicts the deflections at failure with respect to the test temperature for the three prescribed impact speeds. A continuous increase of the deflection at failure with the temperature was noticed, with a change of the slope between 0°C and 10°C. The experimental points are highly scattered but it seems that the lower the impact speed, the higher the deflection at failure



Figure 4.60 plots the loads at failure as a function of the test temperature for the three prescribed impact speeds. A continuous decrease of the load at failure with the temperature is observed. The slope seems to change between 0°C and 10°C for the curves. At the same temperature, all the data are scattered but it seems that the lower the impact speed, the lower the load at failure.

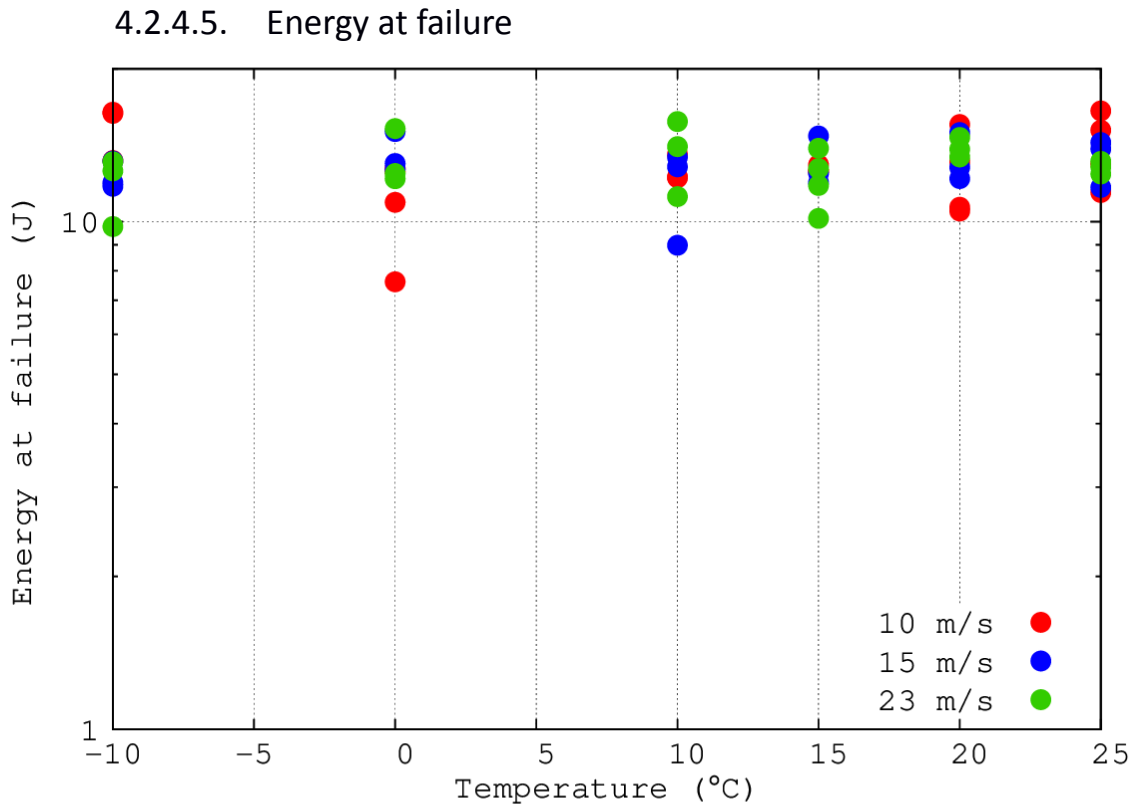


Figure 4.61: Energy at failure on HSTT tests at prescribed velocities of 10 m/s, 15 m/s and 23 m/s

In Figure 4.61 the energy at failure is plotted with respect to the test temperature for the three prescribed impact speeds, in a semi-logarithmic graph. A scattered but stabilized value of the energy (~12 J), whatever the temperature and the impact speed, is shown. The decrease in the load at failure is compensated by the increase in deflection at failure. It results that the energy at failure is not relevant to identify  $T_{dth}$ . The last solution to determine a  $T_{dth}$  is to display either the deflection at failure or the load at failure to determine  $T_{dth}$  with respect to the impact speed: the “inflexion point” method.

#### 4.2.4.6. Evolution of $T_{dth}$ with the impact speeds for scored specimens

##### 4.2.4.6.1. Using separate deflection at failure curves

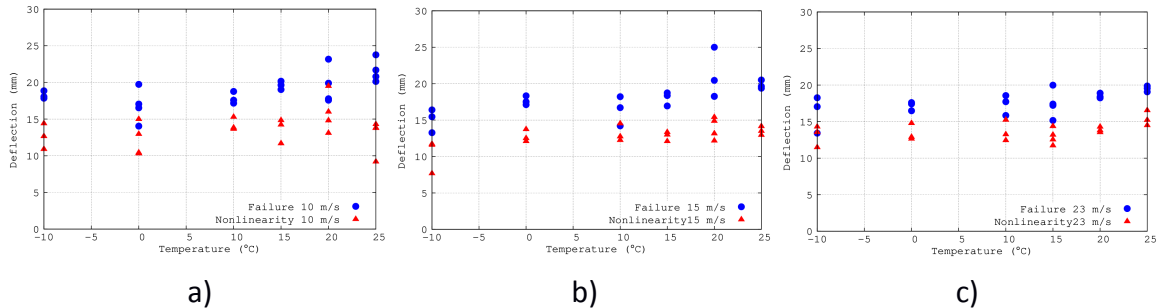


Figure 4.62 : Deflections versus test temperature for HSTT tests at : a) 10 m/s ; b) 15 m/s ; 23 m/s

In fig. 4.62, the deflections  $d(F_{nl})$  and  $d(F_r)$  are plotted with respect to the test temperature at the three imposed impact speeds on the HSTT testing machine. Firstly, it is noticeable that the  $d(F_{nl})$  is always lower than  $d(F_r)$  (significant nonlinearity), but focus is put on  $d(F_r)$ .

Recall that for the CEAST test at 10 m/s, the temperature at the beginning of the ductile plateau (increase of the deflection at failure) was equal to  $-3^{\circ}\text{C}$ . In Figure 4.62a, it can be assumed that the variation starts at  $0^{\circ}\text{C}$  meaning an error of  $3^{\circ}\text{C}$ . It can be judged as acceptable since the points are extremely scattered and no other solution was found. With the same method, in Figure. 4.62b a variation around  $10^{\circ}\text{C}$ , and in Figure 4.62c around  $15^{\circ}\text{C}$  were assumed. Even with these scattered data points, additional temperature tested at  $5^{\circ}\text{C}$  would have been interesting.

##### 4.2.4.6.2. Using separate load at failure curves

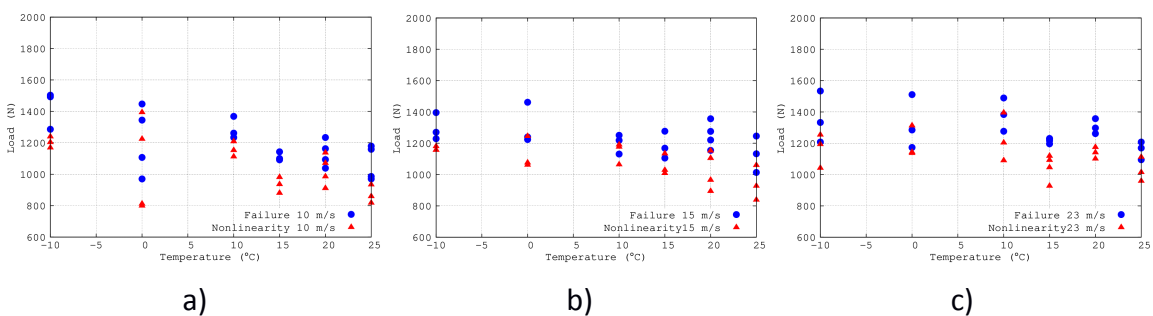


Figure 4.63 : Loads versus test temperature for HSTT tests at : a) 10 m/s ; b) 15 m/s ; 23 m/s

Figure 4.63 displays the loads  $F_{nl}$  and  $F_r$  as a function of the test temperature at the three imposed impact speeds on the HSTT testing machine. The load at nonlinearity  $F_{nl}$  being lower than  $F_r$  means a significant nonlinearity. The focus is set on  $F_r$ . Recall that for the CEAST test at 10 m/s, the temperature at the beginning of the ductile plateau (decrease of the load at failure) was equal to  $-3^{\circ}\text{C}$ . In Figure 4.63a, it can be assumed that the variation starts at  $0^{\circ}\text{C}$  meaning an error of  $3^{\circ}\text{C}$ . It can be judged as acceptable since the points are extremely

scattered and no other solution was found. With the same method, in Figure 4.63b a variation around 0°C, and in Figure 4.63c around 10°C were assumed. Even with these scattered data points, additional temperature tested at 5°C would have been interesting.

Impact speed (m/s)	10	15	23
T <sub>dth</sub> from Deflection (°C)	0	10	15
T <sub>dth</sub> from Load (°C)	0	0	10

Table 4.8: T<sub>dth</sub> determined using the “inflexion point” method on the deflection and load curves

Because the energy at failure seems stable with the temperature for the three impact speeds investigated, it did not allow the determination of the T<sub>dth</sub>. For the previous variables: the deflection at failure and the load at failure, the results obtained with the HSTT for unscored samples presented a higher dispersion than observed on scored samples or unscored with CEAST. Using the inflexion point method to determine a T<sub>dth</sub> is also complicated as the points are scattered, but an attempt was made and the results are displayed on the table 4.8. Additional tests at a temperature between 0°C and 10°C (where all variations seem to appear) would have been appropriate.

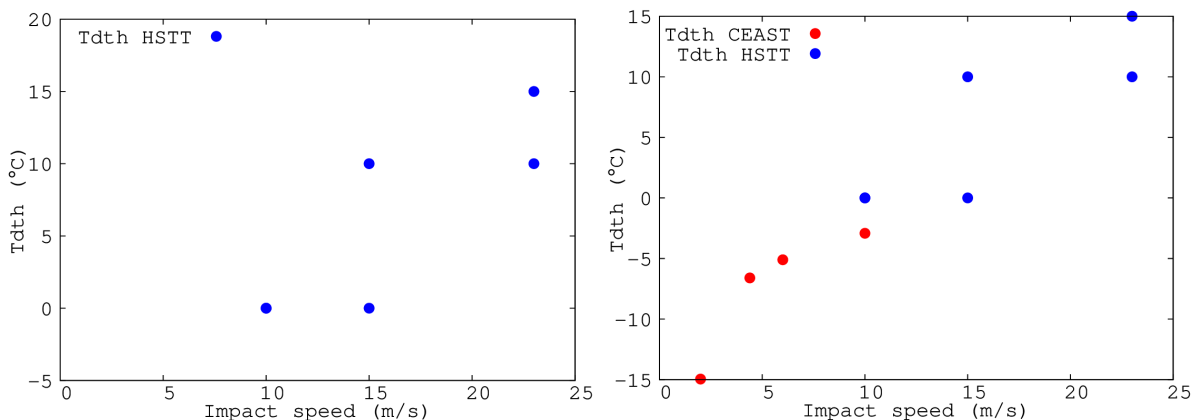


Figure 4.65: Evolution of the T<sub>dth</sub> with respect to the prescribed impact speed for scored skins  
a) HSTT only b) CEAST and HSTT

The Figure 4.65b gathered the T<sub>dth</sub> collected from CEAST and HSTT testing machines. Reminder: the data obtained with the HSTT were not collected using the *tanh* function as usual. As the experimental points were scattered it was also complex to determine the T<sub>dth</sub> by the “inflexion point” method. An attempt was made, and the results, continuous increase in the T<sub>dth</sub>, are quite linear (even if scattered). These results can be corroborated by Figure 4.34 where a similar profile was found for scored specimens.

It shows that the T<sub>dth</sub> increases linearly no matter the instrument and specimen’s geometry.

#### 4.2.5. Fracture surfaces for unscored samples

For unscored specimens, only macroscopic observations were carried out due to the circular forms of the fractured surfaces.

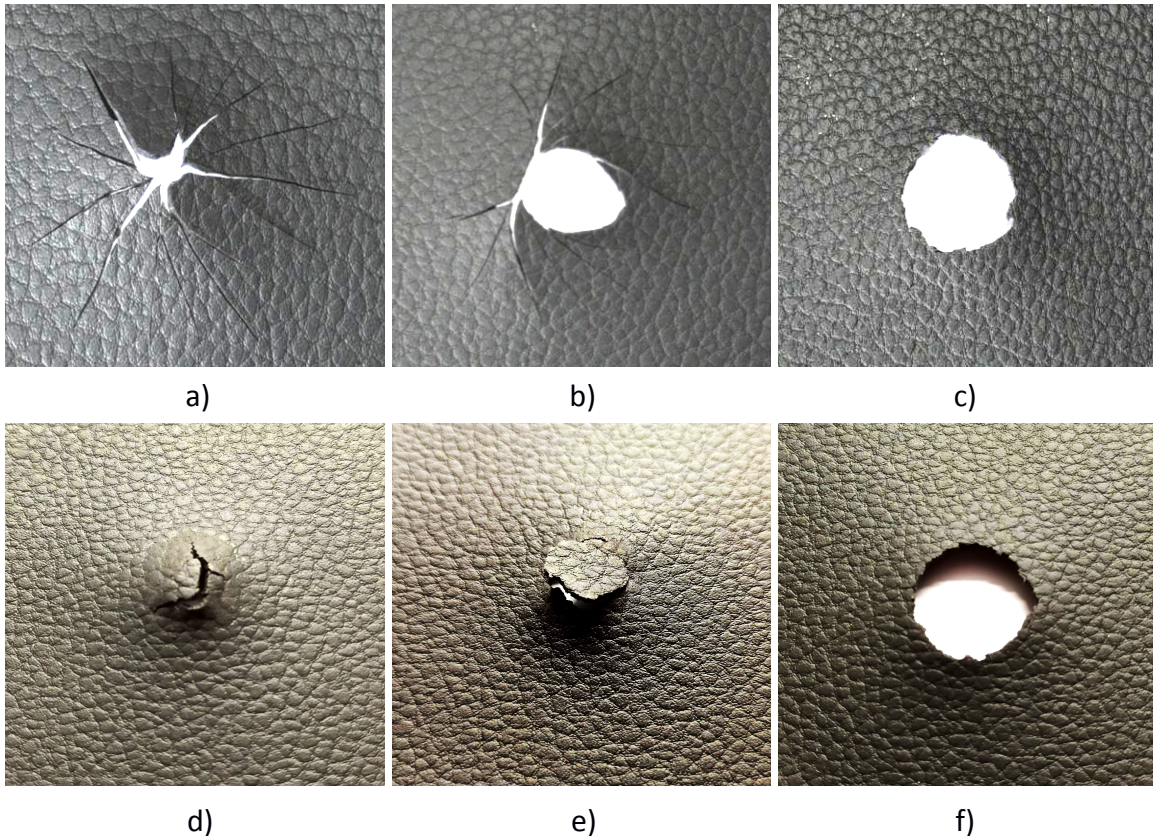


Figure 4.66: Aspect of the fracture surfaces after the impact tests on unscored samples : a) Brittle - CEAST at 4.4 m/s and  $-15^{\circ}\text{C}$  ; b) Transition - CEAST at 4.4 m/s and  $-3^{\circ}\text{C}$  ; c) Ductile - CEAST at 4.4 m/s and  $15^{\circ}\text{C}$  ; d) Brittle - HSTT at 23 m/s and  $-10^{\circ}\text{C}$  ; e) Transition - HSTT at 23 m/s and  $0^{\circ}\text{C}$  ; f) Ductile - HSTT at 23 m/s and  $25^{\circ}\text{C}$  ;

The CEAST tests seem to distinguish the three aspects of the failure (Brittle, Transition and Ductile). For HSTT's samples it is always circular. Contrary to what was observed with CEAST, the diameter of the circular failure decreases with a lower temperature, reaching a diameter of approximately 7 mm at  $-10^{\circ}\text{C}$  and 23 m/s (long after the test), when it was about 18 mm at high temperature ( $30^{\circ}\text{C}$ ). Interestingly, for all the abovementioned temperatures, the striker (reminder: striker's diameter  $d=20\text{mm}$ ) punctured and crossed it entirely.

Without the possibility to record the sample's puncture in the thermostatic chamber, only hypothesis would be applicable to understand how a 20 mm striker went through a 7 mm PVC hole. The first hypothesis would involve a local heat build-up phenomenon, already mentioned for high temperature ( $T>15^{\circ}\text{C}$ ) with the HSTT instrument. It would also explain why the results at low temperature ( $T<0^{\circ}\text{C}$ ) were so different from CEAST's.

### 4.3. $T_{dth}$ comparison between scored and unscored samples

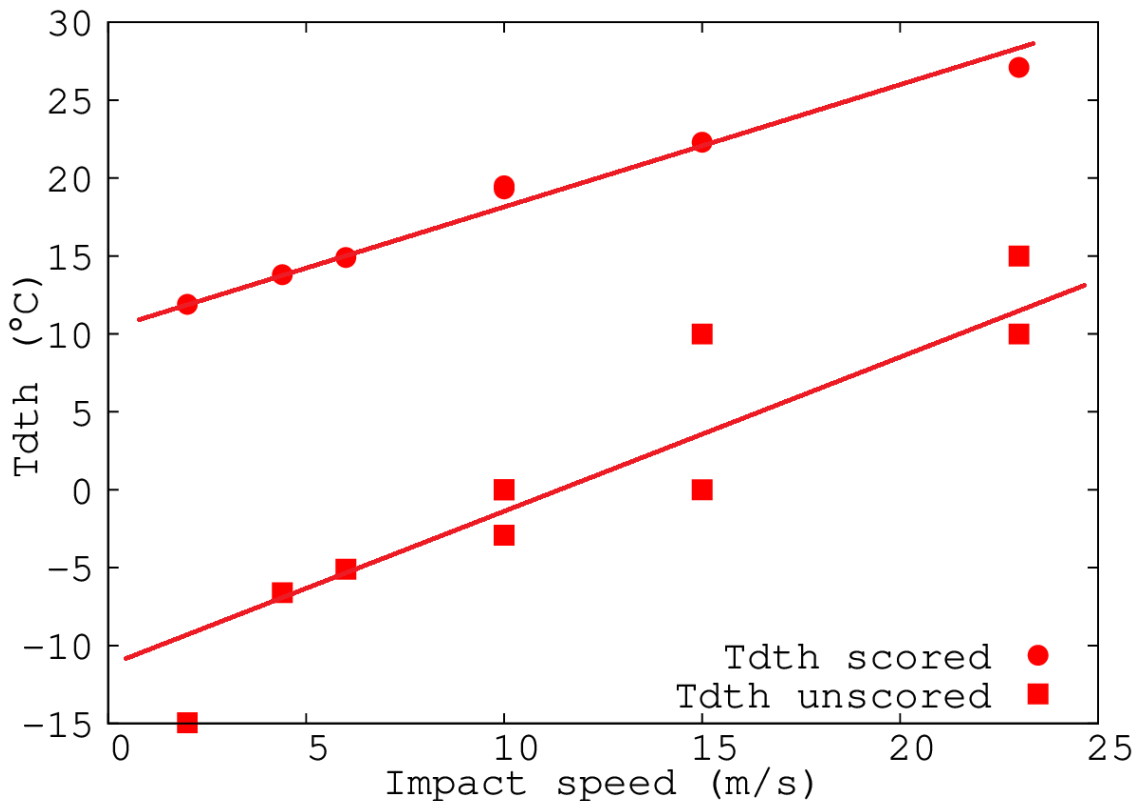


Figure 4.67: Evolution of the  $T_{dth}$  with respect to the prescribed impact speed for scored and unscored skins

The Figure 4.67 gathered the  $T_{dth}$  collected from scored and unscored samples tested on both CEAST and HSTT testing machines. It should be recalled that the data obtained for unscored specimens with the HSTT were not collected using the *tanh* function as usual but determined with the “inflexion point” method from the deflection and load curves (section 4.2.4.6.1 and 4.2.4.6.2). As the experimental points were scattered it was also complex to determine precisely the  $T_{dth}$  with this method. This is why two  $T_{dth}$  appear for impact speeds at 10 m/s, 15 m/s, and 23 m/s.

The Figure 4.67 shows that the  $T_{dth}$  increases linearly no matter the instrument and specimen’s geometry. More interestingly, the two  $T_{dth}$ ’s evolution are quite parallels. If the deviation from perfect parallelism is put into account of the scattered HSTT  $T_{dth}$  determination, it is possible to deduce the following:

- The  $T_{dth}$  evolution with the impact speed is clearly an intrinsic property of the material as both curves possess the same slope (or really close);
- The geometry of the specimens does not modify the curve’s slope, but only has a vertical offset. In this case, the offset seems to be about 20°C.

## 4.4. Application to another material

### 4.4.1. Introduction of the material

The second material, called material 2 (in opposition to material 1 in all the previous sections), is a PVC based skin. Like the material 1, this second material is mixed with additives such as plasticizers, pigments, etc... but in different ratios. The process, names, and ratios of the components are kept untold for the sake of industrial confidentiality (as for material 1). It is then not possible to ensure that the formulation process is similar for both materials in order to obtain the PVC powder.

The transformation method from powder into skins is quite similar for both materials: the slush molding, and is explained in section 2.1.2.1: processing and assembly methods. However, the mold's temperature might differ from one material to the other. The three layers assembly processing stays quite similar too.

In this comparison between both materials, the focus is set on the evolution of the failure performances recorded in the laboratories. It has been determined that the physico-chemical properties such as the glass transition  $T_g$  obtained by DMA (see section 2.1.2.2.4), are better, concerning the industrial requirements, for material 1 than material 2 as shown in Figure 4.68 (tests carried out in the same conditions for both). It revealed a  $T_g$  for the material 1 equal to  $-37.8^\circ\text{C}$ , and equal to  $-30.8^\circ\text{C}$  for material 2. But the first few tests from the industrial partner showed better in real-use performances from material 2. Those premises had to be tested in laboratory conditions. The  $T_{dth}$  determined from the previous sections was selected to compare them.

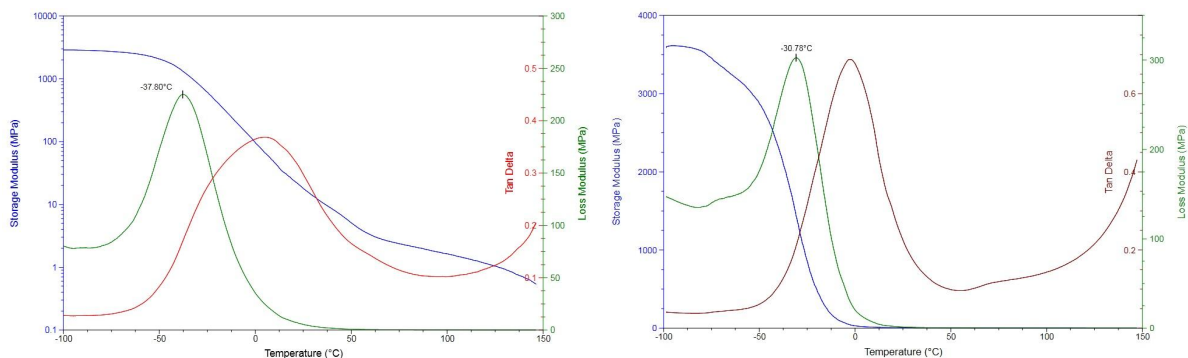


Figure 4.68: DMA results on a) material 1 ( $T_g=-37.8^\circ\text{C}$ ), b) material 2 ( $T_g=-30.8^\circ\text{C}$ )

### 4.4.2. Experimental program

The comparison between the materials 1 and 2 was only carried out on the CEAST instrument. A total of 213 impact tests were performed on material 2, 120 for unscored specimens and 93 for scored ones. The investigated impact speeds and temperatures are displayed in the tables 4.9 and 4.10 for unscored specimens and scored ones, respectively.

Total = 120		Temperatures (°C)									
		-15	-12	-9	-6	-3	0	5	10	15	20
Speed (m/s)	2	3	3	3	3	3	3	3	3	3	3
	4.4	3	3	3	3	3	3	3	3	3	3
	6	3	3	3	3	3	3	3	3	3	3
	10	3	3	3	3	3	3	3	3	3	3

Table 4.9: Test program for unscored samples on material 2

Total = 93		Temperatures (°C)							
		-6	-3	0	5	10	15	20	25
Speed (m/s)	2	3		3	3	3	3	3	3
	4.4	3	3	3	3	3	3	3	3
	6	3	3	3	3	3	3	3	3
	10	3	3	3	3	3	3	3	3

Table 4.10: Test program for scored samples on material 2

#### 4.4.3. Results

The same experiment protocol as detailed in sections 4.1.5 and 4.2.3 was conducted for material 2. It results in the obtention of the  $T_{dth}$  values for all the four impact speeds on scored samples and three for the unscored ones. The analysis was not concluding with 2 m/s as most signals were too perturbed to be treated (even with the protocol set up). The list of  $T_{dth}$  optimized with the *tanh* function is displayed on table 4.11.

Impact speed (m/s)	Tdth scored samples	Tdth unscored samples
2	6	X
4.4	8.1	1
6	11.5	3
10	13	5

Table 4.11: List of  $T_{dth}$  obtained with the corresponding geometry and impact speed for material 2

The  $T_{dth}$  listed on table 4.11 are drawn in blue on Figure 4.69. As expected from the study on material 1, the  $T_{dth}$  on both geometries are continuously increasing. It also follows the trend observed, i.e.  $T_{dth}_{scored\ samples} > T_{dth}_{unscored\ samples}$  with a constant gap of about 7.5°C.

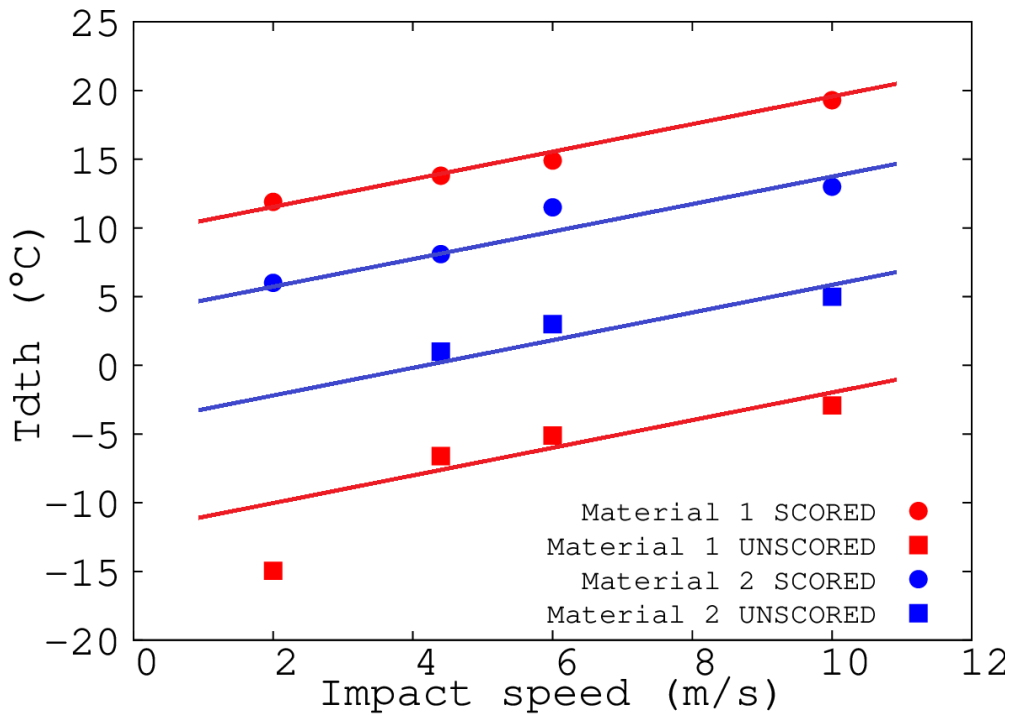


Figure 4.69: Evolution of the  $T_{dth}$  on CEAST only, with respect to the prescribed impact speed for scored and unscored skins and both materials 1 and 2

In Figure 4.69 was also added the  $T_{dth}$  of the material 1 (only determined with the CEAST). The list of  $T_{dth}$  are reminded on table 4.12. Four lines were drawn for a better representation of the  $T_{dth}$ 's evolutions. Interestingly, the four lines are parallels, involving the same increase of the  $T_{dth}$  with the impact speed, whatever the material or the geometry (it was already highlined for the geometry on section 4.3). The result at 2 m/s for the unscored material 1 was put aside of the curve. By looking at Figure 4.49, it is possible to see that the impact speed was reduced up to 50% of its initial speed. This is surely impacting the  $T_{dth}$  of this series of tests, and the reason why it was not taken into account.

Impact speed (m/s)	$T_{dth}$ scored samples	$T_{dth}$ unscored samples
2	11.9	-14.95
4.4	13.8	-6.6
6	14.9	-5.1
10	19.3	-2.92

Table 4.12: List of  $T_{dth}$  obtained with the corresponding geometry and impact speed for material 1

If the geometries are studied separately, starting with the unscored samples (as recommended by the ISO standard [16]), the  $T_{dth}$  from the material 2 is higher than material 1. It corroborates the results obtained with the DMA and the glass transition. But it is to be remembered that in fracture mechanics, materials are studied with a scoring, which is also the geometry in the material's real-use conditions. Unlike the previous statement (with DMA and unscored samples), the performances are inverted. The  $T_{dth}$  for material 1 is higher than the  $T_{dth}$  from material 2. It is mostly due to the difference of gap between unscored/scored samples which is 20°C for material 1 and 7.5°C for material 2. This contradicts the results obtained by the DMA

## 4.5. Conclusions

From the chapter 4, on the impact tests, it can be concluded that:

- $E_{nl}$  was used to determine  $T_{dth}$  for scored specimens meanwhile  $E_r$  was used for unscored ones ;
- The *tanh* function on energies ( $E_{nl}$  or  $E_r$ ) is useful to optimize the identification of  $T_{dth}$ , but it is also possible to approximate it with the different inflections observed on deflection, load or energy's curves (and sometimes it is the only way: section 4.2.4.6)
- The  $T_{dth}$  is always increasing with the impact speed ;
- Some peculiar increases were spotted with HSTT at high speeds: it was put on the account of build-up heat of the specimen ;
- The  $T_{dth}$ 's slope is identical no matter the differences in formulation (at least for the two PVCs studied) ;
- The difference in geometry (scoring or no scoring), influences only with a vertical shift of the  $T_{dth}$  for a specified impact speed, with the scoring increasing the  $T_{dth}$  ;
- With the same geometry, two different PVCs won't have the same level of  $T_{dth}$  ;
- The impact of the geometry on the  $T_{dth}$  will differ with the formulation of PVC. It can then alter the performance ranking of the studied PVC (section 4.4.3) ;
- For the use of scored materials the glass transition is not sufficient to characterize and compare the materials as the weakening, concerning the score, impacts the materials differently.

## CHAP 5: Conclusion

Les travaux présentés dans ce document ont pour objectif de mieux comprendre les différents paramètres pouvant influencer sur la transition ductile fragile des peaux en PVCs utilisées dans l'industrie automobile. Alors que la caractérisation de ces matériaux se limite généralement à des mesures de température de transition vitreuse, une approche basée sur la température seuil de rupture ductile  $T_{dth}$  (une variante de la Température de transition ductile-fragile DBTT) est proposée dans ce document.

Une première analyse des mécanismes de rupture ductile des échantillons pré-entaillés a été menée. Elle a consisté en l'étude des concepts de la mécanique de la rupture que sont le paramètre de chargement et le critère de rupture, au travers de résistance au choc ( $\Gamma_c$ ) et la ténacité ( $J_c$ ) du matériau. En réalisant des essais sur éprouvettes de flexion à trois point encastées et des simulations par éléments finis avec fissure propageante et des calculs de l'intégrale  $J$ , il a été possible de déterminer certains paramètres notamment le facteur de calibration  $\eta_p$  permettant un calcul analytique de  $J_c$  afin de déduire la ténacité du PVC plastifié étudié. Cette étude a aussi et surtout permis d'observer que l'amorçage de la rupture ductile correspond à la déviation par rapport à la linéarité de la courbe Force-flexion. Consécutivement, la fissure se propage à travers le ligament restant.

Les essais d'impact ont, eux, permis de montrer une évolution continue et linéaire de la  $T_{dth}$ , en fonction de la vitesse d'impact. En observant son évolution, il a été possible d'établir que la pente n'était pas dépendante de la géométrie, ni de la formulation (au moins pour les deux PVCs étudiés). Il faut cependant noter que ces paramètres ont un impact sur la valeur de la  $T_{dth}$  pour une même vitesse d'impact: les éprouvettes entaillées possèdent une  $T_{dth}$  plus élevée que les éprouvettes non-entaillées, et pour une même géométrie deux formulations n'auront pas la même  $T_{dth}$ . Par ailleurs l'écart entre la  $T_{dth}$  pour une éprouvette entaillée et non-entaillée varie d'une formulation à une autre. En effet, il est montré dans cette étude que le matériau 1 est plus performant lorsque l'échantillon est non-entaillé, alors que le matériau 2 est plus performant avec la géométrie entaillée (sa condition d'utilisation réelle). Cette notion n'est pas du tout observable grâce à la  $T_g$ .

Enfin, plusieurs pistes ont été explorées afin de proposer de nouvelles perspectives d'études dans le but d'approfondir les connaissances sur ce matériau. Alors que cette thèse s'est concentrée sur l'étude de la couche supérieure de l'ensemble composant le tableau de bord, une étude sur la propagation des entailles dans ces trois couches via des essais de flexion quatre points pourrait permettre la compréhension de l'interaction entre les trois matériaux, lors d'un tir airbags en conditions réelles. Puis une étude de stéréo-corrélation lors de tirs airbags permettrait de déterminer un bon nombre de paramètres encore mal connus, comme la vitesse de déformation de la peau en PVC. Couplée avec une analyse thermique pour mesurer un potentiel auto-échauffement, ces informations enrichiraient fortement les connaissances actuelles des matériaux étudiés lors de la thèse. Pour terminer, une étude plus approfondie des simulations par éléments finis sur les essais d'impact permettrait à terme de pouvoir prédire le comportement des peaux en PVC à partir d'un set de données.

## 5. Conclusion and prospects

### 5.1. Conclusion

The work presented in this document aims at proposing a new way of characterizing impact tests on thin and flexible polymer materials (i.e. skins). This new approach was based on a rich experimental database obtained thanks to a collaboration between Westlake/NAKAN, the industrial partner and the Centre des Matériaux (Materials Center). In order to improve the comparison method between PVC skins, initially performed with the glass transition temperature ( $T_g$ ), impact tests were carried out allowing the Ductile to Brittle Transition Temperature (DBTT) transformed into the Ductile Failure Threshold Temperature ( $T_{dth}$ ) to be investigated.

The ISO standard 6603-2 was the initial reference to this kind of study. But it only concerns unscored rigid samples. As the materials are scored in their real-use conditions, and the ductile failure on dashboards is the major concern of the industry of automotive, the usual DBTT was twisted to evolve into the ductile failure threshold temperature ( $T_{dth}$ ). However, this  $T_{dth}$  must comply with the fact that it should be studied on unscored as well as scored specimens. That's why the failure mechanisms had to be studied.

The first topic discussed was to understand the failure mechanisms of scored skins. In chapter 3, this phenomenon was tested with adapted "clamped" SENB tests recorded with a video camera. The need to adapt the standard SENB test involved a variation in the characterization method used, and the value  $\eta$  had to be redefined.

The second part concerns the performing of impact tests carried out on CEAST and HSTT for a wide range of temperatures and impact speeds. The samples impacted were designed to present a scoring on half of the scope while the rest were kept unscored.

#### 5.1.1. Failure mechanisms

Dedicated clamped SENB specimens were used to characterize the mechanisms of ductile crack initiation and propagation for the studied material. In contrast to the route recommended by nonlinear fracture mechanics, the crack initiation occurred before the maximum load prior to the final failure of the specimen. In fact, it was observed when the loss of linearity in the load vs. COD appeared. Thanks to the "release nodal degree of freedom" procedure the in-house FE code allowed the simulation of the crack extension to be performed. The calibration factor of the clamped SENB specimen with respect to the crack depth ratio was established. Moreover, the fracture toughness  $J_c$ , defined as the numerical J-integral at the crack initiation, was evaluated to be  $10.8 \text{ kJ/m}^2$ , in agreement with values reported in the literature.

Focusing on the crack initiation, the corresponding impact strength for the previous drop tower tests in the upper shelf was corrected. Instead of the previous  $0.25 \text{ kJ/m}^2$  this critical value was reduced to  $0.11 \text{ kJ/m}^2$ . The modified fracture toughness and the impact strength values were proposed in the methodology allowing the ductile crack initiation to be predicted for the drop tower test results where the COD and the crack extension were not available. Two methods were proposed. The first one by running FE analysis of the test and selecting the time when the J-integral reached the value of  $10.8 \text{ kJ/m}^2$ . The second one by detecting the loss of linearity in the load vs. deflection curve for which the fractured surface energy density was equal to  $0.11 \text{ kJ/m}^2$ .

As mentioned above, the crack initiation appeared when the load versus deflection deviated from the linearity. The crack then propagates through the remaining ligament. This important result was used in the interpretation of scored skins such that the energy of failure was assumed to be that corresponding to the appearance of the non linearity.

Taking advantage of this and with the help of FE code, the calibration factor  $\eta$  of a clamped SENB specimen was established, as a function of the crack depth ratio.

### 5.1.2. Impact tests

This chapter was first dedicated to the determination of the  $T_{dth}$ . Data treatment was detailed, starting from seeking the initial stiffness so as to correct the deflection. Further characteristic parameters were analysed: the loads and the corresponding deflections at the appearance of non linearity and at the load drop; the energies at these two events.

The evolution of these characteristic parameters with respect to the test temperature was comprehensively analysed. First, data at a deflection speed of  $10 \text{ m/s}$  were selected so as to compare results from the two testing machines (CEAST and HSTT). Attempts were made to identify upper and lower shelves for the load, deflection and energy.  $T_{dth}$  was introduced as the temperature corresponding to the start of the upper shelf, *i.e.* the ductile plateau. Then, the parameters of a tanh function including  $T_{dth}$  were fitted in order to follow the trend of the scattered experimental points. It was observed that even if the characteristic parameters were not always at the same level (few gaps appeared), they show the same curve's variation and most importantly: the same  $T_{dth}$ . The approach was then extended to higher/lower impact speeds on the HSTT and CEAST, respectively.

For scored samples, the energy at the appearance of the nonlinearity was found to be the relevant parameter to determine  $T_{dth}$ .  $T_{dth}$  as a function of the deflection speed showed the same trend for the two aforementioned methods: from  $12 \text{ }^\circ\text{C}$  to  $27 \text{ }^\circ\text{C}$  at deflection speeds ranging respectively from  $2 \text{ m/s}$  to  $23 \text{ m/s}$ .

For unscored specimens, the mechanisms of deformation ahead of the tip of the striker were not the same as those of the unscored sample. There is first an axisymmetric bending of the skin, followed by a crushing of the striker tip into the skin. The failure occurred then leading to a sudden drop of the load. Therefore the characteristic parameters at the load drop were considered as the relevant one. The specificity of unscored specimens results was that, with increasing deflection speed, the deflection and the load at the load drop, respectively increased and decreased continuously. The energy which combined the two parameters remained quite constant whatever the impact speed, at least for the material under study. The “guess” of  $T_{dth}$  was then operated by using the evolution of the load at failure. The fit of  $T_{dth}$  using the *tanh* function could not be carried out. The obtained results showed an evolution of the  $T_{dth}$  from -15 °C to 15 °C at deflection speeds ranging respectively from 2 m/s to 23 m/s.

Fractography analysis was tried on all the samples from both geometries. At macroscopic scale it only allows the determination of the type of failure (brittle, transition or ductile). For unscored HSTT's samples, peculiar geometries were observed. The circular shape's perimeter from the ductile failure was decreasing with the temperature without showing any of the identified signs of embrittlement. At the lowest temperature the perimeter was measured at 7mm (long after the test) which is lower than the diameter of the stricker (20mm) which is known to have punctured. An hypothesis of high strain from build-up heat phenomenon was the only explanation found at the moment. On scored samples the analysis went further with a microscopic scale observation, and an investigation of the evolution of the brittle surface ratio over the total failure surface. A constant decrease of the brittle surfaces showed no peculiar inflexions allowing the determination of a property variation.

In order to check out the performance prevision of the glass transition between two materials, a second PVC formulation was added to the study. A reduced experimental program on the CEAST instrument only was carried out and the  $T_{dth}$  results of these two materials with both geometries were compared.

About the  $T_{dth}$  properties themselves, it was observed that this temperature was increasing linearly from whatever the geometry or the material. From the two PVCs studied it was also noted that they shared the same slope, meaning that the slope is an intrinsic property of the PVC and does not depend on the formulation. It was also deduced that the difference in the sample's geometry did not influence the slope of the  $T_{dth}$  evolution, but added a vertical shift specific to each material. Since two unscored PVCs did not have the same level of  $T_{dth}$ , and that a scoring was adding a specific shift depending on the formulation, it was shown that the performance of two materials can be inverted in function of its geometry (material 1 > material 2 when unscored, but material 2 > material 1 when scored). This last concept is impossible to observe with the glass transition and shows that it is not relevant to compare the performances of materials under impacts.

## 5.2. Prospects

### 5.2.1. Additional experimental studies

#### 5.2.1.1. Three layers 4 points bending

To better understand the mechanisms of ductile crack initiation and propagation near the impacted zone of the three layers assembly, four points clamped bending specimens were tested using an Instron 5966 with a load cell of 10 kN.

The previous clamping system assembly had to be adapted for a much thicker sample (~1mm thickness for the clamped SENB specimens while the assembly is up to 14mm). Jaws had to be drawn using a Computer-Aided Design (CAD) software (Autodesk inventor) to adapt to the specimen geometry in grey in Fig 5.1. The blue, green, and yellow parts are present to compress the sample and prevent any displacement or rotation. The green part was welded to support bars in order to elevate the system and prevent any contact with the specimens. These colored parts were machined in the Centre des Materiaux's workshop. A picture of the jaws assembly with a carrier layer specimen only is displayed on Fig 5.2.

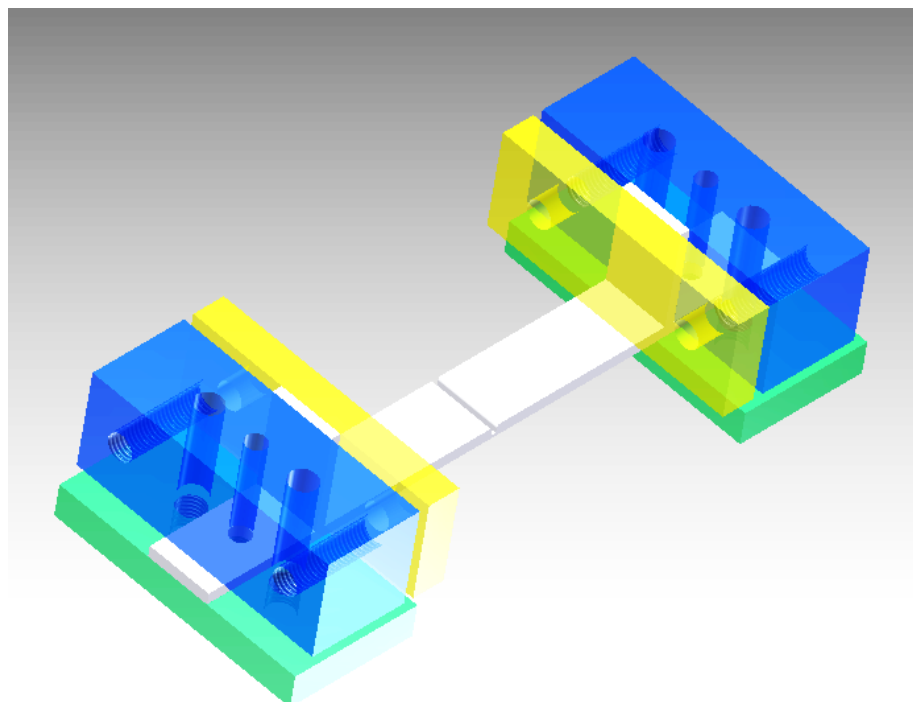


Figure 5.1: Representation of the jaws used for four points clamped bending on three layers assembly

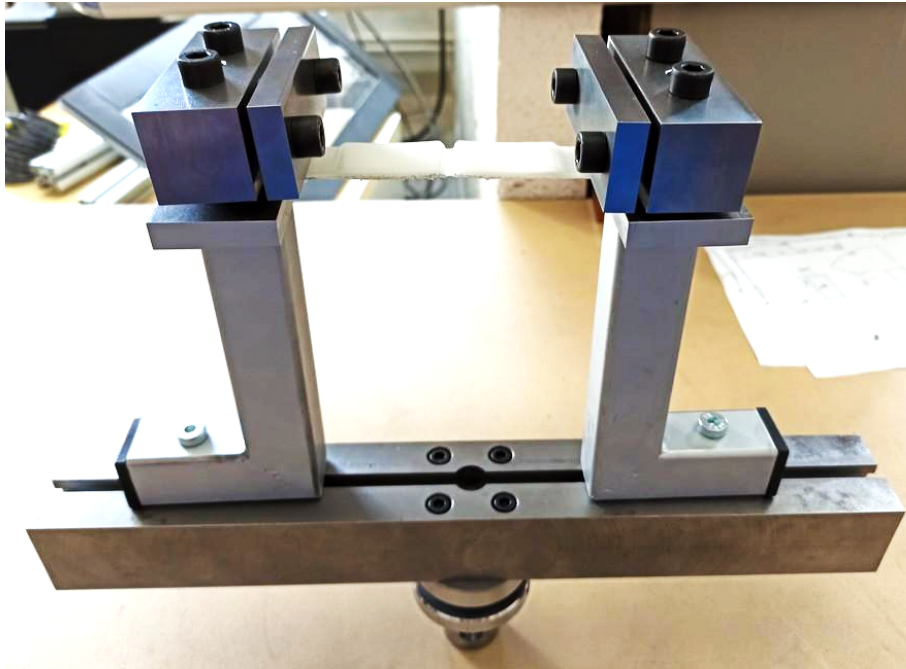


Figure 5.2: Picture of the four points clamped bending system machined

Several airbag firing channels composed of the three materials obtained following the industrial production method were provided.

The assembly is cut with a bandsaw in the Centre des Matériaux's workshop, in slices (2cm x 20cm) with the weakened part (scoring) in the middle. This is the part that is going to be tested with clamped four points bending to study the dashboard failure, and the crack propagation in the different layers with a video camera. A representation of the specimen used for these tests is displayed on Figure 5.3. The out of plan part of the specimen is originally used for fixing the assembly in the global dashboard. Instead of removing it, it was preserved in order to prevent the specimen from slipping between the jaws.

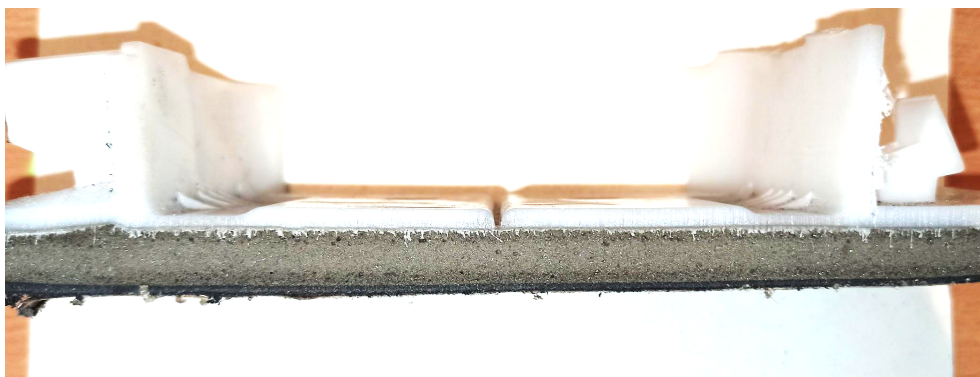


Figure 5.3: Side view of the specimen used for four point clamped bending

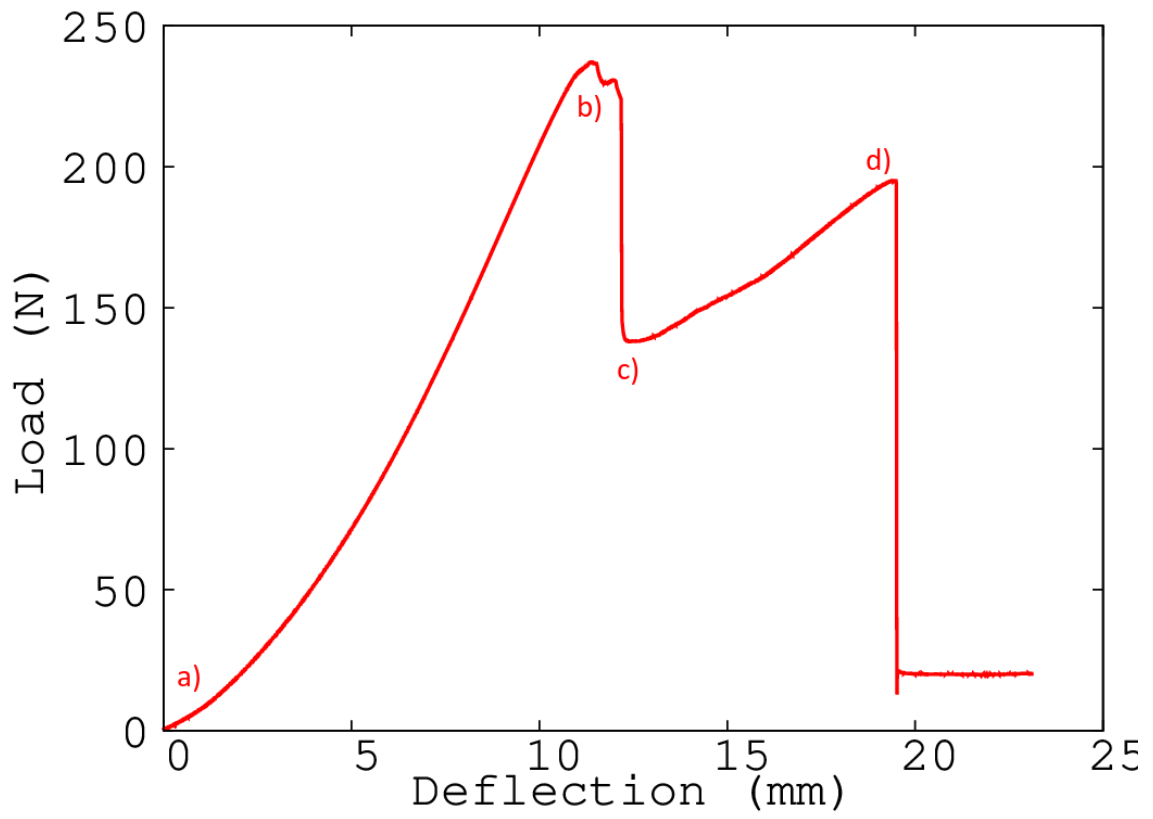
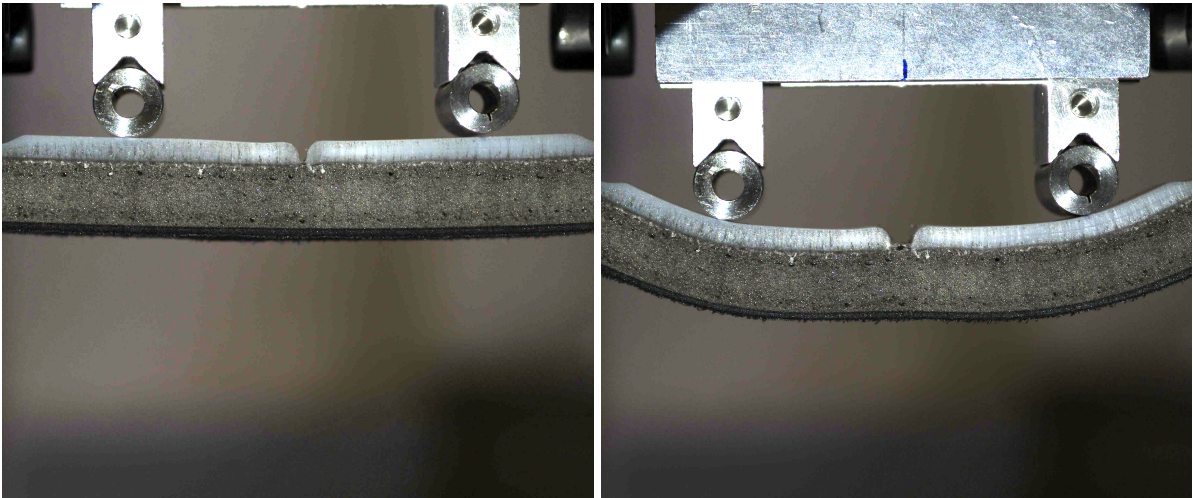
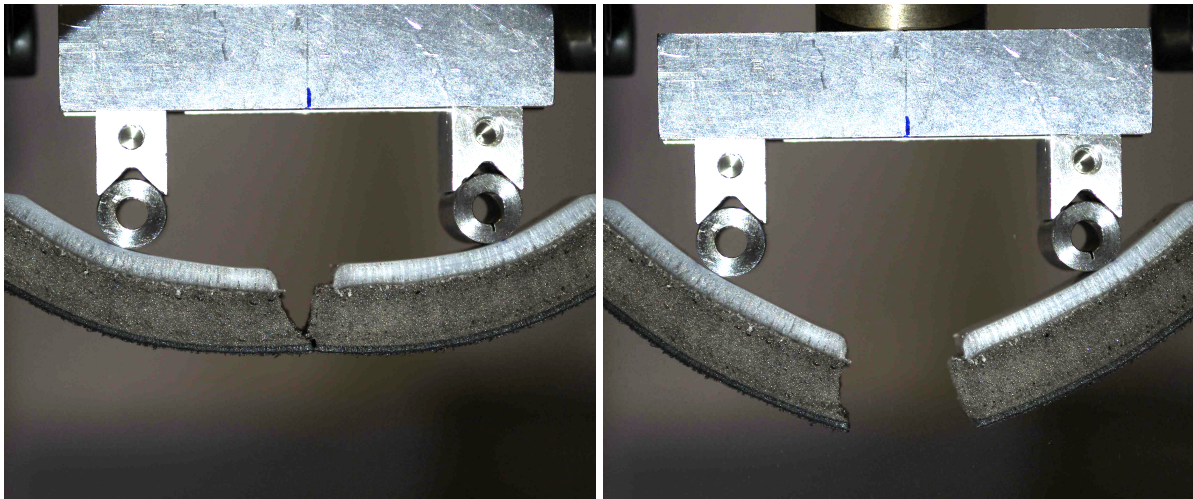


Figure 5.4: First results from four points bending



a)

b)



c)

d)

Figure 5.5: Viewgraphs at the four different instants localised on Figure 5.4 a) beginning of the test, b) failure of the carrier, c) failure of the foam, and d) failure of the skin

In the present work , attention was paid to the skin only. In order to improve the entire dashboard's failure mechanisms, comprehensive testing of such a geometry would be a major key. On Figures 5.4-5 are shown the premises of this study with the evolution of the load with the deflection. On the four located curve's stages a), b), c), and d) are shown the respective sample's picture.

#### 5.2.1.2. 3D DIC on real conditions dashboard opening

In order to test the material in real conditions which means real airbag shots, entire dashboards (PVC skin, PU foam and fiber reinforced PP carrier) were assembled in SMRC's technical center at Harnes (an industrial material [foam and carrier] and service [entire dashboard assembly] provider). For a more realistic observation of the real airbag shot, equipment close to the airbag module are installed, such as the aeration systems but also a metallic structure to represent the weight fixed to the dashboard. A grid is then drawn on the dashboard's top surface above the airbag zone, to allow a camera tracking for the use of Digital Image Correlation (DIC), in two or three dimensions. Recall that a picture of a dashboard ready to be shot is represented in Figure 2.2.

The purpose of such tests would be to improve the skin's failure behaviour during a real airbag shot. By using DIC softwares such as VIC2D or VIC3D, and the right patterns, the software would be able to reconstruct the displacement of located points on the images taken by the cameras in three dimensions. Thus a lot more information would be obtained, such as the real "impact speed" (= the displacement speed in the direction normal to the dashboard's plan), the strain rates in every direction of the plan, etc...

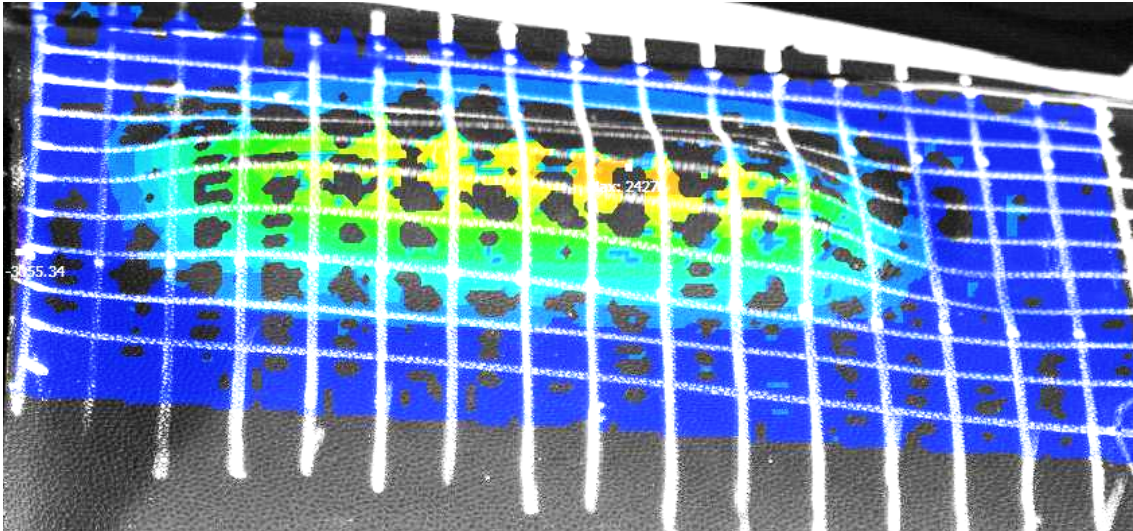


Figure 5.6: Example of results obtain from an airbag shot analysed with 2D DIC

On the figure 5.6 is shown an example of the data analyses thanks to VIC2D's software. It measured the velocity from points on the dashboard in the direction of the top of the picture (2D). The velocity measured was about 24m/s. This measure should be taken with cautions as many sources of uncertainty are present, such as the quality of the pattern which is not suitable for DIC or the out of plane velocity measure in 2D pictures.

### 5.2.1.3. Thermo-mechanical analysis to study self-heating

As observed in section 4.2.4 with some curves' profile, a peculiar increase of the deflection at load drop appears for high temperatures at high impact speeds. It was mentioned that it might come from a build-up heat phenomenon during the test. As it starts to appear at 10m/s, this phenomenon should be amplified with real airbag shots as the impact speed reaches 25m/s on a larger surface. A thermo-mechanical analysis on some HSTT tests at room temperature and with real airbag shot would be of interest.

## 5.2.2. Finite Elements study

As mentioned at the end of the chapter 3, using FE code would allow the optimization of many parameters to lead to a safe deployment of the air bag. In addition, it would enable a better understanding of the material's characteristics no longer in the global sample's scale but in a local area scale (i.e. the crack tip). In order to discover the possibilities few FE simulations were launched on different models:

- the SENB experimental tests (some results appear on the chapter 3)
- Impact tests on unscored samples
- Impact tests on scored samples

### 5.2.2.1. Meshes

The mesh used for SENB simulations and seen on chapter three is presented again on Figure 5.7. Only half of the sample is represented and it is composed by three distinct elements:

- the impactor (semi-circle on the top side left)
- the support (semi-circle on the bottom right side)
- the sample (rectangular part)

The boundary conditions imposed are:

- a clamping on the support and the right side of the sample
- symmetries on the impactor as well as the remaining ligament of the sample
- a vertical displacement on the impactor to control the load
- contacts managed by the Coulomb method

The mesh is composed of 410 2D iso-parametric plane strain elements with reduced integration for a total of 964 Degree Of Freedom (DOF) during the simulation. A “release nodal degree of freedom” (rndof) technique was implemented to simulate the crack propagation.

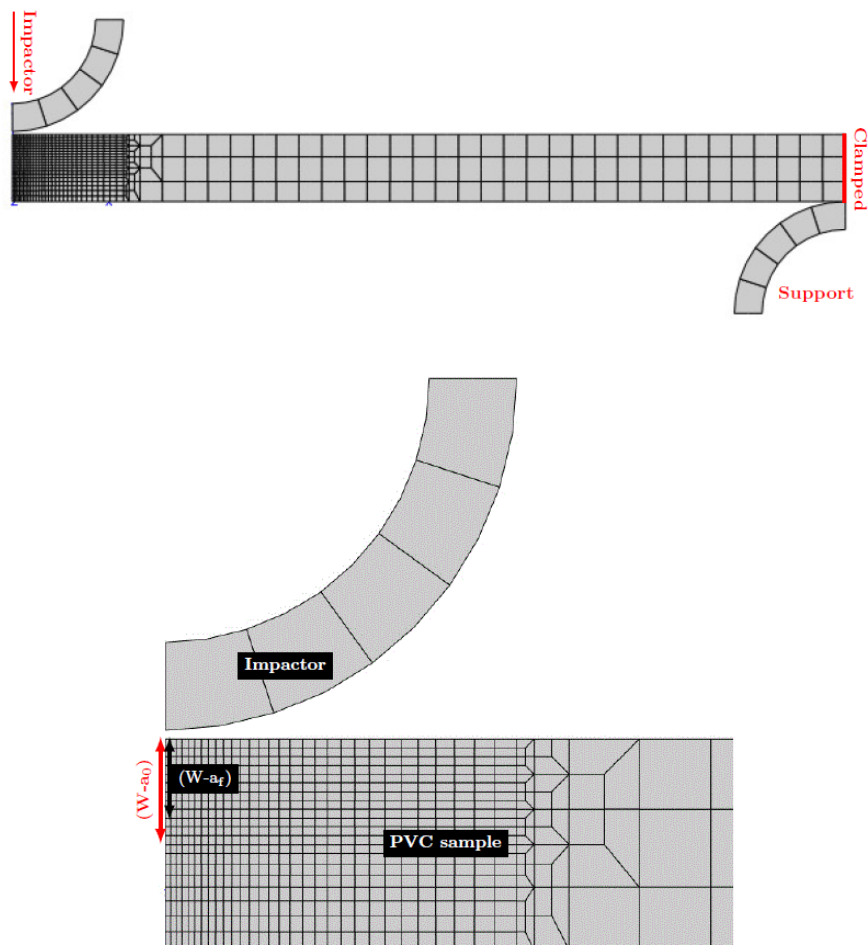


Figure 5.7: Mesh used for SENB simulation

On Figure 5.8 is presented the mesh used for unscored axi-symmetric impact tests. A vertical axis of symmetry on the far right side of the mesh allows a simulation on two dimensions to be compared with three dimensions experimental results. The mesh is composed by:

- the striker (semi-circular part)
- the sample (rectangular part)

The boundary conditions imposed are:

- a clamping on the far left side of the sample
- a symmetry on the vertical axis on the far right side of the impactor and the sample
- a vertical displacement on the impactor to control the load
- a contact managed by the Coulomb method

The mesh is composed of 2062 CAX4 elements for a total of 4748 DOFs during the simulation.

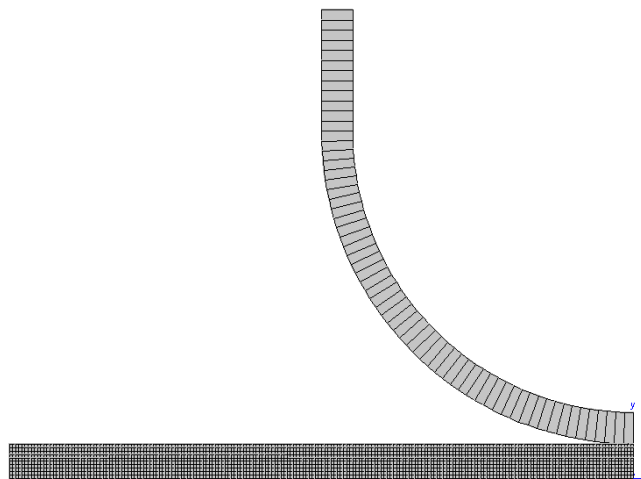


Figure 5.8: Mesh used for axi-symmetric unscored impact simulation

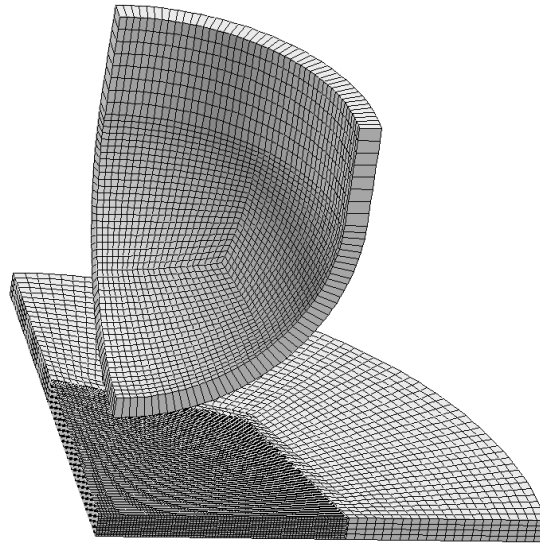
Figure 5.9 displays the mesh used for three dimensions unscored simulations. Only a fourth of the mesh is needed as two plane symmetries allow the whole sample reconstitution. The mesh is composed by:

- the striker (domed surface)
- the sample (plane part)

The boundary conditions imposed are:

- a clamping on the external side of the sample (circular side)
- Plane symmetries along both sides of the impactor and the sample
- a vertical displacement on the impactor to control the load
- contacts managed by the Coulomb method

The mesh is composed of 206200 cax4 elements for a total of 723222 DOFs during the simulation. It is possible to also use this mesh for score three dimensional simulations by changing the symmetry parameters applied on the sample.



The Figure 5.9: Mesh used for axi-symmetric unscored impact simulation

#### 5.2.2.2. First results

All those meshes were at first tested with a simple elasto-plastic model in order to optimize the parameters and reproduce the experimental results. The results obtained with the SENB simulations are displayed in chapter 3 on the FE simulation's section. For the impact simulation it was not sufficient and the simulations were hardly converging. An example is shown on Figure 5.10 with axi-symmetric simulation (here at 6m/s and 15°C).

In this FE on impact tests approach, the purpose was to see if a single (rather) simple constitutive model was enough to simulate all the impact tests with every condition of temperature and impact speed. It meant that a simulation had to be run for every of these conditions and the parameters kept in a table to model their evolutions by an equation. This method was proven to be energy and time consuming, and couldn't be completed.

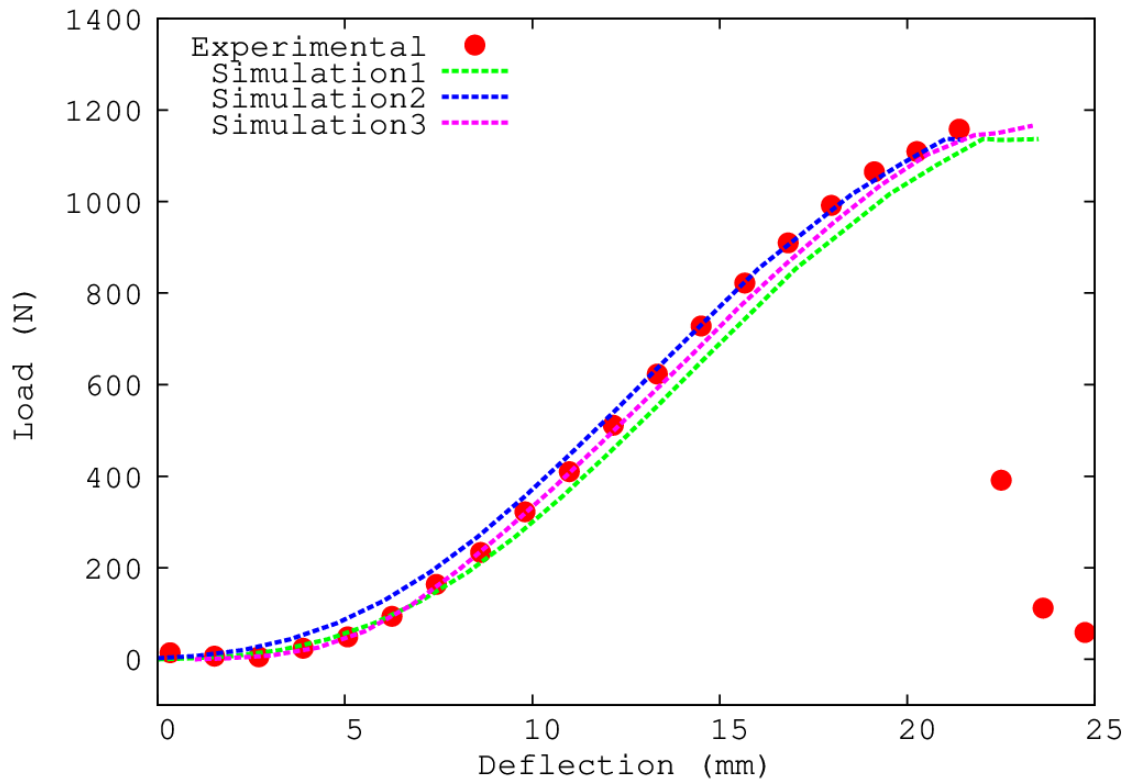


Figure 5.10: Comparison between experimental and simulated results for an unscored impact test of 6m/s and 15°C, with an axi-symmetric geometry.

In Figure 5.11 is shown the deformed mesh after the impact test simulation at 6m/s and 15°C from the above example. The colors here are not relevant to be observed as no physical parameter is the subject of the discussion. Narrowing of the thickness appears, located in the curved part close to the extremity. It can be assumed that it would lead to the failure of the unscored sample. Interestingly, when compared to the hit sample, the simulated and real samples share the same location of the failure. This suggests that the present constitutive model might be sufficient to simulate these impact tests on unscored samples with an axi-symmetric model.

Figure 5.13 shows an example of three dimensional simulations. Only a few simulations were started with this geometry due to its computation cost..

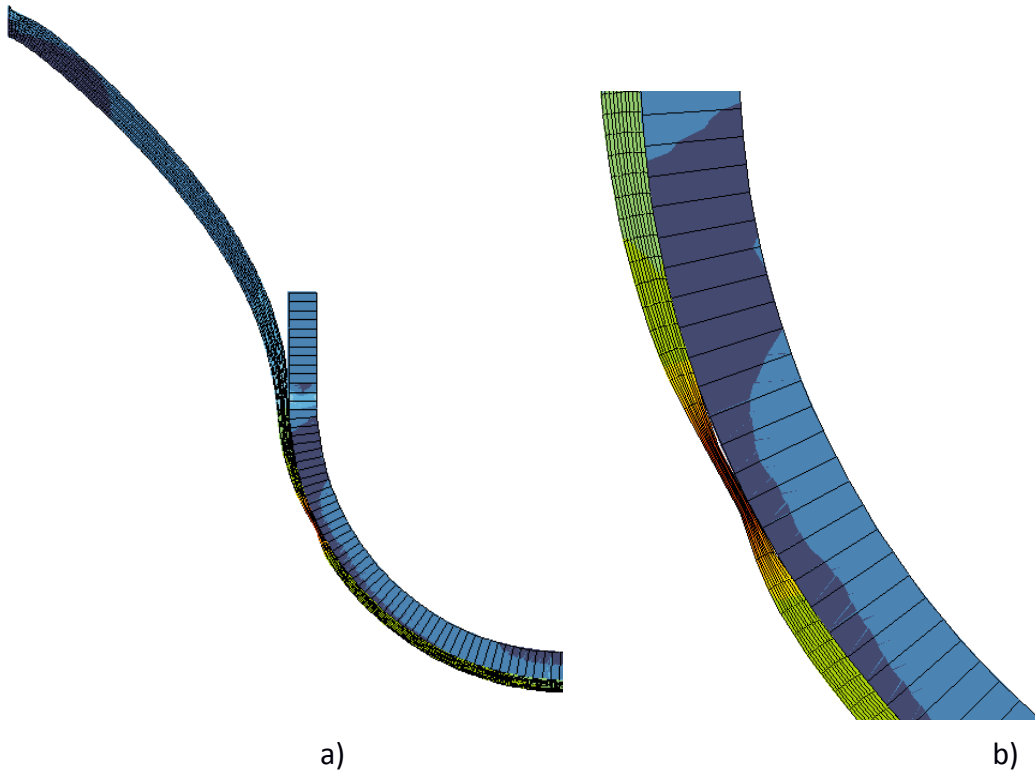


Figure 5.11: Observation of a strained mesh after an impact test simulation a) global mesh and b) zoom on the deformed area

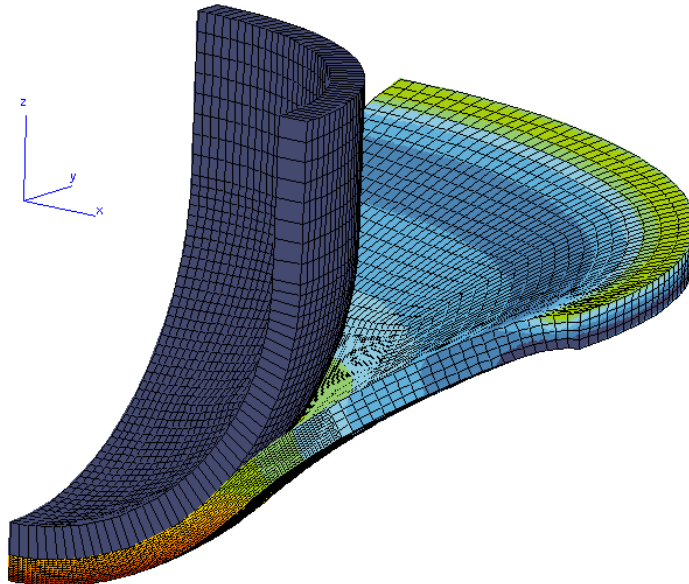


Figure 5.12: Observation of a deformed mesh after an impact test simulation on a 3D unscored simulation

## References:

1. K.R. Cox and R.E. Robertson, Controlling Failure of Polymer Skin/Foam Bilaminate Sheets, SAE Technical Paper 2007-01-1216, SAE International, Warrendale, PA, (2007)
2. Brown, N., Ward, I.M.: The influence of morphology and molecular weight on ductile-brittle transitions in linear polyethylene. *J. Mater. Sci.* 18, 1405–1420 (1983)
3. Corté, L.: Renforcement des polymères semi-cristallins, PhD thesis, ESPCI ParisTech (in French) (2006)
4. Jang, B.Z., Uhlmann, D.R., Sande, J.B.V.: Ductile-brittle transition in polymers. *J. Appl. Polym. Sci.* 11, 3409–3420 (1984)
5. Kambour, R.P., Bernier, G.A.: Craze formation yield stress and the so-called Ductile–Brittle transition in glassy polymers. *Macromolecules* 1(2), 190–191 (1968)
6. Serenko, O.A., Goncharuk, G.P., Obolonkova, E.S., Bazhenov, S.L.: The brittle-ductile transition in rubber-filled polymers. *Polym. Sci. Ser. A* 48(3), 302–313 (2006)
7. van Melick, H.G.H., Govaert, L.E., Meijer, H.E.H.: Prediction of brittle-to-ductile transitions in polystyrene. *Polymer* 44(2), 457–465 (2003)
8. Collyer, A.A.: Rubber Toughened Engineering Plastics. Springer, Berlin (2012)
9. Messiha, Mario & Frank, Andreas & Berger, Isabelle & Heimink, Jan & Laak, Hermann & Arbeiter, Florian & Pinter, Gerald. (2018). Determination of the Slow Crack Growth Resistance of PA12 Pipe Grades
10. L. Laiarinandrasana, Y. Nziakou, J.L. Halary, Fracture behavior of amorphous and semicrystalline blends of poly(vinylidene fluoride) and poly(methyl methacrylate), *Journal of Polymer Science Part B: Polymer Physics*, 50(24), 1740–1747 (2012)
11. M. Challier, J. Besson, L. Laiarinandrasana, R. Piques, Damage and fracture of polyvinylidene fluoride (PVDF) at 20°C: experiments and modelling, *Engineering Fracture Mechanics*, 73, 79–90 (2006)
12. "Matériaux métalliques – Essai de flexion par choc sur éprouvette Charpy" (NF EN 10045-1, indice de classement A 03-011)
13. Abdeldjalil, Alghem. (2016). Comportement de transition ductile-fragile de l'acier X60. 10.13140/RG.2.1.5193.4483
14. Marais, Anthony. (2012). Influence of the static strain ageing on the ductile-to-brittle transition in C-Mn steel.
15. C. Bertaux, N. Amouroux, C. Ovalle Rodas, L. Laiarinandrasana, Impact speed dependency of the ductile failure threshold temperature for a plasticized Polyvinylchloride, *submitted to Continuum Mechanics and Thermodynamics* (Bertaux et al. 2021, #) (2020)
16. ISO 6603-2:2000, Plastics – Determination of puncture impact behaviour of rigid plastics – Part 2:

Instrumented impact testing. <https://www.iso.org/en/standard/25172.html>

17. Ashida K. Polyurethane and Related Foams Chemistry and Technology. Taylor & Francis Group; Boca Raton, FL, USA: 2007

18. Szycher M. Szycher's Handbook of Polyurethanes. 2nd ed. CRC Press; New York, NY, USA: 2006

19. Tcharkhtchi, A.: Rotomoulage de pièces en matière thermoplastique. Techniques de l'ingénieur Plasturgie : fabrications de corps creux, de films et de fils, TIB149DUO. am3706 (2004). <https://www.techniques-ingenieur.fr/base-documentaire/materiaux-th11/plasturgie-fabrications-de-corps-creux-de-films-et-de-fils-42149210/rotomoulage-de-pieces-en-matiere-thermoplastique-am3706/>

20. Crawford, R.J., Throne, J.L.: 2-Rotational Molding Polymers. In: Crawford, R.J., Throne, J.L. (eds.) Rotational Molding Technology, pp. 19–68. William Andrew Publishing, Norwich (2002)

21. Y. Saeki, T. Emura, Technical progresses for PVC production, Progress in Polymers science, Volume 27, Issue 10, 2002

22. Stanley R. Sandler, Wolf Karo, Suspension Polymerization 378 in [Polymer Syntheses \(Second Edition\), Volume 2](#), 1994

23. Bao, Y.Z. and Brooks, B.W. (2003), Particle features of poly(vinyl chloride) resins prepared by a new heterogeneous polymerization process. J. Appl. Polym. Sci., 90: 954-958. <https://doi.org/10.1002/app.12685>

24. C. Pasquet. Raw material, slush formulation training, NAKAN INNOVATIVE VINYLs, Février 2017

25. M. Schiller. PVC Additives, Performance, Chemistry, Developments, and Sustainability, Hanser, 2015

26. Melissa Gurgel Adeodato Vieira, Mariana Altenhofen da Silva, Lucielen Oliveira dos Santos, Marisa Masumi Beppu, Natural-based plasticizers and biopolymer films: A review, European Polymer Journal, Volume 47, Issue 3, 2011, Pages 254-263

27. S Rajendran, M Sivakumar, R Subadevi, Investigations on the effect of various plasticizers in PVA–PMMA solid polymer blend electrolytes, Materials Letters, Volume 58, Issue 5, 2004

28. C. E. Wilkes, C. A. Daniels, J. W. Summers. PVC Handbook, ISBN 3-446-22714-8, chap 5

29. B. DIEGO. Présentation des plastifiants, ARKEMA, Janvier 2005

30. T.J Turton, J.R White, Effect of stabilizer and pigment on photo-degradation depth profiles in polypropylene, Polymer Degradation and Stability, Volume 74, Issue 3, 2001

31. Greco, A. and Maffezzoli, A. (2017), Rotational Molding of Poly(lactic acid): Effect of Polymer Grade and Granulometry. Adv. Polym. Technol., 36: 477-482. <https://doi.org/10.1002/adv.21630>

32. ASTM B213 - 20, Standard Test Methods for Flow Rate of Metal Powders Using the Hall Flowmeter Funnel

33. ISO 4490:2018 - Poudres métalliques — Détermination du temps d'écoulement au moyen d'un entonnoir calibré (appareil de Hall)
34. ASTM B964 - 16 Standard Test Methods for Flow Rate of Metal Powders Using the Carney Funnel
35.  
<https://www.google.com/imgres?imgurl=https%3A%2F%2Ffilab.fr%2Fwp-content%2Fuploads%2F2021%2F08%2Ftest-coulabilite-hall-carney-1.jpg&imgrefurl=https%3A%2F%2Ffilab.fr%2Ftest-coulabilite-hall-carney&tbnid=FsL-nKYOVlob0M&vet=12ahUKEwjhsYzdruPzAhXC3eAKHWaaDcwQMygAegQIARAR..i&docid=jYRzJS7bD1nfM&w=500&h=330&q=filab%20cone%20de%20hall&client=firefox-b-e&ved=2ahUKEwjhsYzdruPzAhXC3eAKHWaaDcwQMygAegQIARAR>
36.  
[https://www.google.com/url?sa=i&url=https%3A%2F%2Fknowledge.ulprospector.com%2F10780%2Fpc-the-cielab-lab-system-the-method-to-quantify-colors-of-coatings%2F&psig=AOvVaw2QqZAAm5fNji\\_DDSIGTH\\_t&ust=1635176621344000&source=images&cd=vfe&ved=OCAsQjRxqFwoTCNjS6uWx4\\_MCFQAAAAAdAAAAABAE](https://www.google.com/url?sa=i&url=https%3A%2F%2Fknowledge.ulprospector.com%2F10780%2Fpc-the-cielab-lab-system-the-method-to-quantify-colors-of-coatings%2F&psig=AOvVaw2QqZAAm5fNji_DDSIGTH_t&ust=1635176621344000&source=images&cd=vfe&ved=OCAsQjRxqFwoTCNjS6uWx4_MCFQAAAAAdAAAAABAE)
37. R.Duane Douglas, Color stability of new-generation indirect resins for prosthodontic application, *The Journal of Prosthetic Dentistry*, Volume 83, Issue 2, 2000
38. Yong-Keun Lee, Comparison of CIELAB  $\Delta E^*$  and CIEDE2000 color-differences after polymerization and thermocycling of resin composites, *Dental Materials*, Volume 21, Issue 7, 2005
39. Kadam, A.A., Karbowski, T., Voilley, A. *et al.* Plasticization of amorphous polystyrene by volatile organic compounds. *Polym. Bull.* **73**, 1841–1853 (2016). <https://doi.org/10.1007/s00289-015-1580-4>
40. Torres, Juan Pablo & Frontini, Patricia & Machado, Martín & Major, Zoltan. (2016). Deformation and failure of semicrystalline polymers under dynamic tensile and biaxial impact loading. *International Journal of Impact Engineering*. 98. 10.1016/j.ijimpeng.2016.08.004
41. Instron, CEAST, Impact Testing Handbook
42. A. Pavan et al, Determination of fracture toughness (GIC and KIC) at moderately high loading rates, *European Structural Integrity Society*, Volume 28, Pages 27-58, [https://doi.org/10.1016/S1566-1369\(01\)80026-1](https://doi.org/10.1016/S1566-1369(01)80026-1)
43. L.Laiarinandrasana, C.Bertaux, N.Amouroux, C.Ovalle Rodas, Ductile crack initiation and growth on a plasticized Polyvinylchloride during air bag deployment, *Journal of Theoretical, Computational and Applied Mechanics*, DOI 10.46298/jtcam.7401, 2021
44. ISO 179-1:2010, *Plastics – Determination of Charpy impact properties – Part 1: Non instrumented impact test*. <https://www.iso.org/>
45. ASTM D6110, *Standard Test Method for Determining the Charpy Impact Resistance of Notched Specimens of Plastics* <https://www.astm.org/Standards/D6110>
46. J.G. Williams,  $K_C$  and  $G_C$  at low speed for polymers, *Fracture Mechanics testing methods for polymers, adhesives and composites*, Edited by D.R. Moore, A. Pavan and J.G. Williams, ESIS Publication 28 , p. 159-175, (2001)

47. G. Hale et F. Ramsteiner, J-Fracture toughness of polymers at slow speed, Mechanics testing methods for polymers, adhesives and composites, Edited by D.R. Moore, A. Pavan and J.G. Williams,ESIS Publication 28 p. 123–157 (2001)
48. B. Tanguy, C. Bouchet, S. Bugat, J. Besson, Local approach to fracture based prediction of the  $\Delta T_{56J}$  and  $\Delta TK_{c100}$  shifts due to irradiation for an A508 pressure vessel steel, Engineering Fracture Mechanics, 73, 191–206 (2006)
49. F. Baldi, S. Agnelli, T. Ricc`o, On the determination of the point of fracture initiation by the load separation criterion in J-testing of ductile polymers, Polymer Testing 32, 1326–1333 (2013)
50. S. Agnelli, F. Baldi, B.R.K. Blackman, L. Castellani, P.M. Frontini d, L. Laiarinan drasana, A. Pegoretti, M. Rink, A. Salazar, H.A. Visser, Application of the load separation criterion in J-testing of ductile polymers: A round-robin testing exercise, Polymer Testing 44, 72–81 (2015)
51. F. Baldi, S. Agnelli, L. Andena, B. Blackman, L. Castellani, P. Frontini, J. Kucera, L. Laiarinandrasana, A. Pegoretti, A. Salazar, L. Warnet, Determination of the Fracture Resistance of Ductile Polymers: The ESIS TC4 Recent Experience, Materials Performance and Characterization 9 (5), 675–687 (2020)
52. W. Bohme, H.J. MacGillivray, Experience with instrumented Charpy tests obtained by a DVM round-robin and further development, Evaluating Material Properties by Dynamic Testing ESIS 20, Edited by E. van Walle, Mechanical Engineering Publications, London p. 1-23, (1996)
53. J.H.Bulloch, A study concerning material fracture toughness and some small punch test data for low alloy steels, Engineering Failure Analysis, 11(4), 635–653 (2004)
54. H.J. MacGillivray, Fracture toughness of polymers at impact speed, Fracture Mechanics testing methods for polymers, adhesives and composites, Edited by D.R. Moore, A. Pavan and J.G. Williams, ESIS Publication 28 , p. 159-175, (2001)
55. L. Laiarinandrasana, M.R. Kabiri, M. Reytier, Effect of specimen geometries on the  $C^*$  versus  $da/dt$  master curve for type 316L stainless steel, Engineering Fracture Mechanics 73, 726–737 (2006)
56. A. Marcellan, A. Bunsell, R. Piques, L. Laiarinandrasana, In Situ Tensile Tests to Analyze the Mechanical Response, Crack Initiation, and Crack Propagation in Single Polyamide 66 Fibers, Journal of Polymer Science, Part B: Polymer Physics 57, 680–690 (2019)
57. H.G. de Lorenzi, On the energy release rate and the J-integral for 3-D crack configurations, International Journal of Fracture 19, 183 –193 (1982)
58. W.Brocks, G.Knecke, H.D. Noack, H.Veith, On the transferability of fracture mechanics parameters from specimens to structures using fem, Nuclear Engineering and Design, 112, 1–14 (1989)
59. Mohagheghian I, McShane G, Stronge W. Impact perforation of monolithic polyethylene plates: projectile nose shape dependence. Int J Impact Eng 2015;80:162–76
60. W. Oldfield" Fitting Curves to Toughness Data." *Journal of Testing and Evaluation* 7, no. 6 (1979): 326-333. <https://doi.org/10.1520/JTE11508J>
61. Y. Sakai, K. Tamanoi, N. Ogura, Application of tanh curve fit analysis to fracture toughness data of

Japanese RPVS, Nuclear Engineering and Design, Volume 115, Issue 1, 1989, [https://doi.org/10.1016/0029-5493\(89\)90257-4](https://doi.org/10.1016/0029-5493(89)90257-4)

62. Cedric Regrain, Lucien Lailarinandrasana, Sophie Toillon, Kacem Saï, Multi-mechanism models for semi-crystalline polymer: Constitutive relations and finite element implementation, International Journal of Plasticity, Volume 25, Issue 7, 2009, <https://doi.org/10.1016/j.ijplas.2008.09.010>

## RÉSUMÉ

---

Dans cette thèse est analysée la résistance à l'impact de deux peaux en PVC plastifiées utilisées dans l'industrie automobile. En règle générale, ces matériaux sont comparés entre eux via des techniques physico-chimiques comme la transition vitreuse ( $T_g$ ) qui ne permet pas toujours de représenter les performances en conditions réelles d'utilisation de ces matériaux, notamment leur rupture. Dans le but d'améliorer la compréhension de la rupture de ces peaux et de proposer une alternative plus pertinente que la  $T_g$ , la notion de Température seuil de rupture ductile ( $T_{dth}$ ), variante de la DBTT, a été proposée sur des éprouvettes non-entaillées comme entaillées. Dans un premier temps, une étude sur les mécanismes de la rupture appliqués aux éprouvettes entaillées a été menée grâce à des essais de flexion trois points encastres avec suivi vidéo, complétée par une simulation numérique aux Éléments Finis (FE). Cette étude a notamment permis d'identifier le facteur de calibration utilisé pour la mesure de la ténacité  $J$ . Cela a également permis d'observer que dans le cas de ces matériaux, la propagation de la fissure commence à l'apparition de la non linéarité et non au moment de la charge maximale  $C_e$  résultat a par la suite été utilisé pour définir les paramètres à utiliser afin de déterminer la  $T_{dth}$  via les essais d'impact. Ces essais d'impact ont été réalisés en utilisant deux machines différentes: la CEAST9350 et la machine de Traction à Grande Vitesse (TGV ou HSTT) afin d'explorer une large gamme de vitesses d'impact (de 2 m/s à 23 m/s). L'utilisation d'une fonction  $\tanh$  a permis d'optimiser l'identification des paramètres de la  $T_{dth}$  puis de les comparer pour les deux géométries ainsi que les deux matériaux. Les résultats obtenus montrent que la  $T_{dth}$  croît de manière linéaire avec la vitesse d'impact et possède la même pente quelle que soit la géométrie ou la formulation. Par contre, à une vitesse d'impact donnée, la  $T_{dth}$  d'un matériau entaillé sera toujours supérieure mais cet écart est différent pour chaque PVC étudié. De même, pour une même géométrie, les deux PVCs ne possédaient pas la même  $T_{dth}$ . Une inversion dans les performances des matériaux a été observée avec un matériau 1 non entaillé plus performant que le matériau 2, mais moins compétitif dans le cas des éprouvettes entaillées. Cette notion n'est pas possible à observer avec la  $T_g$  seule.

## MOTS CLÉS

---

PVC plastifié, transition ductile-fragile, rupture ductile, tests d'impact

## ABSTRACT

---

In this thesis, the impact resistance of two plasticized PVC skins used in the automotive industry is analyzed. Generally, these materials are compared between them by using physico-chemical techniques such as the glass transition ( $T_g$ ) which does not always allow to represent the performances in the real condition of use of these materials. In order to improve the understanding of the failure of these skins and to propose a more relevant alternative to the  $T_g$ , the notion of ductile failure threshold temperature ( $T_{dth}$ ) has been proposed (variant of the DBTT) on unscored and scored specimens. In the first step, a study of the fracture mechanisms applied to scored specimens was carried out thanks to clamped SENB tests with video monitoring, completed by a numerical simulation with Finite Elements (FE). This study allowed the identification of the calibration factor used for the measurement of the fracture toughness. It also allowed the observation that for these materials, the crack propagation starts at the apparition of the nonlinearity and not at the maximum load. This result was then used to define the parameters to be used to determine the  $T_{dth}$  via impact tests. These impact tests were performed using two different machines: the CEAST9350 and the High Speed Tensile Test (HSTT) machine in order to explore a wide range of impact speeds (from 2 m/s to 23 m/s). The use of a  $\tanh$  function allowed to optimize the identification of the parameters of the  $T_{dth}$  in order to compare it for the two geometries and the two materials. The results obtained show on the one hand that the  $T_{dth}$  grows linearly with the impact speed and has the same slope whatever the geometry or the formulation. On the other hand, at a given impact speed, the  $T_{dth}$  of a scored material will always be higher than unscored's, but this difference changes for each PVC studied. Similarly, for the same geometry, the two PVCs did not have the same  $T_{dth}$ . An inversion in the performance of the materials was observed with material 1 performing better unscored than material 2, but is less competitive in the case of scored specimens. This notion is not possible to observe with  $T_g$  alone.

## KEYWORDS

---

Plasticized PVC, ductile to brittle transition, ductile failure, impact tests